Sonar Systems Performance in the Mediterranean Sea

by

Sela Mordechai Meyouhas

B.S. in Electrical Engineering and Computer Science
Ben–Gurion University of the Negev, 1989

SUBMITTED TO THE DEPARTMENT OF OCEAN ENGINEERING IN PARTIAL
FULFILLMENT OF THE REQUIREMENTS FOR THE DEGREE OF

MASTER OF SCIENCE IN OCEAN ENGINEERING
AT THE
MASSACHUSETTS INSTITUTE OF TECHNOLOGY

FEBRUARY 1997

Author ....
......../..
Department of Ocean Engineering

January 17, 1997

Certified by ....~....................../...
/ Ira Dyer, Professor of Ocean Engineering
Thesis Supervisor, Department of Ocean Engineering

Accepted by ..../..
/ J. Kim Vandiver, Professor of Ocean Engineering
Chairman, Departmental Committee on Graduate Studies

Sonar Systems Performance in the Mediterranean Sea

by

Sela Mordechai Meyouhas

Submitted to the Department of Ocean Engineering

on January 17, 1997 in Partial Fulfillment of the

Requirements for the Degree of Master of Science in

Ocean Engineering

Abstract

A comparative study has been performed to evaluate the performance of three passive sonar systems at three different locations in the eastern Mediterranean sea. The study includes a typical diesel electric submarine as a sound source and the transmission loss calculations were based on ray theory that incorporated the local environmental conditions as well as a simplified bottom bathymetry and structure. The environmental conditions during the summer and winter are considered two extreme cases and the analysis is, therefore, carried out separately for the two seasons. Three types of passive Sonar systems were evaluated. Each sonar system is based on the same receiver but different array configuration — towed array, hull mounted array, and bow array. The sonar systems, used as receivers, were placed at a distance of up to 50 (km) from the source, at different depths, and in different directions to reflect the bottom's slope influence on the transmission loss. Primary interest is on the signal to noise ratio at the receiver's output where the ambient noise estimations are based on the classical paper by Wenz [12]. Results show high dependency of transmission loss on bottom topography, season, and sonar system. The performance analysis of the sonar systems, presented in terms of their figure of merit, is shown for different frequency bands due to their different array configurations. Results show that during the winter (cold season) convergence zones are formed near the sea surface while during summer (warm season) the convergence zones do not reach the sea surface due to down refractive sound velocity gradient at the surface theromcline. Also shown that the performance of sonar systems are better for up and cross-slope cases than down-slope case. Generally, the detection of the source is most probable with towed array, for narrow-band, and with bow array, for broad-band. Finally, the structure of this study can establish a convenient framework for analyzing sonar systems.

Thesis Supervisor: Ira Dyer

Title: Professor of Ocean Engineering

Acknowledgments

I would like to thank Prof. Dyer for his advise and guidance. His knowledge and experience have guided me, throughout the last 18 months, in my thoughts and in practice. His helpful suggestions and hints served the basis of this thesis. Thanks also to the students from the acoustic group for their good advice.

As a Lieutenant in the Israeli Navy I could not thank enough the Israeli Navy that sponsored me and enabled me to pursue my education in the fascinating field of underwater acoustics and sonar systems.

I would also like to thank my wife that with her continuous love, care, and support, both mentally and physically, the writing of this thesis came to an end. Thanks for being my wife.

Many thanks are sent from here to our families in Israel that supported us in any way possible.

Contents

List of Figures

List of Tables

Nomenclature

- A : amplitude

- a : coefficient

- AG : array gain

- $B(k)$: beampattern in k domain

- $B_n{}^2$: the average of $B^2(f,\Omega)$ on the noise main axis

- $B(s)$: beampattern in s domain

- $B(f,\Omega)$: beampattern in (f,Ω) domain

- b : bandwidth

- b_{BB} : bandwidth for broadband

- b_{NB} : bandwidth for narrowband

- c : sound velocity

- c_o : reference sound speed

- c_v : sound speed of vertexing rays

- D : diameter

- d : distance between the sensors

- d_f : directivity factor

- d_{fb} : directivity factor of buffled arrays

- DFT : discrete Fourier transform

- DI : directivity index

- DT : detection threshold

- f : frequency

- f_l : lower frequency limit

- f_o : center frequency

- FOM : figure of merit

- f_u : upper frequency limit

- g : SVP gradient

- H : transmission loss

13

- H_1 : transmission loss due to spreading alone

- h : altitude of both receiver and target

- K : number of independent samples

- k : wave number

- L : length of the array

- L_n : noise spectrum level

- L_{n_e} : post array noise spectral level

- L_p : pressure level

- L_{p/N_e} : signal to noise level

- L_{N_e} : post array noise level

- L_s^T : source level

- N : number of elements

- NB : narrow band

- P : hydrostatic pressure (chapter 2)

- P : output pressure (chapter 6)

- $P(d)$: probability of detection

- $P(fa)$: probability of false alarm

- $P(t,\mathbf{x})$: pressure field

- R : range from source to receiver

- R : average path length from source to bottom (section 4.2)

- r_c : radius of curvature of the ray

- ROC : receiver operator characteristics

- RPM : rotations per minute

- S : salinity

- s : $\sin(\theta)$

- S_a : value of S_n on array main axis

- SE : signal excess

- $S(f,\Omega)$: noise spatial density

- S_g : area of the great circle of the spherical shell

- S_n : noise spectral density

- S_{n_e} : post array noise spectral density

- SNR : signal to noise ratio

- S_T : source spectrum density

- SVP : sound velocity profile

- T : temperature

- t : time

- T_i : discrete taper function

- $\mathbf{x}$: spatial vector

- z : depth

- z_i : vector to sensor i location

- z_0 : reference location

Greek Letters

- α : absorption coefficient (chapter 4)

- α : vertical angle, measured from the vertical (chapter 6,7)

- α_1 : angle to the first zero of the beampattern

- α_e : equivalent angle width

- β : average bottom slope

- $\Delta\phi$: the beamwidth of the active source

- δ_b : RMS roughness height of the bottom

- δ_s : RMS surface wave height

- η : error in refraction angle

- η_e : equivalent beamwidth

- θ : vertical angle measured from the horizontal

- θ_e : equivalent angle width

- θ_0 : steering angle

- θ_s : propagation angle of the ray with respect to the horizontal

- $\kappa(x)$: wave front function

- λ : wave length

- λ_c : characteristic length scale of the bottom

- λ_i : direct observation scale

- λ_j : transverse observation scale

- λ_{os} : observation scale

- σ : RMS bottom slope

- τ : integration time (chapter 3)

- τ : pulse width (chapter 4)

- ϕ_e : equivalent beamwidth of the receiver (chapter 4)

- $\Phi(x)$: amplitude of the wave solution

- ω : radial frequency

- Ω : solid angle

- Ω_e : equivalent solid angle

- Ω_{eb} : equivalent solid angle of buffled arrays

- Ω_n : noise equivalent solid angle

Chapter 1

Introduction

The evaluation of sonar systems' performance not only involves the unique characteristics of the systems themselves but also the environmental conditions that influence the propagation of sound in the sea. The sound velocity profile, which affects the direction to which sound propagates, is a function of the thermodynamics parameters that include salinity, temperature, and pressure. As opposed to pressure and salinity, the temperature of the upper water column changes substantially over seasons and even from day to night. These substantial differences in temperature change the sound velocity profile in the upper water column and therefore affect the propagation of sound in the water. The changes in the sound velocity profile between the cold season and the warm season can, sometimes, represent two extreme cases of propagation.

During the cold season the temperature gradient in the upper water column is relatively small, causing, in open ocean, a positive isogradient sound velocity profile. During the warm season, however, the temperature profile gradient, in the upper water column, becomes negative causing a negative sound velocity gradient. A positive sound velocity gradient is often referred to as "upward refractive" gradient, which bends the acoustics "rays" upward, while the negative gradient is referred to as "downward refractive" and bends the acoustic rays downward. This bending effect can cause a substantial change in acoustic pressure as a function of range and depth between the seasons, and thus directly affects the performance of the sonar system. The change in acoustic pressure due to transmission or propagation of sound in the medium is often called the "transmission loss."
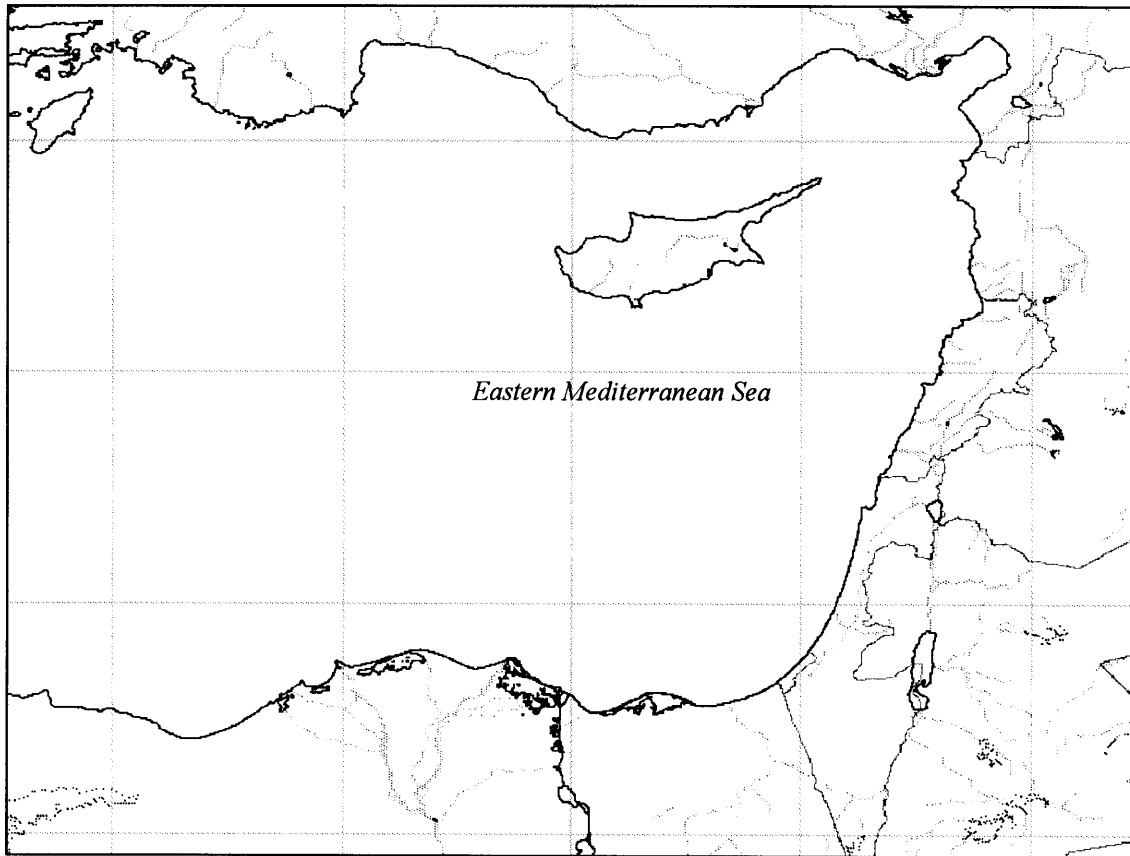
Figure 1.1: A map of the eastern Mediterranean sea

In addition, when investigating the propagation of sound for relatively short distances, less than 50 km, and for relatively shallow water the bottom characteristics may substantially affect the transmission of sound because of bottom interaction with the acoustic pressure. The bottom shape and structure determine how reflective the bottom is, or in other words, the "bottom loss."

The area being investigated in this research is the eastern Mediterranean sea, which is bounded from the east by Israel and Lebanon, from the south by Egypt, and from the north by Turkey. A map of the eastern Mediterranean area can be seen in Figure 1.1. The Mediterranean sea is open to the Atlantic ocean via the Strait of Gibraltar which is only about 400 m deep. This is one of the reasons that this sea has unique characteristics which are different than one might find in the open ocean. Among its unique characteristics are the

temperature profile, salinity profile, and sound speed profile. As an example, the water temperature at the bottom never goes below 13° C as opposed to the open ocean where the water temperature at the bottom reaches 4° C. Furthermore, the average salinity in the Mediterranean sea is 39 ppt and not 35 as in the open ocean. The unique salinity and temperature profiles directly affect the sound speed profile in this area and therefore affect the propagation of sound as well.

The geological structure of the upper layers of the eastern Mediterranean sea bottom is constructed mostly out of layers of various types [17]. The most common are sand, silt, and clay, and as one goes deeper the upper layer is composed mostly of silty clay, or mud. These facts are, in general, true for most of the eastern Mediterranean seabed. The main sources of the sediments are the Nile River, which transports yearly about 57 million tons of sediments, shore abrasion, and beach sediments. Due to the existing counter-clockwise currents in the eastern basin of the sea, a relatively large portion of the sand and the mud reaches the bottom of the eastern Mediterranean basin. The sand layer thickness varies from several meters deep to less than a meter. In average, the thickest sand layers can be found in troughs and the narrowest are most probable to appear near the edge of a cliff. Underneath the sand layers there are layers of Kurkar (carbonate-cemented quartz eolianites [17]). The sand and mud layers are relatively soft compared to the Kurkar, which is a relatively hard sediment.

As mentioned earlier, the bottom must be described by both structure and bathymetry. A rough bathymertric map of the area of interest is presented in Figure 1.2. Morphologically, the continental margin off the western part of Israel and Lebanon is divided into two distinct areas where Haifa and mount Carmel separate the two. The southern continental margin is wide, about 40 - 50 km, and has a generally smooth and rounded topography. The northern continental margin is, however, much narrower, 12 - 13 km, and much more disturbed. The continental slope of both the northern part and the southern part is scarred by ancient evaporates and volcanic activity that form a disturbed slope. Together with the adjacent mountains in the northern part of the continent, the northern continental slope is rather steep, and in some areas can even be greater than 10° in average. In addition, the northern continental slope can be characterized by its submarine

canyons, which form a rough bottom surface. The southern continental slope is much more moderate and has an average slope of less than 1°. On the other hand, it is covered with large scale slumps and fault blocks so that the seabed can be described as rough and can have different properties in different areas, depending on the scale of the disturbance. A much more detailed discussion on this can be found in [17, 18, 19].
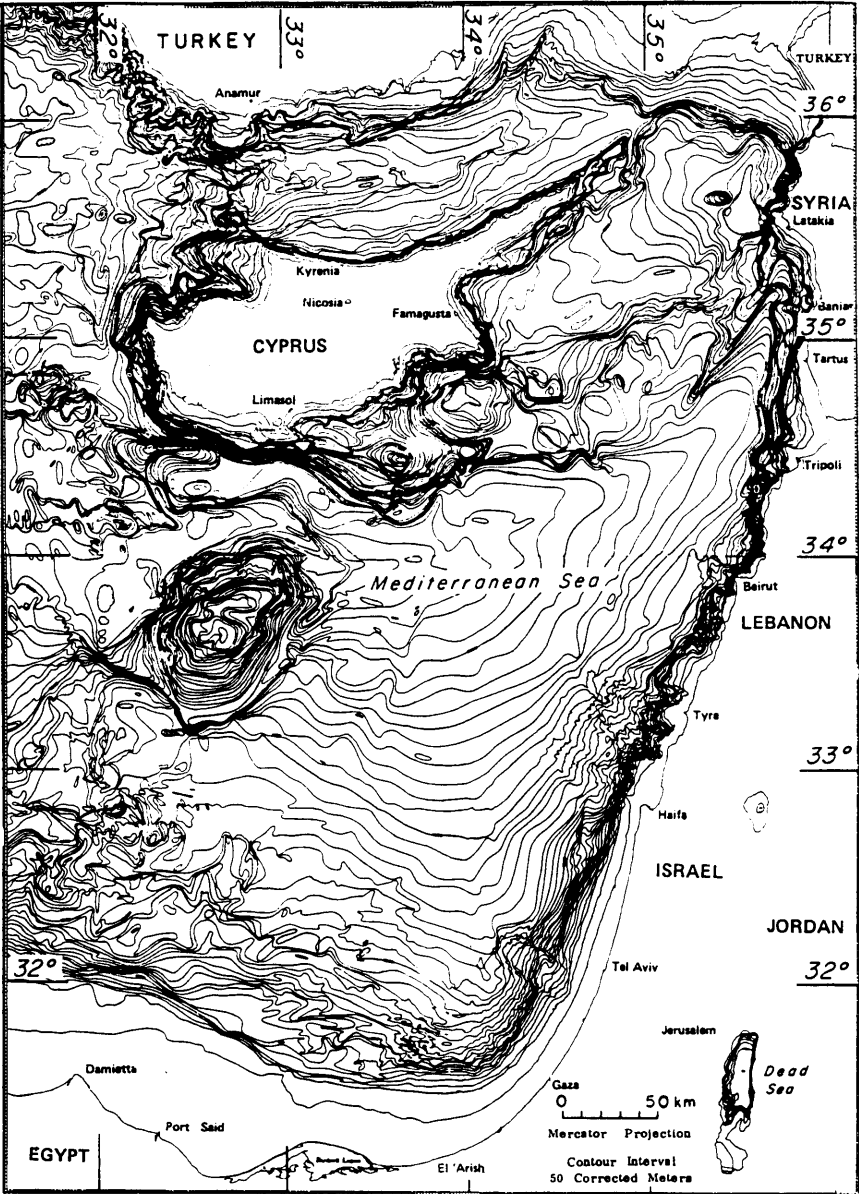
Figure 1.2: Bathymetric map of the eastern Mediterranean sea [17].

Although true in general, a detailed description of the bottom at each location, in sufficient resolution, simply fails to exist. The resolution required to treat the bottom as a deterministic shape and structure depends on the frequency so that the resolution should be finer than a single wavelength. However, even for relatively low frequencies, say 1500 Hz, the resolution required should be finer than 1 m. Such resolution is currently not accessible. Note that even if the resolution would have existed, the effort to incorporate all the details into an existing transmission loss model would probably not result in much better accuracy due to errors introduced by the existing model. The alternative for the engineer is to treat the bottom by its statistics.

From the preceding discussion, the exact Mediterranean's bottom shape and structure is better described as an unknowable. The statistics of the bottom may include the root mean square (RMS) slope, σ, the disturbance scale, λ_c, and the average slope of the particular area of interest, β. This statistical description of the bottom can vary from area to area but easier to determine than the actual bottom shape. This description must be combined with a bottom loss model that predicts the loss of acoustic energy due to bottom interaction with the propagating acoustic pressure.

Following these guide lines, different areas that are statistically different might have different effects on the analysis of sonar performance. The simplest bottom characteristic that can distinguish one area from another is the average bottom slope. In this research, therefore, three areas with different average bottom slopes are considered. The analysis of sonar performance is carried out for an up-slope, down-slope, and cross-slope cases. The three areas along with their averaged slopes are described in chapter 2.

Apart from the complexity of the problem due to the seabed structure, one type of sonar system might have better or worse performance than the other for a particular scenario. On the other hand, the result might be the opposite in another scenario. The scenario defines the problem's parameter space. It includes location, direction of propagation, time of year, frequency, and the type of sonar system used as receiver. The parameters mentioned above are joined through the so called "sonar equation" which sets the framework for this study. The sonar equation, often written in dB notation, combines all

the parameters that affect the signal to noise ratio (SNR) at the output of the receiver, such as, source level, transmission loss, noise level, array gain, and frequency, and is dealt with in sufficient details in chapter 3.

As mentioned earlier, in order to analyze the performance of any sonar system one must calculate the transmission loss from the source to the receiver. The literature offers many methods, or models, to calculate the acoustic field for an ocean environment. Some of them are normal modes [8,15], coupled normal modes [8], the parabolic equation [8], SAFARI [26], and ray theory [7,8,15]. All those methods solve the wave equation and agree very well even for long ranges [28]. The first four methods solve the wave equation coherently [8] using different approaches to the boundary value problem. The boundary value problem, however, introduces the problem of describing the bottom shape and structure as deterministic, which is in most cases an unknowable. On the other hand, using ray theory, a statistical representation of the bottom can be used in order to determine the bottom loss, or surface loss, and enables one to calculate, in a simple way, the transmission loss incoherently, ignoring the phase. An incoherent transmission loss calculation is more reasonable when the exact boundary (bottom or surface) structure is not known exactly. Ray theory is used for the present work to calculate the transmission loss and is described in more detail in chapter 4.

The bottom and surface losses are modeled as Fresnel forward scatter model [7]. In order to generate the associated losses the RMS roughness height of the surface must be introduced among other parameters. The RMS surface roughness height can be interpreted by the surface wave height while the RMS roughness height of the bottom is evaluated using the observation scale [10] of a particular sonar, described in more detail in chapter 4. The transmission loss combined with bottom and surface losses can be used to estimate the acoustic pressure at a distance R from the source.

In any event where the signal to noise ratio is to be evaluated, one must consider the amount of background noise in the medium. The background noise, also referred to as ambient noise, is addressed in chapter 5, in both directionality and level. Although, actual

22

analyses should be carried out using the actual noise levels, those were not handy at this time. Alternatively, the noise data is taken from the classical paper by Wenz [12].

Three types of sonar systems are considered here. The systems are based on different array designs connected to a similar receiver. Since the systems are passive the source signal is not known precisely and therefore the receiver is based on the energy detector [7]. The sonar systems are described in more detail in chapters 7 and consist of the following types of array design:

- horizontal towed line array;

- hull mounted line array;

- spherical bow array.

The performance analysis results are listed in chapter 8 and plotted in chapter 9 and in appendix A. The transmission loss results are presented for each location, each direction (up, down or cross-slope), each season (cold and warm), three different depths, for several frequencies. The transmission loss results are than compared to the figure-of-merit (FOM) to estimate the performance of the sonar system. In dB notation, reducing the FOM from the transmission loss gives the signal to noise level (or the signal excess) at the output of the receiver. It is interesting to note the convergence zones near the surface created during the cold season give rise to a higher probability of detection near the surface. During the warm season, however, the convergence zones do not reach the surface and therefore degradation in sonar performance is expected near the surface.

Although not necessarily so, it turns out that the different sonar systems operate in different frequency bands due to the different physical array dimensions. The towed array operates in the lower frequency band, the hull mounted array operates in the mid frequency range, and the bow array operates in the upper frequency band. It is interesting to note also that the increase in transmission loss as the frequency increases does not necessarily mean degradation in sonar performance. As the frequency increases, the noise level, in general, decreases while the array gain increases.

Finally, the results were obtained after making several assumptions which may be inaccurate for the particular area of interest. The assumptions include bottom losses estimations, which are based on actual measurements from the Gulf of Oman, and surface wave height that is incorporated into the surface loss mechanism. Naturally, those assumptions affect the transmission loss results. Direct conclusions, drawn here, may then be inaccurate in reality. The intention here, however, is to establish a relatively convenient framework for the analysis of sonar systems' performance of any kind at any place once the relevant transmission loss is calculated accurately using actual bottom and surface losses.

Chapter 2

Source Locations

Three locations were chosen for this study in order to examine the effects of the bottom slope and depth as well as the environmental conditions on the performance of the sonar system. The locations are in the eastern part of the Mediterranean Sea, which is the area of interest. The bathymetric data, which was available for this area at the time of writing, is based on a 5 km resolution database ("dbdb5" source file.) The general contour map of the eastern Mediterranean bathymetry is shown in Figure 2.1, which was produced based on this source file. The contour lines are isodepth lines separated by 100 m depth. The higher slope regions are located where the isodepth lines are close to one another while the milder slopes are located where the distance between the contour lines is larger. The effect of different bottom slopes can be analyzed by performing the analysis at the locations that have different bottom slope properties. This argument, along with the actual bathymetric map, is the basis for selecting the locations, which are also shown in Figure 2.1. Each location is marked with "+" and the local bottom depth. Each one has different bottom slope and bottom depth that shall be reviewed subsequently. The coordinates of the three locations are as follows:

1st location: (35N,31E), west of Cyprus;

2nd location: (34N,35E), west of Lebanon;

3rd location: (32°30'N,34E), west of Israel and north of Egypt.

The depth at the center of the locations varies from about -2300 m to about -1200 m. The depth at each location changes as a function of the average slope of the bottom, β. The difference in depth between the three locations does not seem to be substantial but becomes one for different bottom slopes. The source is assumed to be at 100 m depth for each of the three locations. The source can have velocity associated with it but throughout the analysis the source location is considered constant except for its effect on the integration time limit of the receiver as discussed further in chapter 4.
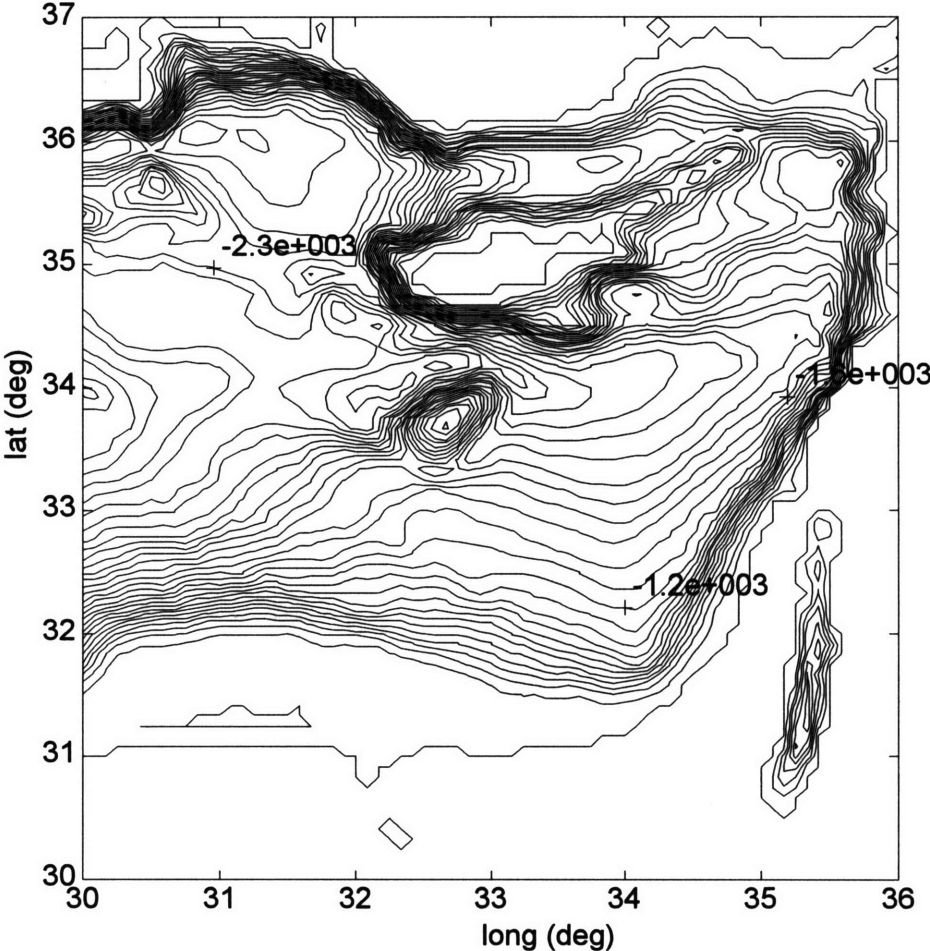
Figure 2.1: Contour map of the eastern Mediterranean sea. Bottom depth at source locations are marked with '+' and depth in meters.

Apart from the bottom properties, which do not change in time, the thermodynamics properties of the ocean do change not only in time but also in space. The sound velocity in the water, c, is a function of those thermodynamics parameters of the ocean - temperature, T, salinity, S, and hydrostatic pressure, P, [7]. The dependency of the sound speed on those environmental variables has not been analytically derived yet and instead empirical functions have been developed based on measurements. Detailed discussions on the sound speed profile and its relations to the environmental variables can be found in the literature (for example [7, 9].) One of the useful empirical functions from which $c(T,P,S)$ can be found is [7]

$$
\begin{aligned}
c = {} & 1448.96 + 4.591T - 5.304 \times 10^{-2} T^2 + 2.374 \times 10^{-4} T^3 \\
& + 1.340(S - 35) + 1.630 \times 10^{-2} z + 1.675 \times 10^{-7} z^2 \\
& - 1.025 \times 10^{-2} T(S - 35) - 7.139 \times 10^{-13} Tz^3
\end{aligned}
\qquad (2.1)
$$

where T is measured in °C, S in ppt, z is in m (replaces the pressure term), and c in m/s. This function is used here to determine the sound velocity profile, SVP, given temperature, and salinity profiles at any depth, z. The SVP gradient with respect to z can then be calculated

$$
g = \frac{dc}{dz}.
\qquad (2.2)
$$

The gradient of the sound velocity profile has a substantial effect, sometimes crucial, on the propagation of sound in the sea. Due to variations in SVP, its gradient, g, can vary significantly especially in the upper water column, which is exposed to temperature changes in the open atmosphere. An illustration of a sound speed profile is given in Figure 2.2 that marks the various thermoclines as a function of depth.

In the sections that follow each of the location's bathymetry is described and its environmental conditions are presented. The environmental conditions include the temperature, salinity, and sound speed profiles, for both winter and summer, and bottom shape. It is assumed, here, that the sound velocity profile does not change with range within 50 km radius from each location. Although true to first order, slight changes in SVP may
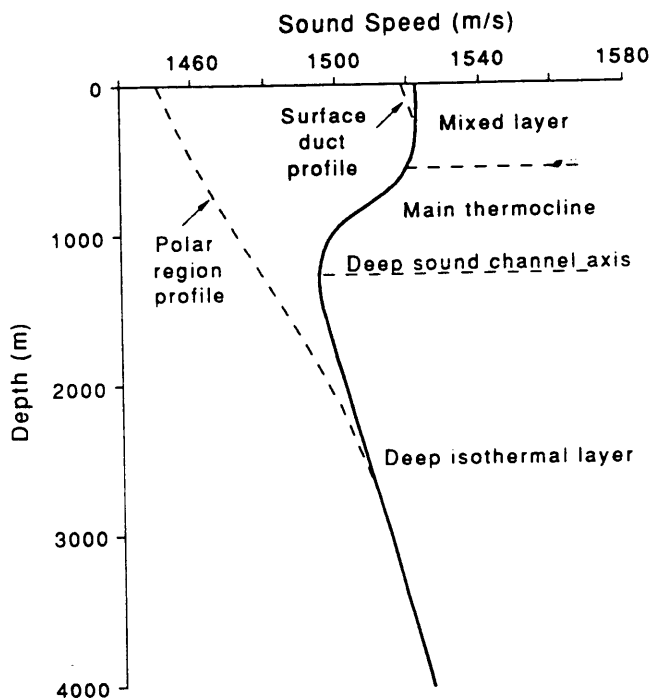
Figure 2.2: An example of a generic sound speed profile with layers description [8].

occur. This adds another degree of complexity to the problem which is beyond the current framework and should be investigated separately.

Although quiet mild, the winter is the cold season in the area and reaches its peak during February while the summer is the warm season with its peak during August. The temperature surrounding the area directly influence the temperature profile in the upper water column and has, therefore, an effect on the propagation characteristics of sound in the sea, as shall be further discussed.

The ability to uniquely describe each location's environmental conditions is directly affected by the availability of accurate data, measured in the area, as a function of time and space. In reality, though, the inability to predict precisely what are the conditions at a particular place and time leads the scientists to create databases that statistically describe the

environmental conditions by means of averaging by seasons and places. As a result, one cannot expect the results of any analysis to be precisely true, but only true in average. Such data bases may exist with different spatial or time resolutions and some provide in addition the probability of occurrence. An example is the wave generated ambient noise.

Waves have substantial contribution to the total background noise level, which is controlled by the wave height [12]. Waves are mostly dominated by surface winds that may vary even on an hourly basis. As a result the waves can be described only statistically, or in other words, in terms of probability of occurrence. Furthermore, the wave height database, which is available at this time, is not fine enough to distinguish between the different locations in the eastern Mediterranean sea, and is therefore discussed only in general for this region.

In general, it is statistically known that the period of maximum wave activity is during the winter, or the cold season, and less wave activity occurs during the summer. This means that in order to fully analyze the performance of a sonar system one must repeat the analysis for several wave heights at each season that can be observed at the desired probabilities. For simplicity, the wave heights, considered here for winter and summer, represent two distinct cases that enable one to more easily see its effect. For the winter, the wave height is chosen to be 1 m (highly probable in sea state 3 - see appendix C) and for the summer the wave height is chosen to be 0.2 m (corresponding to sea state 1.) These choices cannot be judged as "right" or "wrong" but as choices that may represent reality for a probability of about 50% for February and August (courtesy, Israeli Navy). The corresponding characteristics of the wave generated noise, for both seasons, are discussed in more detail in chapter 5 where other noise sources are presented. Wave height is also used as a parameter for the surface loss mechanism as discussed in chapter 4.

2.1 First Location

The coordinates of the first location are (35N,31E). The area is located west of Cyprus at an averaged depth of about -2200 m. A bathymetric map of the area is shown in Figure 2.3. The contour plot represents approximately 91 km (long.) by 110 km (lat.) and is based on the dbdb5 source file which gives about 5 km resolution. The contour lines, again, represent isodepth contour lines plotted every 100 m depth change. This location was chosen to represent areas of very mild bottom slope. Due to the rough resolution available in this plot, the actual detailed structure of the bottom cannot be noticed. The contour map, however, serves as a tool to estimate the first order approximation to the bottom slope in different directions.
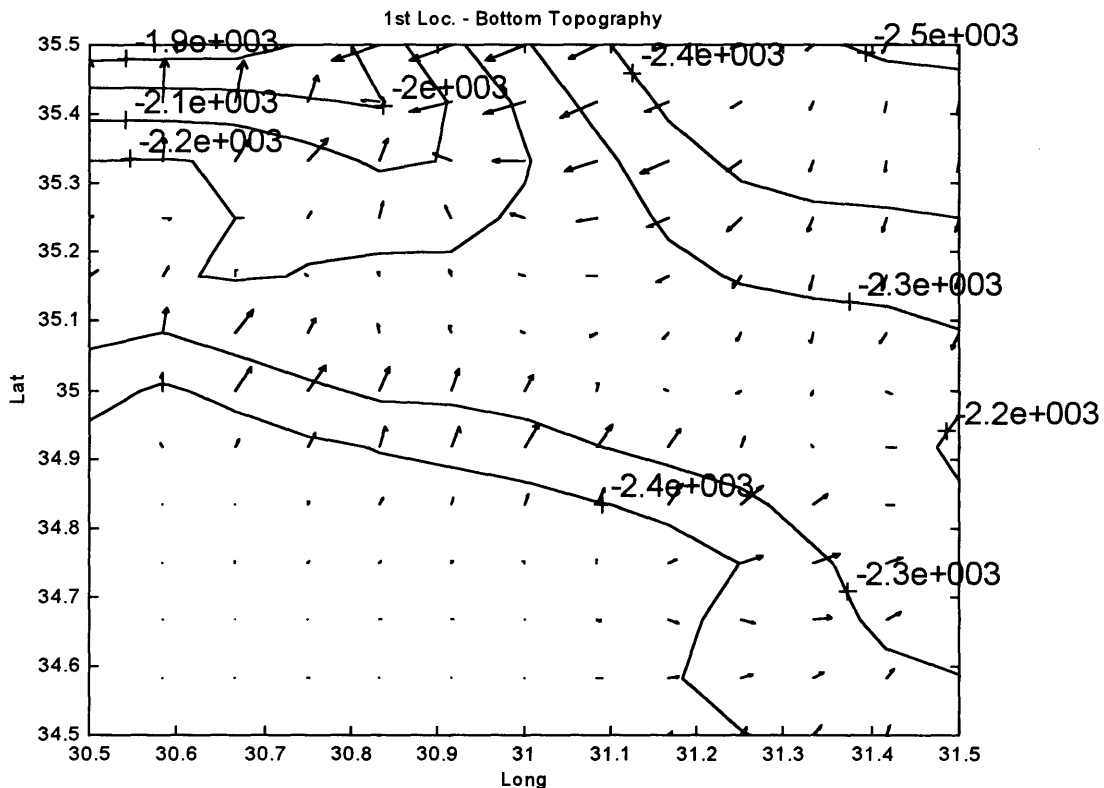
Figure 2.3: A Bathymetric map of the first location. The arrows represent the direction towards the shallower points.

It is assumed in this study, that the isodepth lines also connect the points of the bottom roughness. In other words, as one goes directly up-slope one crosses the isodepth contour lines in the direction normal to the lines. Assuming that each point is locally flat then by doing so one is climbing stairs that can represent roughness lines. Following this argument, the arrows, shown in Figure 2.3 always pointing to shallower depths and therefore locally represent the up slope direction. Similarly, the cross-slope direction is along the contour lines, and the down-slope direction is the opposite direction shown by the arrows. Following the above description of the roughness, the propagation of sound in the up-slope, cross-slope, and down-slope directions represent three different cases of bottom interaction as can be pictorially described as one goes up the stairs, down the stairs, or across the stairs. In each direction, therefore, the bottom effect on the propagation of sound is different. Intuitively, however, it is reasonable to believe that the more roughness the sound "sees" the more loss the bottom introduces. This qualitative and somewhat abstract description is considered more deeply in chapter 4 to determine the bottom loss.

From this motivation, three directions of sound propagation need to be identified. From Figure 2.3 the cross-slope direction is from the west (left) to east (right) and vice versa where no contour lines are crossed. The up-slope case can be defined as the direction from the bottom-left corner of the plot to the center, or alternatively from the south-west part of the figure to the north-east. The down-slope can be defined the other way around.

One should note that the bottom bathymetry is much more complex than described in such a way. However, it serves the purposes of this study by defining those three cases. The three approximated bottom slopes that shall be considered here for the first location are then

- up-slope: $\beta \approx 0.1°$;

- cross-slope: $\beta \approx 0°$;

- down-slope: $\beta \approx -0.1°$.

31

2.1.1 Environmental Data

The average temperature and salinity profiles during the winter [31], for the first location, are plotted in Figure 2.4 along with the corresponding sound velocity profile. The sound velocity at each depth is calculated using equation (2.1) and interpolated linearly between the discrete measured points spaced from $z = 0$ m to the bottom, $z = 2200$ m.

During the winter, the water temperature stays at about $16.7°$ C for the upper tens of meters, or surface duct. Below this the temperature decreases rapidly in the thermocline and reaches about $13°$ C from $z = 500$ m to the bottom. The salinity profile stays at 39 ppt in the upper 200 m, and then decreases to 38.75 ppt at 750 m and stays relatively constant for the deeper water column. The salinity changes only slightly and therefore, has only a
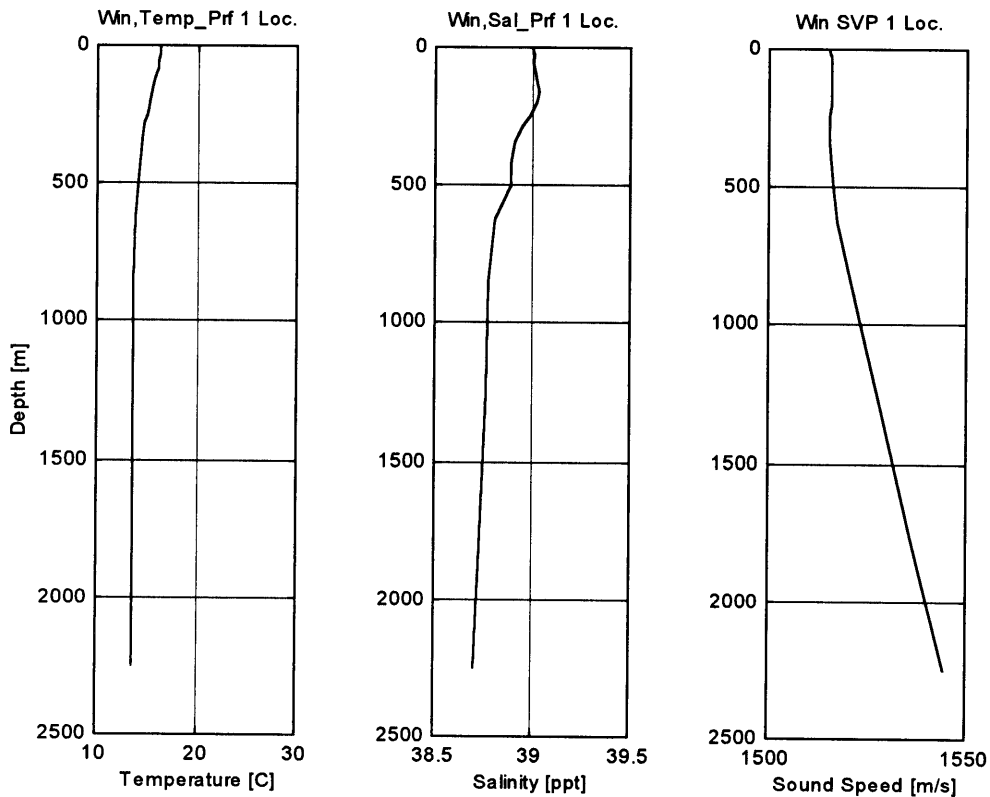
Figure 2.4: Temperature, salinity, and sound speed profiles for the first location during the winter season [31].

minor effect on the SVP, and can be considered constant at 39 ppt. The corresponding SVP has a slight upward refractive gradient very close to the surface. Below the surface duct the SVP stays relatively constant up to 500 m depth with a slight downward refractive gradient, and then becomes upward refractive again under the influence of the hydrostatic pressure. As a result, at great depth, below 500 m, the sound velocity gradient is approximately 0.016 (1/s).

During the summer, however, the temperature at the surface is relatively high, about 26° C, and decreases rapidly at the upper tens of meters, creating down refractive SVP at the surface. The corresponding temperature, salinity, and sound velocity profiles [31] are plotted in Figure 2.5.
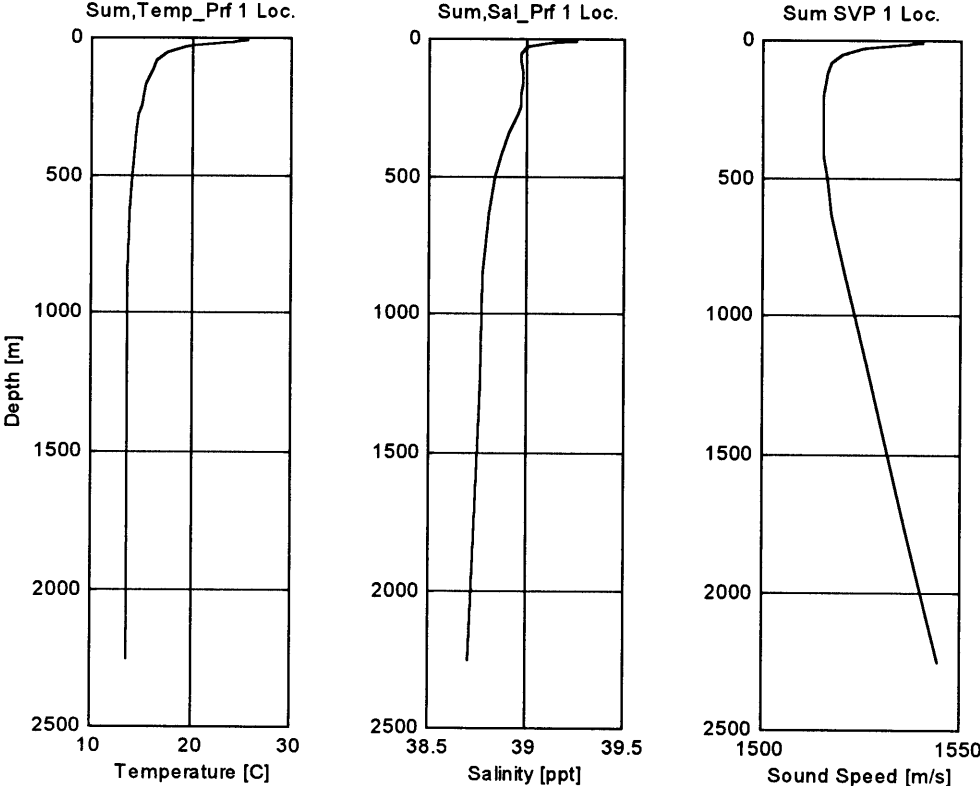
Figure 2.5: Temperature, salinity, and sound speed profiles for the first location during the summer season [31].

Except near the surface the salinity, on the other hand, does not seem to vary with season. Below 200 m, the SVP gradient reaches, as in the winter, a constant value up to about 500 m, and then becomes positive, or upward refractive, due to the increase of hydrostatic pressure. The differences in the SVP behavior, just below the surface, between the summer and the winter have a crucial effect on the transmission loss at relatively shallow depth, as shall be explained in chapter 4 and emphasized in chapters 8 and 9.

2.2 Second Location

The coordinates of the second location are (34N,35E). The area is located off the coast of Lebanon, right at the bottom of the continental slope. The depth around the location varies significantly, therefore, from west to east. The depth at the center of the location is estimated to be around 1700 m, getting shallower towards the east and deeper towards the west. The continental slope is rather narrow, 10-13 km [29] and causes the isodepth contour lines to be very dense at the slope. A bathymetric map of the second area is shown in Figure 2.6. As argued previously, the contour lines represent isodepth-roughness contour lines plotted every 100 m depth change. This location was chosen to represent areas of steep bottom slope. The bottom slopes for the up, cross, and down cases are estimated using the data given in Figure 2.6.

The up-slope direction is from the north-west (upper-left corner) to the south-east (bottom-right corner) perpendicular to the contour lines toward the shallower points. One should note that the maximum range from the center of the location is, in this case, about 30 km to zero depth. The cross-slope can be defined as one goes from the south-west to the north-east and vice versa, along the contour lines. The down-slope can be defined as the direction opposite to the up-slope, from the south-east to the north-west.

The actual bottom bathymetry is far more complex than the way it is described here, in fact it is known to be extremely disturbed at the continental slopes [17]. As mentioned earlier, this is only a first order approximation to the bottom, and higher order
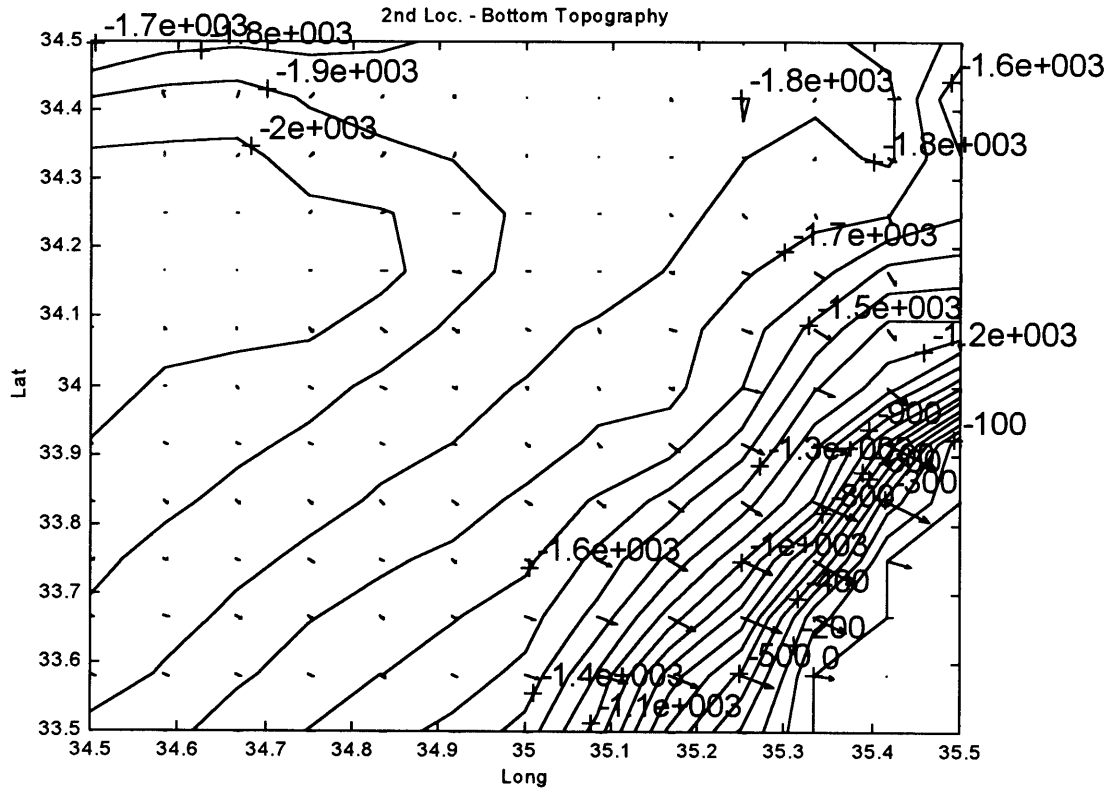
Figure 2.6: A Bathymetric map of the second location. The arrows represent the direction towards the shallower points.

approximations are to be encouraged. However, they are beyond the scope of the current study. The three approximated bottom slopes that shall be considered are then

- up-slope: $\beta \approx 3°$;

- cross-slope: $\beta \approx 0°$;

- down-slope: $\beta \approx -3°$.

2.2.1 Environmental Data

The temperature, salinity, and sound velocity profiles [31] for the second location are plotted in Figure 2.7 and Figure 2.8 for the winter and summer respectively. The description of the sound velocity profile resembles in its shape the one plotted in section 2.1.1 for the first location, as does the temperature profile. The salinity profile, during winter, has a positive gradient at the upper hundred meters and during summer has a negative gradient causing only negligible effects on the SVP behavior. Accordingly, the SVP during the winter has an upward refractive gradient at the upper tens of meters, followed by a slightly downward refractive gradient and becomes upward refractive again below 500 m, where the hydrostatic pressure dominates.

During the summer, the sound velocity has a downward refractive gradient at the upper hundred meters, followed by a zero gradient up to 500 m, and then becomes upward refractive as described for the winter below 500 m. The changes in the sound velocities between winter and summer come into play in the transmission loss calculations results, in chapter 8 and 9.
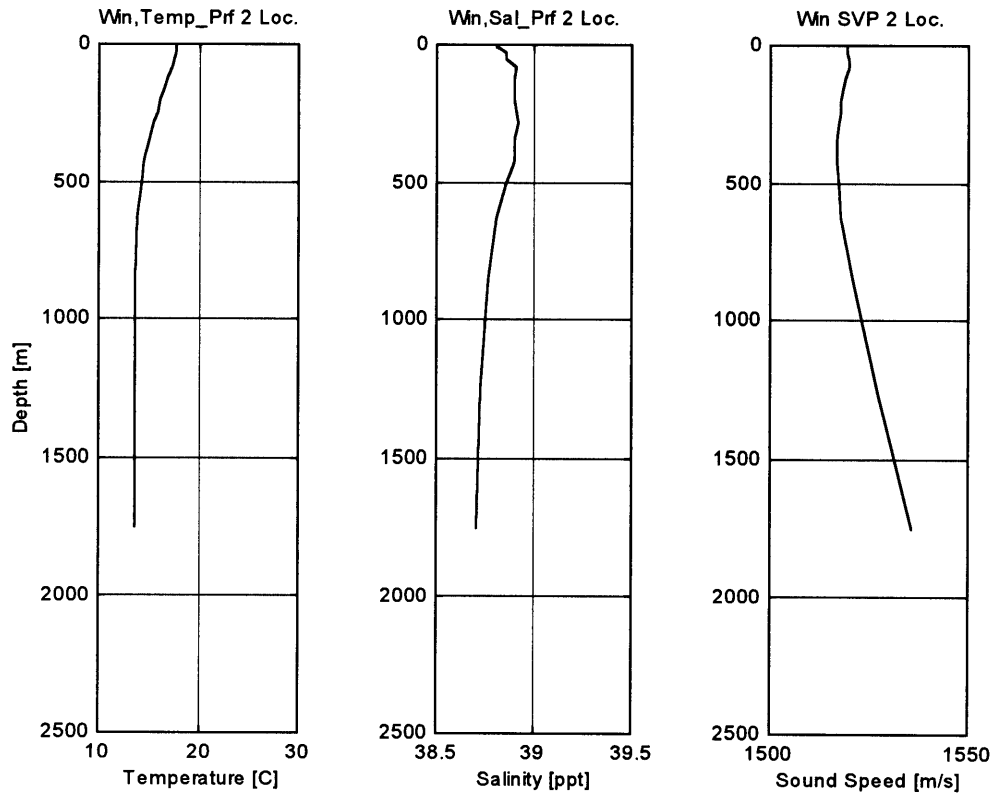
Figure 2.7: Temperature, salinity, and sound speed profiles for the second location during the winter season [31].
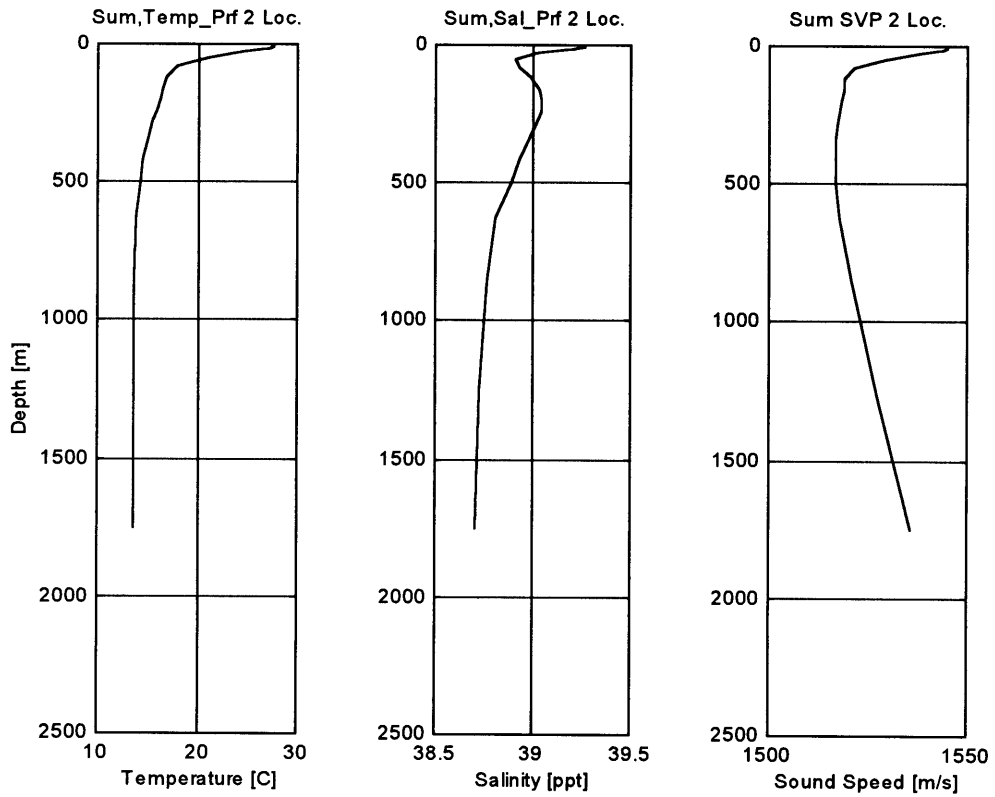
Figure 2.8: Temperature, salinity, and sound speed profiles for the second location during the summer season [31].

2.3 Third Location

The coordinates of the third location are (32°30'N,34E). The area is located west of Israel and north of Egypt on the continental slope of the south-eastern part of the Mediterranean basin. As opposed to the second location, the continental slope around this area is relatively mild and wide, however, not less disturbed [17, 29]. The depth at the center of the location is estimated to be around 1200 m, getting shallower towards the south and deeper towards the north. The continental shelf around this location is about 40-50 km wide [29], which is much wider than the one around the second location. A bathymetric map of the third area is shown in Figure 2.9.
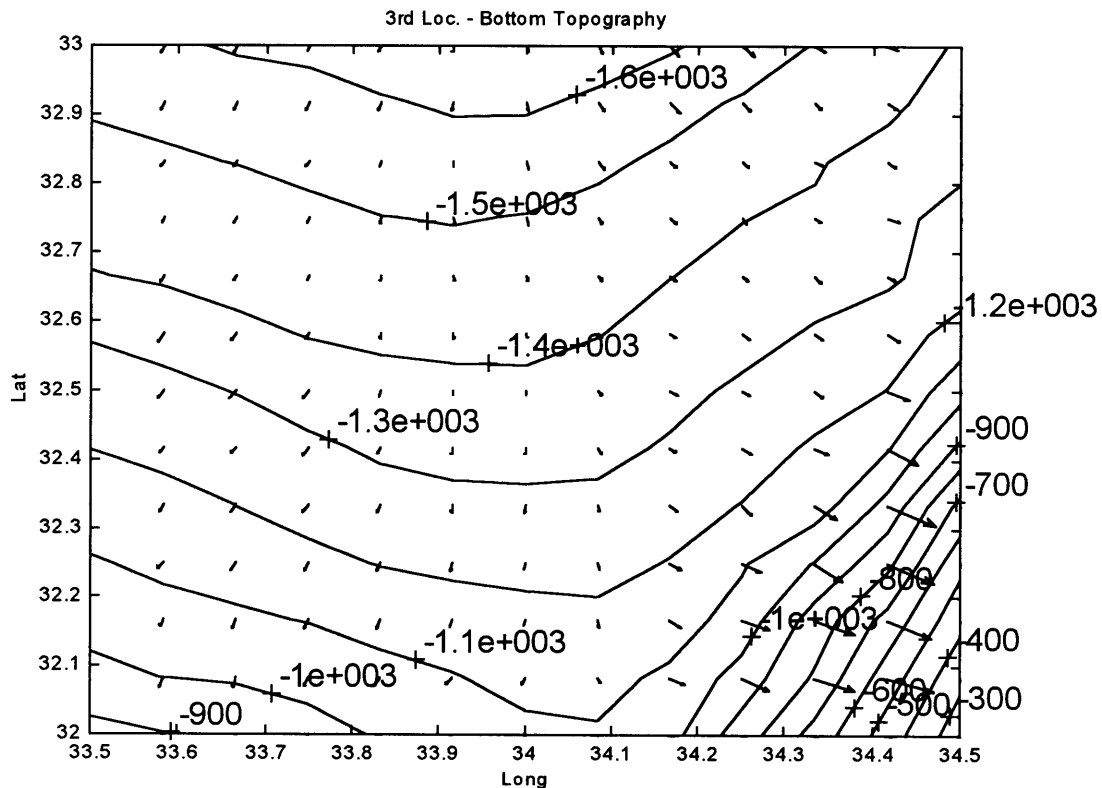
Figure 2.9: A Bathymetric map of the third location. The arrows represent the direction towards the shallower points.

As argued previously, the contour lines represent isodepth-roughness contour lines plotted every 100 m depth change. This location was chosen to represent areas of relatively mild bottom slope. The bottom slope for the up, cross, and down propagation is estimated using the data given in Figure 2.9.

The up-slope direction is from the north (upper portion of the figure) to the south (bottom portion) perpendicular to the contour lines towards the shallower points. The cross-slope can be approximated by going from the west to the east and vice versa, along the contour lines. The down-slope can be defined as the direction opposite to the up-slope, from the south to the north. The three approximated bottom slopes that shall be considered here, calculated from the center of the second location are then

- up-slope: $\beta \approx 0.4\ °$;

- cross-slope: $\beta \approx 0°$;

- down-slope: $\beta \approx -0.4°$.

2.3.1 Environmental Data

The temperature, salinity, and sound velocity profiles [31] for the third location are plotted in Figure 2.10 and Figure 2.11 for the winter and summer respectively. The description of the sound velocity profile resembles in its shape the one plotted in section 2.2.1 for the second location, as does the temperature profile. The salinity profile, for both winter and summer is relatively constant with negligible changes except at the surface. During the summer it has a negative gradient at the upper tens of meters causing only negligible effects on the SVP behavior. Accordingly, the SVP during the winter has an upward refractive gradient at the upper tens of meters, followed by a slightly downward refractive gradient and becomes upward refractive again below 500 m, where the hydrostatic pressure dominates.

During the summer, the sound velocity has a downward refractive gradient at the upper hundred meters, followed by almost zero gradient up to 500 m, and then becomes upward refractive as described for the winter below 500 m. It is important to emphasize that the sound velocity at the bottom is less than the sound velocity at the surface, during the summer. This fact, which is also true for the other two locations, causes a narrower angular spectrum to be channeled in a wave guide due to bottom losses. In other words, this creates high transmission loss for a receiver near the surface, and pushes the convergence zones down so that they do not reach the surface.
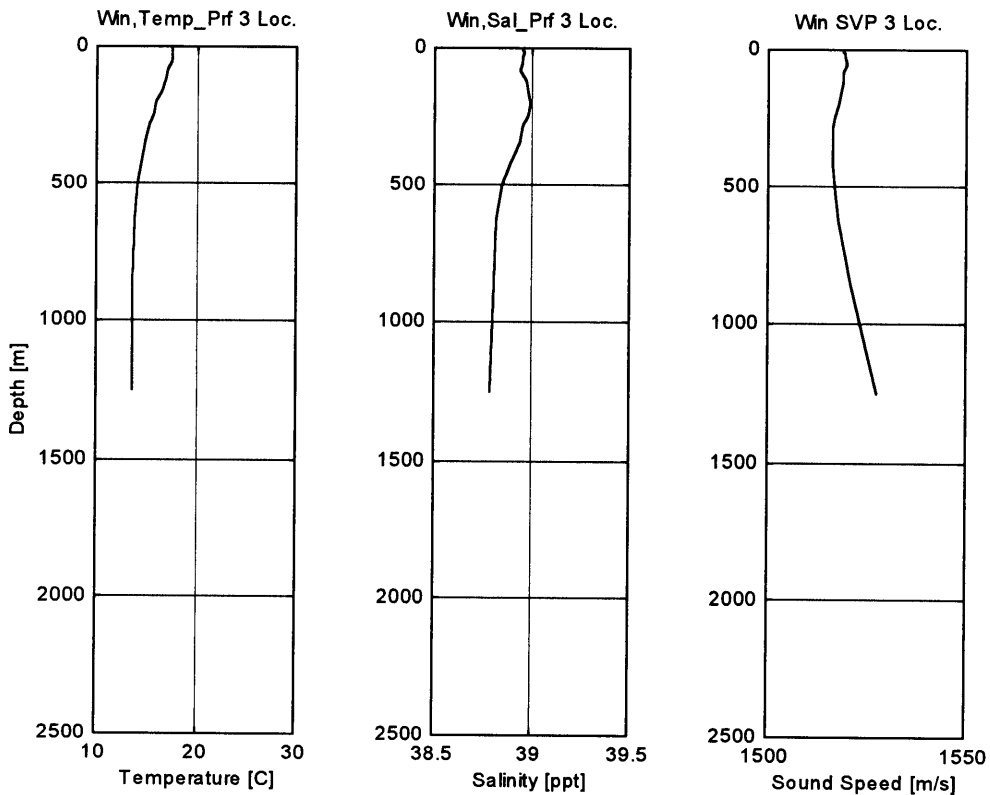
Figure 2.10: Temperature, salinity, and sound speed profiles for the third location during the winter season [31].
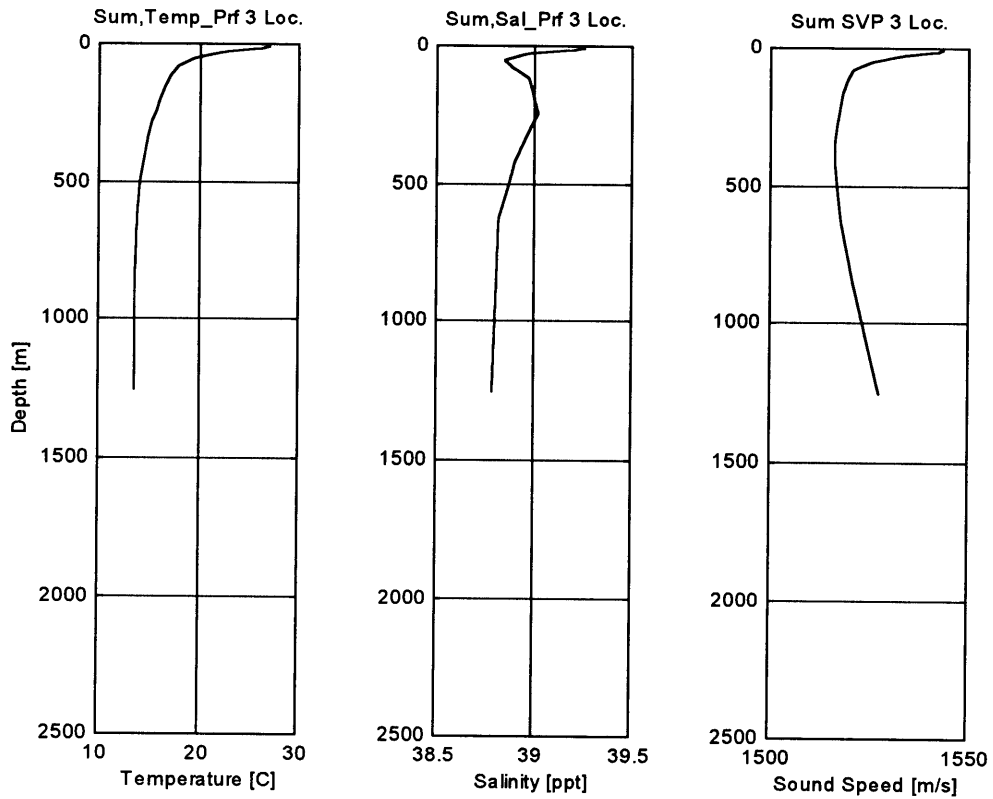
Figure 2.11: Temperature, salinity, and sound speed profiles for the third location during the summer season [31].

Chapter 3

The Sonar Equation

Whenever there is a sound source to be detected in the ocean it involves the problem of receiving the source signal in the presence of noise. The signal to noise ratio at the input to the receiver is a function of the source characteristics and the medium through which the sound propagates. On the other hand, the signal to noise ratio at the output of the receiver not only is a function of the input signal to noise ratio but it is also a function of the receiver array design and the processing gain. This is the point where the different types of sonar systems come into play using different shapes of arrays and different processing capabilities.

The sonar equation is simply a summary of the different aspects of signals and noise that affect the signal to noise ratio at the output of the receiver and it is used in the process of analyzing sonar systems. There are two types of sonar equations. The passive sonar equation is associated with passive systems, and the active sonar equation is associated with active systems. Although active sonar systems are beyond the scope of this study, it should be noted that the idea behind both of the equations is essentially the same. The standard reference for this material is Urick's book [11], however, I follow here the convention suggested in [7]. The general form of the sonar equation at the output of the receiver can be written in dB notation as [7]

$$L_{P/N_e} = L_p - L_{N_e} , \text{dB} \qquad\qquad (3.1)$$

where L_P represents the signal pressure level and is measured in dB re 1μPa. L_{N_e} represents the effective, or post array, noise level measured at the output of the receiver and is

measured using the same units as the pressure level. L_{P/N_e} is in dB and represents the signal to noise level at the output of the receiver. For passive systems the pressure level at the output is

$$L_p = L_S^T - H, \text{ dB re } 1\mu\text{Pa} \tag{3.2}$$

where H is the transmission loss measured in dB re 1m, and

$$L_S^T = 10\log(S_T), \text{ dB re } 1\mu\text{Pa \& 1m} \tag{3.3}$$

is the source level of the sound source limited to the frequency bandwidth of the sonar, b, so that

$$S_T = \int_b s_T(f)df, \tag{3.4}$$

and $s_T(f)$ is the source spectrum density. Accordingly, L_s^T is defined as the source spectral level relative to 1Hz (see Figure 3.1) and is equal to

$$L_s^T = 10\log(s_T(f)), \text{ dB re } 1\mu\text{Pa \& 1m, 1Hz,} \tag{3.5}$$

If $s_T(f)$ does not change much within the bandwidth, b, then equation (3.3) can be approximated by

$$L_S^T \cong L_s^T + 10\log(b), \text{ dB re } 1\mu\text{Pa \& 1m} \tag{3.6}$$

and the pressure level at the input to the receiver is then given by

$$L_p \cong L_s^T + 10\log(b) - H, \text{ dB re } 1\mu\text{Pa.} \tag{3.7}$$

Similarly, the noise counterpart of the equation, L_{N_e}, is for passive systems

$$L_{N_e} = L_n + 10\log b - AG, \text{ dB re } 1\mu\text{Pa} \tag{3.8}$$

$L_s^T(f)$

(dB re 1μPa, 1m, 1Hz)

f (Hz)
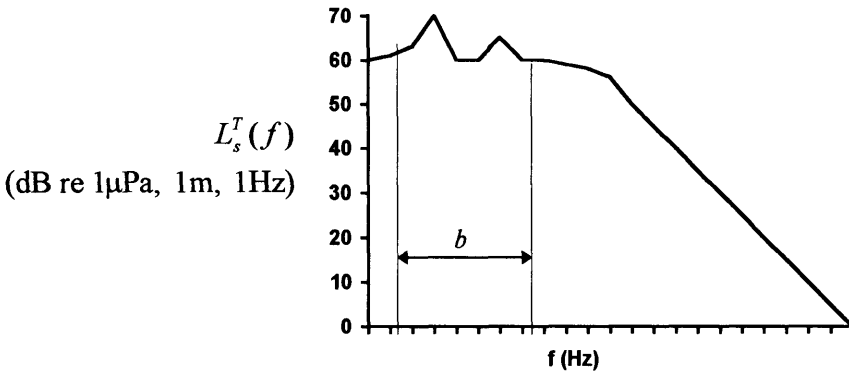
Figure 3.1: A simple example of a spectrum density, $L_s^T(f)$. b is the receiver bandwidth in Hz and should be designed to match the target effective spectral bandwidth.

where L_n is the noise spectrum level in dB re 1μPa & 1Hz, and AG is the array gain of the receiver array, which should be calculated separately for the different noise sources that exist in the scenario being investigated. A more detailed discussion on the array gain will follow in chapter 6.

Following these definitions, one should note the unimportance of the bandwidth, b, as it appears both in the signal level and in the noise level terms. This argument holds, in fact, for broadband signals, which have spectrum density. Narrowband components, however, appear, in the perfect sense, as delta functions in the frequency domain, and therefore have no bandwidth associated with them. In reality, though, narrowband signals do have a bandwidth but a very narrow one. Therefore in the narrowband case the bandwidth of the receiver is of great importance and should be chosen appropriately.

For active systems the sonar equation has the same form but with different L_P and different L_{N_e} that correspond to the fact that in the active case we have a two way propagation problem in which the source of the signal is actually a pulse generated by the sonar system itself. The result depends also on the portion of the acoustic energy scattered from the target - better known as target strength. In the case where the sonar transmitter is surrounded by scatterers the sonar becomes usually reverberation limited and the AG is

zero. Furthermore, for the latter case the sonar equation is reduced to the target strength minus the scatterer strength. For an active system we have then [7, 11]

$$L_{p/N_e} = L_p - L_{N_e} \quad (dB)$$

$$L_p = L_S(0) - 2H + T \quad (dB \ re \ 1\mu Pa) \quad (3.9)$$

$$L_{N_e} = \begin{cases} L_n + 10\log b - AG, & (dB \ re \ 1\mu Pa); \quad \text{Noise limited sonar} \\ L_S(0) - 2H + \begin{cases} T_V \\ T_S \end{cases}, & (dB \ re \ 1\mu Pa); \quad \text{Reverbaration limited sonar} \end{cases}$$

where $L_S(0)$ is the source level of the transmitted signal on the main radiation axis [7], and T_V, T_S are the volume reverberation and surface reverberation levels respectively. As mentioned before, passive systems are the focus of this study and therefore active systems are not discussed further. A more detailed discussion on this topic can be found in Urick [11], and Dyer [7].

The analysis of passive sonar system performance involves estimation of the pressure level, L_P, and the effective noise level, L_{N_e}, both measured at the output of the receiver. In order to evaluate the pressure level one has to calculate the transmission loss, H, as a function of frequency and range and then reduce it from the target source level. Since the target source level is usually given, the main problem here is to evaluate the transmission loss. Most of chapter 4 deals with this problem in detail using a ray-based model.

In order to evaluate the effective noise level it is essential to measure the different noise spectral densities for the different noise sources and then deduct the corresponding array gain, AG, from each of the noise levels separately after taking into account the bandwidth of the receiver. The different noise spectral densities are not only a function of frequency and angle but also a function of the particular place we are interested in. Therefore, if the spectral density of the noise is a critical issue one must have some measurements done in the particular area of interest in order to get the accurate noise levels.

One must note, however, that measuring the noise in every place can be a very costly process and in many cases accurate measurements in sufficient resolution may not be available. In addition, acceptable database should include noise level measurements at different times of the year in order to reflect seasonal changes. Since such database is not accessible at this moment one should consider an alternative. As an acceptable alternative one can rely on existing averaged measurements of the noise done in a wide ocean environment, and calculate the effective noise level based on those measurements [12]. Of course, once a more accurate data is available, the analysis should be repeated.

Another version of the passive sonar equation is the figure-of-merit or *FOM*, which is the transmission loss that gives zero signal excess for a particular probability of detection and probability of false alarm. The signal excess is the signal to noise level, L_{P/N_e}, at the output of the receiver minus the detection threshold, *DT*. In other words, *DT* is a measure of L_{P/N_e} needed for detection, given a probability of detection $P(d)$, and a probability of false alarm, $P(fa)$. The detection threshold is a complicated function of the processing gain of the sonar system and the sonar operator's capabilities. Detection theory is not included in this study but can be found in the literature for various models [11, 13, 14]. In this study, a simple model is used to evaluate the detection threshold [7], and is discussed in section 3.2. If the signal excess, *SE*, is given as

$$SE = L_P - L_{N_e} - DT$$
$$= [L_S^T - H] - [L_n + 10\log b - AG] - DT \text{ , dB} \qquad (3.10)$$

then the *FOM* can be written in the following way (for *SE*=0)

$$FOM = L_S^T - [L_n + 10\log b - AG] - DT \text{, dB re 1m.} \qquad (3.11)$$

Thus the *FOM* is a fictitious transmission loss that includes the target source level, noise level, and the sonar system parameters. Once the actual transmission loss is known *FOM* can be a measure of the maximum transmission loss possible, or the maximum detection range possible, for a particular area and a particular sonar system.

3.1 The Target Source Level

The target source level represents the source level of any noise source that exists in the ocean environment which one chooses to listen to. Almost every living creature or any active machinery can be considered as a noise source. In most common applications people are interested in detecting man-made sources in order to localize them. Man-made sources can be any kind of a ship that travels on the surface or any underwater vehicle. Each of these sources can have many types of machinery on board that can be active at times and non active at other times. Therefore, every ship at sea generates noise which has unique characteristics associated with it. This statement is general but amazingly true even for ships that are the same type and were made by the same manufacturer. In most cases this noise source is frequency dependent as well as angle dependent. In other words, the target might have different acoustic signatures when its noise is received from different aspects of it. In this study, however, a simple model is used to describe the target as an omni directional noise source with a simple frequency dependency. The reason for this simplification is that the primary goal here is not to identify the target but to compare how a simple target is received by the various sonar systems.

The target that was chosen here is a simplified version of a typical small diesel-electric submarine and its spectrum density, L_s^T, is shown in Figure 3.2. The spectrum density consists of a broadband spectrum and narrowband components. The broadband spectrum is continuous and is measured in dB relative to $1\mu Pa$, 1m, & 1Hz. The narrowband spectrum consists of narrowband tonals at specific frequencies with a very narrow bandwidth associated with them. Therefore its accumulated level over this band is presented only relative to $1\mu Pa$, & 1m. The narrowband spectrum of this target represents two types of rotating machinery with different RPM's that generate noise at their basic rotation frequency and the first four harmonics. The broadband noise starts at 100Hz and falls-off at a rate of 10 dB/decade up to 1000 Hz and then falls-off at 20 dB/decade.

48

Target spectral density
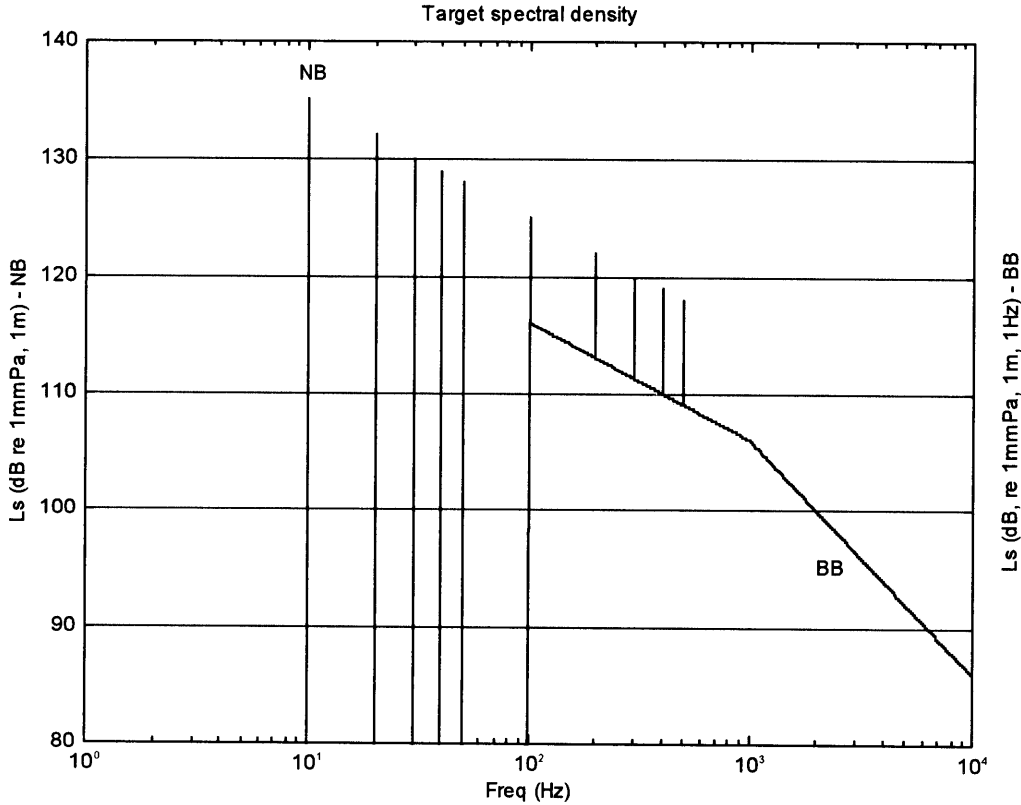
Figure 3.2: The target spectral density chosen to represent a diesel-electric submarine operating in a quiet mode. NB tonals are in dB re 1μPa, 1m. BB noise is in dB re 1μPa, 1m, 1Hz.

Due to high attenuation in the water and due to the mentioned frequency characteristics of the source for the frequencies beyond 10 kHz, it is unlikely that any sonar receiver, located more than 10 km away, would be able to detect any machinery noise beyond 10 kHz, and therefore this frequency regime is not considered in this work. The useful frequency band is, therefore, 10 Hz - 10 kHz.

In the broadband case the target source level around f_0 can be written as (see equation (3.6))

$$L_S^T \approx 10\log(b) + L_s^T(f_0) \qquad (3.12)$$

49

for a relatively narrow bandwidth, b. For the narrowband case there is no frequency band associated with the tonals and therefore equation (3.10) still holds with $b = 1$.

The source is located at a 100 meters depth and is capable of moving at a velocity of less than 3 knots ($\approx$ 6 km/h.) The fact that the target can move is an important issue when shallow water propagation is considered. In shallow water, a portion of the acoustic energy is scattered by the bottom at a particular location. Once the target has moved more than a certain distance it is probable that the received signal will have a different realization of the target and therefore can not be averaged with the previous received information from the target. This issue brings us to the next topic to be considered here which is the detection threshold, DT.

3.2 The Detection Threshold

The detection threshold is defined here as the signal to noise level at the output of the receiver that results in a 'detection' by the sonar's operator with a probability of detection of $P(d) = 0.7$, and a probability of false alarm of $P(fa) = 0.001$. In general, one has different detection thresholds for different $P(d)$ and $P(fa)$ and for different types of systems. A more detailed discussion about detection theory can be found for example in Urick [11], and in Burdic [14]. Often the dependency of the detection threshold on $P(d)$ and $P(fa)$ is described using the Receiver Operating Characteristics, or the ROC, which are set of curves, each corresponds to different detection requirements (see Figure 3.3).

In any detection process one has to include the processing gain of the system in order to trace back the necessary signal to noise ratio at the input to the receiver needed for detection. Since this study is focused on the detection of passive signals, which are not known in advance, the model that is used here to represent the detection system is based on the energy detector model [7]. Its block diagram can be seen in Figure 3.4.

The energy detector includes a windowing block, an amplifier, and an integrator. The windowing block sets the bandwidth of the receiver, b, which is different for
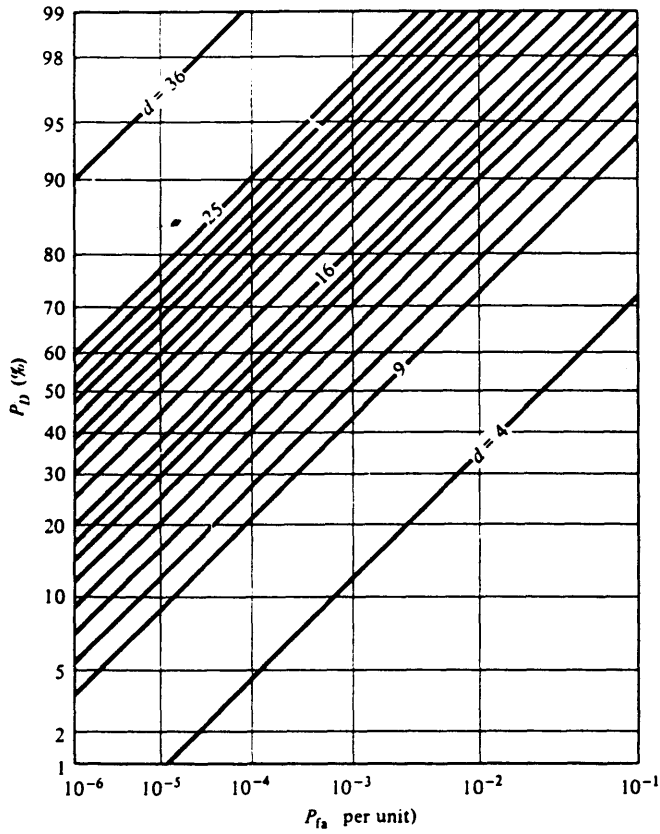
Figure 3.3: Receiver Operator Characteristics, ROC. d represents the required detection threshold using a single independent realization of the target as an output from an energy detector. from Burdic [14]

narrowband or broadband processing. It is clear, though, that for narrowband signals b should be as small as possible, while for broadband signals it is less important. It is assumed here that the bandwidth for the narrowband signals is $b_{NB} = 0.1$ Hz and for the broadband portion $b_{BB} = f_o/2$, where f_o is the center frequency of the receiver band or sub-band.

The windowing block is followed by a whitening amplifier. This amplifier is responsible for making the signal and noise spectra flat by compensating the fall-off of the narrowband and broadband spectra due to filtering done by the ocean (usually referred to as volumetric absorption which is dicussed in more detail in chapter 4.) The compesation is

usually done for the interesting frequency band, which in this case, 10 Hz to 10kHz (see Figure 3.2). The next block is the integrator which integrates the signal's power over the time, τ, that corresponds to a single realization of the received signal. This block is in fact the energy accumulator after which this component is named. In the literature [11, 14] τ is often called the integration time of the receiver. The integration time for passive systems is a very crucial parameter. Its value should be set as the maximum time for a single independent realization of the target. A single realization of the target, assuming bottom bounce propagation, is a function of the characteristic length scale of the bottom, λ_c, so that the "listening time" shall not be larger than the time it takes the propagating signal to cover more than such a length. This issue is addressed chapter 4.

The last block within the system is the time-recorder. The time-recorder together with the human eye integrate the output of the previous component by forming a record of independent samples of the received signal.

Once the system is known it is possible to determine the proccessing gain of the receiver or to determine the detection threshold, DT, that corresponds to the chosen probablities of detection and false-alarm. From Figure 3.3 the detection threshold for an operator to detect a target using only a single sample of the received signal is

$$DT = 13\,\mathrm{dB} \qquad\qquad (3.13)$$

$$p(t) \longrightarrow \boxed{} \longrightarrow \boxed{\mathrm{Amp}} \longrightarrow \boxed{\frac{1}{\tau}\int_{t_1}^{t_1+\tau} p^2(t)\,dt} \longrightarrow \boxed{\mathrm{Recorder}} \longrightarrow \mathrm{Eye}$$
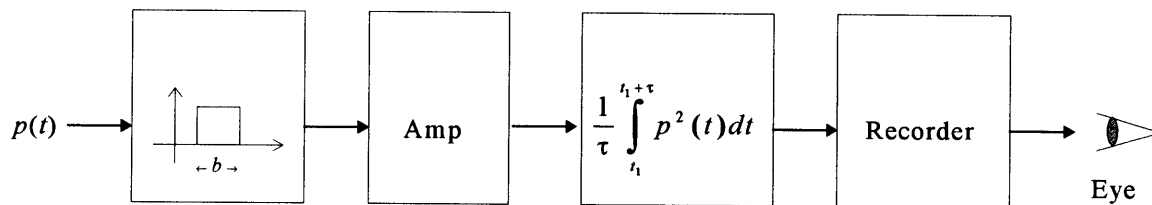
Figure 3.4: An Energy detector block diagram [7].

for

$$P(d) = 70\%, \quad P(fa) = 0.1\% . \tag{3.14}$$

From [7] it is known that as long as the samples of the received signal are independent the detection threshold of the operator given K independent samples can be reduced to

$$DT = 13 - 8\log K . \tag{3.15}$$

It can be easily seen that for K large the detection threshold can even be negative. However, one must be careful because K cannot be chosen arbitrarily but as a function of the time that the target is within a nearly fixed operating area. More importantly, one must understand that the above behavior of the detection threshold as a function of K is only an assumption. It is very hard to predict the exact detection threshold because it might be different for different operators and different sonar systems. Equation (3.15) can be interpreted as if it fits a single operator whose skills do not change with time nor with place. Of course, such an operator is hard to find, but he exists for the purpose of this analysis. If a more accurate detection threshold is needed one should conduct an experiment with a certain group of people that operate a particular sonar system. The detection threshold for each one of the operators may be different when operating a different sonar system. Thus there is no general and accurate detection threshold for all operators and systems.

The detection ranges are also a function of DT which means that like most engineering problems, a trial and error approach should be used in order to estimate the number of samples needed for detection at any range. For the sake of this study, however, it is assumed that at least $K = 200$ independent samples can be received from the target. It should be emphasized that in reality this is not necessarily so, and this serves as an arbitrary choice based on the assumption that the target is moving slowly (3 knots) and that it is within the possible detection ranges during the reception of the 200 samples. The detection threshold in this case is

$$DT \cong -5.4 , \text{dB}. \tag{3.16}$$

Chapter 4

Transmission Loss Calculations

Ray theory has been used for many years to solve underwater acoustics problems. This theory is by nature a high frequency approximation which means that the solutions given by ray–based models are perfectly true for infinite frequencies. However, even for low frequencies (in the range of 100 Hz) the results agree very well with full wave solutions, such as SAFARI [26], as shall be verified subsequently.

In addition, ray theory is easy to implement and it provides the tools that enable one to account for slanting and rough bottoms. In contrast to ray theory, existing full wave algorithms, like SAFARI, are usually range independent and therefore assume horizontal stratification. Furthermore, ray diagrams, which are the solutions to the ray equation [7, 8], give easier physical insight which other models lack. As a result, especially for shallow water propagation problems, a ray based model is the right choice and therefore is used in this work.

4.1 Ray Based Model

The first step in deriving a ray based model is determining the ray trajectories. The ray trajectories are curved lines perpendicular to the surfaces of constant phase. These trajectories are determined by the local gradient of the sound velocity profile, g, which is one of the most important parameters in sound propagation problems. The sound velocity

profile, as discussed in chapter 2, can vary substantially at different places and at different times and its gradient, g, with respect to depth, z, can be sometimes far from constant in the upper thermocline (0~200 m.)

The easiest way to derive the ray equations is to consider Snell's law and the geometry of the problem. The geometry of the problem is shown in Figure 4.1 and in Figure 4.2. Although the ray equations are not new ideas [7, 8, 9, 15], their derivation is presented here to illustrate its simplicity. Snell's law states that along each ray

$$\frac{\cos\theta(s)}{c(s)} = constant = \sigma \qquad (4.1)$$

where θ and c are measured along the ray path, s. Since each ray follows a different path, σ can be thought of as the *name* of the ray. An alternative name of the ray can be the sound speed, c_v, at which the ray vertexes ($\theta = 0$) yielding,

$$\frac{1}{c_v} = \sigma . \qquad (4.2)$$

Taking the differential form of Snell's law one sees that

$$\frac{d\theta}{dc} = -\frac{\sigma}{\sin\theta} . \qquad (4.3)$$

Assuming horizontal stratification, where c is only a function of z, equation (4.3) can be written also in the following way

$$\frac{d\theta}{dz} = -\frac{\sigma g}{\sin\theta} \qquad (4.4)$$

where g is the *SVP* gradient as a function of depth, z.

From Figure 4.1, it can be easily seen that the radius of curvature of the ray can be defined as

$$r_c \equiv \frac{ds}{d\theta} = \frac{ds}{dz}\frac{dz}{d\theta}. \qquad (4.5)$$

Also from Figure 4.1 it can be argued that

$$\frac{ds}{dz} = \frac{1}{\sin\theta}. \qquad (4.6)$$

Substituting equation (4.6) and equation (4.4) into equation (4.5) the radius of curvature of the ray is simply

$$r_c = -\frac{1}{\sigma g} = -\frac{c_v}{g}. \qquad (4.7)$$

Note that for a linear sound speed profile (where g is constant) the radius of curvature of the ray is constant. In other words, the ray, in this case, is an arc of a circle. Also note that the minus (-) sign determines whether the ray is bent upwards or downwards.
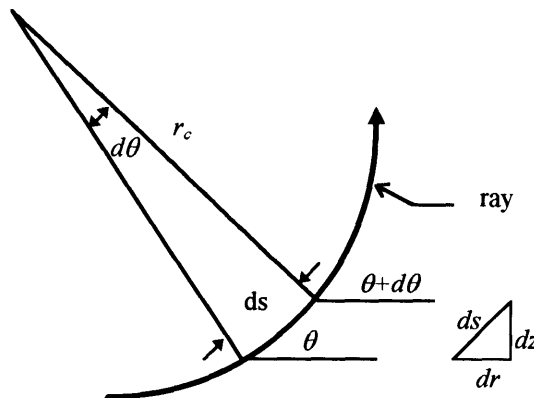
Figure 4.1: Schematic of 2-D ray geometry for upward refractive gradient.

Using Figure 4.2 and equations (4.7) and (4.5) the ray trajectories can be written as [7]

$$R_{12} = \int_{\theta_1}^{\theta_2} \frac{c_v}{g} \cos\theta \, d\theta$$

$$Z_{12} = \int_{\theta_1}^{\theta_2} \frac{c_v}{g} \sin\theta \, d\theta$$

(4.8)

and the travel time of the ray is given by

$$T_{12} = \int_1^2 \frac{ds}{c} = \int_{\theta_1}^{\theta_2} \frac{1}{g \cos\theta} \, d\theta$$

(4.9)

where the limits 1 and 2 in the above integral correspond to two places on the ray associated with angles θ_1 and θ_2, measured from the horizontal axis as can be seen in Figure 4.2. Equations (4.8) are used here to calculate the ray trajectories of any sound
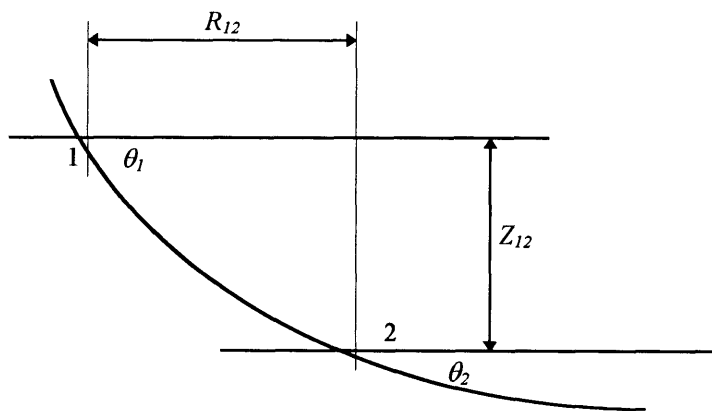
Figure 4.2: Ray geometry for calculating the ray trajectories

57

velocity profile. Equation (4.9) can be used to calculate the travel time and therefore the phase along the ray. One can go one step further and divide the water column into a layer of constant sound velocity gradient (g is constant). In this case, and with the use of a small angle approximation (for $\theta < 20°$) the ray trajectories within any such layer can be simplified and written as [7]

$$R_{12} \approx \frac{c_v}{g_0}(\theta_2 - \theta_1),$$

$$Z_{12} \approx \frac{c_v}{g_0}(\theta_2 - \theta_1)\left(\frac{\theta_1 + \theta_2}{2}\right). \qquad (4.10)$$

$$T_{12} \approx \frac{\theta_1 - \theta_2}{g_0}$$

As an example the ray equations (4.8, 4.9 or 4.10) were used to generate the ray paths for a sound speed profile taken in the eastern Mediterranean sea during the winter. The ray diagram and the corresponding sound speed profile are shown in Figure 4.3. The source is located at a depth of 100 m and the bottom depth is approximately 2200 m (marked by the dotted line). Although rays that hit the bottom are not included, the ray trace diagram gives a very good idea of how the sound propagates. For example note the clear convergence zone at ranges of 30 - 40 km, and the shadow zone formed at the lower water column beyond 25 km. Clearly, all the rays hit the surface so the paths can be thought of as refracted-surface-reflected (RSR).

The mean square pressure associated with a ray bundle can be derived in a very simple way using the conservation of energy. The ray bundle is formed by two adjacent rays with launch angles that differ by $d\theta$. A cross section of the ray bundle can be seen in Figure 4.4. The power that is put into the bundle at point 1 is [7]

$$dW_1 = \frac{A^2 2\pi \cos\theta_1 d\theta_1}{\rho_1 c_1}. \qquad (4.11)$$
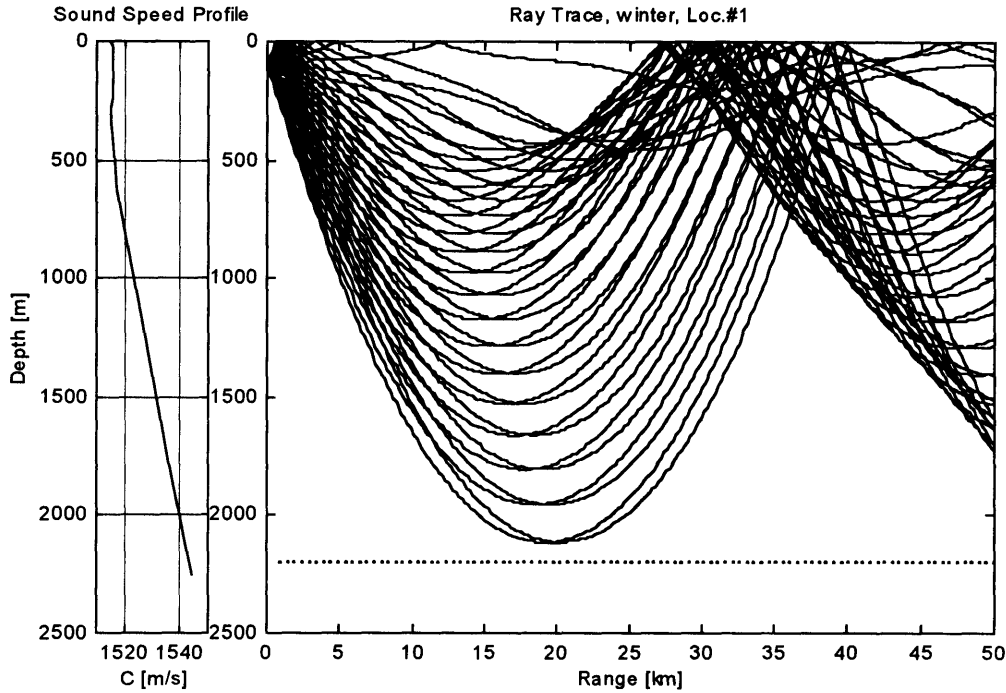
Figure 4.3: Sound-speed profile and ray trace diagram during the winter. Rays that hit the bottom have been excluded. Angular spectrum shown ± 10°, angular resolution: 0.6°.

where A is the source amplitude measured at a reference distance from the source, ρ_1 is the density at point 1, and c_1 is the sound velocity at point 1. At point 2 the ray bundle has a diameter of $\sin(\theta_2)dR$ and the power there can be shown to have the following expression [7]

$$dW_2 = \frac{p_2^2 \, 2\pi \sin\theta_2 \, RdR}{\rho_2 c_2}.$$

(4.12)

where p^2_2 is the mean square pressure at point 2. Assuming a lossless medium $dW_1 = dW_2$, neglecting minor changes in the medium density, and using Snell's law (Eq. 4.1) the mean square pressure at the output of the bundle is

$$p_2^2 = \frac{A^2}{R \tan \theta_2} \frac{d\theta_1}{dR}.$$

(4.13)

This result is precisely correct without any approximations for a lossless refractive medium with constant density. This equation is used here to calculate the loss due to refraction for the ray trajectories generated for each location. It should be noted that this expression should be applied with care due to the non physical results obtained for locations where rays vertex ($\theta_2 = 0$) and around caustics ($dR = 0$).

This solution to the wave equation is not full without considering the phase of the pressure along the ray. The phase can be added by multiplying equation (4.13) by a phase term which can be derived from the travel time along the ray, T_{12}, multiplied by the radian frequency, ω. The pressure along the ray is then

$$p_2 = \left(\sqrt{\frac{A^2}{R \tan \theta_2} \frac{d\theta_1}{dR}} \right) \exp(j\omega T_{12}),$$

(4.14)

without crossing any caustic regions and assuming no reflections from the boundaries
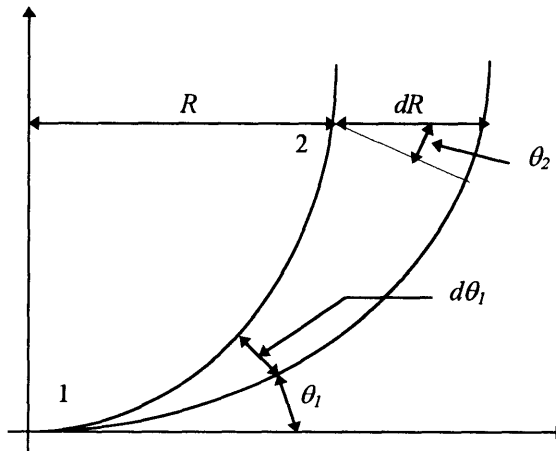
Figure 4.4: The ray tube cross section geometry for energy transport calculations

(surface or bottom.) In reality, however, reflections do occur, in particular in relatively shallow water and thus phase changes must be taken into account. Yet, unless one knows the exact shape of the surface and the bottom, and their effect on the phase of the reflected acoustic pressure, it is quiet impossible to estimate the exact phase of a reflected ray. One way to address this problem is simply to adopt incoherent pressure calculations via equation (4.13) where the mean square pressure of all the rays is appropriately added.

In order to verify the accuracy of the ray model, it was checked against SAFARI [26] which is a full wave solution. In order to compare to a full wave solution equation (4.14) must be used, in which the phase along the ray is taken into account. Figure 4.5 shows the result of coherent transmission loss calculations based on equation (4.14), and SAFARI (marked with '+'). Equation (4.14) used the ray trajectories shown in Figure 4.3 with 180 m range resolution. SAFARI used the sound velocity profile also shown in Figure 4.3 to generate the transmission loss with 105 m range resolution. The transmission loss is plotted as a function of range for a receiver located at a depth of 500 m, away from caustics regions. The similarity between SAFARI and ray theory verifies the validity of the ray equations and justifies using ray theory for this study. Note the differences between 0 - 3 km, which are the result of a slightly different angular spectrum of the source for the two methods. Such a similarity cannot be expected of course near caustic regions.

The singularity in both equations (4.13) and (4.14) at regions where the rays vertex and near caustics is integrable [7] and can be removed by means of integration or averaging. Therefore, an acceptable way of overcoming this problem is by smoothing the root mean square pressure around the singularity. The smoothing algorithm that I chose is a five point moving window that has the following form

$$a_n^s = 0.1a_{n-2} + 0.2a_{n-1} + 0.4a_n + 0.2a_{n+1} + 0.1a_{n+2} \qquad (4.15)$$

where a_n^s is the smoothed version of a_n, and the index represents the samples of the mean square pressure. The window is applied in caustic regions and where the rays vertex. It should be noted that this process is often applied at the singularities by averaging

over a wavelength distance if such a resolution is available in range. However, acceptable results are obtained even when the smoothing algorithm is applied over a larger and fixed range as done here using 200 m range resolution. One might think that this process is applied in reality by nature itself as the ocean is not a totally fixed environment that does not change with time. In fact, internal waves, mass transport, and other fluctuations in the ocean are to some extent a smoothing or an averaging process.

Another point that should be pointed out is that computers cannot deal with actual singularities as they cannot process infinite numbers. Instead, once the computer hits a singularity the program should limit the infinite result by a very large number the same way it is done in this study. Next, the bottom loss associated with the rays that hit the bottom is addressed.
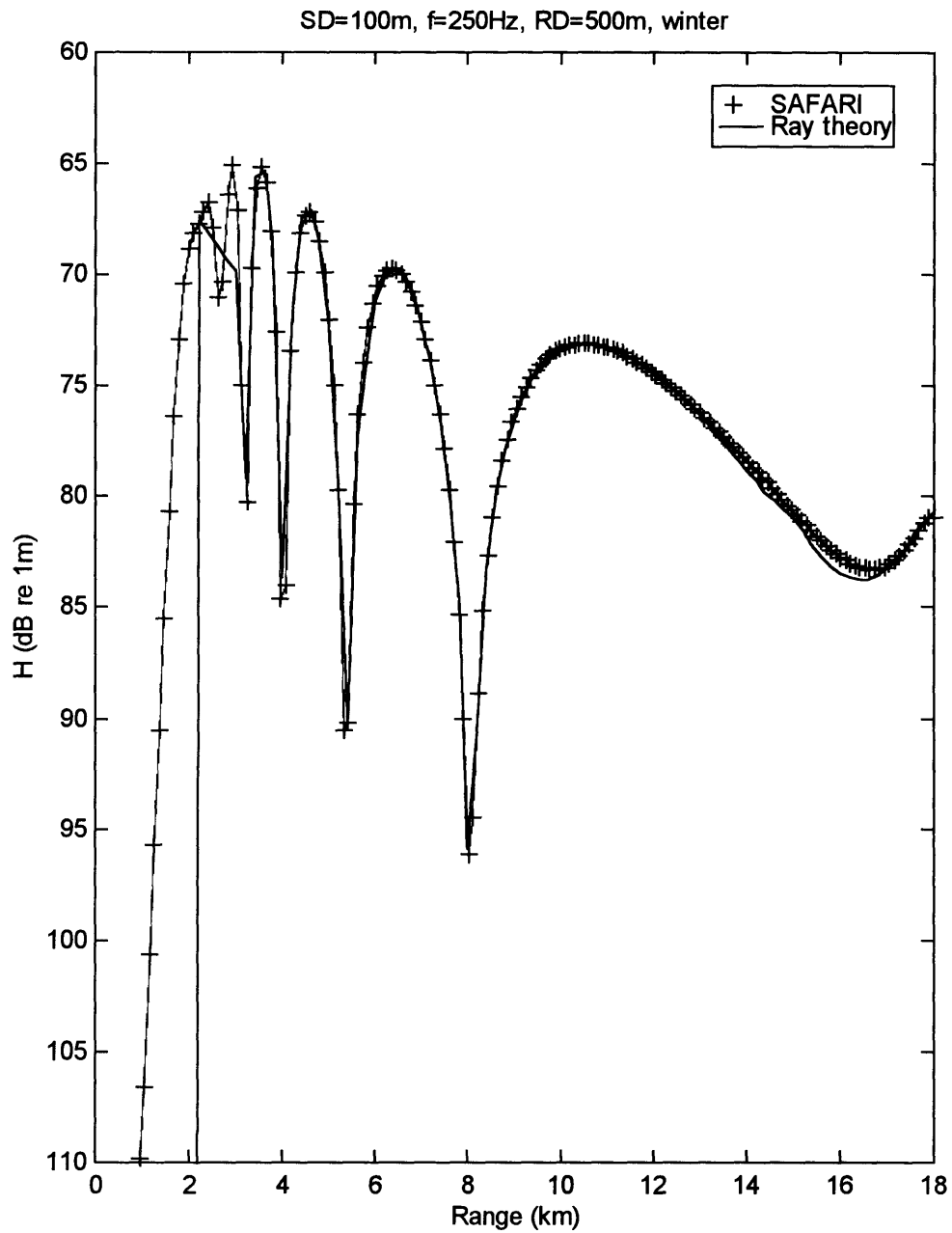
Figure 4.5: Coherent transmission loss calculated using ray theory (solid line) and SAFARI (marked with '+'). Receiver depth is 500m, source depth is 100m, source frequency is 250 Hz. The sound velocity profile is shown in Figure 4.3.

4.2 Bottom Loss

Bottom loss has been a subject of controversy over the past twenty years or so. Some have modeled the bottom roughness as a function of the bottom's surface elevations and slopes alone, while others have included the observation scale, λ_{os}, as a parameter in determining the RMS roughness height of the bottom, δ. T. H. Bell [10] is one of the researchers who provides the latter and verifies his model using actual data collected from the Pacific and the Atlantic oceans. The RMS roughness of the bottom, if known, can be used in the Fresnel forward scatter model [7] to determine the bottom loss. It is reasonable to believe that a similar approach is applicable to other ocean basins and therefore applicable in this study. Specifically, the RMS roughness height, δ, for $\lambda_{os} \geq 250$ m obeys the relation [10],

$$\delta \approx a \cdot \lambda_{os}^{1/2} \qquad (4.16)$$

where δ and λ_{os} are measured in meters, and a is a coefficient (with dimension $m^{1/2}$) that remains to be determined for the particular area of interest. For $\lambda_{os} \leq 250$ m,

$$\delta \approx b \cdot \sigma \lambda_{os} \qquad (4.17)$$

where b is a non dimensional coefficient, and σ is the RMS roughness slope. Bell [10] shows that the coefficients a and b for open oceans are approximately 0.6 and 0.3 respectively.

In order to determine the coefficients a and b for our case, one must have some bottom loss measurements that can represent the typical bottom loss of the eastern Mediterranean sea. Due to lack of actual bottom loss measurements from the eastern Mediterranean, the calculations here are based on bottom loss data taken from the Gulf of Oman, assuming that close results can be expected in the area of interest (which may not be true). The bottom loss data from the Gulf of Oman is shown in Figure 4.6 where there are differences between up-slope, down-slope, and cross-slope losses.

Coherent Forward Scatter Loss
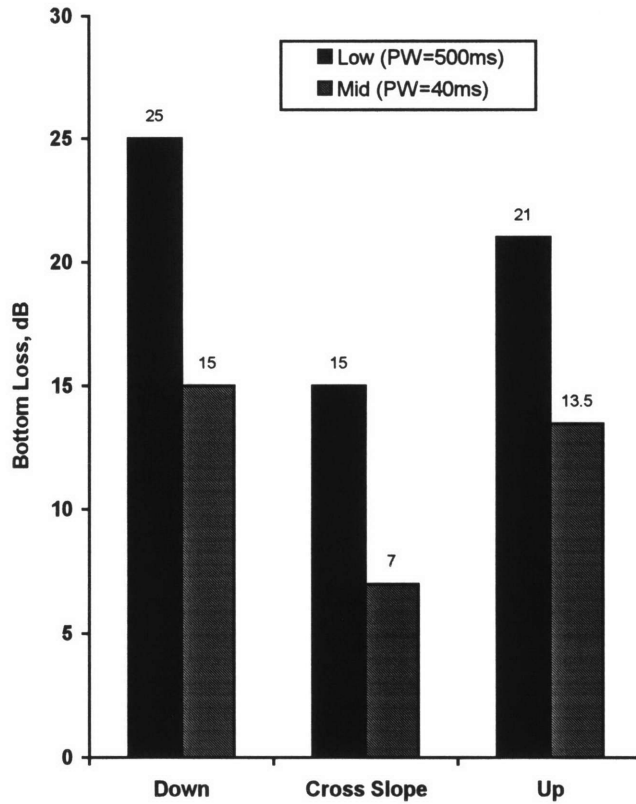
Figure 4.6: Bottom loss data taken at the Gulf of Oman, 15° bottom angle, $\Delta\phi$=0.1(rad). Bottom loss is shown for up, cross, and down slopes, for low frequency: 3.9kHz (pw=500ms) and mid frequency: 7.5 kHz (pw=40ms). courtesy Prof. I. Dyer.

The bottom loss measurements were obtained using active pulses generated from a directive source. Figure 4.6 also shows that there is a difference in bottom loss due to a change in the pulse width, which affects the observation scale. Given the pulse width, τ, and the propagation angle with respect to the bottom, θ_b, the ensonified portion of the bottom can be written as (see Figure 4.7)

$$\lambda_i = \frac{c\tau}{\cos\theta_b} \, . \tag{4.18}$$

λ_i is called here the direct observation scale. On the other hand, the transverse interaction scale, λ_j, is given by (see Figure 4.8)

$$\lambda_j = R \cdot \Delta\phi. \qquad (4.19)$$

Where R is a measure of the range between the source and the bottom, and $\Delta\phi$ is the horizontal beam width of the source. Modeling the scattering process as Fresnel forward scattering model [7], the bottom loss is given by

$$Loss = 5k\delta \sin\theta_b, \quad (dB / bounce) \qquad (4.20)$$

where k is the wave-number.

For our data (see Figure 4.6) assuming $c \approx 1535$ m/s, given $\theta_b \approx 15°$, and assuming a locally flat bottom, $\lambda_i = 64$ m when $\tau = 40$ ms, and $\lambda_i = 795$ m when $\tau = 500$ ms. On the other hand, the transverse observation scale, assuming that $R \approx 20$ km approximately (see Figure 4.3) and using equation (4.19), is $\lambda_j = 2000$ m. In order to determine which observation scale one should use, it is necessary to understand what the inherent differences are between the up-slope, down-slope and the cross-slope bottom losses.

Imagining the bottom slope as horizontal stairs connecting all the points on the bottom with the same depth it is reasonable to argue that they represent the bottom roughness. The bottom roughness is, then, modeled as unidepth contour lines. In the up-slope/down-slope case one samples "more" bottom roughness as the transverse observation scale increases as opposed to the cross-slope case where "more" bottom roughness is sampled as the direct observation scale increases. This is a reasonable argument where the two observation scales are of the same order of magnitude. In the case where the direct observation scale and the transverse observation scale are of different orders of magnitude the geometrical mean of the two can be used as a measure of the larger observation scale.
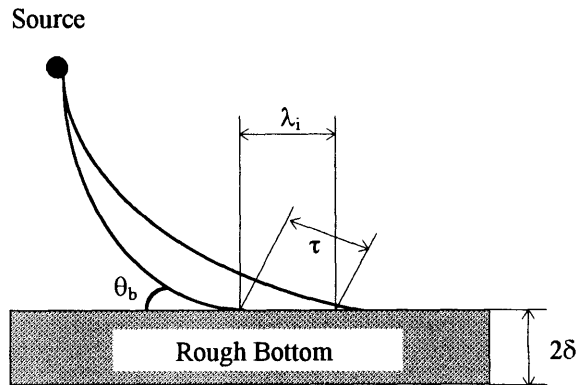
Figure 4.7: Diagram for bottom roughness calculations. τ is pulse width, λ_i is the direct observation scale, and δ is the RMS bottom roughness height.
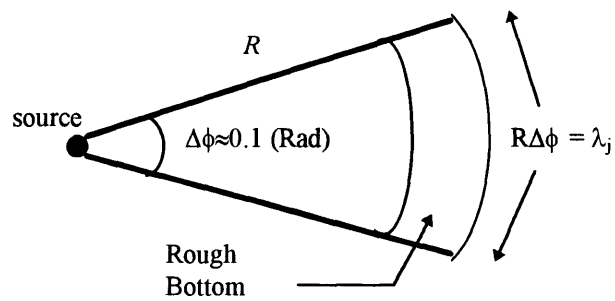
Figure 4.8: Diagram for transverse observation scale calculations. Top view of Figure 4.7. R is the range between the source and the bottom, $\Delta\phi$ is the horizontal beam width of the source.

As a result, for τ = 500 ms the two observation scales are of the same order and therefore one should choose λ_j for the up-slope and down-slope cases, and λ_i for the cross-slope case, as discussed earlier. For the second case, τ = 40 ms, the observation scales are not of the same order of magnitude and therefore the geometrical mean is used instead of the larger observation scale. Also, we know from equation (4.20) that the RMS bottom roughness can be calculated directly knowing the loss in dB/bounce, the bottom angle, and the wavenumber. As a result, once the bottom roughness, δ, and the observation scale, λ_{os}, are known it is possible to determine the coefficients a, and b using equations (4.18) and (4.19).

Table 4-1 and Table 4-2 summarize the results for the coefficients a and b for the two different cases given in Figure 4.6. In Table 4-1 the observation scale is more than 250 m and therefore the coefficient a can be determined and averaged over the down-slope, cross-slope, and the up-slope cases. Note that the observation scale for the cross-slope case is 795 m corresponding to λ_i, and the observation scale for the up and down-lope cases is λ_j, as discussed previously. From Table 4-1 a $\approx$ 0.025.

In Table 4-2 the observation scale is more than 250 m for the up and down-slope cases but less than 250 m for the cross-slope case. Here, both a and b can be evaluated

Table 4-1: Bottom roughness and coefficients calculation for PW=500ms, f=3.9kHz

	Pulse Width = 500 ms ; f=3.9kHz			
	λ_{os} [m]	Loss [dB/bounce]	$\delta = \dfrac{Loss}{5k\sin\theta_b}$, [m]	$a = \dfrac{\delta}{\lambda_{os}^{1/2}}$, [m$^{1/2}$]
Down Slope	2000	25	1.21	0.027
Cross Slope	795	15	0.72	0.026
Up slope	2000	21	1.01	0.023

Table 4-2: Bottom roughness and coefficients calculation for PW=40ms, f=7.5kHz

Pulse Width = 40 ms ; f=7.5kHz					
	λ_{os} [m]	Loss [dB/bounce]	δ [m]	$b = \delta / (\sigma \lambda_i)$		a
				σ=0.35 [rad]	σ=0.7 [rad]	
Down Slope	357	15	0.38			0.021
Cross Slope	64	7	0.18	0.008	0.004	
Up slope	357	13.5	0.34			0.019

as a ≈ 0.020 and b ≈ 0.008 for σ = 0.35 and b ≈ 0.004 for σ = 0.7 radians. The RMS slope, σ, should be chosen such that it would represent the actual RMS bottom slope. Since the actual slope of the bottom is not known in the required resolution for determining the RMS bottom slope, it is reasonable to guess one using actual RMS in-land roughness slopes. In-land roughness slopes are ~ 20° (from observations) and therefore σ ~ 0.35 rad. Following this logic the RMS roughness height, δ, for the eastern Mediterranean is given by

$$\delta \approx \begin{cases} 0.023 \cdot \lambda_{os}^{1/2}, & \lambda_{os} \geq 250m \\ 0.008 \cdot \sigma \cdot \lambda_{os}, & \lambda_{os} \leq 250m, \quad \sigma \approx 0.35\,\text{rad} \end{cases} \qquad (4.21)$$

where the coefficient 'a' is the average of the values found in Tables 4-1 and 4-2, and the bottom loss is given by equation (4.20). It should be emphasized that this model should be recalculated once actual bottom loss measurements from the eastern Mediterranean are available.

4.3 Determining the Dominant Propagation Type

One of the most important parameters in sound propagation is the propagation type as a function of depth and range. One must distinguish at least between two classes of propagation which have a substantial effect on the sonar performance. The first class is the *bottom-bounce* propagation and the other is the *RSR* (refracted surface reflected) or any other propagation type that does not involve bottom-bounced rays like direct refracted rays.

Bottom-bounce propagation introduces the bottom influence on the transmission loss while the other is affected by the ocean and (sometimes) the surface. Since, the bottom and the ocean have different characteristic length scales, the observation scale of the sonar should be chosen appropriately to reflect those differences.

Naturally, with an omni directional source these two types of propagation coexist at some point in range. More importantly, however, one should determine which type dominates in order to correctly choose the observation scale. Since the observation scale is directly related to the integration time of the receiver, the sonar operator should choose the appropriate integration time according to the propagation type.

One of the most common and most useful tools that are frequently used to determine the propagation type is the ray trace diagram. The ray diagram depends on the sound velocity profile and on the bottom properties (in our case bottom depth and slope). As a result, the ray diagram should be generated for each case being investigated here. Total of 14 ray diagrams were generated to account for the different locations, different seasons, and different bottom slopes except for the first location where only two diagrams are shown because of a negligible bottom slope. The ray diagrams are depicted in Figures 4.9 - 4.22 as outlined in Table 4-3.

Table 4-3: Figures of ray trace diagrams used to determine the propagation type

Figure #	Location #	season	slope
4.9	1	winter	up
4.10	1	summer	up
4.11	2	winter	up
4.12	2	winter	cross
4.13	2	winter	down
4.14	2	summer	up
4.15	2	summer	cross
4.16	2	summer	down
4.17	3	winter	up
4.18	3	winter	cross
4.19	3	winter	down
4.20	3	summer	up
4.21	3	summer	cross
4.22	3	summer	down

Since the receiver in this study can be placed between 50 m - 150 m at ranges 0 - 50 km the analysis is carried out for a receiver at 100 m depth realizing that only negligible error in range is introduced for the whole available depth range of the receiver.

Another factor that should be addressed is the operating frequency. This is, of course, since the bottom loss is directly related to frequency. In other words, for low frequencies the loss associated with the bottom is small and it increases as the frequency increases. It is useful therefore to divide the frequency regime to two main bands. Namely, the upper frequency band where the bottom loss is large, and the lower frequency band where the bottom loss is small as discussed subsequently. This analysis should be in practice carried out for finer frequency bands for which the dominant propagation type is determined after estimating the bottom loss in comparison to the RSR propagation. In this study, however, the ray trace diagram is analyzed for these two extreme cases where the results of the analysis for the mid frequency regime is expected to be limited by the results for the upper and lower frequency bands.

Based on the above argument a detailed analysis is presented subsequently for the first ray trace diagram (see Figure 4.9). A similar approach is then applied to each of the

remaining ray diagrams and the results for the different cases are summarized in Table 4-4 through 4.5 for the lower frequency band (50 Hz - 500 Hz), and the upper frequency band (1k Hz - 5 kHz) which both cover the whole useful frequency regime for the different array types as shall be verified in chapter 7.

Figure 4.9 shows the propagation pattern for the first location during the winter, up-slope case. An RSR propagation type seems to exist at all ranges (the figure shows only 0 - 50 km). However, for a receiver at 100 depth, the RSR is relatively weak for 10 km $< R <$ 26 km. In other words, for 10 km $< R <$ 26 km bottom-bounce propagation might dominate in the low frequency band while in the upper band the RSR propagation dominates everywhere. Note that the RSR always dominates at the convergence zone 26 km $< R <$ 40 km. Due to a very mild bottom slope no slope effects are observed at the interesting ranges (0 - 50 km). As mentioned earlier, the results for this case as well as for the rest of the cases are summarized in Tables 4-4, and 4-5 for the low, and high frequency bands respectively.

Table 4-4: Dominant propagation type. Receiver depth 100 m, 50Hz $< f <$ 500Hz.

Location	slope	season	propagation type	
			RSR (km)	Bottom-Bounce(km)
1	all	winter	0 - 10, 26 - 50	10-26
1	all	summer	0 - 2, 25 - 42	2 - 25, 42 - 50
2	up	winter	0 - 7	7 - 30
2	cross	winter	0 - 7, 27 - 42	7 - 27, 42 - 50
2	down	winter	0 - 7, 29 - 42	7 - 29, 42 - 50
2	up	summer	0 - 2	2 - 30
2	cross	summer	0 - 2, 29 - 36	2 - 29, 36 - 50
2	down	summer	0 - 2, 30 - 34	2 - 30, 34 - 50
3	up	winter	0 - 6, 28 - 40	6 - 28, 40 - 50
3	cross	winter	0 - 6, 28 - 40	6 - 28, 40 - 50
3	down	winter	0 - 6, 28 - 40	6 - 28, 40 - 50
3	up	summer	0 - 2, 28 - 34	2 - 28, 34 - 50
3	cross	summer	0 - 2, 28 - 34	2 - 28, 34 - 50
3	down	summer	0 - 2, 28 - 35	2 - 28, 35 - 50

Table 4-5: Dominant propagation type. Receiver depth 100 m, $1\text{kHz} < f < 5\text{kHz}$.

Location	slope	season	propagation type	
			RSR (km)	Bottom-Bounce(km)
1	up	winter	0 - 50	-
1	up	summer	0 - 2, 25 - 42	2 - 25, 42 - 50
2	up	winter	0 - 7	7 - 30
2	cross	winter	0 - 7, 27 - 50	7 - 27
2	down	winter	0 - 7, 29 - 50	7 - 29
2	up	summer	0 - 2	2 - 30
2	cross	summer	0 - 2, 29 - 36	2 - 29, 36 - 50
2	down	summer	0 - 2, 30 - 34	2 - 30, 34 - 50
3	up	winter	0 - 6, 28 - 43	6 - 28, 43 - 50
3	cross	winter	0 - 6, 28 - 44	6 - 28, 44 - 50
3	down	winter	0 - 6, 28 - 44	6 - 28, 44 - 50
3	up	summer	0 - 2, 28 - 34	2 - 28, 34 - 50
3	cross	summer	0 - 2, 28 - 34	2 - 28, 34 - 50
3	down	summer	0 - 2, 28 - 35	2 - 28, 35 - 50
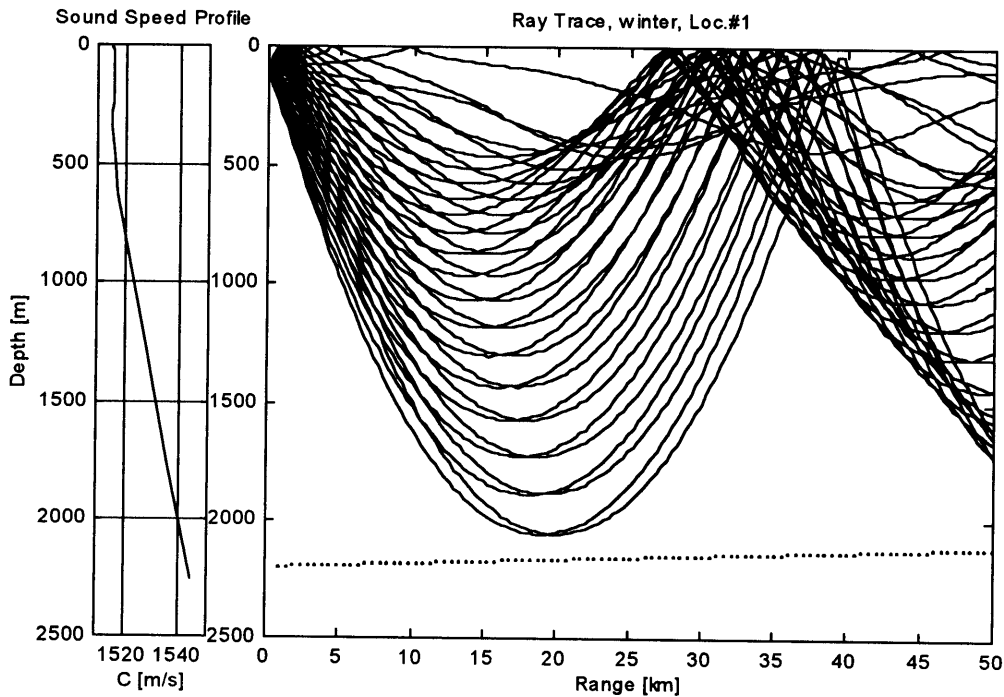
Figure 4.9: Ray trace diagram for the first location during the winter season. The SVP is plotted on the left hand side. Rays that hit the bottom are excluded. Bottom depth is about 2200 m, up-slope of 0.1°, angle resolution is 0.6°. Angular spectrum shown ± 10.3°
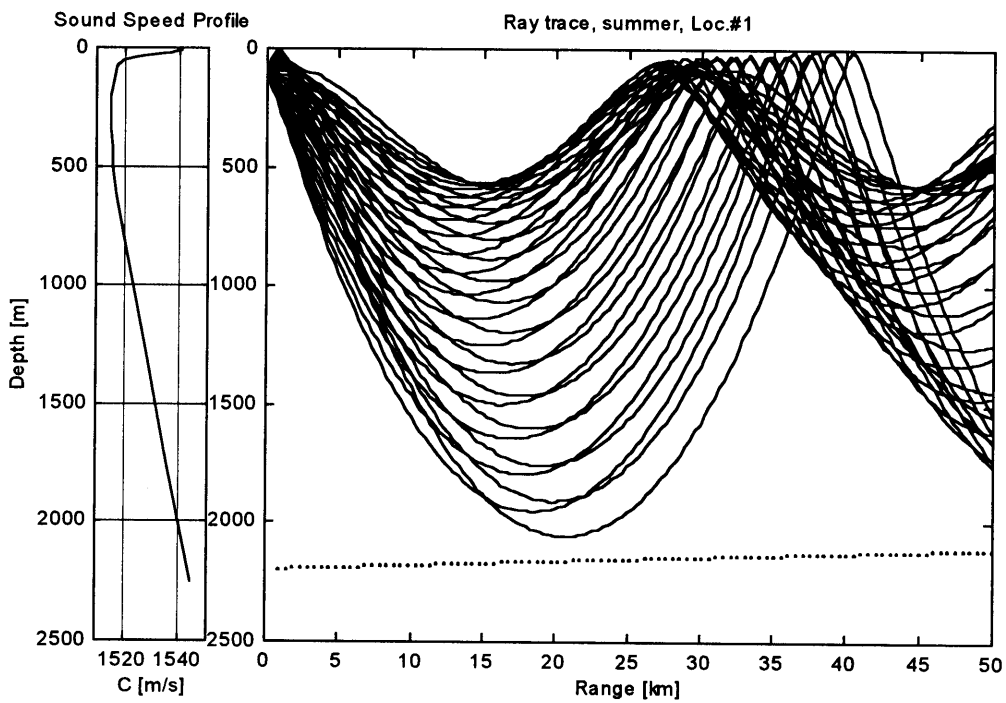
Figure 4.10: Ray trace diagram for the first location during the summer season. The SVP is plotted on the left hand side. Rays that hit the bottom are excluded. Bottom depth is about 2200 m, up-slope of 0.1°, angle resolution is 0.6°. Angular spectrum shown: ± 10.3°

Figure 4.11: Ray trace diagram for the second location, up-slope case during the winter season. The SVP is plotted on the left hand side. Bottom depth is about 1200 m, bottom slope is 3°, angle resolution is 0.6°. Angular spectrum shown ±8.5°. Note the massive bottom interaction as the depth gets shallower. Note also that all the rays hit the bottom.

Figure 4.12: Ray trace diagram for the second location, cross-slope case during the winter season. The SVP is plotted on the left hand side. Bottom depth is about 1700 m, bottom slope is 3°, angle resolution is 0.6°. Angular spectrum shown: ±7.3°.

Sound Speed Profile

Ray Trace, winter, Loc.#2

Figure 4.13: Ray trace diagram for the second location, down-slope case during the winter season. The SVP is plotted on the left hand side. Bottom depth is about 1700 m, bottom slope is -3°, angle resolution is 0.6°. Angular spectrum shown: -3.0° to 4.3° .

Figure 4.14: Ray trace diagram for the second location, up-slope case during the summer season. The SVP is plotted on the left hand side. Bottom depth at the source is about 1700 m, bottom slope is 3°, angle resolution is 0.6°, angular spectrum shown is ±8.5°. Note the massive bottom interaction as the depth gets shallower. Note also that all the rays hit the bottom.

Figure 4.15: Ray trace diagram for the second location, cross-slope case during the summer season. The SVP is plotted on the left hand side. Bottom depth is about 1700 m, bottom slope is 0.0°, angle resolution is 0.6°, angular spectrum shown is ±7.3°.

Figure 4.16: Ray trace diagram for the second location, down-slope case during the summer season. The SVP is plotted on the left hand side. Bottom depth changes substantially with range, bottom slope is -3°, angle resolution is 0.6°, angular spectrum shown is ± 3°.
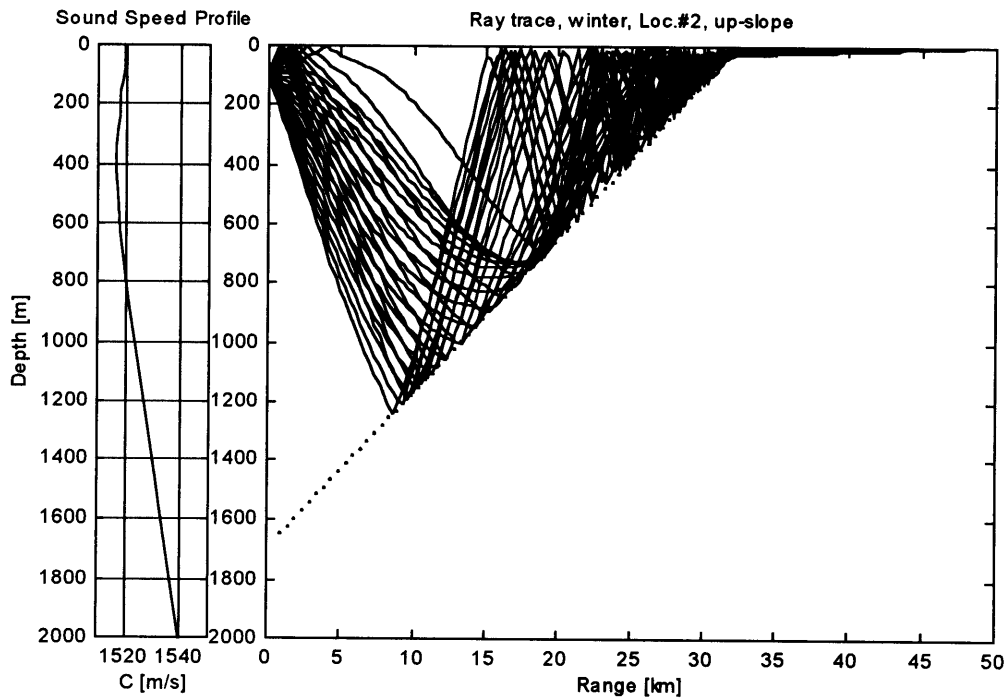
Figure 4.17: Ray trace diagram for the third location, up-slope case during the winter season. The SVP is plotted on the left hand side. Bottom depth is about 1200 m, bottom slope is 0.4°, angle resolution is 0.6°, angular spectrum shown ±5°.

Figure 4.18: Ray trace diagram for the third location, cross-slope case during the winter season. The SVP is plotted on the left hand side. Bottom depth is about 1200 m, bottom slope is 0.0°, angle resolution is 0.6°, angular spectrum shown ±5.5°.

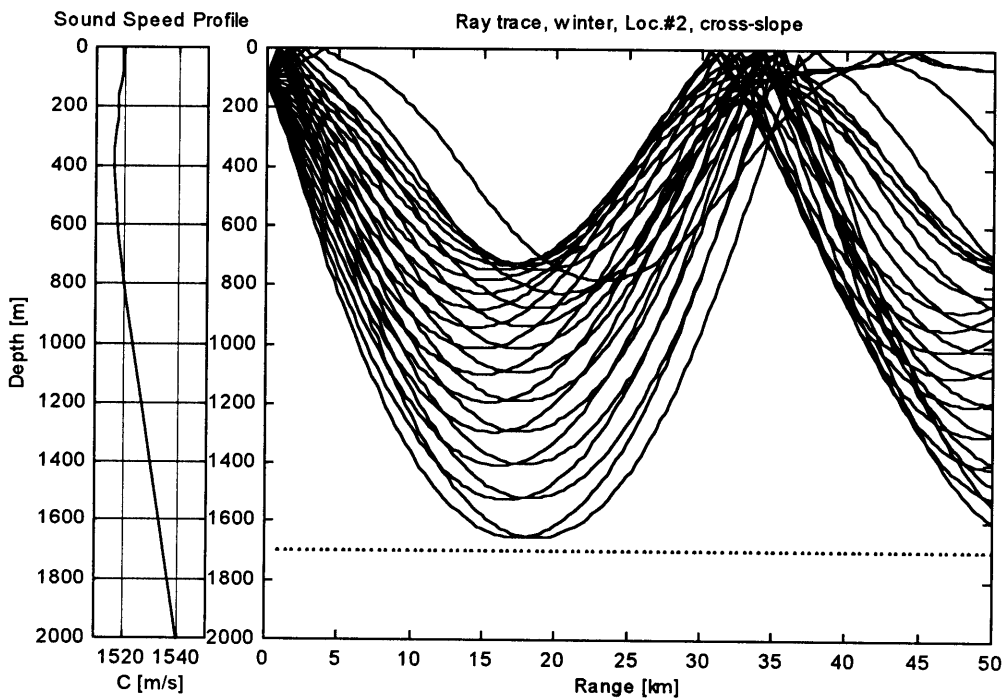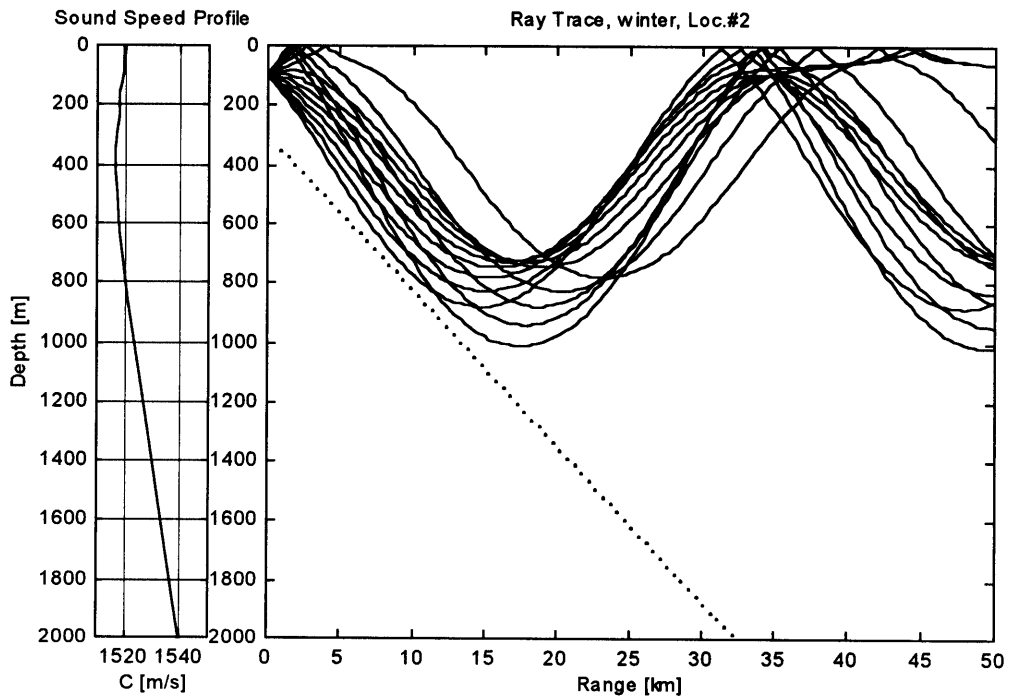**Sound Speed Profile**

Ray Trace, winter, Loc.#3, down-slope

Figure 4.19: Ray trace diagram for the third location, down-slope case during the winter season. The SVP is plotted on the left hand side. Bottom depth is about 1200 m and increasing, bottom slope is -0.4°, angle resolution is 0.6°, angular spectrum shown ±6.1°.

Sound Speed Profile   **Ray Trace, summer, Loc.#3, up-slope**
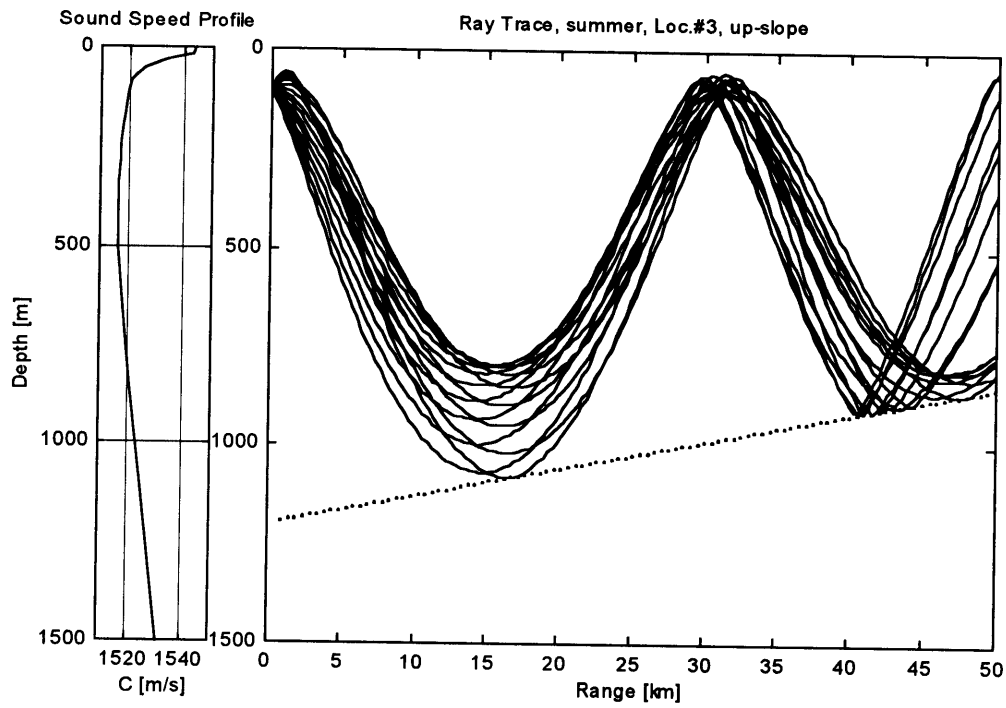
Figure 4.20: Ray trace diagram for the third location, up-slope case during the summer season. The SVP is plotted on the left hand side. Bottom depth is about 1200 m, bottom slope is 0.4°, angle resolution is 0.6°, angular spectrum about ±4.3°.

Sound Speed Profile

Ray Trace, summer, Loc.#3, cross-slope
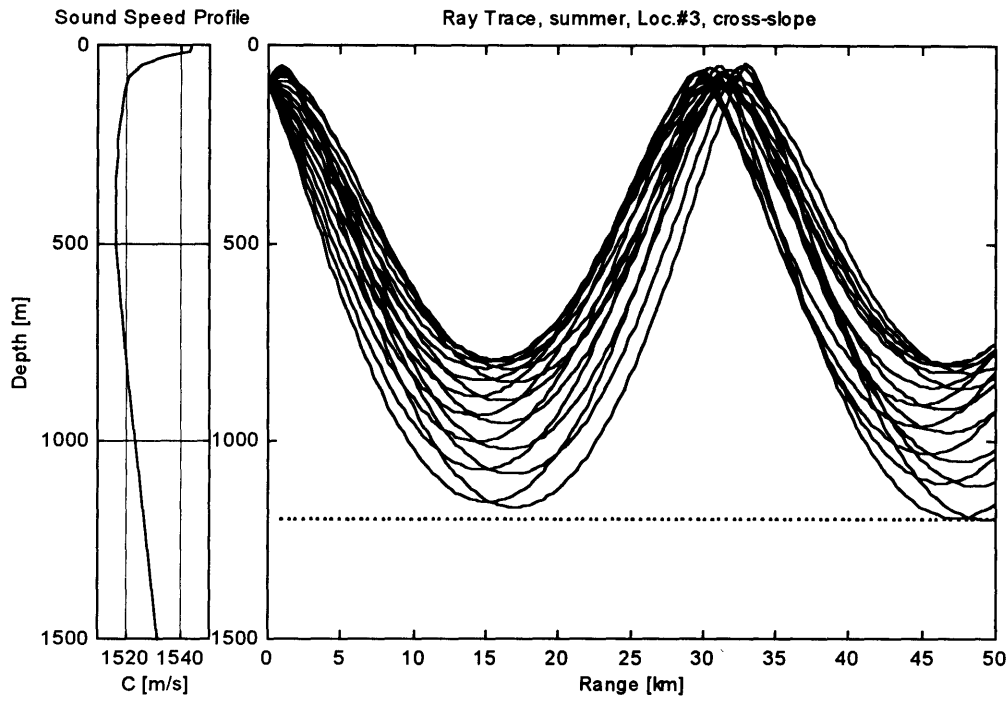
Figure 4.21: Ray trace diagram for the third location, cross-slope case during the summer season. The SVP is plotted on the left hand side. Bottom depth is about 1200 m, bottom slope is 0.0°, angle resolution is 0.6°, angular spectrum about ±4.9°.
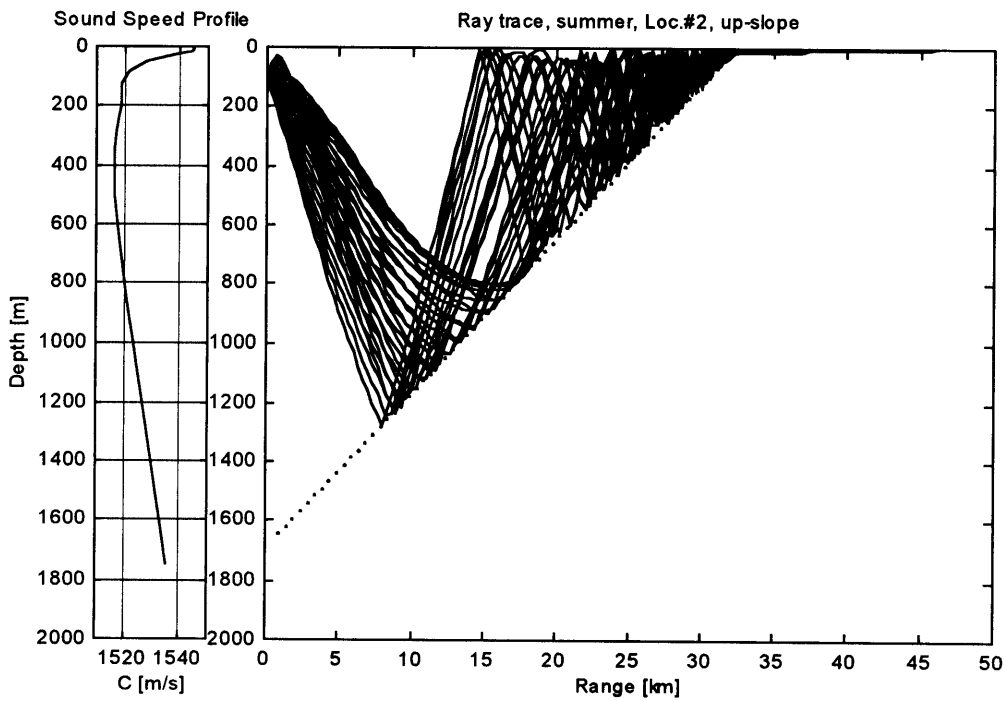
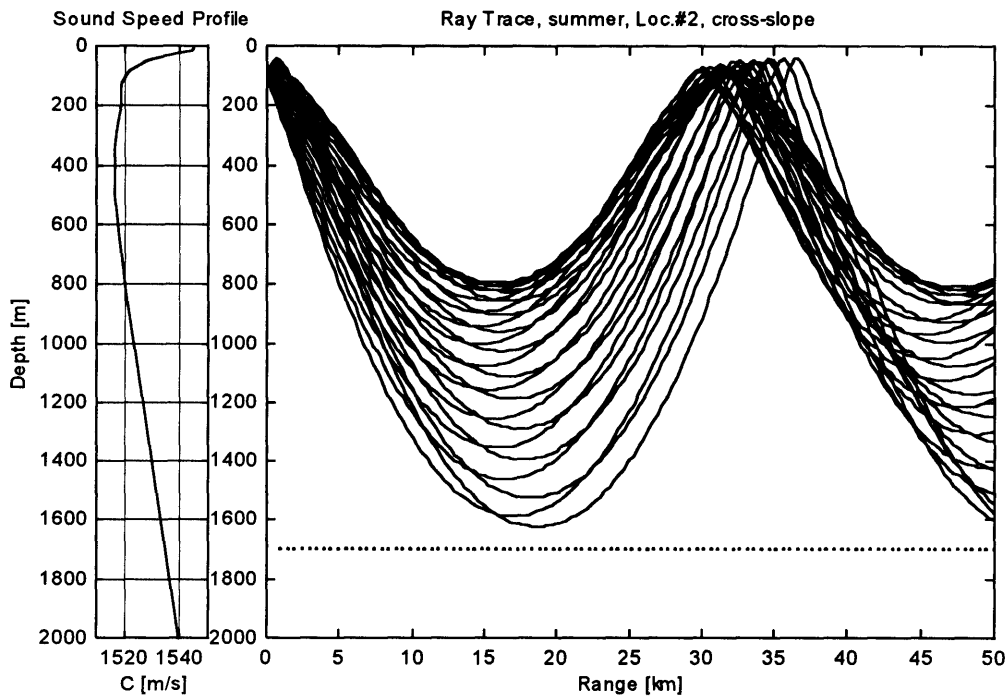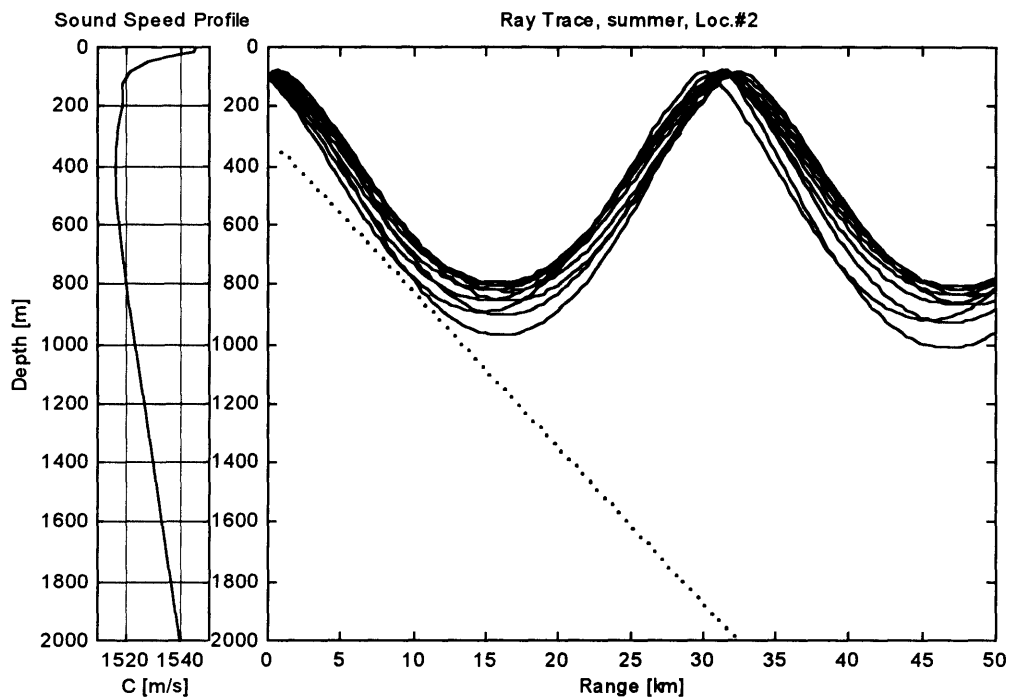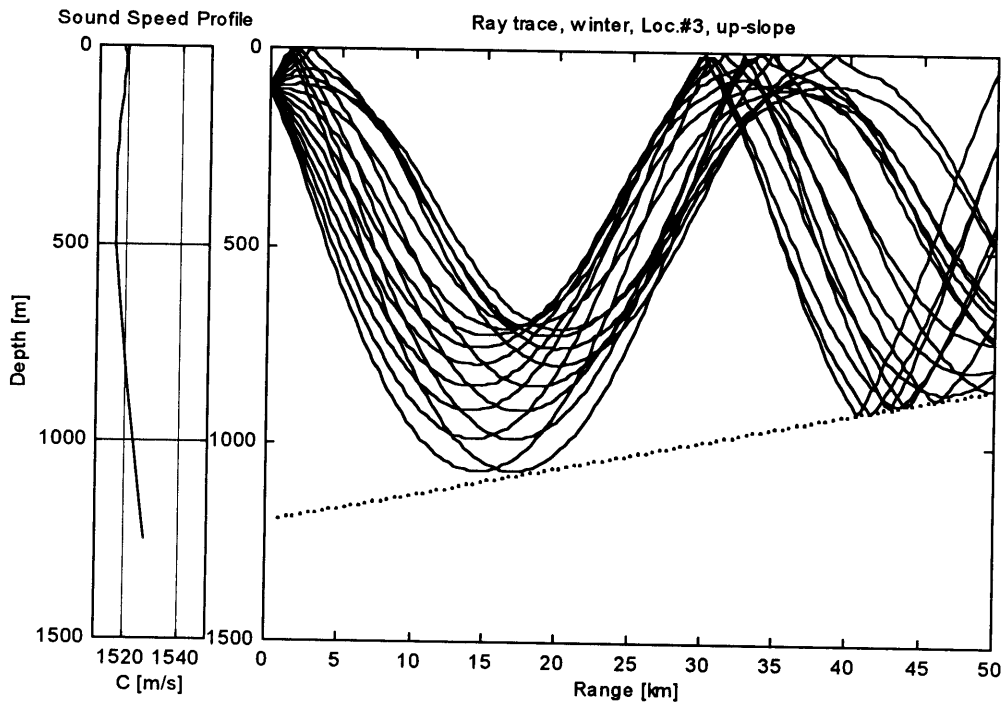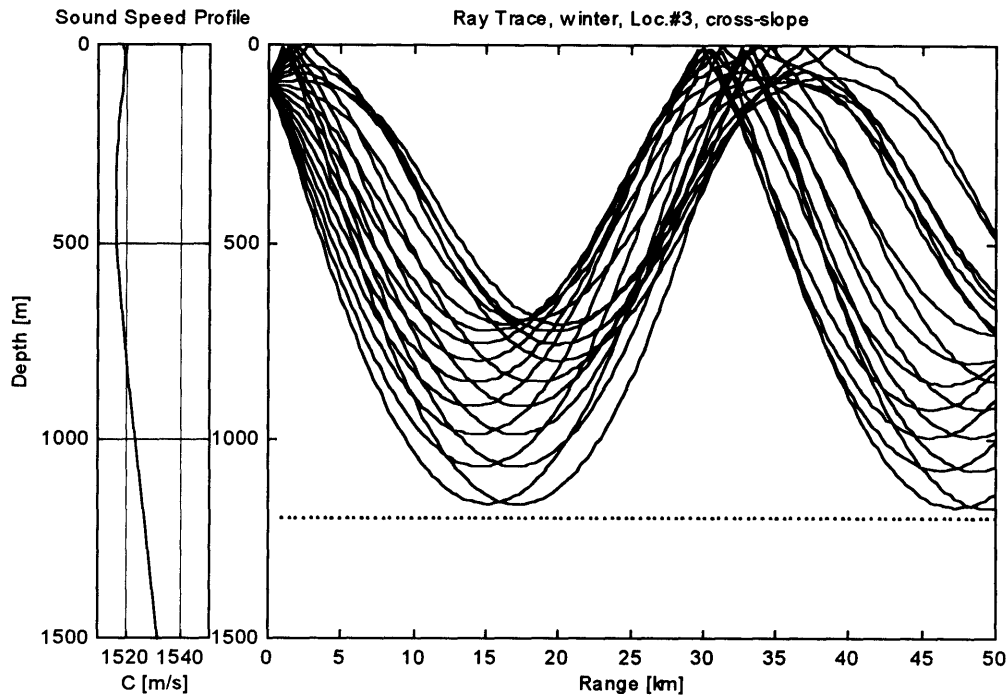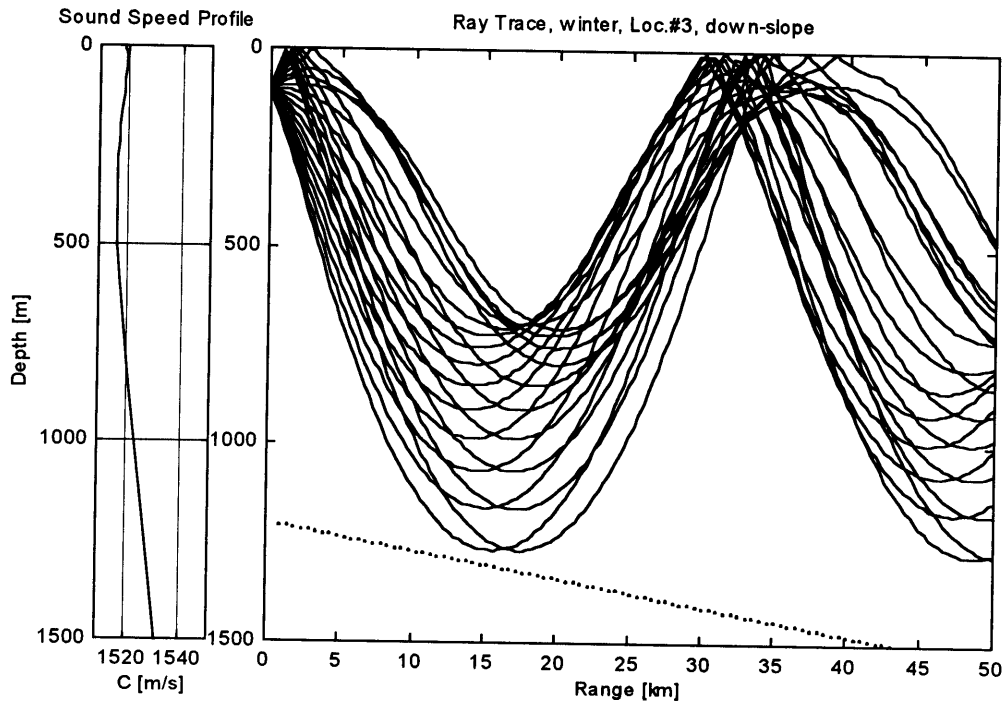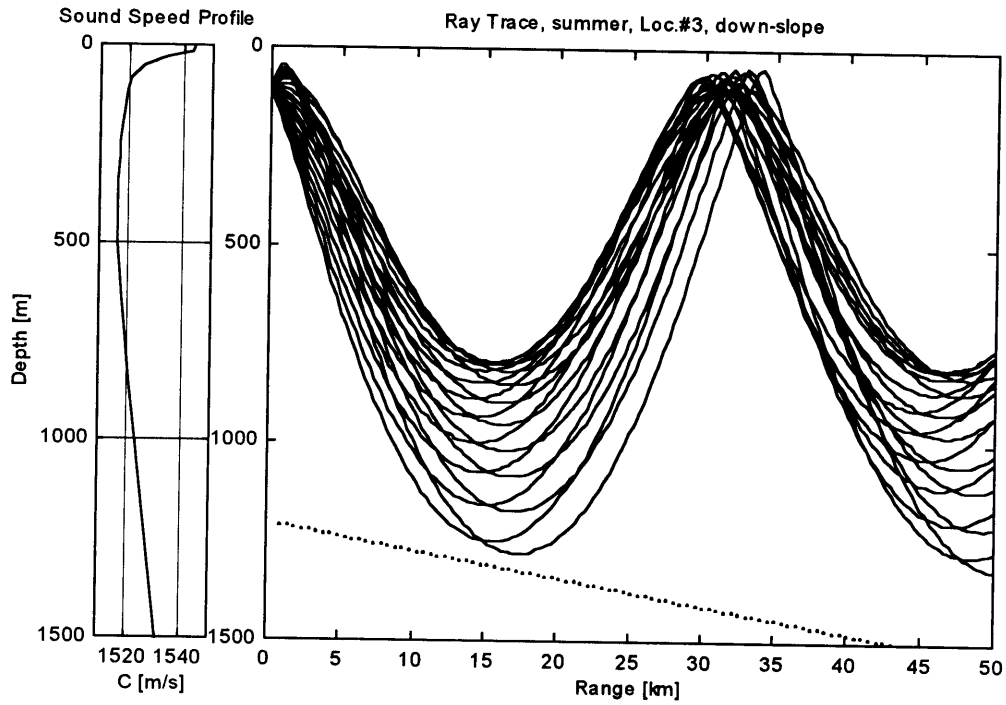Figure 4.22: Ray trace diagram for the third location, down-slope case during the summer season. The SVP is plotted on the left hand side. Bottom depth is about 1200 m, bottom slope is -0.4°, angle resolution is 0.6°, angular spectrum about ±5.5°.

4.4 Determining the Observation Scale

As mentioned earlier, the observation scale should be chosen so that it would not be larger than the characteristic length scale of the medium. From section 4.3 there are two main propagation types that affect the observation scale of the receiver. The RSR propagation involves only the ocean itself and the ocean surface while bottom-bounce propagation involves the ocean bottom characteristics. Accordingly, two observation scales need to be determined. The first corresponds to the bottom-bounce propagation and the second corresponds to the RSR propagation. Once the observation scale is known the integration time of the receiver should be set appropriately.

4.4.1 Bottom-Bounce Propagation

The observation scale for the bottom bounce propagation plays an important role in determining the bottom loss. In section 4.2 the necessary steps to calculate λ_{os} were provided for active sonar systems. Similarly, the direct observation scale for passive systems can be estimated using the integration time (noted by the variable τ). λ_i for passive systems is then

$$\lambda_i = \frac{c\tau}{\cos\theta_b}.\qquad\qquad(4.22)$$

Note the sensitivity of λ_i to the integration time. This is probably one of the reasons why the integration time is a very crucial parameter in the performance of a passive system and therefore should be optimized for a particular area and sonar system. In other words, τ is the time in which the target is considered statistically stationary. To make sure that this is indeed the case, the condition $\lambda_i < \lambda_c$ (the characteristic length scale of the bottom) should be forced. Once the above condition is met, the receiver integrates the signal over τ and forms a single realization of the target. From the sonar system design point of view, τ should be chosen appropriately. Unfortunately, the characteristic length

scale of the ocean bottom can vary significantly from one place to another and as a result the integration time should vary accordingly in order to stay within a single realization of the target.

The direct observation scale, λ_i, also depends on the sound speed, c, at the bottom. But variations in the sound speed at the bottom of the locations, are relatively small and therefore not critical to the observation scale. An average measure of the sound speed over the three locations can be used to calculate λ_i. In our case the average sound speed at the bottom is $c \approx 1535$ (m/s).

In addition, the direct observation scale also depends on the grazing angle between the ray and the bottom, θ_b, which also varies for each ray, range, and bottom depth. The problem that we are facing now is how to determine the optimal integration time that will be used to calculate the observation scale. From the above discussion, a single integration time cannot be optimal for every case. In most practical cases, however, the integration time of a sonar system is set to a specific value which is optimal for a specific mission. The mission in this study is to receive the target from a range R, with altitude h (of both receiver and target), assuming a single bottom interaction geometry as depicted Figure 4.23. Assuming a constant gradient, g, using a small angle approximation, and equation (4.10), θ_b, should obey the relation

$$\frac{4h}{R} \approx \sqrt{\theta_b^2 + \frac{2\Delta c}{c}} + \theta_b \qquad (\,4.23\,)$$

Other definitions of the mission's geometry can be similarly applied resulting in different relations for θ_b. The range, R, can be found in Table 4-4 or 4-5 that corresponds to a bottom bounce propagation. In addition h varies from 2200 m at the first location to 1200 m at the third location (see chapter 2). From chapter 2 the sound speed near the target (100 m depth) is estimated as $c \approx 1520$ m/s and $\Delta c \approx 20$ m/s, 15 m/s, and 10 m/s for the first, second, and third locations respectively. Δc also varies with season but in our case for a source at 100 m depth it does not. Using equation (4.23), θ_b can now be evaluated for the various cases that are considered here.
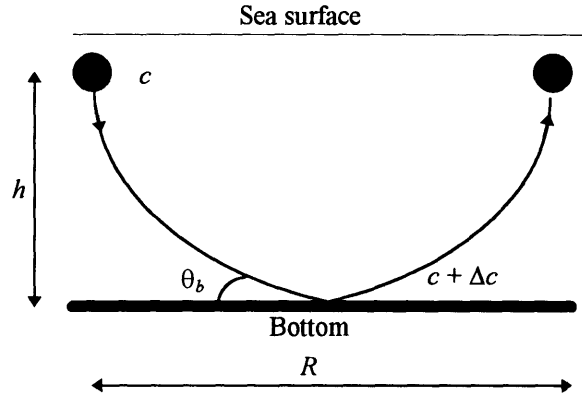
Figure 4.23: Target-source geometry for a single bottom interaction.

In order to finally estimate the integration time one should estimate the characteristic length scale of the bottom roughness, λ_c. The characteristic length scale of the bottom roughness may vary, say, from 10 m, at steep slopes, to 1000 m, at mild slopes. As a result it is reasonable that λ_c varies from one location to another and in reality even within each location. Since the characteristic length scale of the bottom is not known at the time of writing it is reasonable to guess one as $\lambda_c = 500$ m. Although this choice of λ_c may not be true for all cases it will be used here as a measure of the characteristic length scale of the bottom. Once λ_c and θ_b are known, the integration time is given by

$$\tau = \frac{\lambda_c \cos\theta_b}{c} \qquad (4.24)$$

where τ is different for each θ_b and λ_c. In order to see the effect of the different cases on the integration time equation (4.23) and (4.24) were used to generate the integration times in Table 4-6 as a function of R for the different locations. The characteristic length scale of the bottom is $\lambda_c = 500$ m in all cases and Δc is unchanged between winter and summer for a receiver depth of 100 m.

Table 4-6: Integration time (sec) for the bottom-bounce propagation as a function of range between source and receiver (R). λ_c = 500 m.

R (km) (see Figure 4.23)	10	20	30	40	50
Location 1 (h = 2200 m, Δc = 20 m/s)	0.29	0.31	0.324	0.325	0.325
Location 2 (h = 1700 m, Δc = 15 m/s)	0.31	0.32	0.325	0.325	0.325
location 3 (h = 1200 m, Δc = 10 m/s)	0.317	0.323	0.325	0.325	0.325

Once τ is known it is used to determine the direct observation scale, λ_i, via equation (4.22). Accordingly, for each ray that hit the bottom with an angle θ_b, the direct observation scale is given by

$$\lambda_i = \frac{c \cdot \tau}{\cos\theta_b}.$$

(4.25)

In order to calculate the transverse observation scale, the beam width of the active source, $\Delta\phi$, should be replaced now with the equivalent beam width of the receiver, ϕ_e. Using equation (4.19) the transverse observation scale can be written as

$$\lambda_j = R\phi_e.$$

(4.26)

The equivalent beam width of the receiver can be determined from the array design, its dimensions and the frequency. This topic is covered in more detail in chapters 6 and 7.

The observation scale to be used in our model can be evaluated using exactly the same approach that was used to find the coefficients a and b in section 4.2. Figure 4.10 presents the final algorithm used to estimate the observation scale for bottom-bounce.
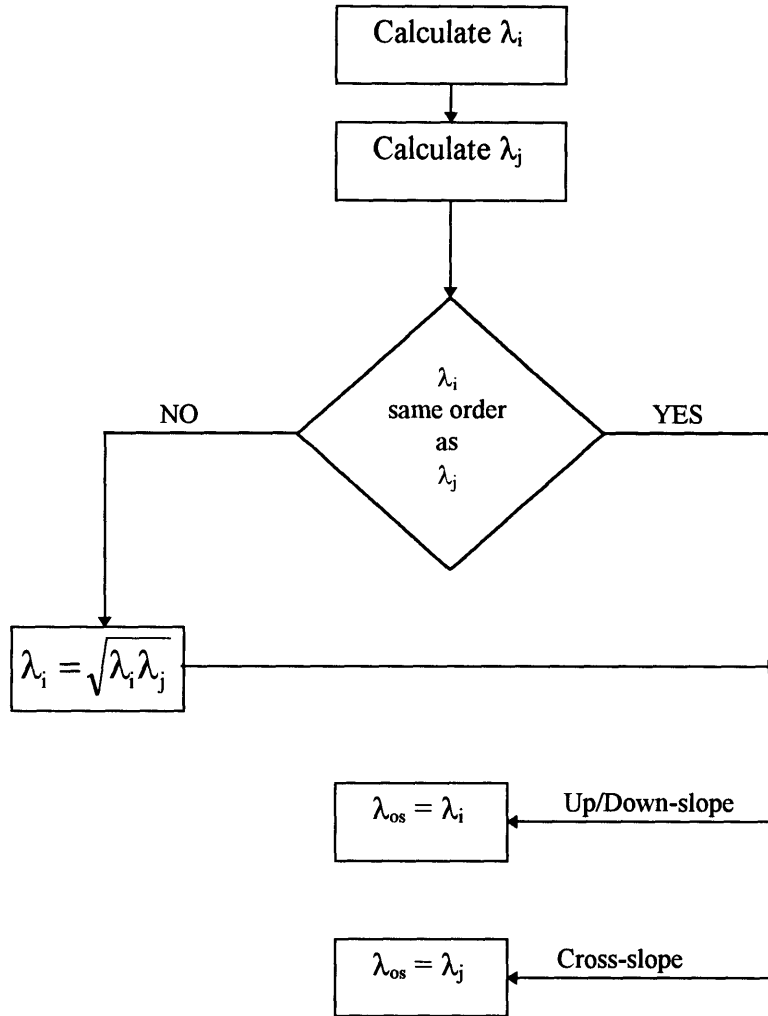
Figure 4.24: Flow chart for determining the observation scale for bottom loss calculations. This procedure is repeated for each ray that hits the bottom.

Once the observation scale is determined the RMS roughness height, δ, is calculated using equation (4.21), and the bottom loss results using equation (4.20).

4.4.2 RSR Propagation

The RSR propagation is defined in this study as the propagation that does not involve any bottom-bounced rays. In this case, the characteristic length scale of the ocean can be approximated by the following frequency dependent formula

$$\lambda_c = 500\lambda$$

where λ is the wavelength. λ_c again limits the maximum observation scale so that $\lambda_{os} \leq \lambda_c$. In this case the observation scale depends on the frequency of the received signal only. The integration time of the receiver, however, depends not only on the observation scale but also on the relative velocity of the source and the receiver. In this study the source (target) can move with a velocity of 3 knots ($v \approx 6$ km/h) relative to the receiver and therefore the integration time is given by $\tau = \lambda_{os}/v$. Table 4-7 lists the integration time results the for various frequencies in the interesting frequency regime. As can be seen the integration time for the RSR propagation is much longer than the one found for the bottom-bounce propagation. This enables the sonar system to be operated with a longer integration time and by that to decrease the detection threshold. In other words, in case of an RSR propagation the sonar is more capable of detecting the target than in the bottom-bounce case.

Naturally, with longer integration times the bottom loss increases since the observation scale increases. The bottom loss can be obtained by repeating the algorithm suggested in sections 4.2 and 4.4.2 for the new integration time.

Table 4-7: Integration times for RSR propagation as a function of frequency. $v \approx 6$ km/h.

f (Hz)	100	200	500	1k	2k	5k
τ (min)	78	39	15	7.8	3.9	1.56

4.4.3 Overall Observation Scale

In order to choose the overall observation scale the sonar operator should know which type of propagation dominates. From Tables 4-4 and 4-5, the receiver location, and the

receiver position relative to the target (or the source) assuming that the receiver depth is between 50 m - 150 m the sonar operator can determine whether the dominant propagation type is an RSR or a bottom-bounce.

The sonar operator then should choose the integration time appropriately from Table 4-6 if the propagation type is a bottom-bounce, or from Table 4-7 if the propagation type is an RSR. At low frequencies, however, there is a possibility that both propagation types dominate due to a low bottom loss. In this case the integration time should be chosen as the smaller of the two.

In summary, although the integration times and the therefore the observation scales were generated for some particular locations with specific properties (like bottom slopes and bottom depths) the procedure outlined in sections 4.3 - 4.4 can be repeated for each location of interest. In reality, then, the sonar operator should correctly switch between the RSR integration time and the bottom-bounce integration time at the right moment in order to achieve the best performance of the sonar system.

Although this is true in general, for simplicity I assume that the integration time for all cases is 0.31 sec. This choice corresponds to a particular case assuming that the bottom-bounce propagation dominates. This is, of course, an arbitrary choice and serves the purposes of this study only. Due to its importance it should be emphasized that in reality the integration time cannot be constant and should be chosen according to the dominant propagation type.

4.5 Surface Loss

The surface loss in this study is treated the same way the bottom loss is (see section 4.2). In other words, the surface loss is modeled as Fresnel forward scatter which gives the loss in dB per bounce in the following form

$$Loss = 5k\delta_s \sin\theta_s, \text{ dB/Bounce} \qquad\qquad (4.27)$$

where δ_s is the RMS surface wave height, θ_s is the propagation angle of the ray with respect to the horizontal surface, and k is the wave number.

The RMS wave height can be thought of as a random process with a probability density that varies with weather (from winter to summer, for example). Since the analysis in this study, is carried out separately for the winter time and the summer time, the surface loss should also be calculated separately for each season. From chapter 2, the wave height that is used to calculate the surface loss is

$$\delta_s = \begin{cases} 1\,\text{m} & \text{winter} \\ 0.2\,\text{m}; & \text{summer} \end{cases}.$$

The loss mechanism is applied for each ray that hits the surface according to the wave height listed above.

4.6 Volumetric Absorption

Volumetric absorption in the sea is usually presented in the literature as an exponential absorption law applied to the mean square pressure [7]

$$p^2 = \frac{A^2}{r^2} \exp(-ar) \qquad\qquad (4.28)$$

where a represents all the absorption mechanisms that result in a loss in the mean square pressure with range. This loss with range should be added appropriately to the loss in the pressure due to spreading.

The absorption mechanisms are associated with relaxation mechanisms in sea water [7]. The classical absorption equation [7, 21] deals with the absorption due to shear viscosity of the fluid. However, modeling the absorption as shear viscosity mechanism

does not agree with the results obtained from experiments [7]. Alternatively, the literature provides three other absorption mechanisms that include structural relaxation, relaxation due to Magnesium-Sulfate (MgSO4), and relaxation due to Boron. Each one of those relaxation processes is associated with a different relaxation time and dominates the volumetric absorption in different frequency bands.

In practice, α (dB/km) is used instead of a where

$$\alpha \cong 4.34 \times 10^3 a, \quad (dB/km) \tag{4.29}$$

and the loss due volumetric absorption can then be added to the decrease in mean square pressure due to spreading in the following way

$$H = H_1 + \alpha r, \quad (dB \ re \ 1 \ m) \tag{4.30}$$

where r is the horizontal range in km, and H_1, which is calculated using the ray theory model suggested in section 4.1, represents the transmission loss result due to spreading alone.

Finally, the absorption coefficient is given by [7]

$$\alpha = \alpha_2 + \alpha_3 + \alpha_4, \quad (dB/km) \tag{4.31}$$

where α_2, α_3, and α_4 correspond to the absorption of sound due to structural relaxation, Magnesium solfate, and Boron respectively. From [7] they have the following form

$$\alpha_2 = 2.94 \times 10^{-2} f_3^{-1} f^2$$

$$\alpha_3 = 2.03 \times 10^{-2} S\left(1 - 6.54 \times 10^{-4} P\right) \frac{f_3 (f/f_3)^2}{1 + (f/f_3)^2}, \tag{4.32}$$

$$\alpha_4 = 1.10 \times 10^{-1} \frac{f_4 (f/f_4)^2}{1 + (f/f_4)^2}$$

where f_n represents the relaxation frequencies that are shown to be equal to [21]

$$f_3 = 1.55 \times 10^4 \, T \exp(-3052/T), \quad \text{(kHz)}$$
$$f_4 = 1.32 T \exp(-1700/T), \quad \text{(kHz)}$$

(4.33)

T is the seawater temperature in °K, S is the salinity measured in ppt, which can be considered a constant for this work, and equal to $S = 39$ ppt, and P is the ambient pressure in atm. Using the above relations the absorption coefficient is calculated along each depth and frequency chosen.

As an example the absorption coefficient, α, is plotted against f Figure 4.25 for $S = 35$ ppt, $T = 4°$ C, and $P = 300$ atm. Note the increase in the volumetric absorption as the frequency increases, and note that each of the different relaxation processes dominates in a different frequency band.
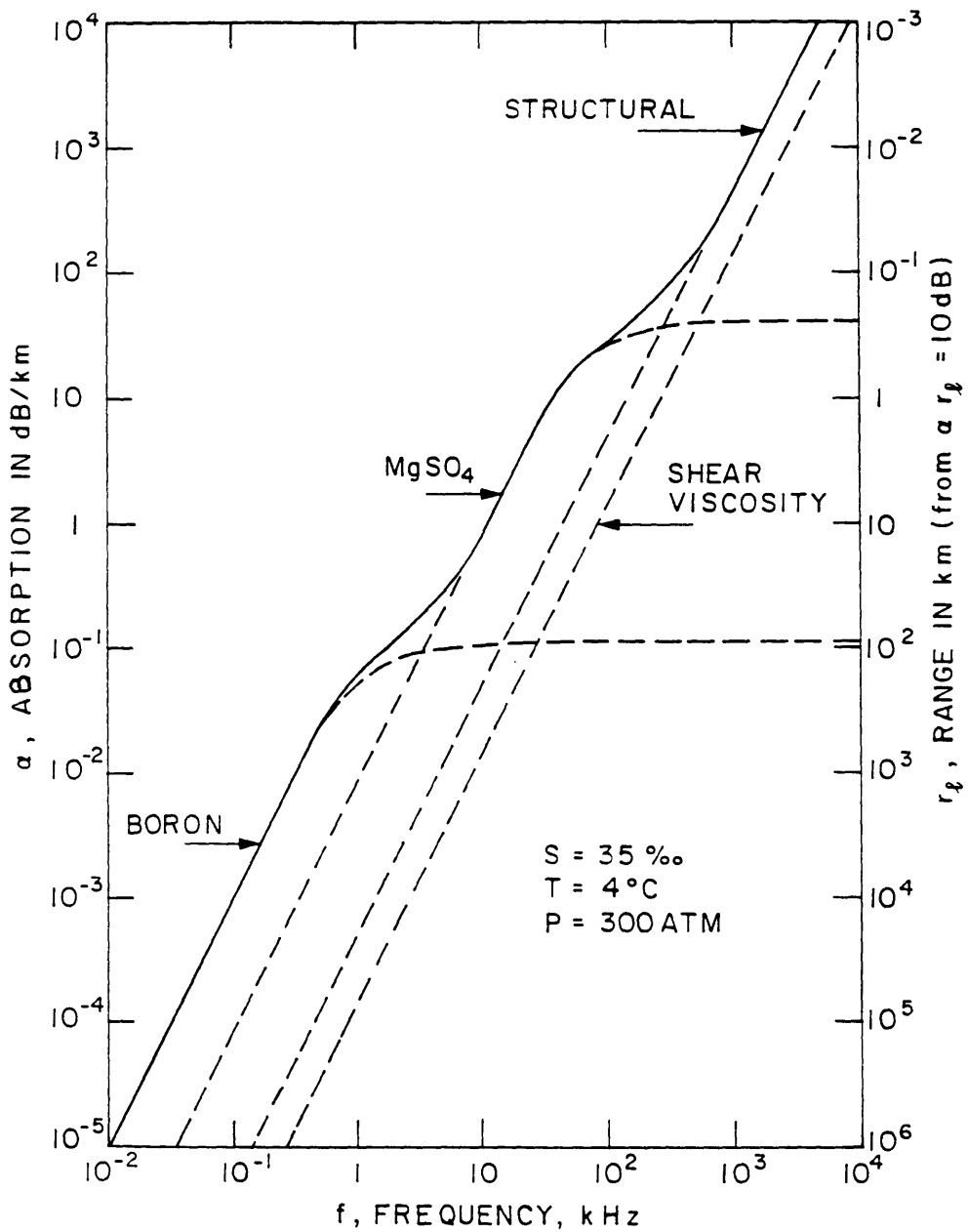
Figure 4.25: Volumetric absorption including all known relaxation processes [7].

Chapter 5

Background Noise

The background noise, or ambient noise, in the ocean exists in every ocean or sea in the form of a generally unwanted sound. The background noise is created by diverse sources that fill up the spectrum ($0 < f < \infty$). In other words, the ambient noise covers the whole useful spectrum for any sonar system.

The background noise can be thought of as a property of the ocean or sea being investigated. The intensity of the various noise sources not only depends on the location itself but also on the direction, and mainly on the frequency. Due to the frequency and direction dependence, the ambient noise should be at least a function of f (frequency), and Ω (solid angle). Hence, the noise spectral density, measured by an omni directional receiver at frequency f is

$$S_n(f) = \int_{4\pi} S(f,\Omega)d\Omega \qquad (5.1)$$

where $S(f, \Omega)$ is the noise spatial density at f, and Ω is the solid angle. $S_n(f)$ is then the pre-array or, in-water, noise spectrum density. The post array noise density is controlled by the band-pass filter in the receiver, and by the shape of the array. The former cuts the noise that lies outside the frequency band of the filter, b, so that the receiver processes the received signal and noise only within b. The latter (the array) determines what direction the receiver listens to, or, equivalently, determines the portion of the solid angle that the receiver is "open" to. In other words, the receiver array can be thought of as a spatial filter, which

filters out "directions" analogously to the frequency filter that filters out unwanted "frequencies." The question of how well an array rejects noise is answered by means of *array gain*. In order to determine the array gain one must take into account the directionality of the array as well as the directionality of the noise. As an example, if the sonar is "looking" toward the direction of the main noise axis then the array gain is minimized, which means that for this particular array configuration there is a minimum gain.

The bandwidth, *b*, and the array shape are the two parameters controlled by the designer of sonar systems, and affect the post array noise level, and therefore are one of the main reasons for the variation of the performance of different passive systems at a particular location. The array gain is defined using the dB notation as

$$AG = 10\log \int_{4\pi} \frac{S_n(f)}{S(f,\Omega)B^2(f,\Omega)}, \text{dB} \qquad (5.2)$$

where $B^2(f, \Omega)$ is the array's mean-square beam pattern, which defines the directionality of the array. The noise spectrum density can also be written using the dB notation by defining the noise spectrum level, L_n, as

$$L_n = 10\log S_n(f) \text{ , dB re 1 } \mu\text{Pa \& 1 Hz.} \qquad (5.3)$$

Using these definitions of the array gain and the noise spectrum level, the equivalent post-array noise level, L_{N_e}, can be written as [7]

$$L_{N_e} = L_n + 10\log b - AG \text{ , dB re 1 } \mu\text{Pa} \qquad (5.4)$$

when the noise spectrum level is considered relatively constant within the bandwidth, *b*. One should note that in order to evaluate the equivalent noise level one basically needs to know the full description of the noise in both frequency and space. The noise is described from both aspects in this chapter, while the array gain is further discussed in the next chapter where it is determined for each array and noise source using the definitions made subsequently for the directionality of the various noise sources.

Due to lack of precise noise measurements for each location being investigated, the noise spectral levels, L_n, are taken from Wenz [12], shown in Figure 5.1. This survey gives the noise spectral levels in 1 Hz bands and is widely used in the literature [7, 8, 13] for such purposes. Wenz [12] describes three major noise sources that affect the frequency band 10 Hz $< f <$ 10 kHz. These include

- distant shipping noise;

- surface agitation noise;

- molecular agitation noise.

These noise sources are described subsequently along with their spectral densities, at the frequencies within the band of interest, and their spatial characteristics. Other sources of noise do exist but do not dominate the spectrum or have only temporal effects. For example, water droplets (rain) do create noise that might even raise the ambient noise levels and flatten the spectrum above 1 kHz. Therefore the ambient noise, created by rain, may be of great concern but due to its temporal effect shall not be considered here. Other noise sources such as turbulence and mammal activity are not considered here as dominant ones.
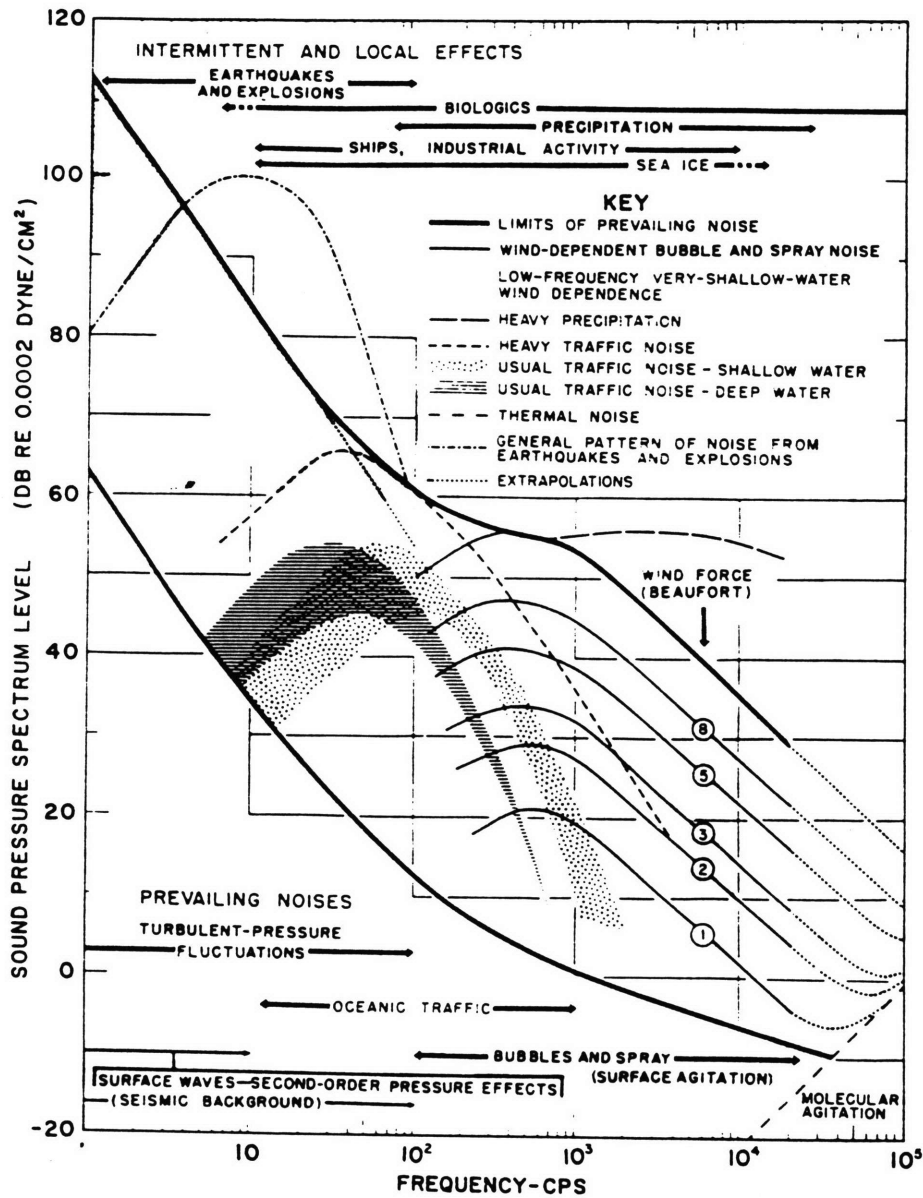
Figure 5.1: Noise spectral densities. Add 26 dB for ref. of 1µPa, 1Hz (from Wenz [12]).

5.1 Distant Shipping Noise

The noise radiated by surface vessels and large ships exits everywhere in the frequency band of interest, however, often dominating the frequency regime $10 \text{ Hz} < f < 100 \text{ Hz}$ (see Figure 5.1). Due to the large number of ships creating this noise, and their variety, its spectral density can be thought of as a continuous one. Wenz [12] also distinguishes between heavy traffic noise and usual traffic noise in deep sea and shallow water. The locations being investigated, are all mid water depth (1200 m to 2200 m). Therefore one way to describe the noise created by distant shipping is *usual traffic noise - in shallow water*. Table 5-1 summarizes the appropriate data taken from Figure 5.1 at the frequencies of interest. These frequencies were chosen such that the analysis can be carried out for the narrow-band components (NB) and broad-band spectra of the source, presented in Figure 3.2.

As is true for the noise spectral level, The directionality of the distant shipping noise varies from place to place especially in shallow water where the bottom characteristics come into play. In practice, however, the directionality of the noise can be approximated by the one observed in deep ocean [7] (when more accurate information is lacking). In the deep ocean the distant shipping noise is horizontally isotropic and symmetric about the horizontal ($\theta = 0°$.) An estimated ambient noise directional spectrum (as a function of vertical angle θ) is depicted in Figure 5.2. The figure shows the directionality of the distant shipping noise near the sea surface. To first order the result is independent of frequency as well as depth once the sensors' depth is above the critical depth, near the seabed [25].

It is useful to calculate the equivalent solid angle of the noise, Ω_n, that approximates the spatial dependency of the noise by a portion of an equivalent 3-D spherical function with a unit radius,

$$\int_{4\pi} S(f_o, \Omega) d\Omega \approx S_o(f_o, \Omega_o)\Omega_n,$$

so that both sides of the equation represent roughly the same power received by the omni directional source. From Figure 5.2 Ω_n can be calculated in the following way
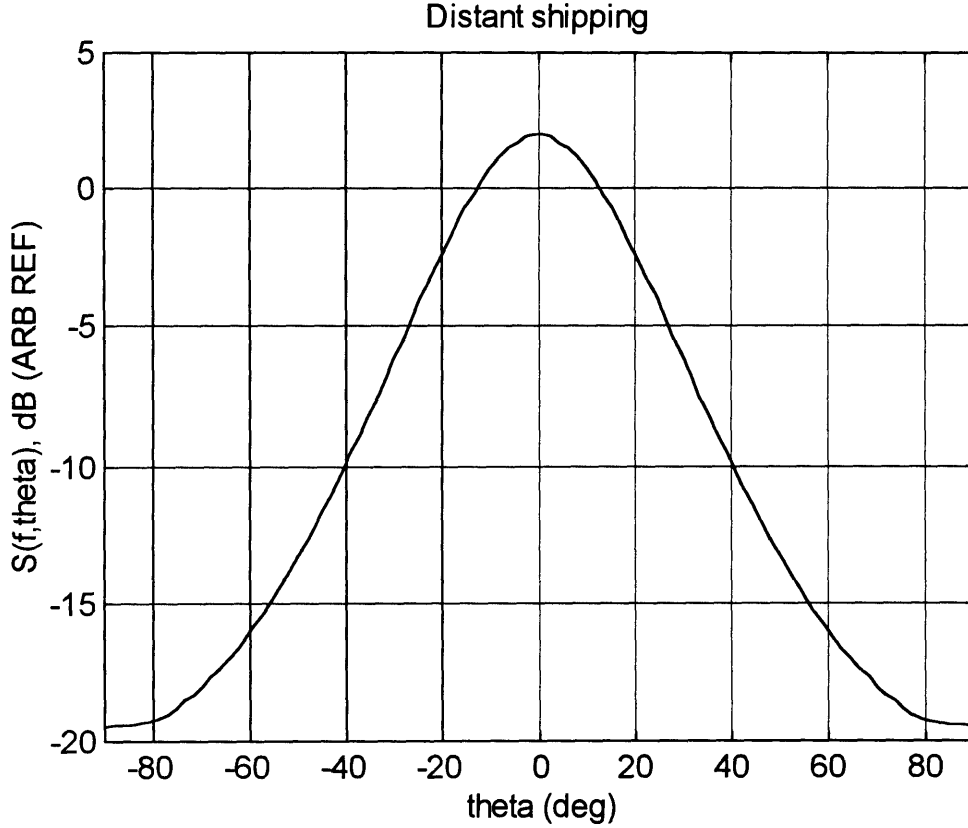
Distant shipping

Figure 5.2: Estimated distant shipping noise directional spectrum in the vertical plane [7].

$$\Omega_n = \int\limits_{-3dB}^{3dB} d\Omega = \int\limits_{-\theta_{3dB}}^{\theta_{3dB}} \cos\theta d\theta \int\limits_{0}^{2\pi} d\phi$$

where θ is the vertical angle and ϕ is the azimuthal angle. Form Figure 5.2, the 3 dB points are located at $\theta_{3dB} = \pm\ 15°$. Taking those values as the limits of the above integral yields the equivalent solid angle for the distant shipping noise as

$$\Omega_n^{ds} \cong 3.3 \text{, srad.} \tag{5.5}$$

This value is used in the next chapter in the process of calculating the corresponding array gain of the three arrays at the three locations. In general, Ω_n may differ from one place to another, in particular near harbors or away from shipping lanes. The assumption made here,

however, is that all the three locations have the same noise spatial density. This assumption, although roughly true, might be corrected for the particular places of interest once a more accurate estimate on the noise spatial density is introduced.

5.2 Surface Agitation Noise

The surface agitation noise is created by oscillating air bubbles created especially near the sea surface [12]. The noise generated by the bubbles due to their oscillations or burst dominates the frequency band 100 Hz $< f <$ 10 kHz. The air bubbles are created in the ocean mostly due to wind stress, and lastly due to decaying matter, and gas seepage from the sea floor. The bubbles created by wind are mostly due to breaking waves. Since the creation of waves along with their height are due to the action of wind on the sea surface, it could be concluded that sea surface agitation is a wind-dependent ambient noise. In Figure 5.1 the surface agitation noise is parameterized by the wind force (Beaufort scale), which is the practical way to describe this type of noise.

Since the analysis is based on a season, there is a need to describe it by means of a wind force. From chapter 2, during the winter the wave height in the eastern Mediterranean sea is in the order of 1 m, corresponds to sea state 3, or 4 in the Beaufort scale. On the other hand, during the summer season the average sea state is roughly ½, or 1 in the Beaufort scale. (The reader is referred to chapter 2 for the complete argument.) These parameters determine the noise spectral levels taken for the winter and summer and are summarized in Table 5-1.

The spatial dependence of the surface agitation noise can roughly be modeled as the radiating pattern of a dipole (the bubbles are considered as noise sources near the sea surface, which is a very good reflector with a reflection coefficient of nearly -1 [7, 8, 15].) In solid angle, the radiation can be shown to be proportional to $\sin(\theta)$ [7], where θ is the vertical angle measured form the horizontal, with 3dB-down width of about 47°, as shown

in Figure 5.3. The equivalent solid angle of the sea surface agitation noise can be derived using the 3dB-down values stated above. In other words, with $\alpha = \theta + \pi/2$,

$$\Omega_n^{sa} = \int_0^{\alpha_{3dB}} \sin(\alpha)d\alpha \int_0^{2\pi} d\phi \cong 1.7 \text{ , srad.} \qquad (5.6)$$

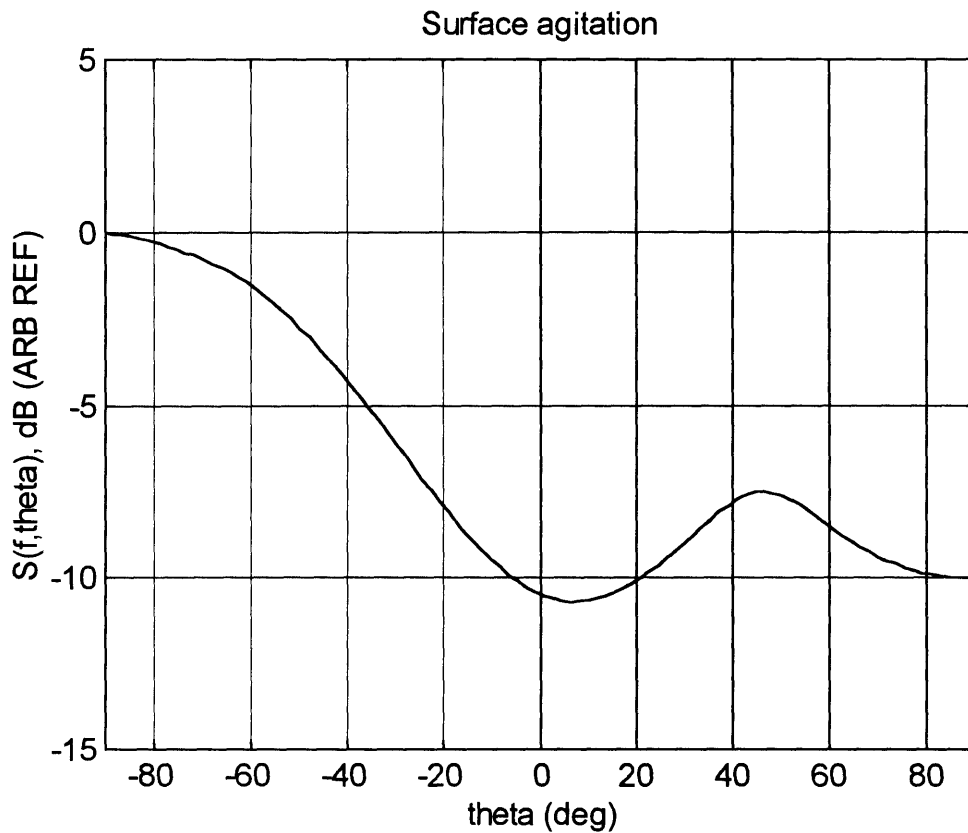This value is used in the next chapter when the corresponding array gain is calculated.

Figure 5.3: Estimated surface agitation noise directional spectrum in the vertical plane [7].

5.3 Molecular Agitation

Molecular agitation noise starts dominating the spectrum at frequencies higher than 100 kHz. The noise is created from molecular momentum reversals at a pressure sensor [7]. Since a molecule's energy is driven by the absolute temperature, which varies only slightly in the Mediterranean sea, or even in the ocean, the molecular agitation noise is roughly the same everywhere in the sea. Also, its spectral level goes as f^2 and can be extrapolated as such for $f < 10$ kHz and $f > 100$ kHz (see Figure 5.1.) In other words [12],

$$L_n^{sa} \approx -65 + 20\log(f), \text{ dB re 1 } \mu\text{Pa \& 1Hz.} \qquad (5.7)$$

The molecular agitation noise determines the minimum noise level of the medium so that even if there is no other noise source around, there is always a minimum noise level with the spectral level shown in equation (5.7). The reader should note that within the frequency band of interest it is unlikely that it is of a significant influence on the total noise level. In addition, the molecular agitation noise has no spatial dependence [7] and therefore has no solid angle associated with it.

Table 5-1: Noise spectral levels (L_n, re 1 μPa &1 Hz.) for different noise sources and desired frequencies. taken from [12].

f (Hz)	Distant shipping	Sea surface agitation		Molecular agitation
		winter	summer	
10	59	-	-	-
20	66	-	-	-
30	69	-	-	-
40	73	-	-	-
50	75	-	-	-
100	76	57	34	-
200	69	62	43	-
300	66	63	45	-
400	61	63	46	-
500	58	63	46	-
1 k	45	60	45	-
2 k	26	56	41	0
3 k	-	53	37	4
4 k	-	50	35	6
5 k	-	49	33	8
10 k	-	43	28	14
Ω_n, (srad)	$\approx$3.3	$\approx$1.7	$\approx$1.7	-

Chapter 6

Array Beamforming

As mentioned in chapter 3, all the receivers considered in this study, are similar except for their receiving arrays. The array is used to filter signals in the space field according to its spatial dependence. This filtering is done by combining the outputs of the array sensors in such a way that enhance or reject signals according to their direction of propagation. Practically, the array is of finite length and therefore the filtering can only be performed imperfectly.

This section was written to provide the reader with the fundamentals of array design that is essential for the purpose of analyzing sonar systems.

6.1 Essentials of Beamforming

The array can be described as an ensemble of sensors distributed in space at a known geometry. The sensors sample the spatial domain analogously to the sampling procedure in the time domain. The sensor locations are the vectors z_n, ($n = 1,...,N$) as shown in Figure 6.1. The output, p, is the sum of the input signals, $p_i(z_n)$, multiplied by the taper function, $T_i(z_n)$,
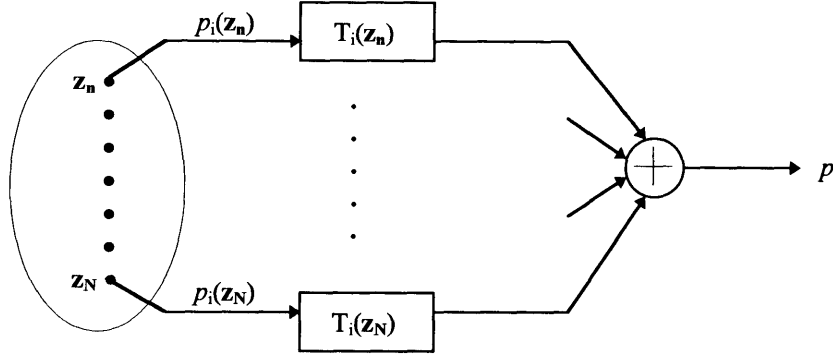
$$p = \sum_{n=1}^{N} T_i(z_n) p_i(z_n) .$$

(6.1)

Figure 6.1: Beamformer operations. z_n represents the vectors to the location of sensor n. $T_i(z_n)$ is the taper function.

Assuming far field operation, the input signal to the beamformer can be approximated by a unit plane wave

$$p_i(z_n) = e^{-jk \cdot z_n} \qquad (6.2)$$

where k is a wave number vector corresponding to the direction of propagation of the sound wave coming toward the receiver. With this assumption, the output, p, takes the form

$$p(k) = \sum_{n=1}^{N} T_i(z_n) e^{-jk \cdot z_n}, \qquad (6.3)$$

which resembles the discrete Fourier transform, DFT [30], applied now to the spatial vector, $T_i(z_n)$, and transforming it to the wave number domain, $p(k)$.

For a unit plane wave, $p(k)$ is practically the beampattern shape of the array, $B(k)$. $B(k)$ introduces a directivity to the beamformer output so that in general

$$p(k) = p_o B(k) \qquad (6.4)$$

where p_o is the magnitude of the plane wave.

One of the most popular as well as important array designs is the *line array* which is the simplest to deal with mathematically but the results are fundamental in an array design.

For a symmetrically placed (along the z axis) and tapered line array with N elements, and d the distance between the sensors, the beampattern has the following form (see Figure 6.2)

$$B(\mathbf{k}) = \sum_{n=-\frac{N-1}{2}}^{\frac{N-1}{2}} T_i(\mathbf{z}_n) e^{-j\mathbf{k}\cdot\mathbf{z}_n} \qquad (6.5)$$

If the angle between the direction of propagation of the acoustic wave and the array is α then

$$\mathbf{k} \cdot \mathbf{z}_n = |\mathbf{k}| dn \cos\alpha . \qquad (6.6)$$

Taking $\alpha = \theta + \pi/2$, and knowing that $|\mathbf{k}| = 2\pi/\lambda$, the above relation can be written as

$$\mathbf{k} \cdot \mathbf{z}_n = \frac{2\pi}{\lambda} dn \sin\theta . \qquad (6.7)$$

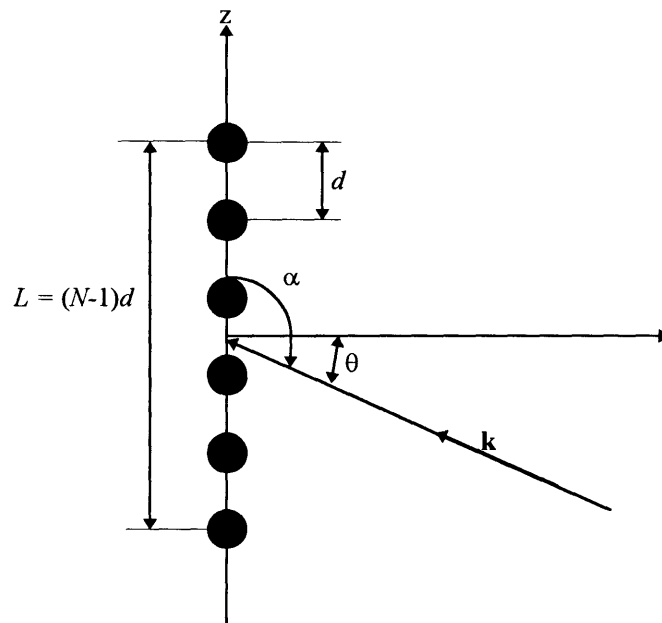The beam pattern, B, can then be written as a function of θ

Figure 6.2: Configuration of the line array

$$B(\theta) = \sum T_i(z_n) e^{-j\frac{2\pi}{\lambda}dn\sin\theta} . \qquad\qquad (6.8)$$

Calling $s = \sin(\theta)$, assuming a uniform taper, $T_n = T_i(z_n) = 1/N$, and using the formula for the sum of a geometric series

$$\sum_{n=0}^{N-1} x^n = \frac{1-x^N}{1-x}$$

equation (6.8) can be written in a closed form as

$$B(s) = \frac{\sin\left(\dfrac{\pi L s}{\lambda}\right)}{N\sin\left(\dfrac{\pi d s}{\lambda}\right)} . \qquad\qquad (6.9)$$

The beampattern, $B(s)$, is fundamental in its importance for analyzing line arrays. Since $B(s)$ depends here only on θ it leads to a "cone of uncertainty" property for line arrays (see Figure 6.3). The dimensionality of the array dictates the dimensionality of the ambiguity. A line array can resolve directionality only in one dimension, in this case, in the θ direction. In order to be able to distinguish between left and right, for example, one has to increase the dimensionality of the array to 2-D array (like a plane array, or two line arrays pointing in two different directions). In order to resolve directions in 4π steradians, so that there is no ambiguity at all, one has to form a 3-D array like a sphere array.

The other property of $B(s)$ comes from the fact that the sensors, separated d apart, are sampling the spatial domain. Analogous to the effect of sampling in time, the beampattern function is periodic and repeats itself every

$$s = \frac{\lambda}{d} .$$

$B(s)$ as written in equation (6.9) is a *sinc* like function repeated every λ/d. The main lobe is located at $s = 0$, and the so called grating lobes are located at $s = n\lambda/d$ for $n > 1$. When the

main lobe is located at $s = 0$ the array is "looking" in the broadside direction. In the case when the array is steered to $s_o \neq 0$ the taper function must include a phase term in the form

$$\mathbf{T}_n = \frac{1}{N} \mathbf{e}^{-j\frac{2\pi}{\lambda}dns_o},\qquad(6.10)$$

applied here to the uniform taper. This taper function shifts the main lobe to be centered at s_o, and $B(s)$ is replaced by $B(s - s_o)$ as depicted in Figure 6.4.
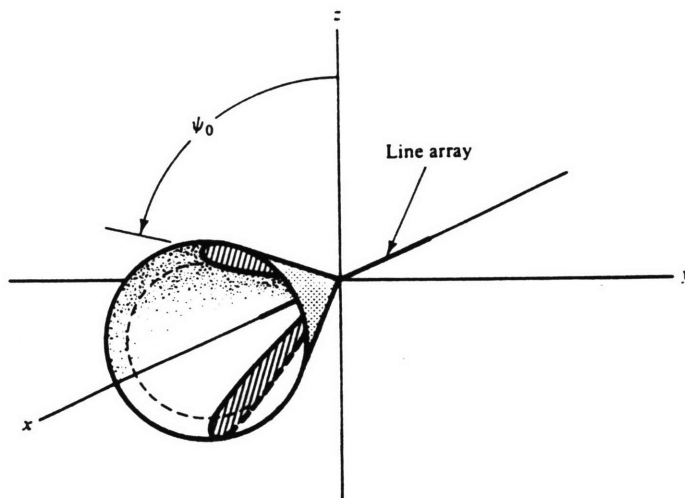

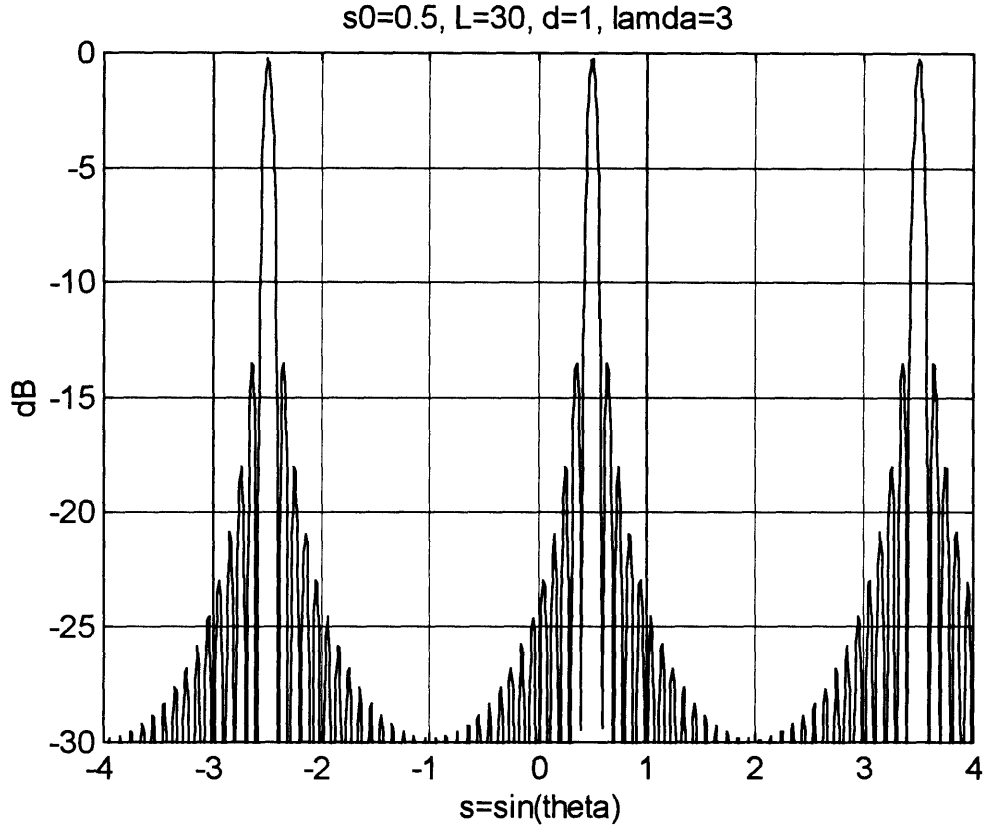Figure 6.3: A cone of uncertainty result for line array [14].

Figure 6.4: The beampattern function, $B(s)$, steered to $s_o=0.5$. The grating lobes shown are located at $s = (s_o \pm \lambda/d)$.

In order to steer the array to endfire while excluding all the grating lobes from the physical space $|s| = |\sin\theta| \leq 1$, one must have

$$\frac{2\lambda}{d} \geq 1$$

or

$$d \leq \frac{\lambda}{2}. \qquad (6.11)$$

In other words, the designer of a sonar system should make sure that the distance between the sensors, d, is smaller than half the minimum wave length, λ. This design criterion is used in the next section to calculate the maximum frequency of an array.

It is very useful to note that once $d \leq \lambda/2$, and the grating lobes have been removed from the physical space, the segmented array may be considered as a continuous one. Replacing dn by the variable z, and defining u as z/λ, equation. (6.8) can be written as a Fourier transform of the taper function and vice versa [7],

$$B(s) = \int_{-\infty}^{\infty} T(u)\, e^{-j2\pi su}\, ds$$

$$T(u) = \int_{-\infty}^{\infty} B(s)\, e^{-j2\pi su}\, du$$

(6.12)

where $T(u) = \lambda T_n(z)$ is zero outside the line array

$$T(u) = \begin{cases} \lambda\, T_n(z); & |z| \leq \dfrac{L}{2} \\ 0; & \text{elsewhere} \end{cases}$$

(6.13)

From this definition, all the Fourier transform properties [30] can be applied to the line array design. Mathematically speaking, $T(u)$ is chosen such that $B(s)$ is always normalized with $B(s_0) = 1$, where s_0 is the main lobe direction or, main radiation or reception axis. Furthermore, for $d \leq \lambda/2$ and a uniform taper, $B(s)$ can be approximated by the *sinc* function,

$$B(s) \approx \text{sinc}\left(\frac{\pi L s}{\lambda}\right),$$

(6.14)

as depicted in Figure 6.5.

As mentioned earlier the *sinc* function serves only an as approximation to the beampattern function, $B(s)$. In addition, for nonuniform tapers the beampattern main lobe's width changes slightly, but the side lobe level (relative to the main lobe level) may change significantly. These two parameters are of great importance from the designer point of view because both have significant effects on the performance of the sonar system. The width of the main lobe can be meassured via the *equivalent beam width*, η_e, in s sapce [7]

114

Properties of continuous line arrays.

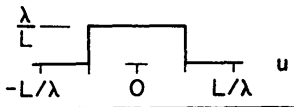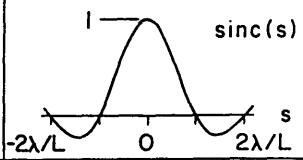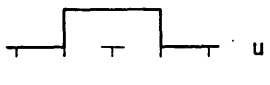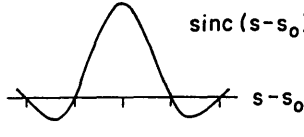$$T(u) = |T| \exp(-i\beta) = |\zeta(u)| rect(u) \exp\left[-i\beta(u)\right]$$

Array	Taper Amplitude, $|\zeta(u)| rect(u)$	Beam Pattern, B(s)
1. Uniform $\zeta = 1$ $\beta = 0$		
2. Steered Uniform $\zeta = 1$ $\beta = 2\pi s_0 u$		

Figure 6.5: Beampatterns and tapers as Fourier transform pairs [7].

$$\eta_e = \int_{-1}^{1} B^2(s)ds.$$ (6.15)

η_e represents the width of a rectangular function having the same power as $B^2(s)$. It can be shown [7] that the equivalent beam width depends only slightly on the shape of the taper function and in most practical cases a uniform taper can be the basis to calculate η_e [7]. For the uniform taper case

$$\eta_e \approx \frac{\lambda}{L}.$$ (6.16)

In angle space, the *equivalent angle width*, θ_e, can be calculated via [7]

$$\sin\left(\frac{\theta_e}{2}\right) = \frac{\eta_e}{2\cos\theta_o}$$ (6.17)

where θ_o is the steering angle of the array. It is important to note how θ_e increases when the array is steered toward endfire. In this study, however, the arrays are limited to broadside operation so that the beamwidth, in angle space, is relatively constant for a certain operating

frequency. This is done only to narrow the cases to be considered in the performance analysis and not because of any other difficulty. One should note that in order to perform endfire analysis care must be taken due to the different beamwidth property of an array steered to endfire [7].

In the case of a segmented array of N elements, and a uniform taper the *equivalent beamwidth*, assuming $L/\lambda \gg 1$ is

$$\eta_e \cong \frac{\lambda}{L} = \frac{\lambda}{nd},$$ (6.18)

as is true for a continuous line array. That means that for broadside operation the equivalent angle width, for relatively small beamwidth, is given by

$$\theta_e \approx \frac{\lambda}{L}.$$ (6.19)

This result is used in this study to determine the beamwidth of the line array that eventually affects the observation scale as discussed in chapter 4.

Another important parameter, directly related to the equivalent beamwidth, η_e, is the directivity factor, d_f, or the directivity index, DI. The former is defined as the average value of $B^2(s)$, and its value is smaller as the main lobe of the beampattern function is narrower. The average value of $B^2(s)$ can be written as

$$d_f = \frac{1}{2}\int_{-1}^{1} B^2(s)ds = \frac{\eta_e}{2}.$$ (6.20)

The directivity index, however, is measured in dB and is defined as

$$DI = 10\log\left(\frac{1}{d_f}\right) = 10\log\left(\frac{2}{\eta_e}\right).$$ (6.21)

116

The directivity index gives a measure on how directive the beam is. The larger DI gets the more directive and narrower the beam is.

In the case of a segmented line array, due to the periodicity of $B(s)$, the directivity factor for $d \gg \lambda/2$ is given by the equivalent beamwidth divided by the period of $B(s)$, which is λ/d. For large L/λ this ratio can be written as

$$d_f = \frac{\eta_e}{\lambda/d} = \frac{1}{N}.$$ (6.22)

For the usual design selection of $d = \lambda/2$, the above result happens to serve as a very good approximation to the directivity factor. Once that L and N are fixed with $d = \lambda/2$, the array is designed for a particular operation frequency, f_o. Higher frequencies than f_o, received by the array, may introduce the grating lobes within the physical space. In this case the directivity factor starts to oscillate around $1/N$ due to the grating lobes effect [22]. Those frequencies are usually removed by the receiver's conditioning unit and thus excluding the effect of the grating lobes. At lower frequencies than f_o, the grating lobes are located outside the physical space and therefore have no effect on the directivity factor. however, the distance between the elements is now smaller than $\lambda/2$ and the array approaches the results obtained for the continuous array, where the averaging process of the beam pattern is limited by $|s| = 1$. This means that

$$d_f = \frac{\eta_e}{2} = \frac{\lambda}{2L}.$$ (6.23)

In other words, the directivity factor gets larger as the wavelength increases or as the operating frequency decreases. Similarly, the directivity index, DI, decreases as the frequency decreases. The main point in this discussion is that optimal design selection for the distance between the elements is $d = \lambda/2$. Choosing smaller distance does not increase DI, but larger distance causes the grating lobes to be included in the physical space and decreases DI.

Any array, no matter what its dimension is, receives information from every direction, or, from 4π steradians. As mentioned earlier, the beampattern of a line array has a cone of uncertainty which prevents the sonar system from determining the exact direction of the signal or noise received by the cone (see Figure 6.3.) It is useful, then, to define the *equivalent solid angle*, Ω_e, which is a measure of the portion of a sphere of a unit radius covered by the beampattern function in 3-D yielding the following definition

$$\Omega_e = \int_{4\pi} B^2(\Omega) d\Omega.$$
(6.24)

In the case of a line array, the equivalent solid angle does not depend on the steering angle (also true for the equivalent beamwidth), and can be shown to have the following form [7]

$$\Omega_e = 2\pi\eta_e.$$
(6.25)

In addition, since the total available solid angle is 4π, then for any array in free space the directivity factor can be related to the equivalent solid angle simply as (see equation (6.20))

$$d_f = \frac{\Omega_e}{4\pi}.$$
(6.26)

The equivalent solid angle is the parameter used to calculate the efficiency of the array to reject noise, or the *array gain* following the discussion in chapter 5.

Intuitively speaking, in order to have better performance one should design the array to have as small an equivalent solid angle as possible. This argument led to the creation of a verity of 2-D and 3-D arrays that are capable of removing the "cone" from the beampattern function and replace it with two "pencils" in the case of a plane array and a single "pencil" in the case of a volume array steered to unifire. In fact, submarines all over the world are likely to be equipped with a version of the volume array mounted at the bow of the submarine. One of the common to be found is the spherical shell array which is considered here. A more detailed discussion on plane arrays can be found in Dyer [7], Molloy [23], and Bobber [24].

The spherical shell array consists of equally distributed elements mounted on the outside shell of a sphere. Due to its structure a volume array must be tapered in order to constructively receive the information from all the elements. The spherical shell has a diameter, D, and it is tapered, say, to receive constructively the signals coming from the z direction, or $\alpha = 0$ (see Figure 6.6 for the definition of the spherical coordinate system). It can be shown that the beampattern function in this case has the form [27]

$$B(\alpha,\phi) = \mathbf{sinc}\left(kD\sin\frac{\alpha}{2}\right) \hspace{3cm} (\,6.27\,)$$

which does not depend on ϕ in this case due to the choice of this particular coordinate system. This function describes the beampattern of a spherical array which is steered to unifire. The spherical shell array has the ability to steer to any direction in space with only a single "pencil" as a receiving (or in other occasions radiating) pattern (see the beam pattern of a spherical shell in Figure 6.7.)
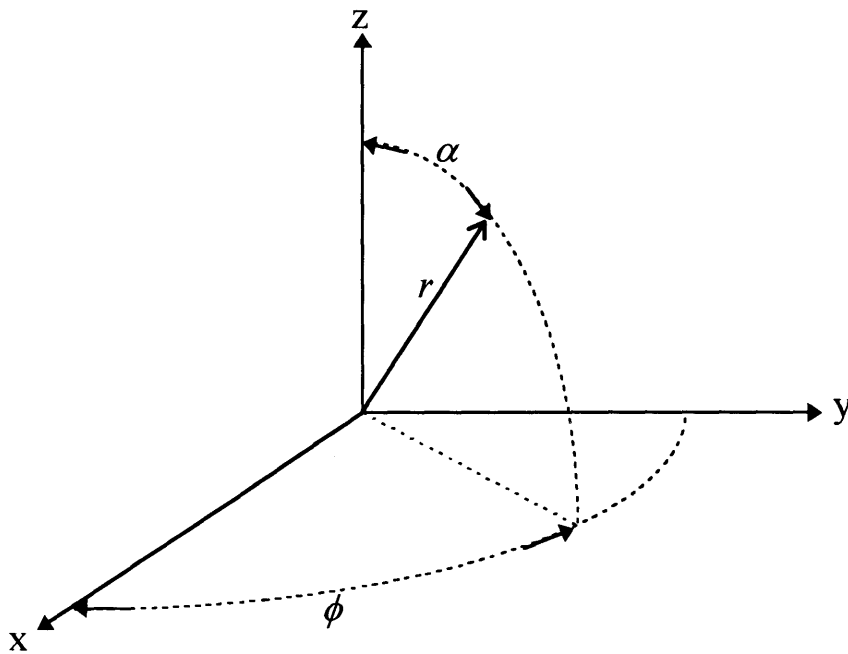
Figure 6.6: Spherical coordinate system

The directivity factor in the case $3 < D/\lambda < 30$, which is the common case, can be shown to have the approximate form [7]

$$d_f \approx \frac{5}{8}\left(\frac{\lambda^2}{2\pi S_g}\right)$$ (6.28)

where S_g is the area of a great circle or, in other words,

$$S_g = \frac{\pi D^2}{4}.$$

The angle to the first zero of the beampattern, α_1, can be derived for relatively small angle width from equation (6.27) yielding

$$\alpha_1 \approx \frac{\lambda}{D}.$$ (6.29)

The equivalent angle width of the beampattern can also be calculated via equation (6.27) to yield the result

$$\alpha_e \approx \frac{4.46}{\pi}\frac{\lambda}{D}$$ (6.30)

and the equivalent solid angle can be derived using the approximate form of the directivity factor, and with the use of equation (6.26), as

$$\Omega_e = \frac{5\lambda^2}{4S_g}$$ (6.31)

which both do not depend on steering angle. This result is often the reason why volume arrays are very common. On top of that, volume arrays have a one sided receiving pattern as opposed to plane arrays, that have a two sided beam pattern. Recall that the equivalent solid angle for the line array does not depend on the angle as well, but this, however, is due to the properties of the axisymmetric "cone" shape radiation pattern which causes the ambiguity associated with the line array.

In practice, there are arrays that are mounted on a surface or on the hull of a ship. This means that they can radiate or receive signals only from the "open" side. Arrays like that (called baffled) are designed to prevent the array from receiving noise generated from the hull itself. For these types of arrays, when perfectly baffled, the receiving pattern is limited to a single side. As a result the averaging process that is done to determine the directivity factor and the equivalent solid angle should now be done only for half the space. In other words, for baffled arrays the equivalent solid angle and the directivity factor are half the ones generated for the unbaffled arrays

$$\Omega_{eb} = \frac{\Omega_e}{2}, \quad d_{fb} = \frac{d_f}{2} \qquad (6.32)$$

where Ω_{eb}, and d_{fb} stand for the baffled equivalent solid angle and the baffled directivity factor respectively. The directivity index for the baffled arrays is thus increased by 3 dB relative to the free standing arrays.
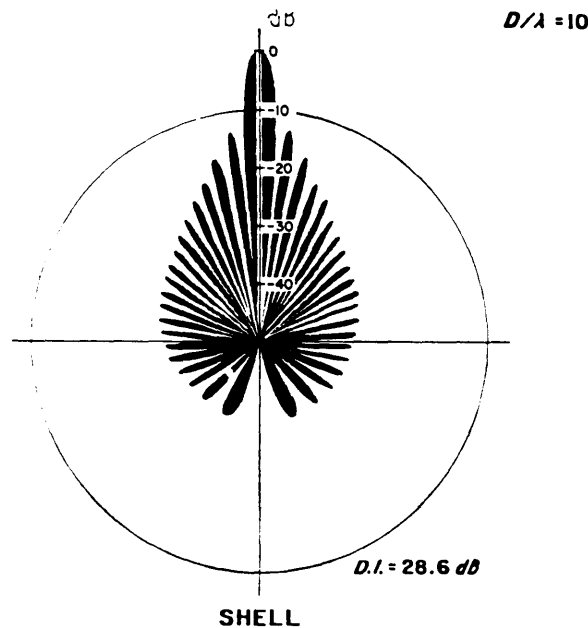

Figure 6.7: The beam pattern of a spherical shell for $D/\lambda = 10$ [27].

6.2 Array Gain

Whenever an array is designed, its goal is to filter its response from all directions except the on-axis direction, or, the one that the main lobe is pointing to. The filtering process is measured by the *array gain* mentioned previously. Intuitively speaking, the array gain is a measure of how good the array is in comparison to a single element, or an omni directional transducer. Then it should be the ratio of the equivalent post array noise levels of the two. Recall the definition of the array gain written in dB notation, from equation 5.2,

$$AG = 10\log\left(\frac{S_n(f_o)}{S_{n_e}(f_o)}\right)$$

where S_n is the noise spectral density at f_o for the omni directional receiver, and S_{n_e} is the post array noise spectral density. For the omni directional receiver the spectral noise density is the integral of the spatial noise density, $S(f_o,\Omega)$, over 4π steradians,

$$S_n(f_o) = \int_{4\pi} S(f_o,\Omega)d\Omega. \qquad (6.33)$$

On the other hand, the post array spectral density must include the beampattern, $B^2(\Omega)$. In other words,

$$S_{n_e} = \int_{4\pi} S(f_o,\Omega)B^2(\Omega)d\Omega. \qquad (6.34)$$

Using the above relations, the array gain takes the following form, as mentioned in chapter 5,

$$AG(f_o) = 10\log\left(\frac{\int_{4\pi} S(f_o,\Omega)d\Omega}{\int_{4\pi} S(f_o,\Omega)B^2(\Omega)d\Omega}\right), \qquad (6.35)$$

The integrals in the array gain equation are in some cases impossible to evaluate analytically and therefore it is useful to identify three different cases that help simplify this equation into a suitable form adequate for the purposes of this study.

The first case is a nonisotropic noise, copointed with array main lobe axis. The noise is associated with its own equivalent solid angle, Ω_n, and one can distinguish between two subcases. For $\Omega_e \geq \Omega_n$, the array receives the signal and the noise via the main lobe. The array gain in this case is zero. For $\Omega_e \leq \Omega_n$ the array receives the noise only through Ω_e, and the array gain can be written as [7]

$$AG = \begin{cases} 0; & \Omega_e \geq \Omega_n \\ 10\log\left(\dfrac{\Omega_n}{\Omega_e}\right); & \Omega_e \leq \Omega_n \end{cases} \qquad (6.36)$$

The second case deals with nonisotropic noise with equivalent solid angle, Ω_n, when the noise axis is not necessarily copointed with the array main lobe axis. In this case, Dyer shows [7] that for this contrapointed case, the array gain takes the following approximate form

$$AG \cong 10\log\left(\frac{\Omega_n/\Omega_e}{S_a/S_o + B_n^2(\Omega_n/\Omega_e)}\right) \qquad (6.37)$$

where S_a is the average value of the noise spectral density, $S(f_o,\Omega)$, on the array main lobe axis, and $B_n^2(\Omega)$ is the average of $B^2(f,\Omega)$ on the noise main axis. This form gives rise to the effect of the minor lobes of the beampattern. For the perfect array, $B_n^2(\Omega) = 0$ so that the array gain increases relative to the ratio of S_a to S_o. In practice, the side or minor lobe level control is a key issue in array design. The goal is to lower the side lobe level without loosing azimuthal resolution. This is done through a careful design of the taper function, which is beyond the scope of this work. However, side lobe level of -30 to -40 dB is a good design goal in practice.

The third case to consider is small scale pressure fluctuations or molecular agitation. Here, the noise is caused by sources that have vanishingly small correlation scale compare to the spacing between the elements of the array, d. It can be shown that the array gain is in this case [7]

$$AG = 10\log N$$

where N is the number of elements in the array. However, since the noise, generated by small scale forces are uncorrelated there should be no effect due to different array designs. As a result, the array *cannot* affect the post array noise level and it must be equal to the noise level received by each of the elements themselves. The array gain, written above, must then be canceled, when calculating the post array noise level, with the increase of noise due to the number of elements, $10\log N$ (in dB).

The next chapter uses the definitions and results from this chapter and describes the properties of the arrays that are considered in this study.

Chapter 7

Receiver Arrays Description

The arrays, which their performance are to be evaluated in this study, were not chosen to meet specific criteria or performance requirements. The arrays represent three classes of popular array designs. Due to their different apertures they have different effects on the performance of the receiver. This chapter provides the reader with the description of the arrays in terms of physical dimensions and array gain.

7.1 Towed Array Sonar

The towed array sonar is commonly used by submarines and surface vessels that operate in mid and deep water. The towed array, here, is based on a single line array that is deployed from the vessel once it is underway. The design of the towed array varies significantly from one need to another in order to meet specific requirements. Except for the space needed in the vessel, for storage purposes, the towed array can be designed to be very long. In fact, the length of common towed arrays may vary from tens of meters to thousands of meters, depending on the application. Relatively long arrays are needed to offer good azimuthal resolution at very low frequencies.

Although the towed array can be deployed by a surface ship, the assumption in this study is that it is towed by a submarine. The depth of the submarine dictates the depth of the array, which stays *generally* horizontal and straight at the submarine depth. The word *generally* means that the actual positions of the hydrophones are not known precisely,

unless there are other sensors installed in the array that transmit their positions along the array. Thus, this information is used in the beamforming process to compensate for the actual shape of the array. In simple arrays, however, this information is not available and therefore the main lobe axis of the towed array may fluctuate around its theoretical direction, making the equivalent beam width wider. In such arrays, the length of the array for slow speed towing cannot be considered longer than ten wavelengths, as a rule of thumb, in the calculation of the beamwidth.

In practice, long towed arrays are built with *split aperture* so that the distance between the elements varies along the array. For each frequency a different set of elements, in the array, is used to reflect the above length limit. The distance between the elements is always kept $d \leq \lambda/2$ for the entire frequency regime for obvious reasons.

The dimensions of the towed array in this study are depicted in Figure 7.1. It is constructed such that the minimum distance between the elements is $d_{min} = 1$ m, and the maximum distance is $d_{max} = 15$ m. These distances dictate the upper and lower frequency limits. The upper frequency limit is

$$f_u = \frac{c}{\lambda} = \frac{c}{2d_{min}} \cong \frac{1500}{2} = 750, \text{Hz.}$$

(7.1)

Similarly, the lower frequency limit, f_l, is

$$f_l = \frac{c}{2d_{max}} = \frac{1500}{30} = 50, \text{Hz.}$$

(7.2)

From the argument stated at the previous section, the length of the towed array is assumed to be always $L = 10\lambda$, so that the length of the array is $L_{min} = 10$ m, and $L_{max} = 300$ m, for the upper frequency and lower frequency limits respectively.
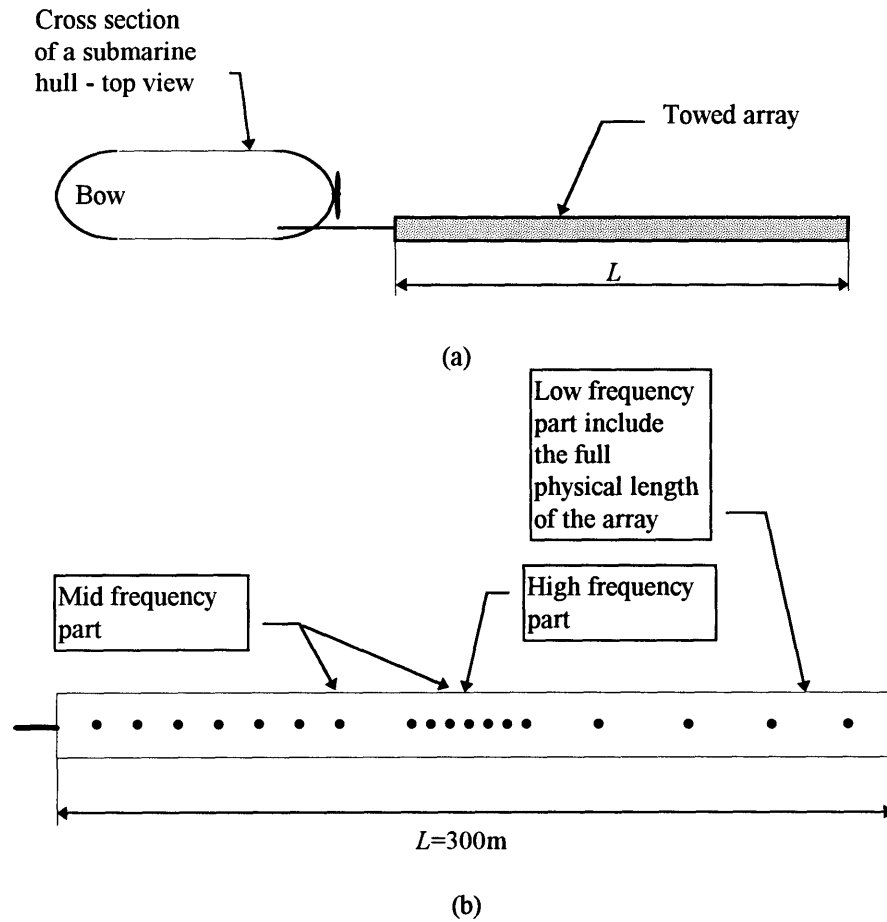
Figure 7.1: Geometry of the towed array. (a) the array is towed by a submarine. (b) the structure of a split aperture towed array.

The lower frequency limit does not mean that the sonar system cannot process information received below this limit. It does say, however, that processing frequencies lower than f_l would result in poorer azimuthal resolution, which is often not acceptable by sonar engineers and clients as far as a towed array is concerned. The horizontal angle width is given by equation (6.19)

$$\phi_e \approx \frac{\lambda}{L} = 0.1 \text{ rad,} \tag{7.3}$$

which is also approximately the equivalent beamwidth, η_e, and twice the directivity factor, d_f. The equivalent solid angle is, from equation (6.25),

$$\Omega_e = 2\pi\phi_e = 0.2\pi.$$ (7.4)

Once the equivalent solid angle is determined, the array gain can be calculated for the various types of noise that were considered in chapter 5. The first noise to be considered is the *wind* (or *surface*) *agitation*. From chapter 5, surface agitation is nonisotropic noise and its main noise axis is straight up, or $\alpha = 0$. Since the arrays, in this study, are restricted to the broad-side operation, the main noise axis and the array main lobe axis are copointed. The array gain for this particular noise and sonar system, AG_{sa}^1, can be calculated using equation (6.36), and the equivalent solid angles of the array and this to get

$$AG_{sa}^1 = 10\log\frac{\Omega_n}{\Omega_e} = 10\log\frac{1.7}{0.2\pi} \text{ (dB)}.$$ (7.5)

One must remember, however, that the array main axis is a "cone" type and therefore Ω_e extends far from the limits of Ω_n. When this fact is taken into account the array gain is increased but not dramatically. In practice equation (7.5) states the lower limit of the array gain due to the surface agitation noise. Also, an array that is steered toward endfire would result in a contrapointed case for which the array gain would be larger [7].

The second noise source to be considered is the *distant shipping*. Due to the fact that the noise main axis is always horizontal ($\alpha = 90°$, or $\theta = 0°$) the array main axis is always copointed with it. The array gain for the distant shipping noise and the towed array, AG_{ds}^1, can be calculated using equation (6.36), and the noise's equivalent solid angle

$$AG_{ds}^1 = 10\log\frac{\Omega_n}{\Omega_e} = 10\log\frac{3.3}{0.2\pi} \text{ (dB)}.$$ (7.6)

For the molecular agitation, the array gain plays no role and therefore the post array, or, equivalent noise level, L_{N_e}, equals to the noise level received by a single receiving element.

7.2 Hull Mounted Array Sonar

The hull mounted array, also called a flank array sonar, is based on two line arrays horizontally mounted on the opposite sides of the submarine. Its length is a function of the length of the submarine's hull that acoustically enables mounting a flank array. Three issues are of concern in this type of array. First, if the hull is not straight the taper function should compensate for that, second, the array should be located as far as possible from the machinery room, and finally, the array should be baffled so that the sound generated inside the hull is reduced at the arrays.

The construction of a baffled array is a totally separate issue and is not considered here. However, it is assumed that the arrays are perfectly baffled. The system consists of two identical arrays and therefore the analysis is carried out based on a single array, assuming that the other array receives signals from the other 2π steradians. Due to the definite dimensions of the submarine's hull the hull mounted array length cannot be chosen freely. The dimensions of the hull determine the maximum length of the array, which limits its aperture. The dimensions chosen for the submarine are not based on an actual design, and are depicted in Figure 7.2. The corresponding number of elements is

$$N = \frac{L}{d} = \frac{30}{0.5} = 60.$$ (7.7)

From the dimensions of the array one can set its frequency bandwidth. The upper frequency limit, f_u, can be calculated from the distance separating two adjacent elements, or equation (6.11) with $c \approx 1500$ m/s as a measure of the sound speed in sea water

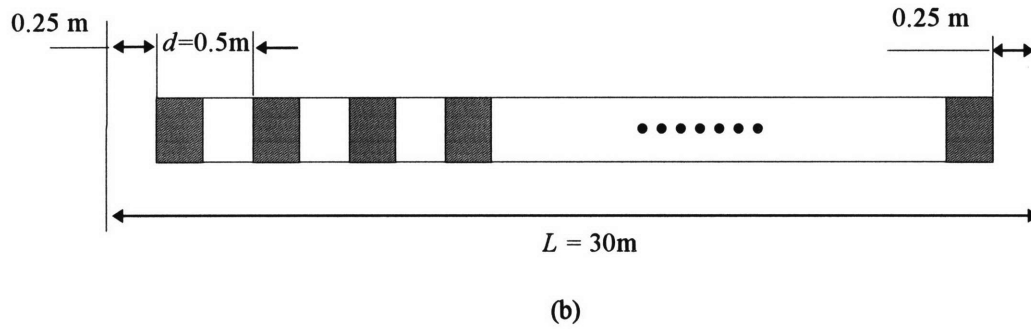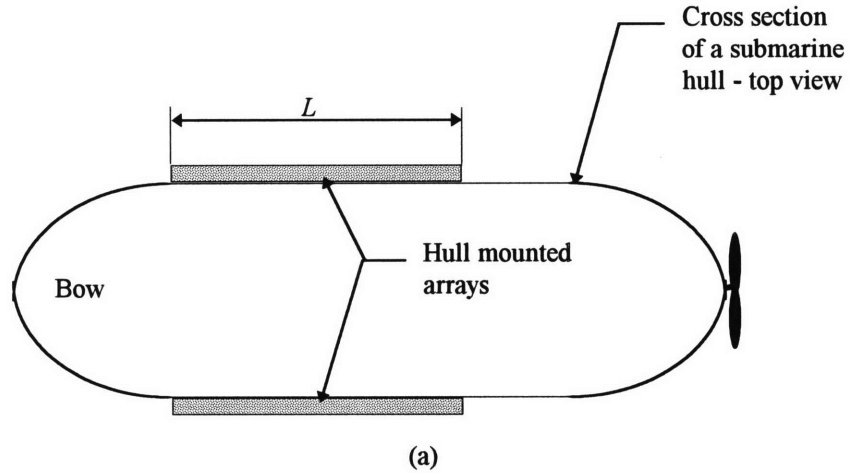$$f_u \le \frac{c}{2d} = \frac{1500}{2(0.5)} = 1500, \text{Hz}.$$ (7.8)

129

(a)

(b)

Figure 7.2: Geometry of the hull mounted array. (a) two line arrays mounted on the submarine hull. (b) the structure of each of the line arrays.

The lower frequency limit, f_l, can be viewed as the frequency in which the ratio of $L/\lambda \geq 10$ is set as a requirement. For this requirement

$$f_l = \frac{c}{L/10} = \frac{1500}{30/10} = 500, \text{ Hz.}$$ (7.9)

The horizontal angle width is given by equation (6.20) yielding

$$\phi_e \approx \frac{\lambda}{L} = \frac{c}{30f} = \frac{50}{f},$$ (7.10)

which is also approximately the equivalent beamwidth, η_e, and twice the directivity factor, d_f, for a free standing array. The equivalent solid angle is, form equation (6.25),

$$\Omega_e = 2\pi\phi_e = 100\frac{\pi}{f}.$$

However, recall that since the array is perfectly baffled the actual solid angle is Ω_{eb}, equals one half the one just calculated

$$\Omega_{eb} = 50\frac{\pi}{f}. \qquad (7.11)$$

As done for the towed array, the array gain is now calculated for the various types of noise that were considered in chapter 5. The first noise to be considered is the *wind* (or *surface*) *agitation*. For broad-side operation the main noise axis and the array main lobe axis are copointed. The array gain for this particular noise and sonar system, AG_{sa}^2, can be calculated using equation (6.36), and the equivalent solid angles of the array and this noise, to get

$$AG_{sa}^2 = 10\log\frac{\Omega_n}{\Omega_{eb}} = 10\log\frac{1.7f}{50\pi} \text{ (dB)}, \qquad (7.12)$$

Again, equation (7.12) states the lower limit of the array gain due to surface agitation. Also, in general, array that is steered toward endfire would result a contrapointed case for which the array gain would be different [7].

The second noise source to be considered is the *distant shipping*. Due to the fact that the noise main axis is always horizontal ($\alpha = 90°$, or $\theta = 0°$) the array main axis is always copointed with it. The array gain for the distant shipping noise and the hull mounted array, AG_{ds}^2, can be calculated using equation (6.36) to get

$$AG_{ds}^2 = 10\log\frac{\Omega_n}{\Omega_{eb}} = 10\log\frac{3.3f}{50\pi} \text{ (dB)}, \qquad (7.13)$$

131

As true for the towed array, the array gain for the molecular agitation plays no role and therefore the post array, or, the equivalent noise level, L_{N_e}, equals to the noise level received by a single receiving element.

7.3 Bow Array Sonar

The bow array sonar is one of the most common array designs for conventional and nuclear submarines. From its name, the bow array is installed in the bow of the vessel, outside the pressure hull. In order to keep the hydrodynamic shape of the submarine, the bow array is limited to the physical diameter of the submarine's bow. The most common designs of a bow array is the cylindrical shell array and the sphere shell array. The advantages of the bow array are being as far as possible from the machinery room and the propeller, and being able to steer to all directions without affecting the equivalent anglewidth (unlike the line array). The spherical shell array is the one which is considered here.

A typical diameter for a bow array is $D = 4$ m, and the spacing between the elements is $d = 0.15$ m, as depicted in Figure 7.3. Accordingly, the number of elements at the great circle is

$$N = \left[\frac{\pi D}{d} \right]_{\mathrm{I}} = 83,$$
(7.14)

where 'I' stands for the small nearest integer. The upper frequency limit, f_u, can be calculated from the distance separating two adjacent elements, with the use of equation (6.11), and $c \approx 1500$ m/s, to get
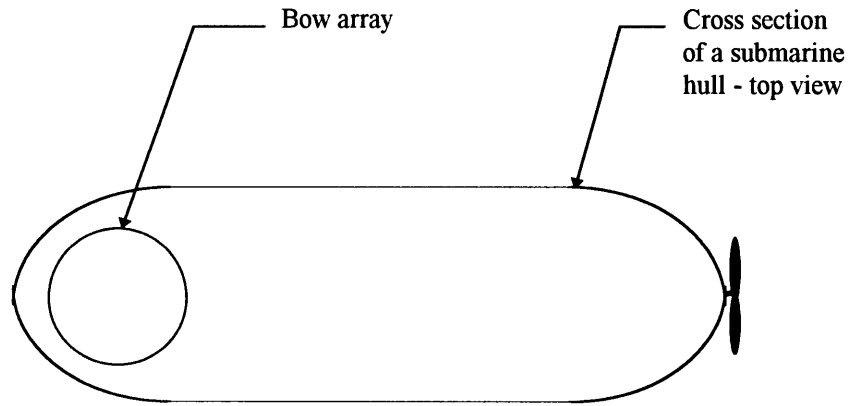
(a)
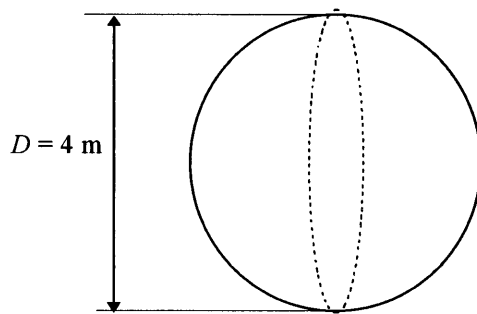
(b)

Figure 7.3: Geometry of the bow array. (a) the bow array is placed at the bow of the submarine. (b) the dimension of the bow array.

$$f_u \leq \frac{c}{2d} = \frac{1500}{2 \cdot 0.15} = 5\,\text{kHz}. \tag{7.15}$$

The lower frequency limit, f_l, is set as the frequency in which the equivalent angle width, α_e, stays less than $15°$ or 0.25 rad. This angle width is rather large but acceptable in bow array designs. (There is always a tradeoff between frequency and physical dimensions, as the beamwidth is directly related to the wavelength.) From equation (6.30) the beamwidth of the spherical shell can be written as

$$\alpha_e = \frac{4.46}{\pi} \frac{\lambda}{D} \leq 0.25.$$

(7.16)

From equation (7.16) the lower frequency limit is then

$$f_l = \frac{4.46c}{\pi D \alpha_e} \cong 2.2\,\text{kHz}.$$

(7.17)

Assuming the array is tapered to unifire, its equivalent solid angle is given by equation (6.31). With $\lambda = c/f$, and $S_g = 4\pi$ the equivalent solid angle, in terms of f, is then

$$\Omega_e = \frac{5}{8}\left(\frac{2(c/f)^2}{S_g}\right) \approx \frac{1}{\pi}\left(\frac{838}{f}\right)^2.$$

(7.18)

As done for the line arrays, the array gain for the bow array must be calculated separately for each noise source. Recall that the surface agitation's main axis is $\alpha = 0$ (pointing upwards), but on the other hand, the array main axis is pointing to the horizontal (toward the target.) This creates a contra-pointed case. From equation (6.37) the array gain is given by

$$AG_{sa}^3 = 10\log\left(\frac{\Omega_n/\Omega_e}{S_a/S_o + B_n^2(\Omega_n/\Omega_e)}\right),\,\text{dB}.$$

(7.19)

S_a is the value of $S(f_o,\Omega)$ on the horizontal, which can be estimated from Figure 5.3 to be roughly $S_a \cong 0.18$ (≈ 7.5 dB down relative to $S_o = 1$.) The problem left here is to estimate the average array response in the vertical direction when its main axis is steered to the horizontal. From equation (6.27) the average array response upward is given by

$$B_n^2 = \left\langle\left(\text{sinc}\left(\frac{2\pi f D}{c}\sin\frac{\alpha}{2}\right)\right)^2\right\rangle \cong \frac{0.5}{\left(\frac{2\pi f D}{c}\right)^2\left\langle\sin^2\frac{\alpha}{2}\right\rangle}.$$

(7.20)

where α is centered about 90° and equation (7.20) should be averaged over the vertical angle width of the surface agitation noise (which is about 43° from Figure 5.3). The result, including all known parameters, is

$$B_n^2 \approx \frac{0.5}{(9.1f)^2}$$ (7.21)

where f is given here in kHz. Note that the array response is frequency dependent. As an example for $f = 2$ kHz, in dB notation, the array average response upward is about -28 dB, and when $f = 5$ kHz, the array response is about -36 dB as can be expected for higher frequencies. From chapter 5, the noise equivalent solid angle is $\Omega_n = 1.7$ srad, and with the use of equation (7.19), the array gain in this case equals

$$AG_{sa}^3 \cong 10\log\left(\frac{1}{(154/f)^2 + B_n^2}\right)$$ (7.22)

where B_n^2 is given by equation (7.20).

The case for the distant shipping noise is a copointed one since its main axis is in the horizontal, like the array. Following the guidelines of equation (6.36) the array gain for the distant shipping noise is

$$AG_{ds}^3 = 10\log\frac{\Omega_n}{\Omega_e} \cong 10\log\frac{3.3\pi}{(838/f)^2}, \text{ dB}$$ (7.23)

As the case for the other arrays, the equivalent noise level due to molecular agitation, L_{N_e}, equals to the noise level received by a single element, L_N.

The table below (Table 7-1) summarizes the array gain results that were obtained for the different arrays and noise sources.

Table 7-1: Summary of array gain results in dB for the various arrays and noise sources

	Surface agitation, dB	Distant shipping, dB	Molecular agitation
Towed array	$10\log\left(\dfrac{1.7}{0.2\pi}\right)$	$10\log\left(\dfrac{3.3}{0.2\pi}\right)$	-
Hull mounted array	$10\log\left(\dfrac{1.7f}{(50/\pi)}\right)$	$10\log\left(\dfrac{3.3f}{(50/\pi)}\right)$	-
Bow array	$10\log\left(\dfrac{1}{(154/f)^2 + B_n^2}\right)$ (see also Eq. (7.21))	$10\log\dfrac{3.3\pi}{(838/f)^2}$	-

Chapter 8

Implementation and Results

The idea behind the implementation is to address the analysis of sonar systems from two opposite sides. The first approach is to calculate the transmission loss, H, as a function of range, for a particular set of parameters, while the other approach is to calculate the figure-of-merit, FOM, for the same set of parameters. From the definition of the FOM, as described in chapter 3, one can interpret it as the maximum transmission loss allowed for detection. Thus by comparing the FOM with H, one can estimate the ability of a particular sonar system to detect the target.

In other words, if the FOM is plotted as a maximum limit on H, then when $FOM > H$ a 'detection' occurs, and accordingly when $FOM < H$ there is 'no detection' of the target. (This is, of course, dependent upon the way of defining a detection as a probability contingent upon the probability of a false alarm.) Another way of looking at this presentation is to understand that the transmission loss is a function of the medium, while the FOM is a function of the sonar characteristics, the target properties, and the noise spectral and spatial density. Although the above is classically true, the sonar system also plays a role in determining the transmission loss, via the bottom loss, as described in chapter 4.

The transmission loss calculations involve several steps. The first step is to generate the ray trace diagrams. The ray trajectories are then generated in the form of solutions to the ray equation (4.8) or (4.10). The sound source, or the target, was placed at $z = 100$ m, and was considered omni directional. The ray angular space was chosen to include the rays

with launch angles within $37.5° < \theta < 37.5°$. The limits on the angular space, stated above, can be considered sufficient but also somewhat arbitrary, and could easily be higher than that. However, larger launch angles would have resulted in higher bottom-surface interaction rate with higher bottom-ray angle. Thus, the corresponding ray bundles would rapidly be attenuated, and would have only minor effects on the total performance analysis. The angular space also limits the number of rays to be accounted for in the calculations and therefore making the computation more efficient.

The angular resolution was chosen to be a constant, $d\theta = 0.6°$, and was chosen as such for computational simplicity. Other choice of $d\theta$ can be launch angle dependent so that $d\theta$ increases as θ increases. However, only the simple case was considered in this study.

The ray trajectories were generated for each location, for up-slope, cross-slope, and down-slope cases, and for the summer and winter conditions. The sound speed profile was linearly interpolated at each depth as can be seen in the ray trace figures (see Figure 4.3 for example).

While generating the ray trajectories, the code also calculates the mean square pressure of each ray tube formed by two adjacent rays with the use of equation (4.13), given a normalized point source ($L_S = 1$ dB re 1μPa & 1m.) The calculation was performed using a 300 m range resolution from the origin (source location) up to 50 km away. The ray RMS pressure result was then smoothed using a 5 point moving window in order to average the caustic effects.

The next step is to obtain the bottom and surface losses. The boundary losses were modeled as Fresnel forward scatterers as stated in equations (4.20) and (4.27) for bottom and surface loss respectively. The RMS roughness waves height was taken as $\delta_s = 1$ m for the winter, and $\delta_s = 0.2$ m for the summer (see chapter 2 for more details on the subject). The bottom RMS roughness height, δ_b, however, is determined by the observation scale which is a function of the sonar integration time, beamwidth, frequency, and the direction of propagation (see section 4.2).

After incorporating the surface and bottom losses to the RMS pressure of the ray tubes, the full field of pressure levels in both range and depth was obtained using incoherent addition of the RMS pressure formed by all the ray tubes.

The final step is to include the volumetric absorption at each range and depth using equation (4.39) (with r representing the horizontal range) to finally form the complete transmission loss, H.

Since the search depths of a conventional submerged vehicle carrying a receiver array is shallower than 200 m, the analysis is performed for three receiver depths: 50 m, 100 m, and 150 m. The transmission loss for each depth was smoothed for presentation purposes using a 5 point smoothing window.

As for the second approach, the FOM must include all the other parameters, such as, target source level, noise characteristics, and sonar properties like bandwidth, b, array gain, AG, and detection threshold, DT. Using table 7-1, the array gains were generated for the three sonar systems for winter conditions as well as summer conditions, and were used to generate the equivalent noise levels for each season, sonar system, and processing type (narrowband and broadband) by the use of equation (3.8). Then the FOM was calculated using equation (3.11). The FOM for a particular sonar and season is general to all three locations since the noise spectral levels were assumed to be the same for those locations.

8.1 FOM Results

A summary of the FOM results is presented in Figure 8.1 for broadband (BB) processing, and in Figure 8.2 for narrowband (NB) processing. The bandwidth for the BB analysis is taken to be

$$b_{BB} = f_o/2 \; ; \; 100 \text{ Hz} > f_o > 10 \text{ kHz}$$

and for the NB, the bandwidth is

FOM, BB
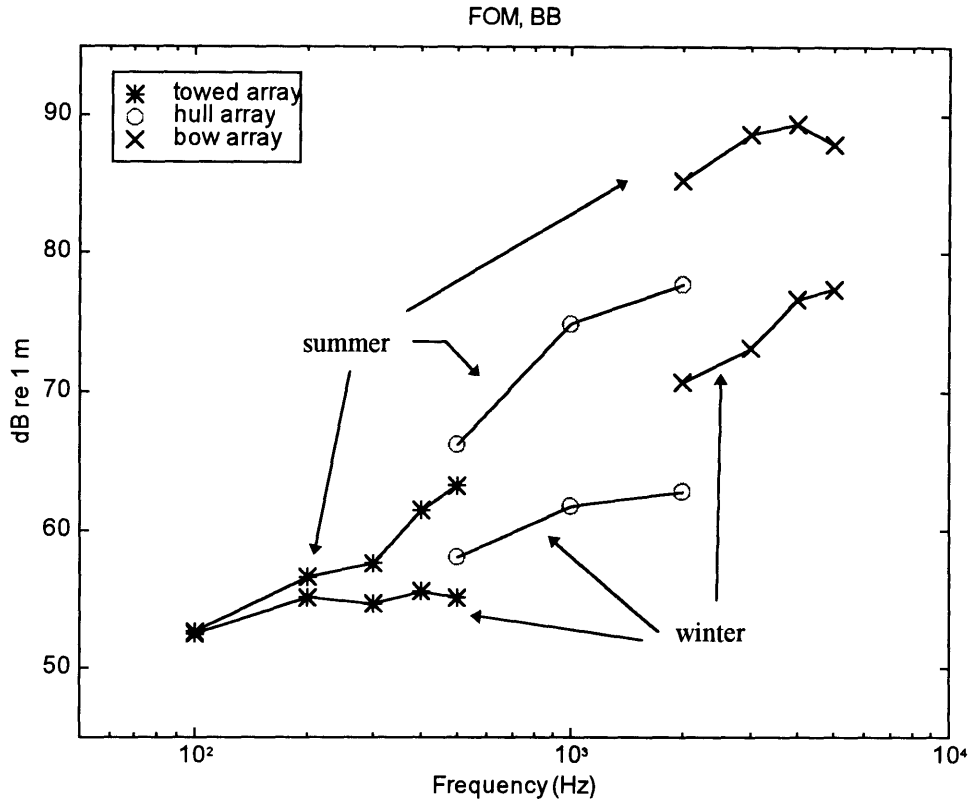
Figure 8.1: *FOM* results (dB re 1m) for BB processing for the various types of arrays as a function of frequency and season.

$$b_{NB} = 0.1 \text{ Hz}; \quad 10 < f_o < 500 \text{ Hz}$$

It should be noted that the *FOM* for the BB analysis is presented only for the broadband regime of the target, and the narrowband results were obtained only for those frequencies where a narrowband component of the target is present (see Figure 3.2.)

As can be seen from Figure 8.1 and Figure 8.2 each sonar system operates at different frequency bands due to their different array dimensions, as described in more details in chapter 7. Accordingly, the towed array operates at the lower frequency band $(50 < f < 750)$, while the spherical shell (bow) array operates at the higher band $(2000 < f < 5000)$. The hull mounted array operates in the mid frequency band $(500 < f < 1500.)$

The *FOM* results, in Figure 8.1 and Figure 8.2, show higher *FOM* for NB processing than BB processing at the common frequency (500 Hz). This is due to the

FOM, NB
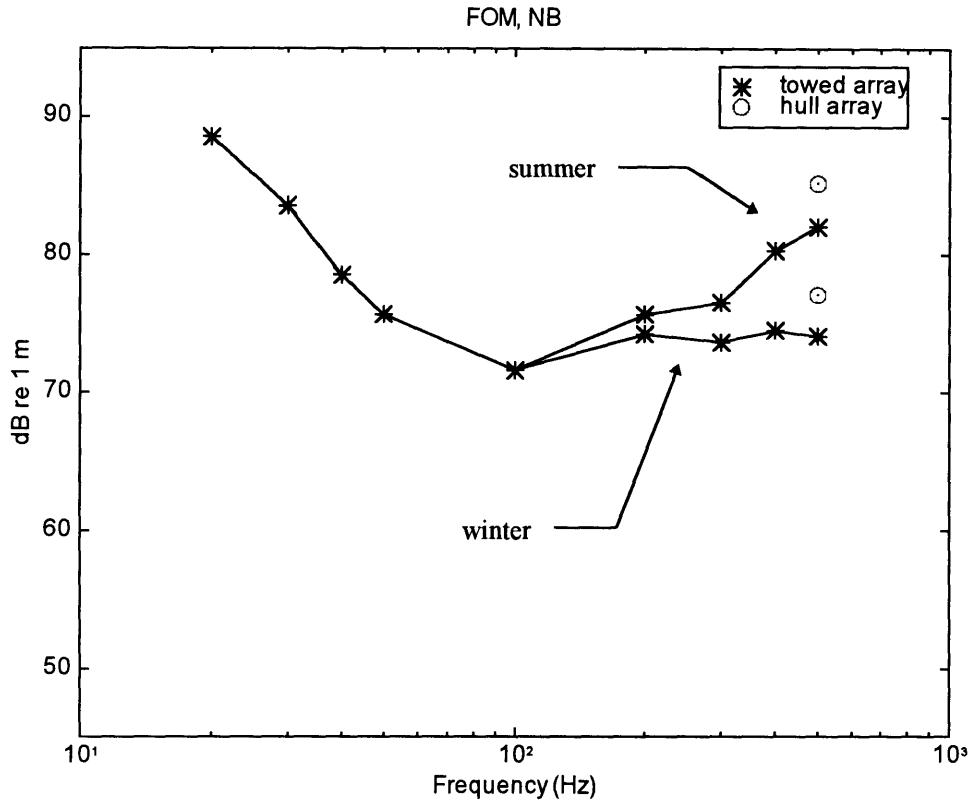
Figure 8.2: *FOM* results (dB re 1m) for NB processing for the towed array and hull mounted array as a function of frequency and season.

narrow bandwidth, $b = 0.1$ Hz, used in the NB calculations (assuming that the NB components of the target are at least narrower than that). It should be emphasized that the *FOM* for NB processing is inversely related to the bandwidth, b. Thus the larger the bandwidth, the lower the *FOM* for NB. Also from Figure 8.1, it seems that the *FOM* for BB processing increases as the frequency increases. This could be due to two reasons. The first is that the higher the frequency the better the array gain (except for the towed array since its beamwidth is considered constant - see chapter 7), and the second is because when the frequency increases, the noise spectral level decreases.

The *FOM* results labeled 'summer' and 'winter' correspond to the definition of these seasons in chapter 2. Accordingly, the surface agitation noise is different for these two seasons, thus causing higher *FOM* in the summer when the surface noise dominates $(f > 100$ Hz$)$.

8.2 Analysis Results

A total of 144 figures of performance results (that include transmission losses and the corresponding *FOM*'s) were generated to cover almost all aspects of the parameter space. All the figures are presented in appendix A following the order outlined in Table 8-1. The parameter space include the following: type of sonar system (or type of array), processing method (NB or BB), receiver depth, season, frequency, and bottom slope. By producing all these figures the sensitivity of the sonar system with respect to each one of the parameter can be analyzed. The enormous amount of data that is presented in figures A.1 through A.144 is fully analyzed in appendix A, where each figure is interpreted separately. One should note that the analysis results for the first location, down-slope case are excluded from appendix A due to the similarity of the results to the up and cross-slope cases. This of course can be expected at locations with almost zero bottom slopes.

The ray trace diagrams for each location, season, and slope (up, cross and down) are also presented in appendix A except for the first location where only the up-slope case is presented. The ray trace diagram is considered a very important tool for the sonar operator as well as the scientist. It represents a rather simple picture of the directions in which sound propagates and gives who ever uses it the needed physical insight to *begin* analyzing the performance of the sonar system.

It is more efficient, however, to discuss the analysis results in terms of a comparison between the various cases. This way the sensitivity of the sonar performance to each of the parameters can be more easily learned. A comparative discussion on the analysis results is presented in chapter 9. It should be emphasized that chapter 9 intends to present the highlights of the analysis results from a broad point of view and side issues are discussed only briefly. In other words, the performance analysis of sonar systems is much too complex to fully cover in a single study from all possible aspects. Therefore the reader is invited to further analyze the figures in appendix A once a narrower and more defined problem is of concern.

Table 8-1: Order of appearance of performance results in appendix A.

Figure #	Location. #	Slope	Season	f (Hz)	Array type	Page
A.1	1	up	winter	100	towed	199
A.2	1	up	winter	200	towed	199
A.3	1	up	winter	500	towed	200
A.4	1	up	winter	500	hull	200
A.5	1	up	winter	1 k	hull	201
A.6	1	up	winter	1.5 k	hull	201
A.7	1	up	winter	2 k	bow	202
A.8	1	up	winter	3 k	bow	202
A.9	1	up	winter	5 k	bow	203
A.10	1	cross	winter	100	towed	204
A.11	1	cross	winter	200	towed	204
A.12	1	cross	winter	500	towed	205
A.13	1	cross	winter	500	hull	205
A.14	1	cross	winter	1 k	hull	206
A.15	1	cross	winter	1.5 k	hull	206
A.16	1	cross	winter	2 k	bow	207
A.17	1	cross	winter	3 k	bow	207
A.18	1	cross	winter	5 k	bow	208
A.19	1	up	summer	100	towed	209
A.20	1	up	summer	200	towed	209
A.21	1	up	summer	500	towed	210
A.22	1	up	summer	500	hull	210
A.23	1	up	summer	1 k	hull	211
A.24	1	up	summer	1.5 k	hull	211
A.25	1	up	summer	2 k	bow	212
A.26	1	up	summer	3 k	bow	212
A.27	1	up	summer	5 k	bow	213
A.28	1	cross	summer	100	towed	214
A.29	1	cross	summer	200	towed	214
A.30	1	cross	summer	500	towed	215
A.31	1	cross	summer	500	hull	215
A.32	1	cross	summer	1 k	hull	216
A.33	1	cross	summer	1.5 k	hull	216
A.34	1	cross	summer	2 k	bow	217
A.35	1	cross	summer	3 k	bow	217
A.36	1	cross	summer	5 k	bow	218
A.37	2	up	winter	100	towed	219
A.38	2	up	winter	200	towed	219
A.39	2	up	winter	500	towed	220
A.40	2	up	winter	500	hull	220

Figure #	Location. #	Slope	Season	f(Hz)	Array type	Page
A.41	2	up	winter	1 k	hull	221
A.42	2	up	winter	1.5 k	hull	221
A.43	2	up	winter	2 k	bow	222
A.44	2	up	winter	3 k	bow	222
A.45	2	up	winter	5 k	bow	223
A.46	2	cross	winter	100	towed	224
A.47	2	cross	winter	200	towed	224
A.48	2	cross	winter	500	towed	225
A.49	2	cross	winter	500	hull	225
A.50	2	cross	winter	1 k	hull	226
A.51	2	cross	winter	1.5 k	hull	226
A.52	2	cross	winter	2 k	bow	227
A.53	2	cross	winter	3 k	bow	227
A.54	2	cross	winter	5 k	bow	228
A.55	2	down	winter	100	towed	229
A.56	2	down	winter	200	towed	229
A.57	2	down	winter	500	towed	230
A.58	2	down	winter	500	hull	230
A.59	2	down	winter	1 k	hull	231
A.60	2	down	winter	1.5 k	hull	231
A.61	2	down	winter	2 k	bow	232
A.62	2	down	winter	3 k	bow	232
A.63	2	down	winter	5 k	bow	233
A.64	2	up	summer	100	towed	234
A.65	2	up	summer	200	towed	234
A.66	2	up	summer	500	towed	235
A.67	2	up	summer	500	hull	235
A.68	2	up	summer	1 k	hull	236
A.69	2	up	summer	1.5 k	hull	236
A.70	2	up	summer	2 k	bow	237
A.71	2	up	summer	3 k	bow	237
A.72	2	up	summer	5 k	bow	238
A.73	2	cross	summer	100	towed	239
A.74	2	cross	summer	200	towed	239
A.75	2	cross	summer	500	towed	240
A.76	2	cross	summer	500	hull	240
A.77	2	cross	summer	1 k	hull	241
A.78	2	cross	summer	1.5 k	hull	241
A.79	2	cross	summer	2 k	bow	242
A.80	2	cross	summer	3 k	bow	242
A.81	2	cross	summer	5 k	bow	243
A.82	2	down	summer	100	towed	244

Figure #	Location. #	Slope	Season	f (Hz)	Array type	Page
A.83	2	down	summer	200	towed	244
A.84	2	down	summer	500	towed	245
A.85	2	down	summer	500	hull	245
A.86	2	down	summer	1 k	hull	246
A.87	2	down	summer	1.5 k	hull	246
A.88	2	down	summer	2 k	bow	247
A.89	2	down	summer	3 k	bow	247
A.90	2	down	summer	5 k	bow	248
A.91	3	up	winter	100	towed	249
A.92	3	up	winter	200	towed	249
A.93	3	up	winter	500	towed	250
A.94	3	up	winter	500	hull	250
A.95	3	up	winter	1 k	hull	251
A.96	3	up	winter	1.5 k	hull	251
A.97	3	up	winter	2 k	bow	252
A.98	3	up	winter	3 k	bow	252
A.99	3	up	winter	5 k	bow	253
A.100	3	cross	winter	100	towed	254
A.101	3	cross	winter	200	towed	254
A.102	3	cross	winter	500	towed	255
A.103	3	cross	winter	500	hull	255
A.104	3	cross	winter	1 k	hull	256
A.105	3	cross	winter	1.5 k	hull	256
A.106	3	cross	winter	2 k	bow	257
A.107	3	cross	winter	3 k	bow	257
A.108	3	cross	winter	5 k	bow	258
A.109	3	down	winter	100	towed	259
A.110	3	down	winter	200	towed	259
A.111	3	down	winter	500	towed	260
A.112	3	down	winter	500	hull	260
A.113	3	down	winter	1 k	hull	261
A.114	3	down	winter	1.5 k	hull	261
A.115	3	down	winter	2 k	bow	262
A.116	3	down	winter	3 k	bow	262
A.117	3	down	winter	5 k	bow	263
A.118	3	up	summer	100	towed	264
A.119	3	up	summer	200	towed	264
A.120	3	up	summer	500	towed	265
A.121	3	up	summer	500	hull	265
A.122	3	up	summer	1 k	hull	266
A.123	3	up	summer	1.5 k	hull	266
A.124	3	up	summer	2 k	bow	267

Figure #	Location. #	Slope	Season	f (Hz)	Array type	Page
A.125	3	up	summer	3 k	bow	267
A.126	3	up	summer	5 k	bow	268
A.127	3	cross	summer	100	towed	269
A.128	3	cross	summer	200	towed	269
A.129	3	cross	summer	500	towed	270
A.130	3	cross	summer	500	hull	270
A.131	3	cross	summer	1 k	hull	271
A.132	3	cross	summer	1.5 k	hull	271
A.133	3	cross	summer	2 k	bow	272
A.134	3	cross	summer	3 k	bow	272
A.135	3	cross	summer	5 k	bow	273
A.136	3	down	summer	100	towed	274
A.137	3	down	summer	200	towed	274
A.138	3	down	summer	500	towed	275
A.139	3	down	summer	500	hull	275
A.140	3	down	summer	1 k	hull	276
A.141	3	down	summer	1.5 k	hull	276
A.142	3	down	summer	2 k	bow	277
A.143	3	down	summer	3 k	bow	277
A.144	3	down	summer	5 k	bow	278

Chapter 9

Discussion and Comparison

Before proceeding to any conclusions it is essential to review the fundamental assumptions maid in creating the analysis framework. Once this is understood the reader will have the necessary knowledge to fully understand the results of the sonar performance analysis as well as the conclusions, and will be able to perform one of his own.

A basic assumption in this study is that the bottom shape can be simplified to a simple plane with a vertical slope that corresponds to the average bottom slope in the direction of propagation. Three directions of propagation were chosen so that the effect of the bottom is perhaps made clearer. The up and down-slope cases were chosen to be mostly perpendicular to the isodepth lines of the bottom and opposite to one another, and the cross-slope direction is chosen to be along the isodepth contour lines. This simplification may not be totally true if the bottom structure is much more complex. For example, near sea mounts, which are common in the seabed as much as in the land, a plane may not be adequate approximation to the bottom shape. Another effect that was ignored in this study is horizontal refraction of rays due to a sloping bottom [2]. The basic idea of horizontal refraction is discussed briefly in appendix B.

Once the bottom slope is determined, ray trace diagrams are generated based on actual sound velocity profiles taken during the winter (cold season) and summer (warm season). One should bear in mind that the sound velocity that was considered here is *not* the exact sound velocity profile that one may find as a result of actual measurements during a specific transmission loss test. The SVP, here, is an average over season and taken from

historical data. Thus, at best, it is only the expected profile. The ray trace diagrams show, therefore, only the expected trajectories at the different locations during both seasons.

Another key issue is the definition of the summer and the winter that affects the surface noise and the surface loss via surface wave height. The wave height that is considered here (1 m for the winter and 0.2 m for the summer) represents only two cases with a probability that may not reflect reality for all winter or summer. In other words, there are times during winter and summer that the situation is the opposite. In practice, then, many such cases should be analyzed to fully cover the effects of waves on the performance of sonar systems. Wave height affects the transmission loss calculations as well the figure-of merit and therefore may have a substantial influence on the analysis results and on the conclusions.

A closely related issue is the background noise data that was considered here. The data is taken from a paper by Wenz [12] who based his results on measurements done in other ocean environments. Although this paper passed the test of time, it is used here due to a lack of more accurate information. Needless to say that once more accurate data is available, the analysis should be repeated to reflect reality in a more precise manner.

The actual properties of the arrays should also be of concern. In this study, the actual positions of the hydrophones in the towed array are not known and therefore its ability to reject noise is, at best, only estimated. If the towed array, in use, is capable of transmitting the absolute positions of its elements, the sonar beamformer processor could phase taper the array to compensate for any position changes in order to keep a high degree of performance. Therefore, the analysis done here is for particular array designs, and thus would not reflect the performance of all towed, hull mounted, and bow arrays. Necessary corrections must be introduced to the calculations in order to analyze a different array design.

The bottom effect on the sonar system is yet another issue that must be considered. In this study, the bottom loss is modeled as a Fresnel scatterer based on the bottom roughness height (see chapter 4 for more details). It must be emphasized, though, that the

model was derived using actual bottom loss measurements from the Gulf of Oman. It is highly probable that the bottom losses in the eastern Mediterranean sea may be different, and thus may affect the transmission loss results.

Finally, the analysis is done for a typical diesel-electric submarine operating *only* at 100 meters depth, with a relatively low speed (in the order of 3 knots). If the source would have been a surface ship the analysis results would be different.

Based on the above, the sonar may perform differently once one introduces either different information or a more accurate one. More importantly, however, this study establishes a framework that can be used, with the appropriate corrections, to perform a full analysis of any sonar system anywhere. In view of the above, the *main* effects of bottom slope, bottom depth, season, receiver depth, and frequency (or array type) on the performance of the sonar systems are reviewed subsequently. All the results are taken from the figures in appendix A (see Table 8-1) which show the results in a larger scale and a different format.

9.1 SVP Changes

Not much of a difference can be observed when comparing the sound velocity profiles at the different location during each season (winter or summer) as can be seen in Figure 9.1. It should be noted, however, that at the first location the SVP gradient at the upper water column (0 - 400 m) is less downward refractive than at the other two locations.

A major difference is observed when the summer SVP is compared to the winter SVP in the upper water column (see Figure 9.2). A large downward refractive gradient is clearly observed in the summer at the upper water column. This has a substantial effect on the refraction and propagation characteristics of sound in the medium as shall be reviewed subsequently.
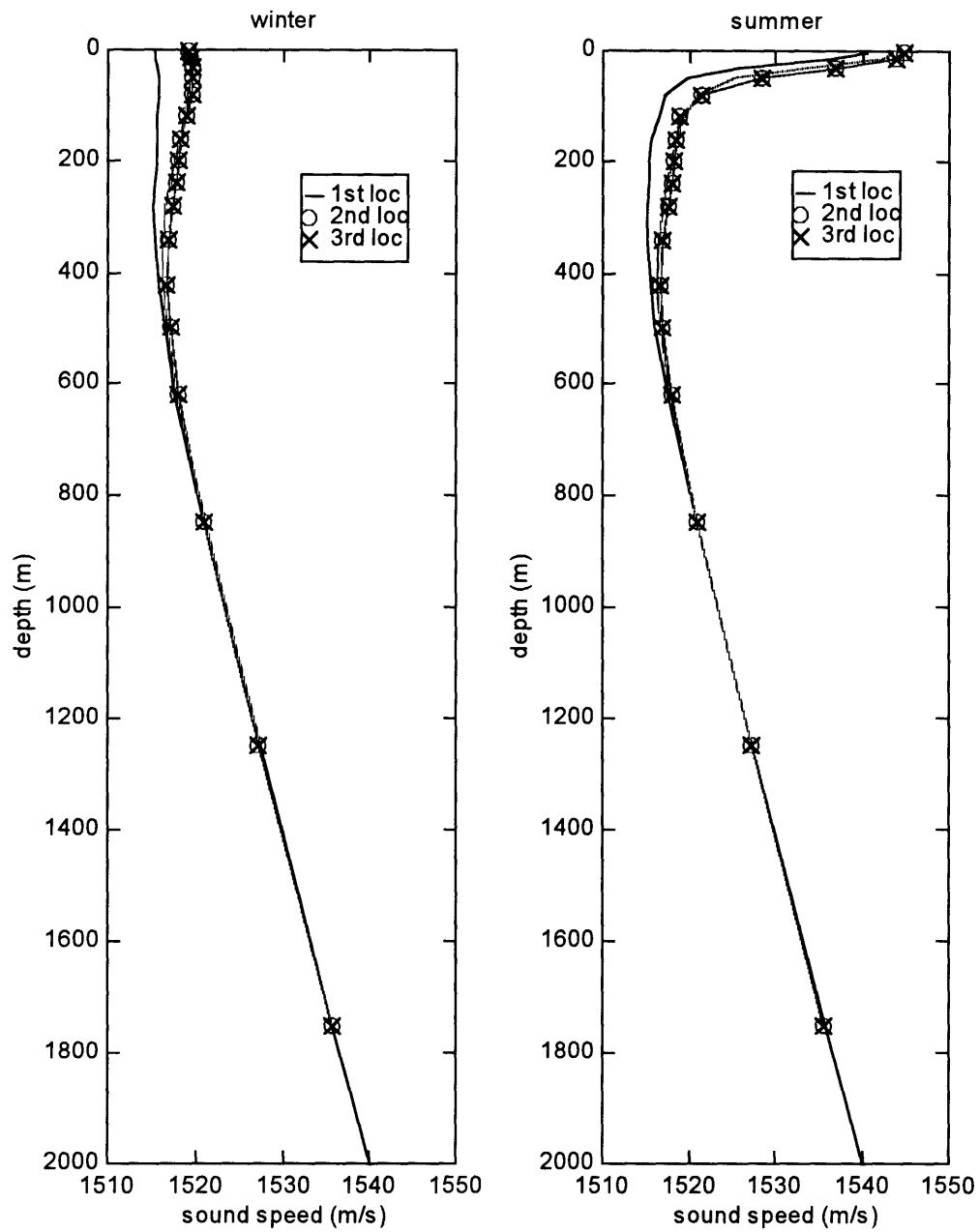
Figure 9.1: Changes in sound velocity profiles during the winter and summer at the three locations [31].
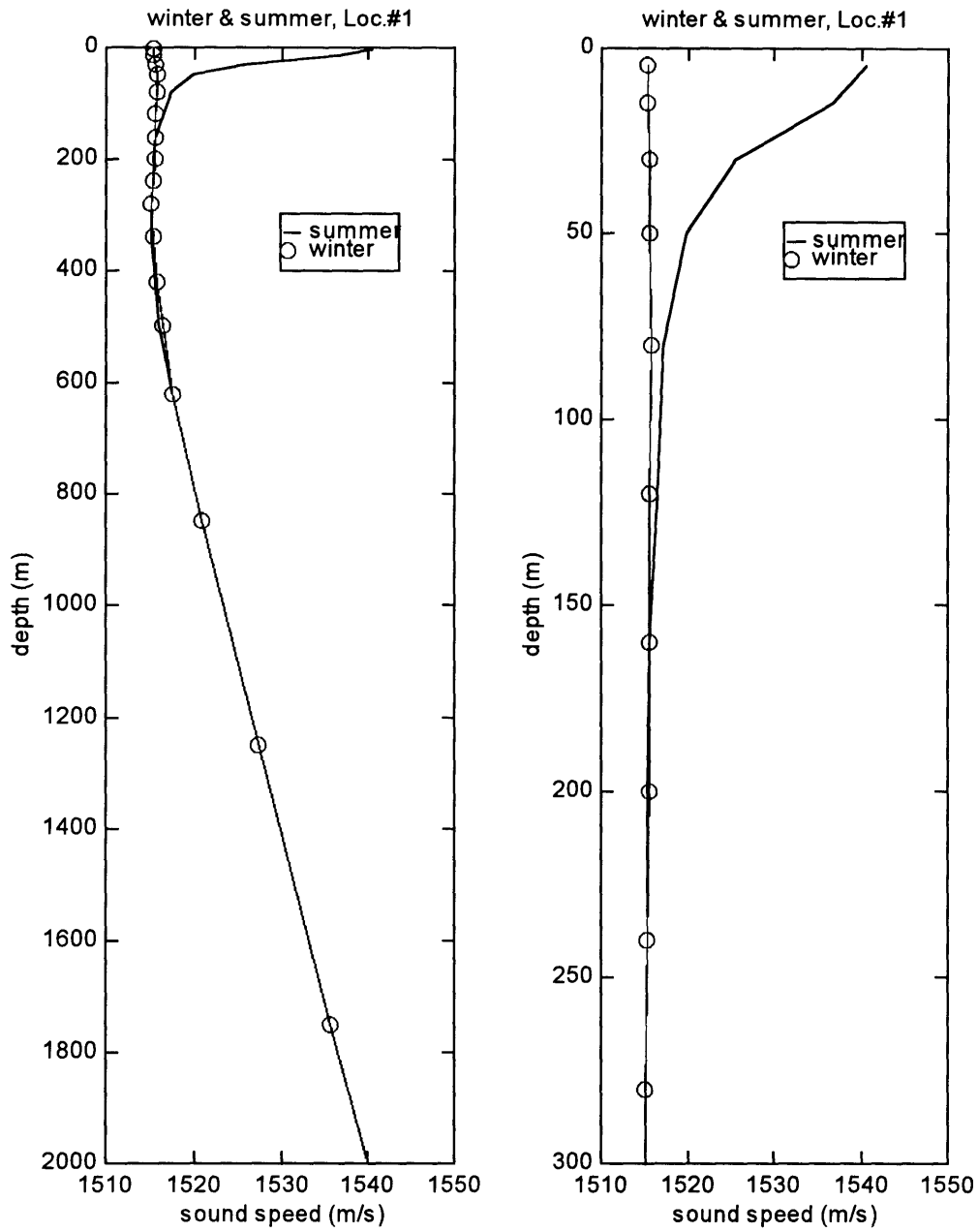
Figure 9.2: Changes in sound velocity profiles at the first location between the winter and summer [31].

9.2 Bottom Depth Effects

Although it cannot be completely isolated, the bottom depth effects can be compared for the cross-slope case at the various locations (which have different bottom depths) while fixing possibly all the other parameters. Figure 9.3 and Figure 9.4 each shows three plots, each plot presents three different curves. As shown in the figures, the three curves in each plot correspond to the transmission loss results obtained at the first location (2200m deep), second location (1700m deep), and third location (1200 m deep). The three plots, however, correspond to the transmission loss results for the towed array at 200 Hz, the hull array at 1000 Hz, and bow array at 2000 Hz. The frequencies for the various array types were chosen to reflect their different operating frequencies. As mentioned in chapter 7 in detail the towed array operates in the lower frequency band, the hull array operates in the mid frequency band, and the bow array operates in the high frequency band. The results are presented for the winter and summer time in Figure 9.3 and Figure 9.4 respectively. Also shown is the *FOM*, where applicable, in order to check the sonar performance sensitivity with respect to the bottom depth.

The most important bottom depth effect is its control over the type of transmission (RSR or bottom-bounce). As discussed in chapter 4 RSR propagation dominates the regions close to the target and at the convergence zone (30 km - 40 km) while the bottom-bounce is notable at ranges 17 km - 30 km approximately and beyond 40 km. By acknowledging this fact one should use, of course, the appropriate integration time in order to fully analyze the substantial differences of any sonar system at these regions. In this study, however, a single integration time is used thus reducing the effect although still strongly notable. In general, as the location becomes deeper the more RSR propagation dominates, and as the location becomes shallower the bottom-bounce propagation has an increasing effect on the transmission loss. The effect of the propagation type can be observed in Figure 9.3 and Figure 9.4.

During the winter, no notable bottom depth effects are seen up to 17 km, and between 30 km - 40 km. At ranges 17 km - 30 km, and beyond 40 km the bottom-bounce propagation can be clearly seen consistently for the various array types. At the closer range the transmission loss is largest for the 2200 m depth and lowest for the 1200 m depth. In fact, 5dB - 10dB differences can be observed which are due to spreading loss controlled by the SVP gradient at the upper water column. In fact, at the first location the SVP is more upward refracting in comparison to the other two locations at the upper water column. This explains the changes of transmission loss at very close ranges. Beyond 40 km, on the other hand, the largest transmission loss is observed for the 1200 m depth, and the lowest one can be seen for the 2200 m depth. This is because of larger bottom and surface losses for the shallower location caused by a higher bottom-surface interaction rate. The differences in transmission loss grow with range and frequency, ranging for example, at 50 km, from 5dB for the towed array, to 15dB for the hull array, and even more than that for the bow array.

It should also be emphasized that the convergence zone shown between 30 km - 40 km is the widest for the deeper location because a larger angular spread of rays can be launched without hitting the bottom. Also, the differences in transmission loss up to 17 km are probably also due to differences in the bottom sound speed among the three locations where smaller bottom sound speeds are found at the shallower locations.

During the summer the SVP structure in the upper 100 m is relatively the same for all the three locations with a large downward refractive gradient. As can be seen from Figure 9.4, up to about 25 km, the bottom-bounce and direct loss dominate and therefore higher transmission loss can be observed for the deeper locations. Beyond 40 km no direct propagation is possible, and one can still see that the deeper location is more lossy. The reason for this is that the bottom-bounce dominates as opposed to the bottom-surface losses that dominate during the winter, caused by higher surface wave scattering in the winter. The effect of a higher bottom-surface interaction rate during the summer is highly probable to be noticed at ranges larger than 50 km (this is not shown in the figures). The widening effect of the convergence zone as a function of bottom depth can also be seen in the summer but

weaker than in the winter. This is also another effect of the downward refractive gradient in the summer.

Accordingly, ignoring the SVP differences between the locations during the winter, the sonar system performs generally better at shallower locations at ranges up to 30 km and at deeper locations beyond 40 km. During the summer, however, better performance is expected at the shallower places at ranges up to about 25 km and beyond 40 km due to less surface loss. It should be noted that the final performance results, as a function of bottom depth, would probably have been the same, for the winter and summer, once the surface loss and the surface noise are the same. (see chapter 2 and the introduction of this chapter for the definition of summer and winter).
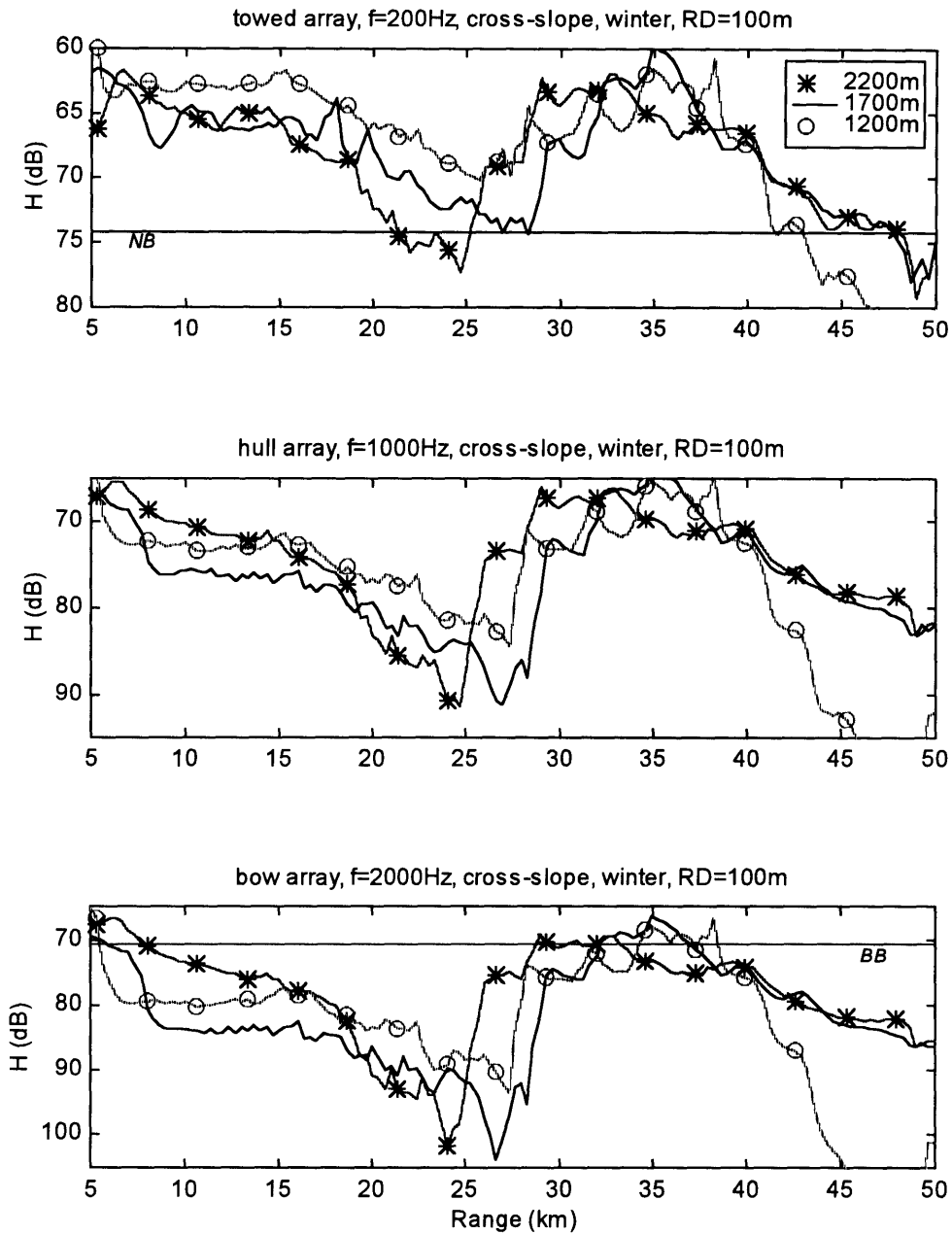
Figure 9.3: The effect of bottom depth on the transmission loss during the winter for the various array types and frequencies. *FOM* is shown for NB and BB when applicable, and is 61 dB for the hull array and therefore does not appear in the figure.
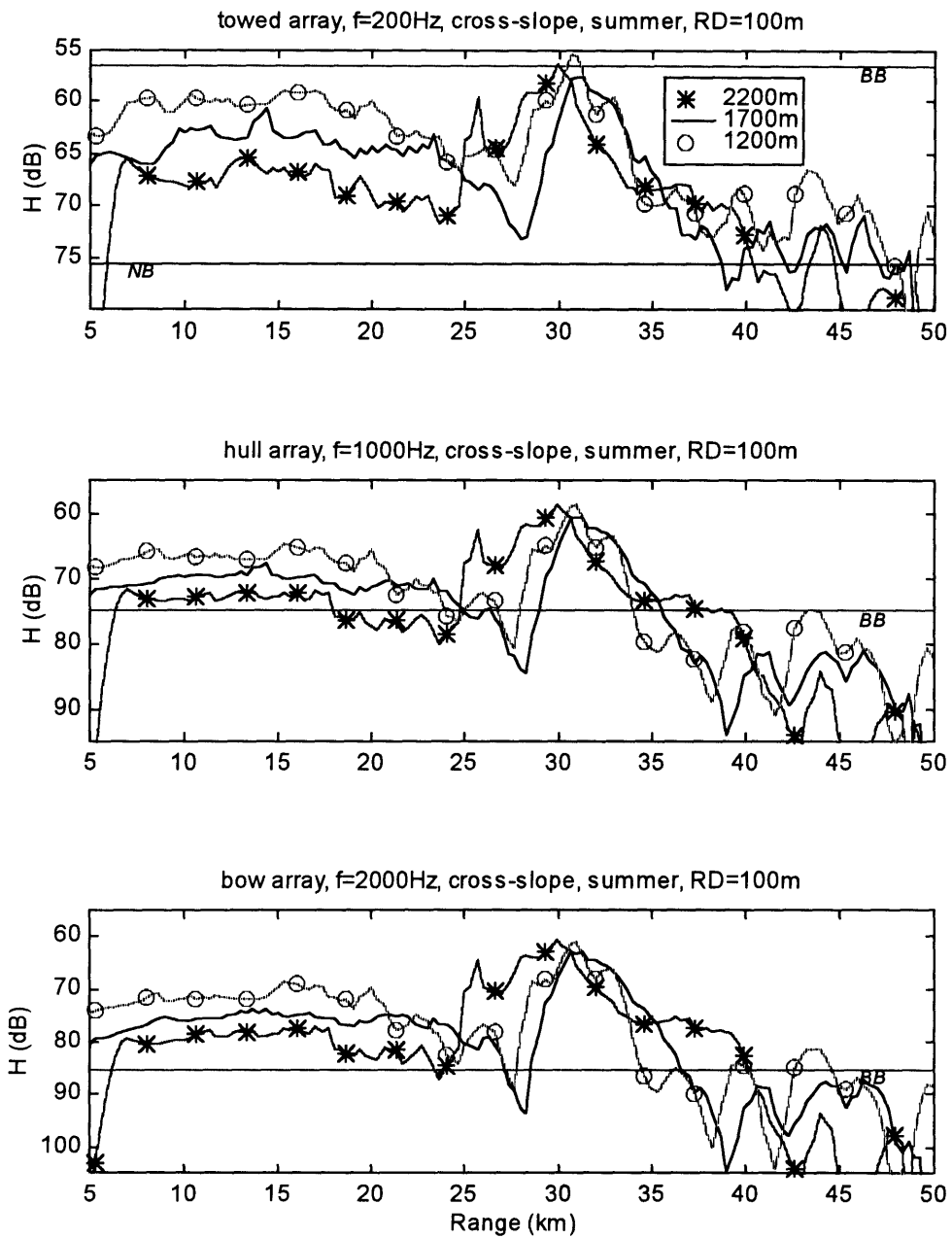
Figure 9.4: The effect of bottom depth on the transmission loss during the summer for the various array types and frequencies. *FOM* is shown for NB and BB when applicable.

9.2 Bottom Slope Effects

Since the bottom slope at the first location shows only minor effects [see the ray diagrams in figures 4.9 and 4.10 and transmission loss results in appendix A] due to its very mild slope (0.1°), the bottom slope effects are presented only for the third location and the second location.

The effects of the bottom slope at the third location on the performance of the sonar systems are shown in Figure 9.5 and in Figure 9.6 for winter and summer respectively. The bottom slopes at the third location are 0.4° up-slope, and -0.4° down-slope. In these figures three plots are shown, one for each array type, each specialized for their typical operating frequency. Each plot includes three different curves that correspond to the up-slope, cross-slope, and down-slope cases.

From Figure 9.5 it looks, in general, that the transmission loss results for the down-slope case are 0dB - 3dB lower than the cross-slope and the up-slope cases except around 27 km where the transmission loss results for the up-slope are larger than the other two. Although the cross-slope case should introduce less bottom loss, there is not much difference when comparing the up and cross-slope results as far as sonar performance is concerned. Two remarks should be said in light of the above results. First, one must remember that the bottom slope changes the spatial distribution of the rays in the medium via reflections from the bottom. In the up-slope case, the rays get more dense with range, a fact that compensates for the higher bottom loss introduced in this case. In the down-slope case, however, the rays become less dense with range, a fact that when combined with the bottom losses, results in a larger transmission loss than the up-slope and the cross-slope cases. The larger transmission loss in the down slope case causes only minor changes in sonar performance when comparing it to the *FOM*.

The results for the summer are shown in Figure 9.6. Due to less surface loss, the analysis yields better performance for the cross-slope case beyond 35 km. Still, the up-slope case results in better performance than the down-slope case.

157

As expected, the differences in transmission loss (and therefore in performance) between the up, cross, and down-slopes increase as the magnitude of the slope increases. Figure 9.7 and Figure 9.8 verify this by showing the analysis results for the second location ($|\beta| = 3°$). It is interesting to note that better performance is expected in the up-slope case in comparison to the other two cases. In addition, the performance in the cross slope case is expected to be better than in the down-slope case. In fact, the differences between the up, cross, and down slope reach more than 10 dB beyond 20 km and are most notable during the summer (see Figure 9.8).
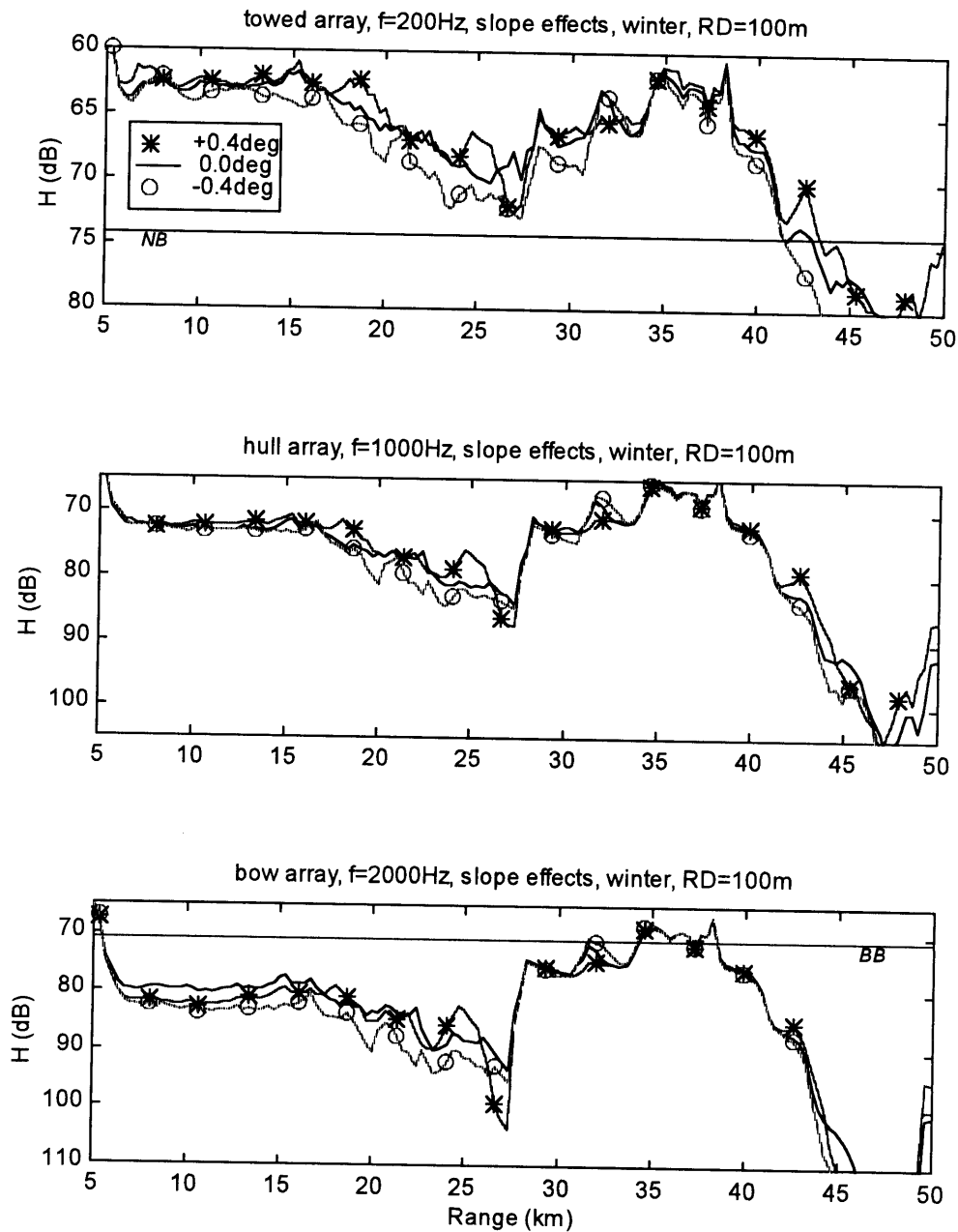
Figure 9.5: The effect of bottom slope (location 3) on the transmission loss during the winter corresponding to the various array types and frequencies. *FOM* is shown for NB and BB when applicable. The *FOM* for the hull array is 61 dB.

towed array, f=200Hz, slope effects, summer, RD=100m

hull array, f=1000Hz, slope effects, summer, RD=100m

bow array, f=2000Hz, slope effects, summer, RD=100m
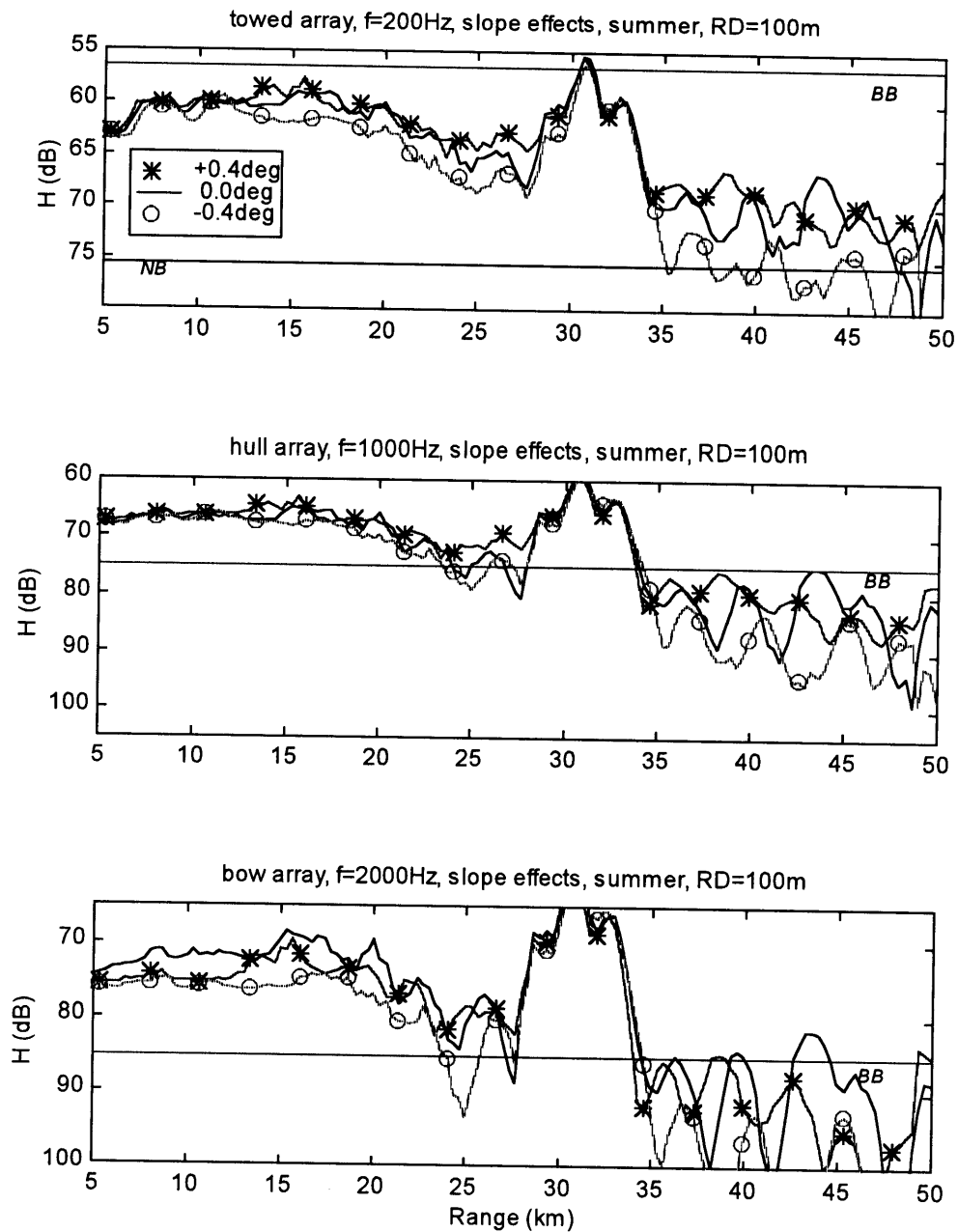
Figure 9.6: The effect of bottom slope (location 3) on the transmission loss during the summer corresponding to the various array types and frequencies. *FOM* is shown for NB and BB when applicable.
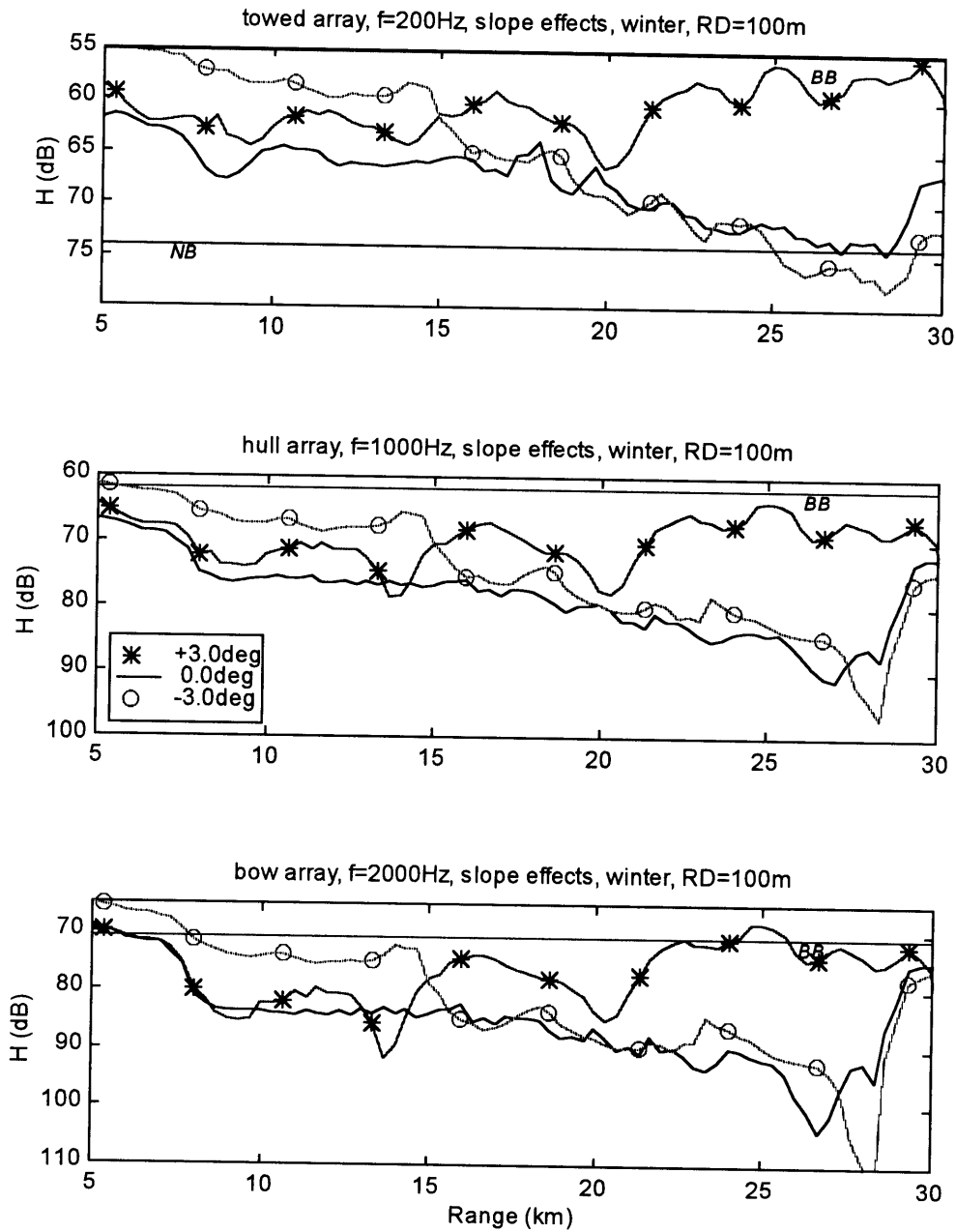
Figure 9.7: The effect of bottom slope (location 2) on the transmission loss during the winter corresponding to the various array types and frequencies. *FOM* is shown for NB and BB when applicable.

161
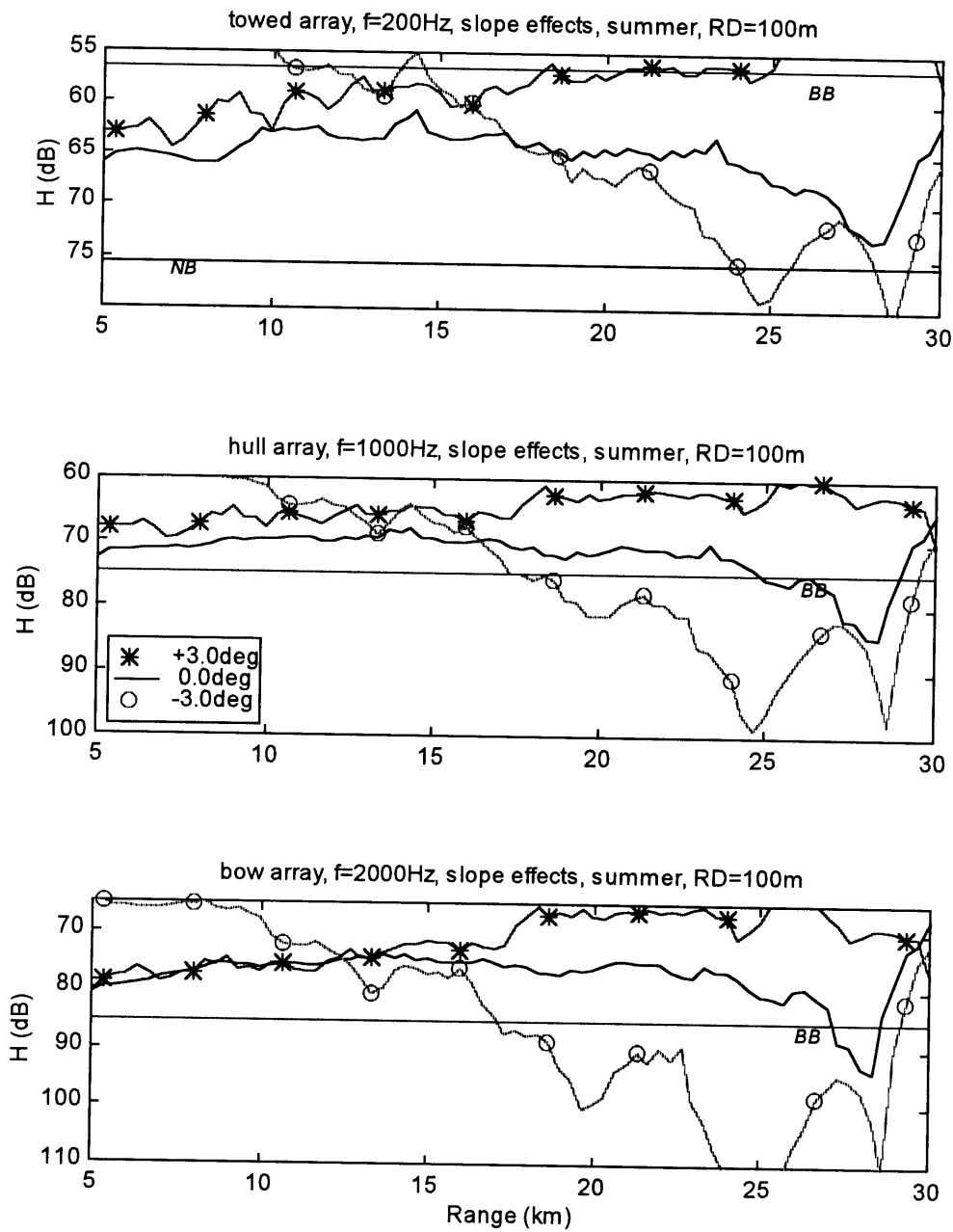
Figure 9.8: The effect of bottom slope (location 2) on the transmission loss during the summer corresponding to the various array types and frequencies. *FOM* is shown for NB and BB when applicable.

9.3 Seasonal Effects

The differences in the expected performance between winter and summer are depicted in Figure 9.9, Figure 9.10, and Figure 9.11 which show, as an example, the cross-slope results from the first location. The season, in this study, has an effect on the transmission loss as well as on the figure-of-merit. Both affect the expected performance of the sonar system substantially. Figure 9.9 shows the expected transmission loss for the various array types, during winter and summer, at 50 m receiver depth.

The range 0 km - 50 km can be divided into five parts. The first is the range 0 km - 12 km, the second is 12 km - 26 km, the third is 26 km - 38 km, the fourth is 38 km - 42 km and the fifth is beyond 42 km. In the first, third, and fifth parts, a lower transmission loss during the winter is observed in comparison to the summer, and at the second, and fourth parts a higher transmission loss is observed during the winter. The differences in the SVP between the winter and the summer and the higher surface loss during the winter are the main reasons for these results. In addition, the seasonal differences in the transmission loss for each array type seem to be a function of range and frequency. In the convergence zone (26 km - 38 km), however, the differences stay relatively constant (0dB - 5dB) for the different arrays when comparing the results for the winter and the summer. In the other parts the differences grow with frequency ranging from 5dB - 10dB for the towed array to more than 20dB for the bow array.

At 100 m receiver depth, the above results still hold except for the ranges 16 km - 32 km where the transmission loss during the summer is lower than during the winter by 5dB - 10dB (see Figure 9.10). This is another effect of the downward refractive gradient of the SVP during the summer and the fact that the sound source is located at the same 100 m depth.

Although the transmission loss during the winter is sometimes lower than during the summer, the performance of the sonar system is better for most cases during the summer. The parameter that affects this conclusion is the figure-of-merit, or *FOM*. In order to see

that the signal excess (*SE*) is plotted for the various array types during the winter and summer in Figure 9.11, for a receiver at 100 m depth. Recall the definition of the signal excess as *SE = FOM - H*, dB as described in chapter 3 (equations 3.10 and 3.11)

At low frequencies, using the towed array, the differences between the summer and winter are relatively low compared to the results for the hull array and the bow array. In the convergence zone region the differences reach 5dB - 10dB for the towed array and more than 20 dB for the hull and bow array. The changes in *FOM* substantially affect the performance analysis but one should remember that the main reason for the differences in *FOM* between the summer and winter is the surface agitation noise which is higher for the winter than for summer (in this study). If the surface agitation noise would have been higher in the summer (which is sometimes true) the results would have been the opposite.
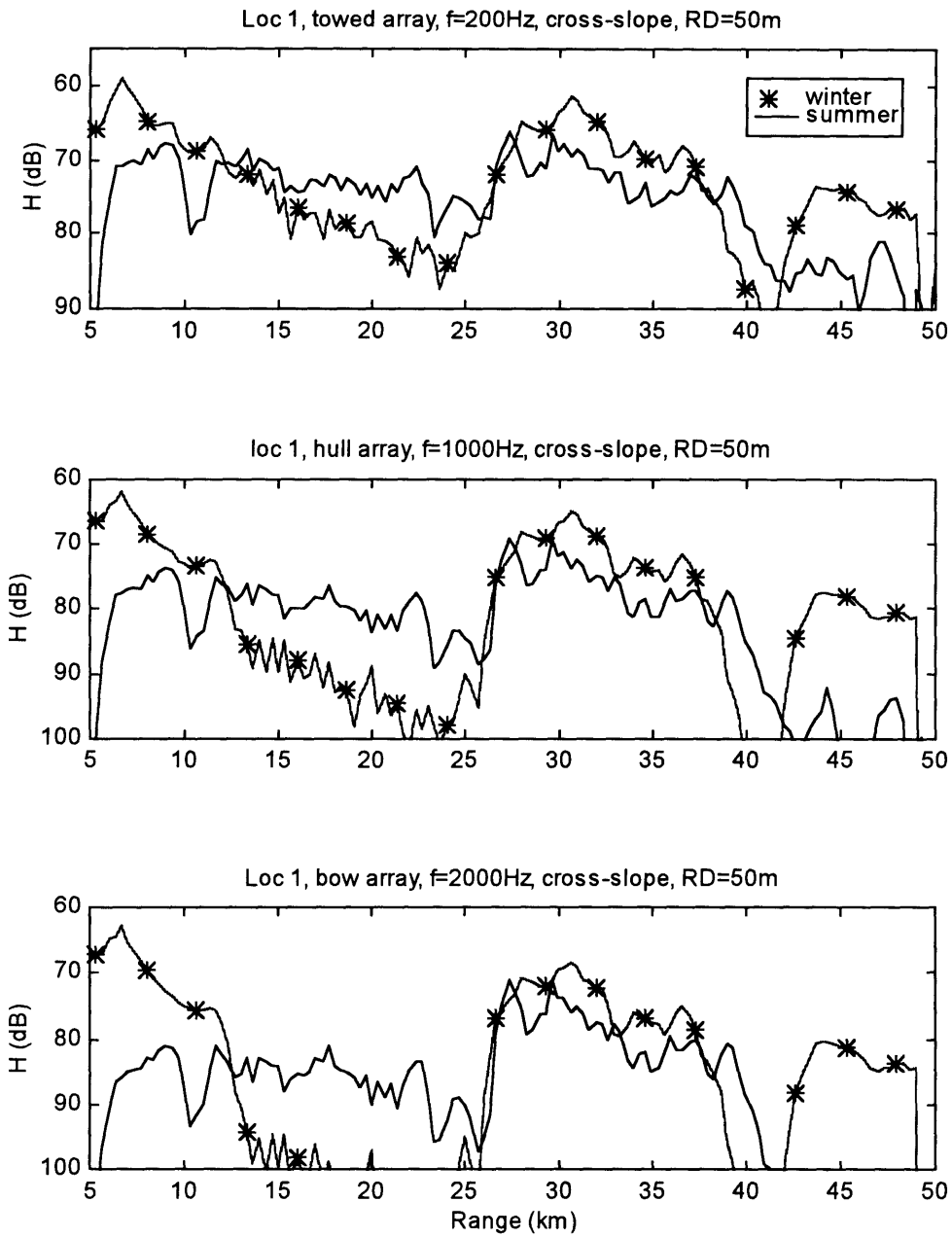
Figure 9.9: The seasonal effect on the transmission loss at 50 m depth corresponding to the various array types. Data taken from the first location, cross-slope case.
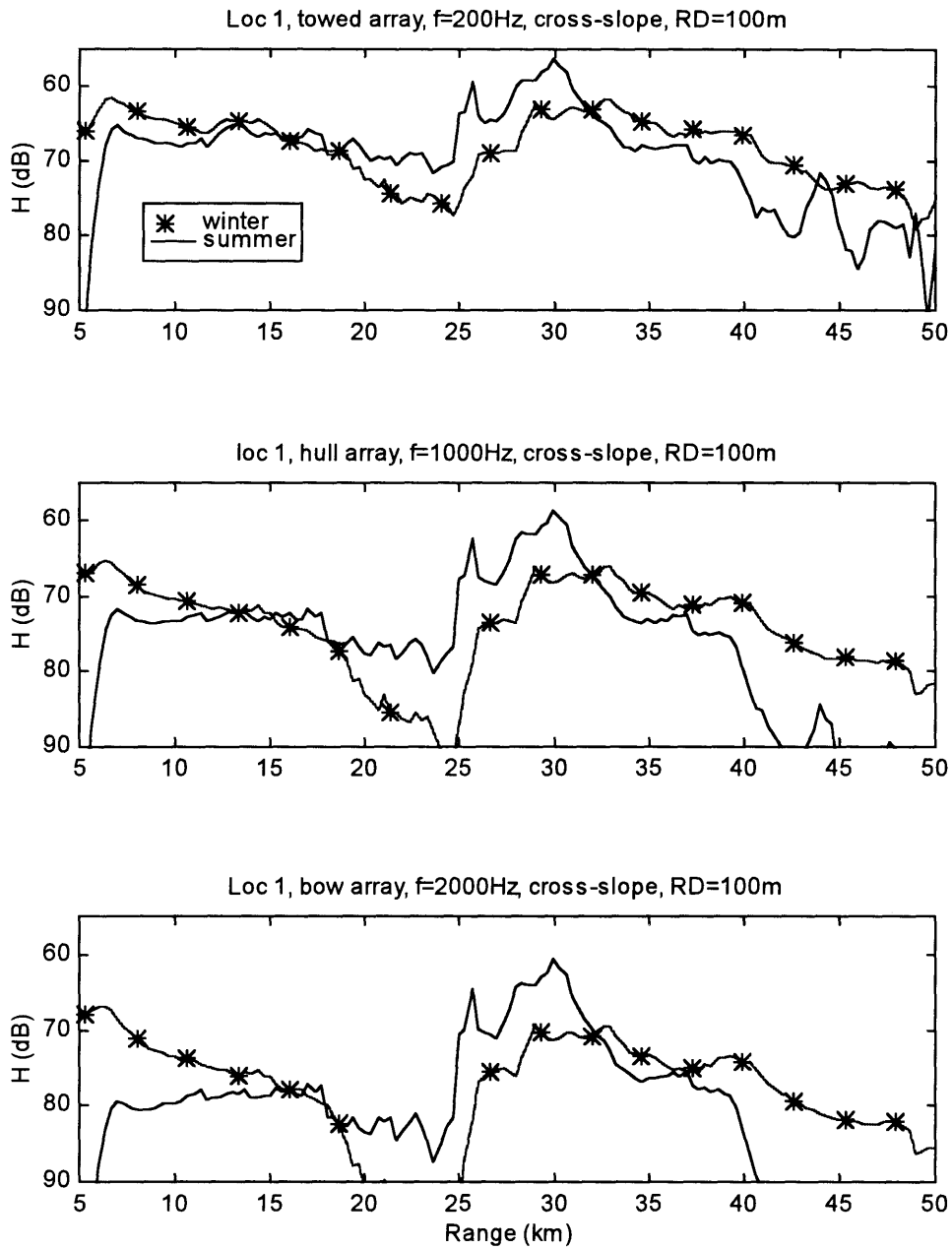
Figure 9.10: The seasonal effect on the transmission loss at 100 m depth corresponding to the various array types. Data taken from the first location, cross-slope case.

Loc 1, towed array, f=200Hz, cross-slope, RD=100m

loc 1, hull array, f=1000Hz, cross-slope, RD=100m

Loc 1, bow array, f=2000Hz, cross-slope, RD=100m
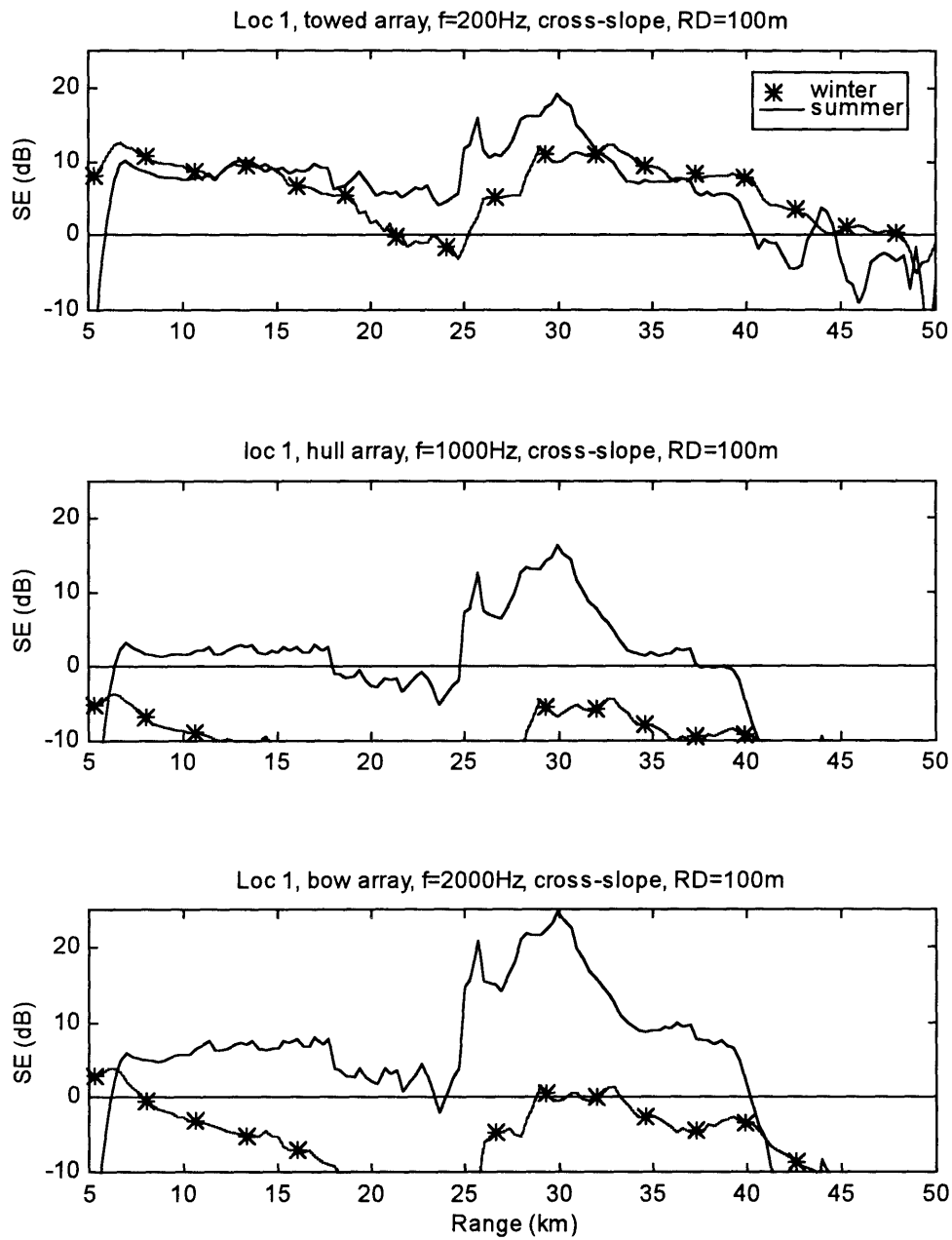
Figure 9.11: The seasonal effect on the *signal excess* at 100 m depth for the various array types. Data taken from the first location, cross-slope case.

9.4 Receiver Depth Effects

It is important for the sonar operator to know which depth is best to detect the sound source. Unfortunately, the case that is being investigated here is limited to a single target at 100 m depth, and therefore general conclusions on the best operating depth cannot be drawn directly from the results shown here. Some understanding of the receiver depth effect, however, can be achieved from Figure 9.12 and Figure 9.13. In Figure 9.12, the transmission loss during the winter (cross-slope case, first location) is plotted as a function of depth at three ranges 15 km, 30 km, and 45 km.

The first range corresponds to about 1/2 the convergence zone range, the second to the convergence zone range, and the last to about 3/2 the convergence zone range. The results obtained for the various array types are that at the convergence zone the array performs equally well at depths 50 m - 150 m. In contrast, at 15 km, and 45 km there is a notable advantage for a receiver located below the 50 m depth with a peak near 100 m.

During the summer, it is clear that even at $R = 30$ km (around the convergence zone range) the receiver performs better if it placed at 100 m than 50 m (see Figure 9.13). In fact, it is also shown that at the same range the receiver performs equally well at 200 m depth. At 15 km, and 45 km range the signal is best received below 150 m.

The differences in the best operating depth is closely related to the SVP measured during the various seasons. With a source at 100 m depth, and a summer SVP the receiver should definitely be put at the 100 m depth. During the winter, however, good operating depth can range between 50 m - 150 m in the vicinity of the convergence zone, but at 15 km, and 45 km the receiver should be put at 100 m as well.
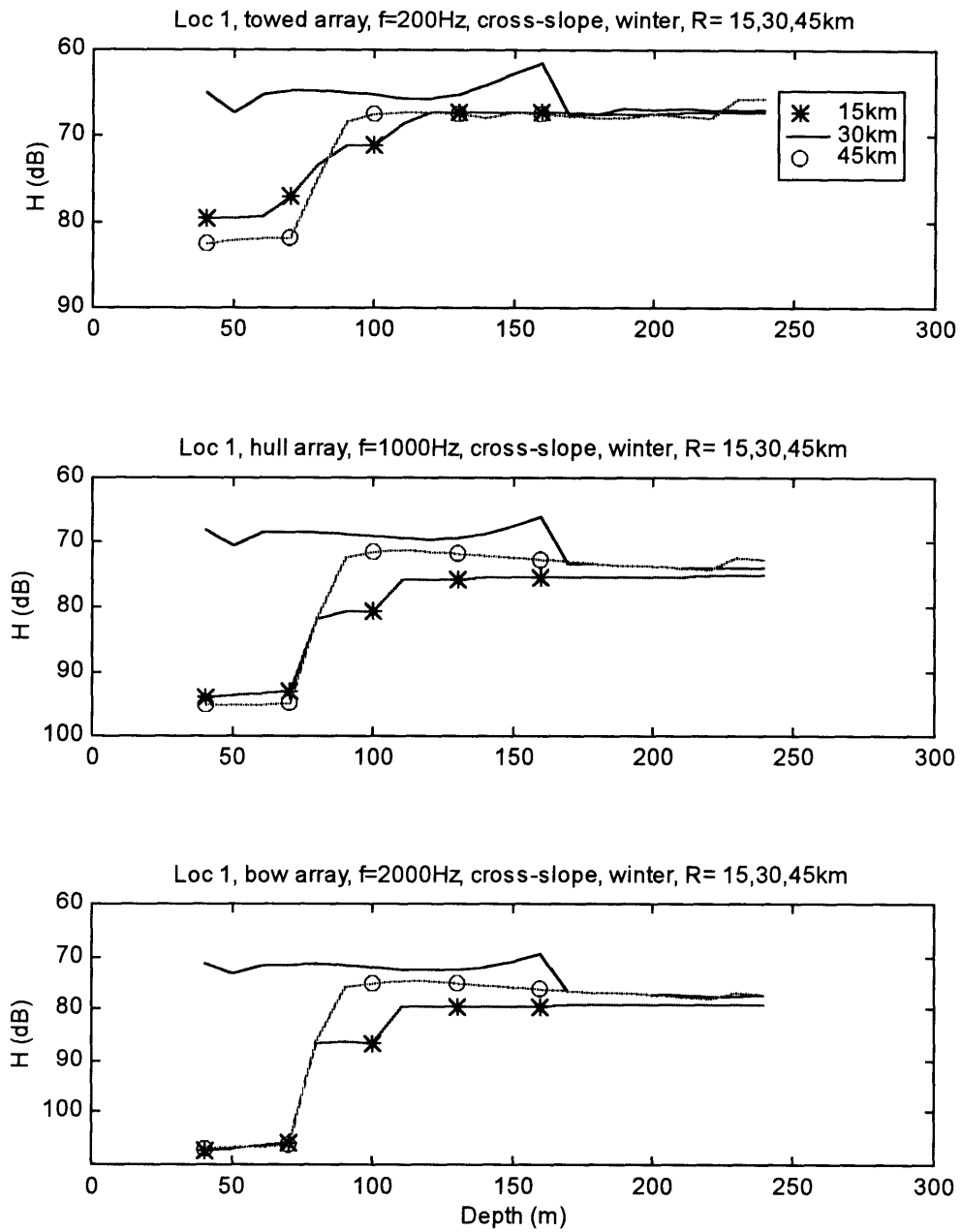
Figure 9.12: Receiver depth effect on the transmission loss at ranges 15, 30, 45 km from the source for the various array types. Data taken from the first location, cross-slope case during the winter.
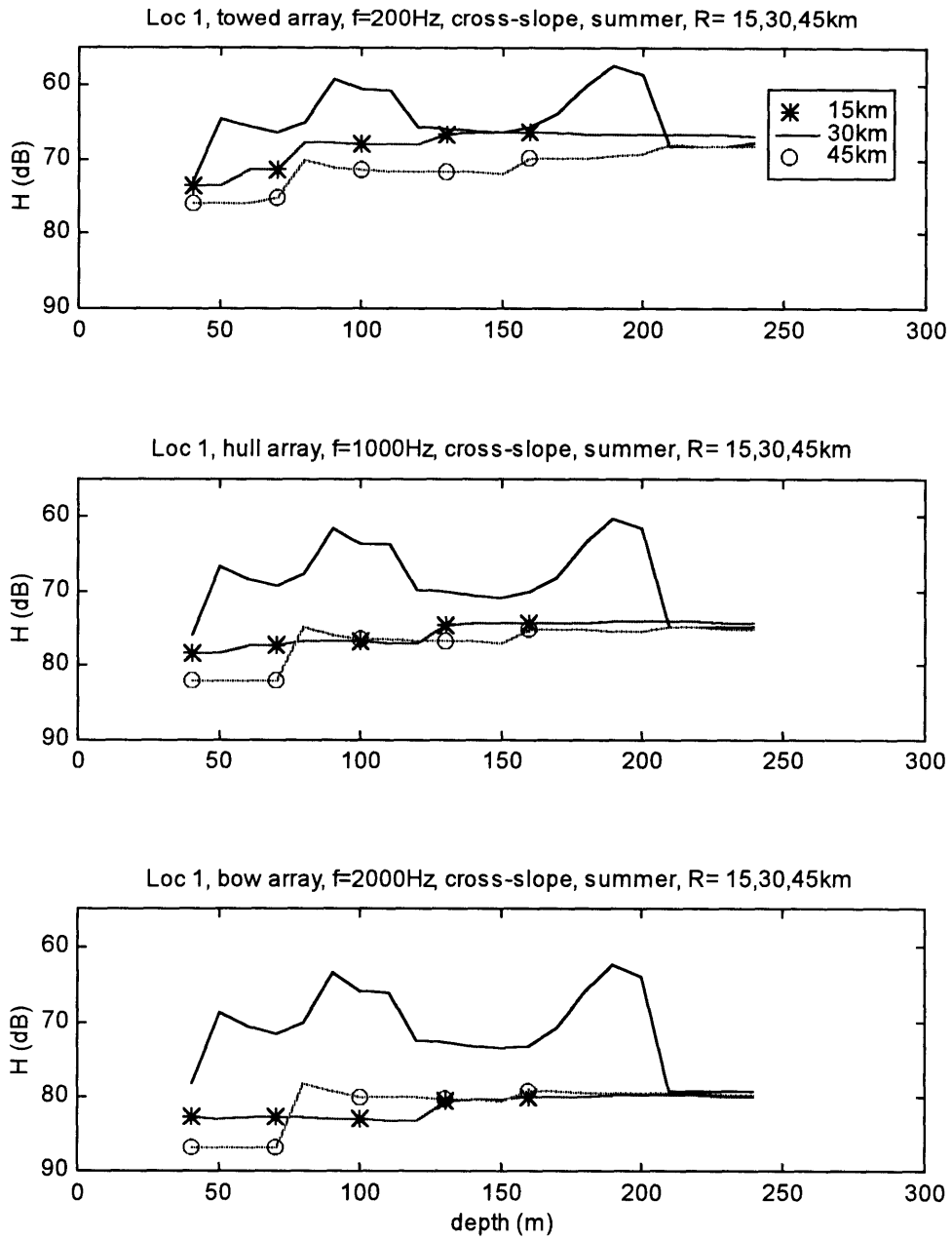
Figure 9.13: Receiver depth effect on the transmission loss at ranges 15, 30, 45 km from the source for the various array types. Data taken from the first location, cross-slope case during the summer.

9.5 Array Effects

This section provides the reader with the main differences in sonar performance for the different array types. In order to compare the performance of the different arrays the signal excess (*SE*) is plotted for NB and BB and for the different arrays.

Figure 9.14 and Figure 9.15 show the expected sonar performance for the cross-slope case during the winter and for the summer respectively. The data is taken from the first location while similar results can also be observed at the other locations [Appendix A]. Each figure includes two plots. The upper plot corresponds to the NB performance and it shows the results for the towed array (for 100 Hz, 200 Hz) and the for the hull array (500 Hz). The lower plot corresponds to the BB performance and it shows the results for the hull array (1000 Hz, 1500 Hz) and for the bow array (3 kHz, 5kHz).

Figure 9.16 and Figure 9.17 show the results for the up-slope during the winter and summer respectively using the same format as in Figure 9.14 and Figure 9.15. The data in this case is taken from the third location as an example.

Figure 9.18 and Figure 9.19 show the performance results for the down-slope case during the winter and the summer, respectively, using the same format. The data here is taken from the second location, acknowledging that similar results can be observed at other locations with a down-slope bottom.

From Figure 9.14 the towed array can be seen to have almost similar detection ranges for NB processing during the winter. Also, one can observe that the hull array has a slightly higher SE than the towed array. In addition, Figure 9.14 also shows that the bow array has a higher SE than the hull array for BB processing during the winter.

During the summer the SE for the hull array is about 10dB higher than the towed array. However, the detection ranges for NB processing are still relatively the same for both arrays (see Figure 9.15). The bow has SE higher than the hull array, except at 5 kHz where the bow array may lose the target at ranges 5 km -25 km.

From Figure 9.16, during the winter with an up-slope bottom the towed array has a higher SE than the hull array for NB processing. Similarly, the bow array performs better than the hull array for BB processing, except between 5 km - 17 km. In fact, the bow array can aquire the BB signal around the convergence zone, where the hull array cannot.

The differences in SE between the arrays for the up-slope case during the summer are essentially the same as the differences for the cross-slope case during the winter (see Figure 9.17). This is expected because the arrays operate under the same environment (summer or winter) and it proves the consistency of the results. It does not mean the same detection ranges but only the same SE proportionality of the arrays.

The results for the winter and summer for the down-slope have the same behavior as in the up and cross-slope cases (see Figure 9.18 and Figure 9.19).

This shows that *to first order* the bottom slope does not change the relative performance behavior of the arrays. This means, in simple terms, that if an array has a higher SE than another array for the same scenario, it would probably remain the same for other bottom slopes. The season, however, does change the relative behavior of the arrays to some extent. This is due of course to the differences in the refraction structure, and the differences in the wave height, between the summer and the winter.

In addition, the results also show that to first order the bow array is better than the hull array for BB detection. On the other hand, the towed array and the hull array are expected to have a relatively similar performance for NB processing. Although this is the case, NB components are likely to be found at low frequencies (less than 500 Hz), and therefore, the towed array is more appropriate for NB detection.

In summary, the properties of the hull array seems to be a mix of the properties of the towed line array and bow array. Its frequency limits enable it to detect NB and BB signals but not as well as the towed array for low frequency NB components and not as well as the bow array for BB signal.
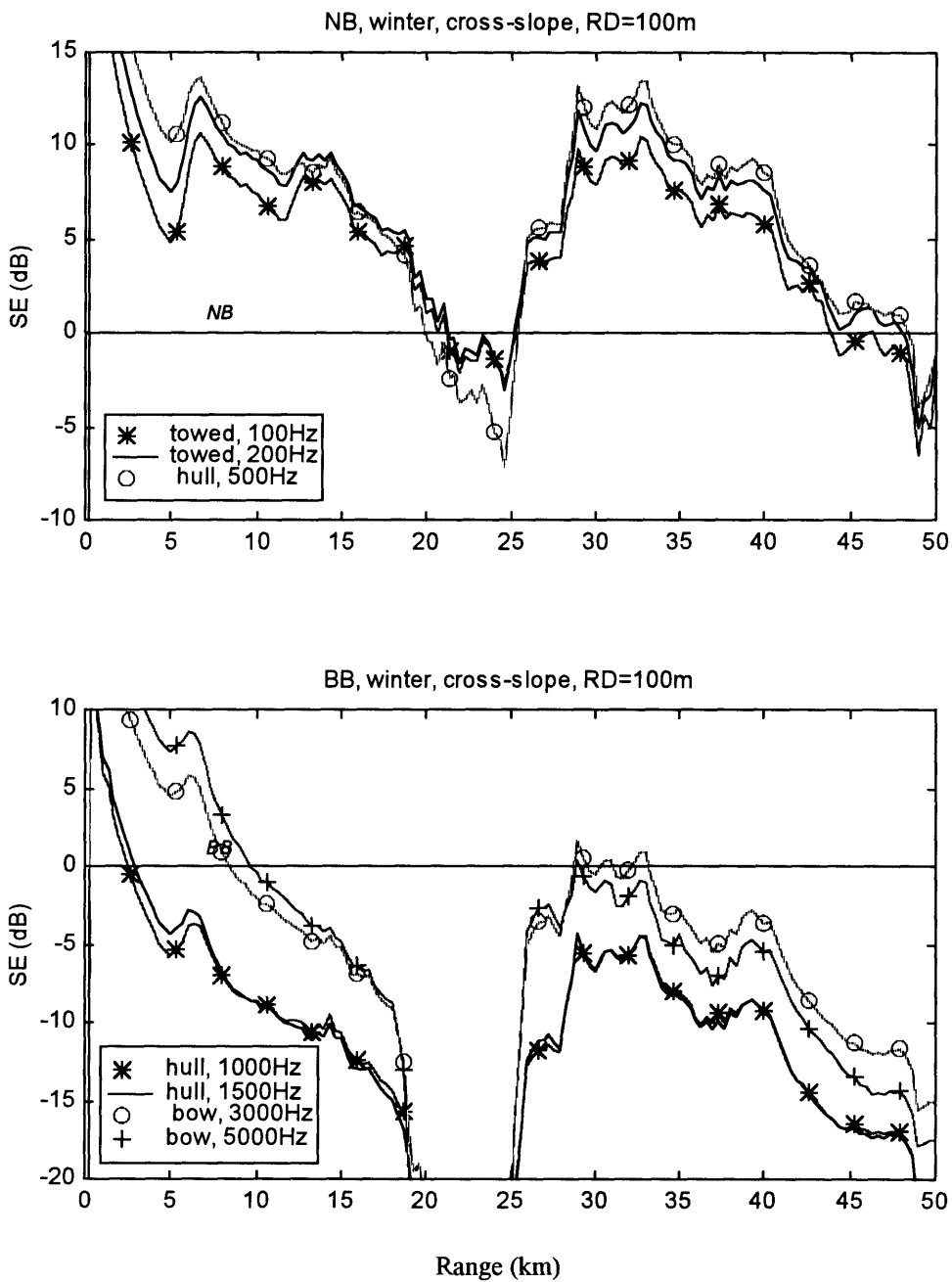
Figure 9.14: The array effect on the performance of the sonar system for the first location, cross-slope case, during the winter. NB performance (upper), BB performance (lower).
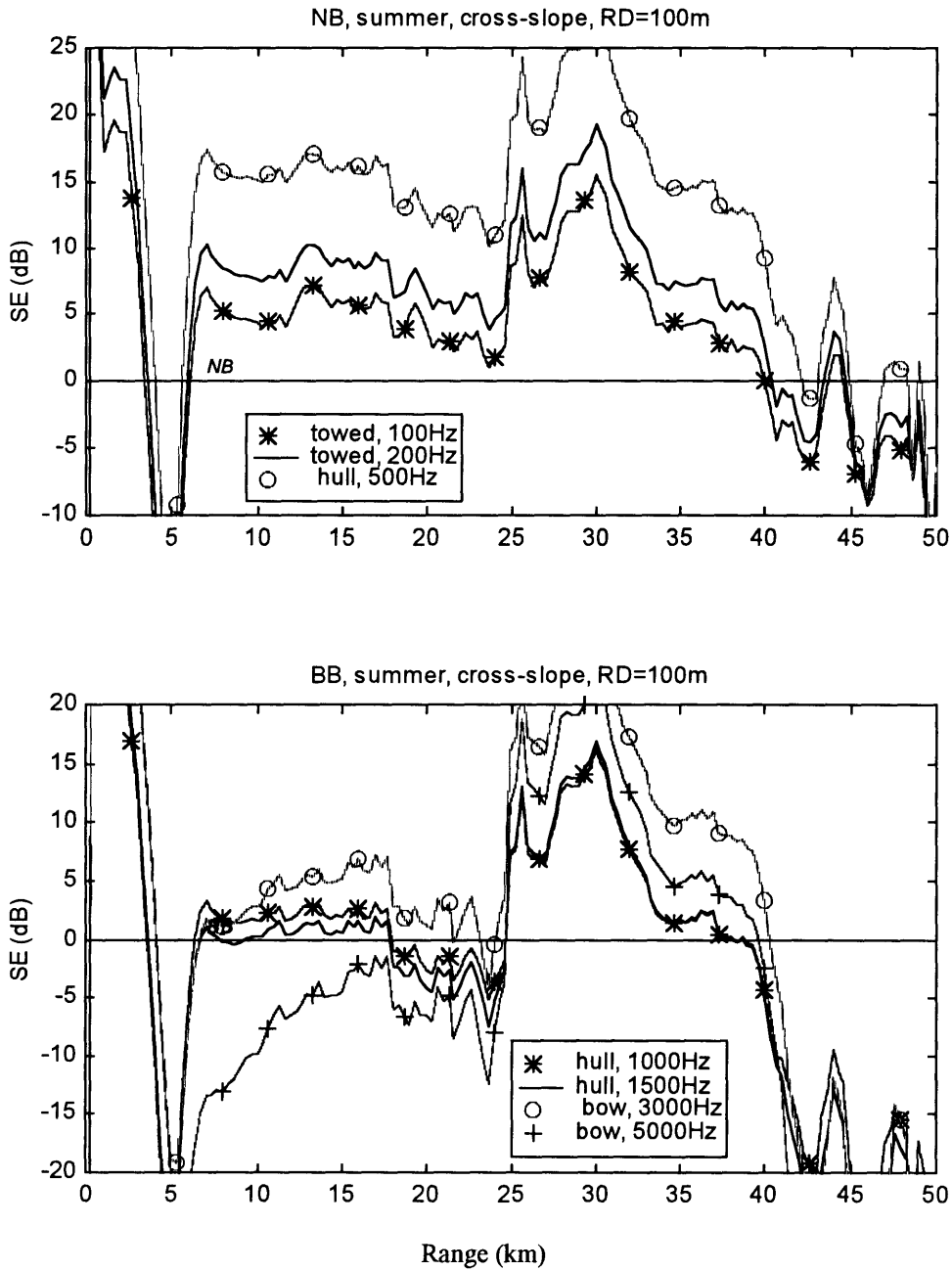
Figure 9.15: The array effect on the performance of the sonar system for the first location, cross-slope case, during the summer. NB performance (upper), BB performance (lower).
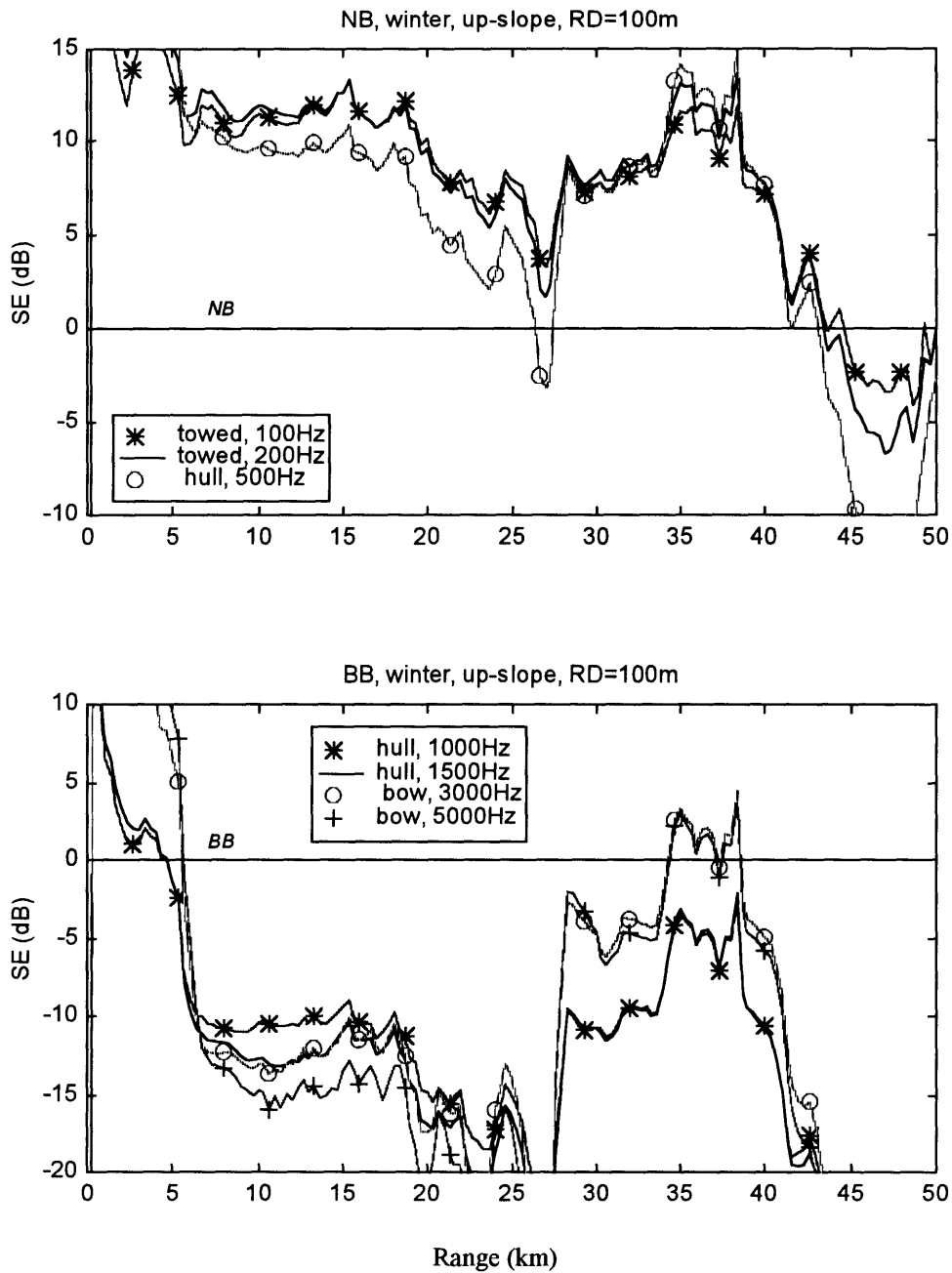
Figure 9.16: The array effect on the performance of the sonar system for the third location, up-slope case, during the winter. NB performance (upper), BB performance (lower).
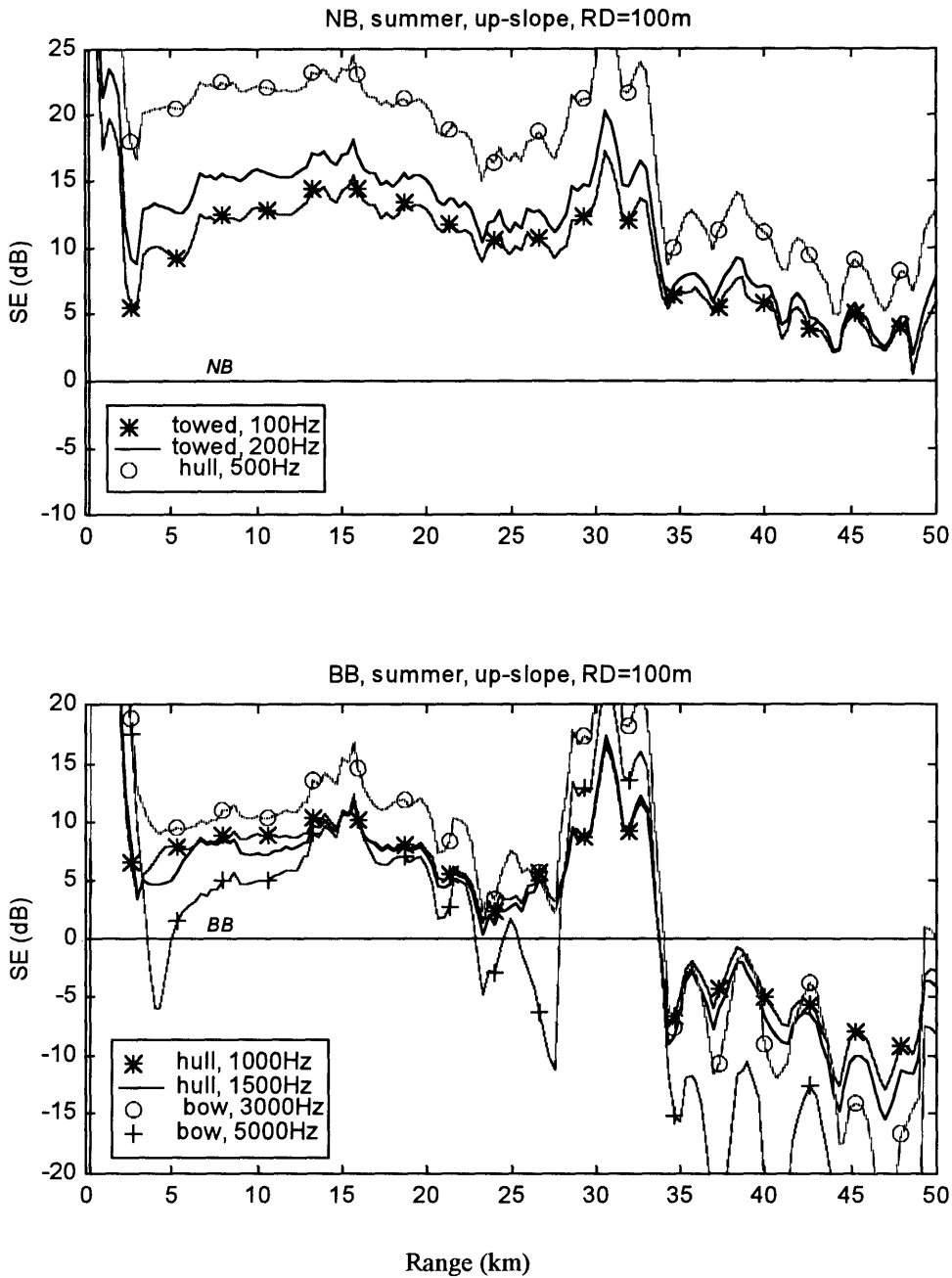
Figure 9.17: The array effect on the performance of the sonar system for the third location, up-slope case, during the summer. NB performance (upper), BB performance (lower).
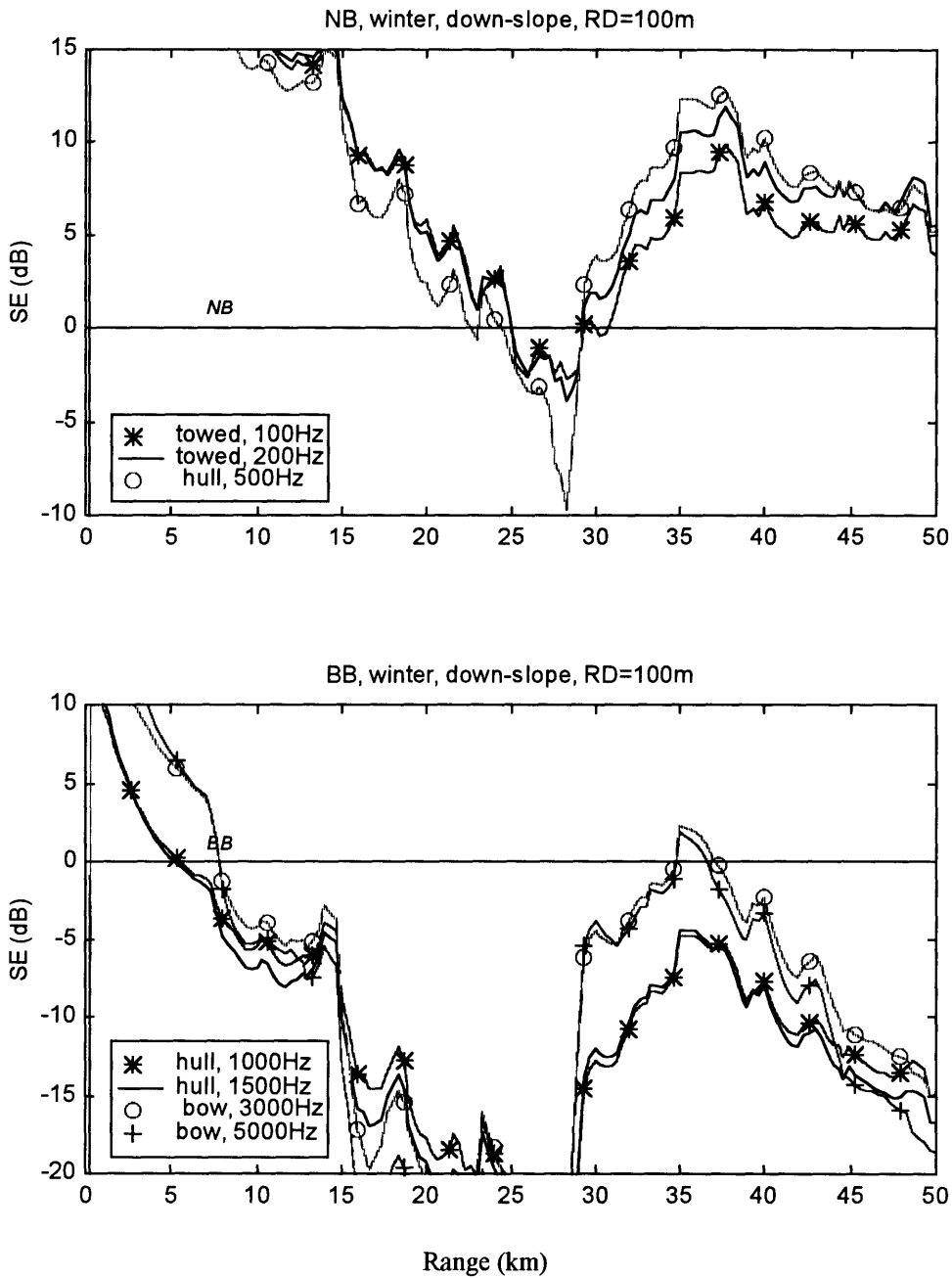
Figure 9.18: The array effect on the performance of the sonar system for the second location, down-slope case, during the winter. NB performance (upper), BB performance (lower).
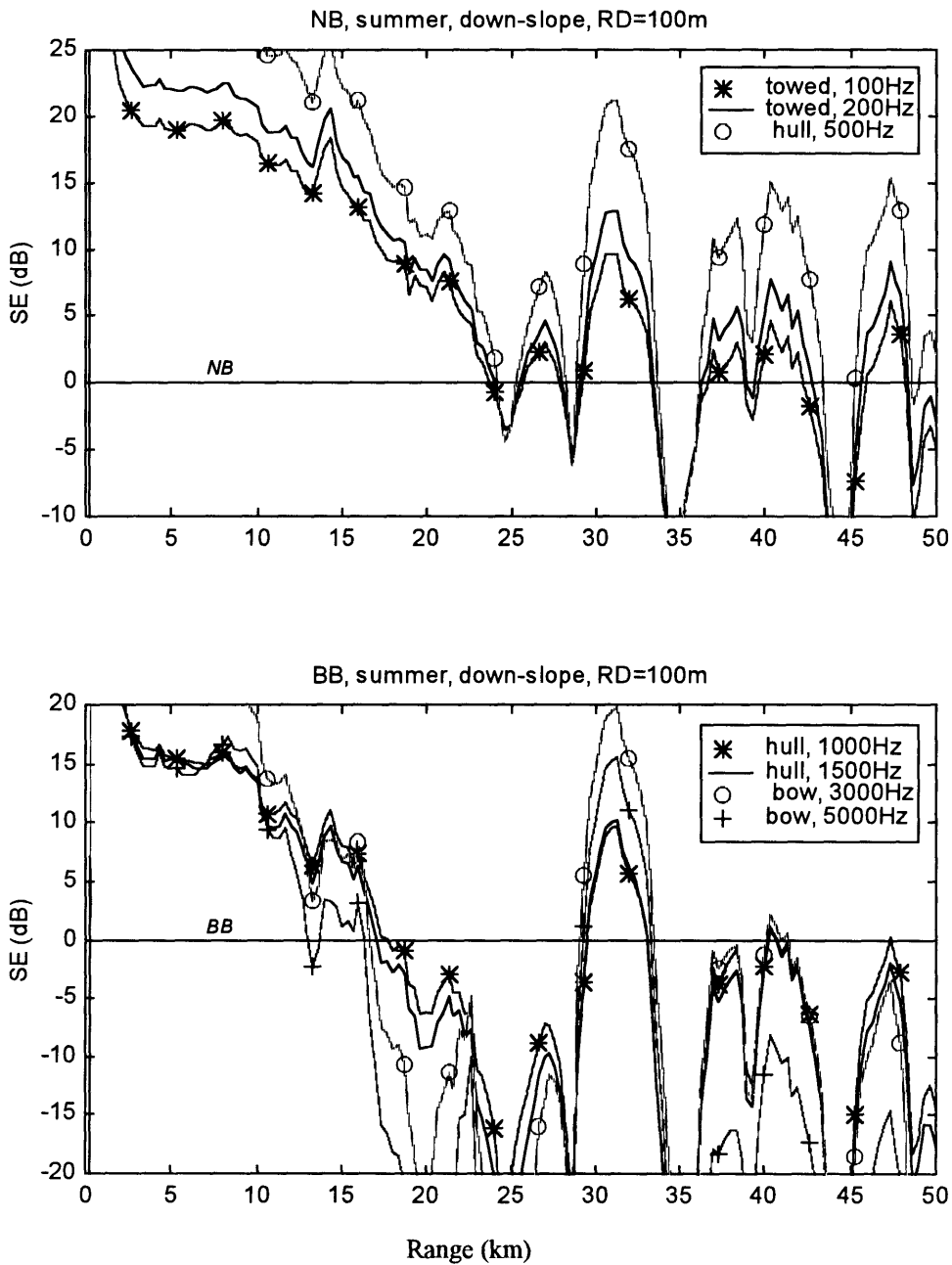
Figure 9.19: The array effect on the performance of the sonar system for the second location, down-slope case, during the summer. NB performance (upper), BB performance (lower).

9.6 Conclusions

Each one of the parameters in the parameter space, which was reviewed in the preceding sections, affects the performance of the sonar system. This section concludes the main results which were observed in Figure 9.1 - Figure 9.19. The results are definitely not general, and are applicable only to the particular array designs and the definitions of the environment made in this study.

- Each type of array operates in a different frequency band. Specifically, the towed array operates in low the frequency band (50 Hz - 750 Hz), the hull array operates in the mid frequency band (500 Hz - 1500 Hz), and the bow array operates in the upper frequency band (2 kHz - 5 kHz). The frequency bands of the various types of array are a direct consequence of their dimensions.

- Changes in the SVP structure during each season for the different locations seems to be only minor. This is a conclusion that is probably applicable in Mediterraneans and not in open oceans. However, there is a major difference in the SVP gradient between winter and summer especially in the upper water column (0 - 200 m). During the summer a downward refractive gradient dominates the upper water column while during the winter the sound speed at the upper water column is relatively constant giving rise to RSR propagation.

- Although is not shown in its full strength in the results, two main types of propagation exist in each location. Namely, the RSR and the bottom-bounce propagation. When RSR propagation dominates the sonar performance are expected to be higher than when bottom-bounce propagation dominates. Integration times should be chosen appropriately. The portions of range at which RSR or bottom-bounce transmission dominates depends on the bottom depth and slope. Bottom-bounce propagation is most probable to dominate at steep up-slope cases and shallower locations while RSR propagation is most probable to dominate at cross and down-slope cases and deeper locations.

- The bottom depth affects the angular spectrum of rays that can be channeled without hitting the bottom and therefore its effect is most notable at large ranges. At deeper locations a lower transmission loss is obtained at large ranges (beyond 40 km) in comparison to shallower locations. However, at shallower locations, a lower transmission loss is expected at closer ranges (up to 30 km). (A lower transmission loss can be translated to a better performance if the FOM stays the same.) In addition, at deeper locations the convergence zone is expected to be wider than at shallower locations.

- The bottom slope has a substantial effect on the performance of the sonar system. The effect's magnitude is a function of the bottom slope's magnitude. in locations with bottom slopes less than 0.1°, only negligible effects can be observed. In locations with somewhat larger slopes, better sonar performance is obtained in the cross-slope and up-slope cases, relative to the down-slope case. In locations with steep slopes the up-slope direction results in a better performance than for both cross and down-slope cases. The effect is mostly notable beyond 15 km for the steep slopes and beyond 35 km for the milder slopes. Again, it should be emphasized that the analysis was carried out using a single integration time suitable for bottom-bounce propagation. An adaptive integration time could have resulted better performance for the cross and down slope cases where RSR propagation dominates. This is, of course, a subject for a separate analysis.

- The season also plays a role in determining the performance of the sonar system. The season controls the SVP structure and the surface noise. The results in this study show that, in general, better performance is obtained during the summer than during the winter. It is important to note that the above conclusion should be treated with care since the definition of the summer and winter in this study might not reflect reality at all times. In practice, there are times during the summer that the performance of the sonar system is worse than during the winter.

- The receiver depth also affects the sonar performance. The results in this study are applicable only to a source placed at 100 m depth. For the case being investigated here,

the receiver should be placed at depths between 100 m - 150 m for best detection. Receivers that are placed at shallower depths would result in smaller probability of detection, especially during the summer.

- It is shown in this chapter that to first order the relative behavior of the arrays *with respect to one another* does not depend on the bottom slope.

- In general it is also can be observed from the results that the bow array works best for BB signals and the towed array is most suitable for NB signals. The hull mounted array is not long enough to receive low frequency NB signals with good azimuthal resolution, and to reject noise at low frequencies, as does the towed array. As far as BB detection is concerned, the bow array (a spherical shell in this case) has higher SE and better detection ranges than the hull array.

Appendix A

Performance Analysis Results

This appendix presents all the analysis results and is divided into two major parts. The first part describes the results based on the ray trace diagrams (Figures 4.9 - 4.22) and on the performance figures (A.1 - A.144), which presents the transmission loss overlying the figure-of merit of the particular sonars that were considered in this study. The second part presents the performance figures which are divided into three major parts. The first part presents the results of the first location (Figures A.1 - A.36), the second part presents the results of the second location (Figures A.37 - A.90), and the third part presents the results of the third location (Figures A.91 - A.144).

The performance results present the transmission loss at 50 m, 100 m, and 150 m depths for up-slope, cross-slope, and down-slope cases (except for the first location where only the up and cross-slope cases are shown), and for winter and summer conditions as described in chapter 2. The 50 m depth is marked with 'o', the 100 m depth is solid line, and the 150 m is marked with 'x'. In addition, the figure-of-merit is presented as a horizontal line marked underneath with 'NB' for narrowband, and 'BB' for broadband.

For each case, several frequencies were considered to reflect the effect of the operating frequency on the performance of the corresponding sonar system. Total of nine frequencies are considered. 100, 200, 500 Hz for the towed array, 500, 1000, 1500 Hz for the hull mounted array, and 2000, 3000, and 5000 Hz for the bow array.

The description of each figure is above it, and it follows the descriptive sequence: Location # {1,2,3}, Slope {up, cross, down-slope}, Season {winter, summer}, Array-type {towed array, hull mounted array, bow array}, and Frequency.

The frequencies were chosen such that the first frequency corresponds to the lower frequency limit of the sonar, the second within the operating frequency band, and the third was chosen to be close to the upper frequency band. The performance of the sonar system can be analyzed by comparing the figure of merit to the transmission loss. Whenever the transmission loss is lower than the figure of merit, one can call it 'a detection', and vice versa, when the figure of merit is lower one can call it 'no detection.'

In addition to the description of the results which are given subsequently, the reader is referred to the discussion in chapter 9 for a comparative look on the results.

A.1   First Location

The first location represent the trivial case where the bottom slope is very small ($\beta = 0.1°$) so that it can practically be ignored. In fact, the results for the up-slope, cross-slope ($\beta = 0°$), and the down-slope ($\beta = -0.1°$) resemble each other very much. However, some differences can be observed between the up/down-slope and the cross-slope cases which is the reason why only the up-slope and cross-slope results are presented in Figures A.1 - A.36. The performance results are presented for the winter and summer respectively.

A.1.1   Winter Conditions

The ray trace diagram for the first location, up-slope case, during the winter season is depicted in Figure 4.9 where rays that hit the bottom were excluded. The mostly upper refractive structure of the SVP during the winter causes the rays to bend upwards and to form a convergence zone at ranges 27 - 37 km. The convergence zone is clearly seen in the

transmission loss results as shown in figures A.1 through A.18 that correspond to the first location during the winter.

Figures A.1 through A.3 show good performance of the towed array for NB processing. For *FOM* of 72 dB at f = 100 Hz (see Figure A.2), detections occur at the first 15 km and between 27 - 37 km when the receiver depth is 50 m. When the receiver depth is 100 m, detections occur in ranges 0 - 22 km and 25 - 44 km, and when the receiver depth is 150 m, detections occur almost continuously up to 45 km. For f = 200 Hz, the transmission loss is about 2 dB higher but since the *FOM* is also 2 dB higher the detection ranges are about the same as in the previous case. For f = 500 Hz the *FOM* is 74 dB but the transmission loss is 3 - 5 dB higher causing the detection ranges for the various depths to be 0 - 12 km and 27 - 37 km for the 50 m depth, 0 - 19 km and 26 - 43 km for the 100 m depth, and 0 - 23 km and 25 - 43 km for the 150 m receiver depth. The BB performance, however, is relatively poor and detection occurs only in the first 2 - 4 km.

Figures A.4 through A.6 show the performance of the hull mounted array. The *FOM* at 500 Hz is 3 dB higher for NB than the towed array. That results, for relatively equal transmission loss, a slightly better performance for NB (in the order of 1 - 2 km increase in detection ranges). The detection ranges for BB are also slightly better (in the order of 1 km). For 1000 Hz and 1500 Hz, the performance analysis is done only for the BB portion due to lack of NB components in this frequency regime (in our case). Detection occurs at the first 5 km for the BB signal.

Figures A.7 through A.9 show the results for the bow array for 2 kHz, 3 kHz, and 5 kHz respectively. For the first two frequencies, BB detections occur in ranges 0 - 7 km and also in the vicinity of 30 km. The detection in the 30 km range is due to the convergence zone formed at this range. At 5 kHz BB detection occurs at ranges 0 - 9 km only. Thus the bow array is slightly better than the hull mounted array as far as detection ranges of BB signal is concerned.

It should be noted that, as the frequency increases, the transmission loss increases due to the volumetric absorption, and due to bottom and surface losses. The effect of the

last two can be clearly seen between the ranges 10 - 25 km that correspond to bottom bounce transmission loss. At the lower frequencies, this regime has a lower transmission loss because of lower bottom and surface losses.

In addition, since the convergence zone reaches the surface, the receivers at the various depths receive the signal equally well in the vicinity of the convergence zone.

The cross-slope case for the first location, during the winter is shown in figures A.10 through A.18. As stated earlier, the results for the cross-slope case resembles very much the results for the up-slope case, and the detection ranges stay almost the same for all cases. It makes sense due to the mild slope of the first location. One can observe, however, that the transmission loss for this case is slightly lower than the up-slope case, in the order of 1dB difference. Although, not significant, it is mentioned here to show the effect of the direction of propagation for mild slopes. It verifies, as expected from chapter 4, that the cross-slope case provides relatively lower bottom loss.

A.1.2 Summer Conditions

The ray trace diagram for the first location, up-slope case, during the summer season is depicted in Figure 4.10 where rays that hit the bottom were excluded. One should note the down refractive gradient of the SVP near the surface, causing a large number of rays to bend downward just below the surface. This causes a significant difference between the performance of the receivers at various depths and between the results obtained during the winter. The convergence zone, does not reach the surface entirely, and therefore is most notable for receivers located deeper 50 m, and in ranges 27 - 37 km.

The performance results for this case are shown in figures A.19 through A.27. In general, the results show about 5 - 10 dB difference in the transmission loss between the 50 m receiver depth and the 100 m receiver depth, for all frequencies (as expected). The lower transmission loss at depths deeper than 50 m is a direct result of the SVP structure in the

summer. The performance of the sonar systems during the summer is also affected by a lower surface loss and an equal or higher array gain due to a lower surface noise.

Figures A.19 through A.21 show good performance of the towed array for NB processing except when the receiver depth is 50 m and f = 100 Hz. For *FOM* of 72 dB at f = 100 Hz, detection occurs in the first 2 km and then the transmission loss fluctuates ($\pm$ 6 dB) around the *FOM* between the ranges 6 - 39 km when the receiver depth is 50 m. When the receiver depth is 100 m, detection occurs at ranges 0 - 3 km and 6 - 40 km, and when the receiver depth is 150 m, detection occurs at ranges 0 - 4 km and then continuously from 6 km to 40 km. For f = 200 Hz, the transmission loss is about 2 - 3 dB higher but since the *FOM* is 3.5 dB higher the detection ranges are even better than the previous case when the receiver depth is 50 m. At f = 500 Hz, the *FOM* for NB reaches 82 dB enabling detection in the first few km, and between 6 - 40 km for all receiver depths except for the 50 m depth where no detection occurs in the vicinity of 24 km and 26 km. The BB performance is relatively poor. The *FOM* for BB is about 63 dB enabling detection of the BB signal only for the 100 m depth receiver between 27 - 33 km, in addition to the first 2 - 3 km where detections occur for all receivers.

Before proceeding, one must note that the abrupt pressure level trough at 5 km range is due to the fact that neither direct rays nor reflected rays reach that range for depths shallower than 150 m. This is because of the chosen angular space allowing the first bottom bounced ray to reach the surface at 6 km range. Thus, one can expect a rather smoothed version of the trough to take place in reality, where the gap at the 5 km range will be filled with pressure levels close to the values found at 6 km. However, a fall-off of the pressure level around the 5 km range may occur as can be seen for the higher frequencies. This suggests that at relatively close ranges (5 - 10 km) poor performance are expected in the summer when it is compared to the winter. Subsequently, the trough is treated appropriately.

The hull mounted array at 500 Hz has 3 dB higher *FOM* (NB) than the towed array enabling a detection up to 40 km even for the 50 m receiver if one ignores the trough at 5

km range [Figure A.22]. BB detections, on the other hand, occur in the first 2 - 3 km for all receivers and then between 25 - 32 km for the 100 and 150 m depths receivers.

Figures A.23 and A.24 show equally well BB performance of the hull mounted array for 1 kHz and 1.5 kHz respectively. For the 50 m depth receiver, detections occur in the first 2 km and again between 26 - 31 km. The performance at 100 m depth is better where detection is taking place at 0 - 17 km and 25 - 37 km. At the 150 m depth, the performance is even better, allowing detection almost continuously up 37 km, except around 24 km where $FOM < H$. Thus the hull array in the summer produces better results than in the winter allowing BB detection around the convergence zone for receivers deeper than 50 m.

Figures A.25 through A.27 show the BB performance of the bow array for 2 kHz, 3 kHz, and 5 kHz respectively. The first two figures show about the same performance as the hull mounted array obtained at 1 kHz and 1.5 kHz [Figures A.23 and A.24]. On the other hand, at 5 kHz, there is no detection by the bow array between 5 - 25 km and beyond 40 km for the various depths. The target can be detected in the first 3 - 5 km and between 26 - 34 km at 50 m depth, and in addition between 25 - 40 km at 100 m and 150 m depths.

The cross-slope case for the summer is shown in Figures A.28 - A.36. As true for the winter the results for the cross-slope resembles the results of the up-slope. However, H can be seen to be up to 5 dB lower at ranges 6 - 24 km when comparing to the up-slope case (Figures A.25 - A.27.) This is due to lower bottom losses in the cross-lope case. This difference allows the bow array to detect the target up to 40 km range for the 100 m and 150 m depths, and to some extent for the 50 m depth (see Figure A.34 and A.35). At 5 kHz, the bow array performs equally well as in the up-slope case (see Figure A.36).

A.2   Second Location

The second location is analyzed here for the up-slope ($\beta = 3°$), cross-slope ($\beta = 0°$) and down-slope ($\beta = -3°$). Unlike the first location, where not much difference was found

between the up/down-slope and cross-slope cases, at the second location the bottom slopes are very different which definitely influence the performance of the various sonar systems. The averaged depth at the center of the location is 1700 m and it is changing substantially for the different slope cases as described below. The transmission loss results for the second location and the corresponding *FOM* are shown in Figures A.37 through A.63 for the winter and A.64 through A.90 for the summer. For each season, the results are described first for the up-slope, then for the cross-slope, and lastly for the down-slope.

A.2.1   Winter Conditions

The ray trace diagram for the second location, up-slope case, during the winter season is depicted in Figure 4.11 where all the rays hit the bottom at some point along the available 30 km range.

Due to the massive bottom interaction no convergence zone is formed in the classical sense. However, the increased density of rays as the depth becomes shallower tends to compensate for the increase in bottom losses, and creates an increase in pressure level from 15 to 30 km. The performance results for this case are shown in figures A.37 through A.45 for the various frequencies and sonar systems.

Figures A.37 through A.39 show good performance of the towed array for NB processing at $f = 100$ Hz, 200 Hz, and 500 Hz. The target is detected within the available 30 km range for the various depths of the receivers. The BB performance, however, is limited to the first 2 km. It is also notable, although do not change the sonar performance, that between 5 and 30 km the transmission loss at 100 m is better than the one at 50 m depth by 5 to 9 dB.

The hull mounted array at 500 Hz may perform slightly better in NB due to the increase of 3 dB in *FOM* (see Figure A.40). Figures A.41 and A.42 show the BB performance of the hull mounted array. BB detection according to these figures occurs in the first 3 km only.

The BB performance of the bow array at 2 kHz, 3 kHz, and 5 kHz is shown in Figures A.43 through A.45. The performance of the bow array sonar is relatively equal for these frequencies. The target is detected up to 6 - 8 km, and in addition around 25 km for the 100 m and 150 m depths only.

The ray trace diagram for the second location, cross-slope case, during the winter season is depicted in Figure 4.12 where the rays that hit the bottom are not shown. A convergence zone is clearly formed between 31 - 36 km. Accordingly, lower transmission loss and good performance are expected at this region as depicted in Figures A.46 through A.52.

The sonar performance results resembles the results for the cross-slope case at the first location and therefore the will not be repeated here. However, one should note that the difference between the first and second locations is the bottom depth which is 500 m shallower at the second location. As a result, bottom bounced rays have less distance to travel. Naturally, lower H should be expected in the ranges 15 - 30 km, which is a region that is affected by bottom bounced rays. This can be seen by comparing the transmission loss results for the towed array at frequencies 100 Hz, and 200 Hz, as shown in Figure A.46 and A.47 to the results of the first location shown in Figures A.10 and A.11. This difference in transmission loss, ranging from 1dB to 3dB, causes the detection ranges at the second location to be larger in the order of 1 to 3 km.

The effect of bottom depth on the transmission loss at high frequencies, however, is the opposite. At high frequencies, more than 1 kHz, the loss due to bottom interaction is larger than the one due to spreading and therefore higher H can be seen at the second location in the ranges 6 - 25 km [Figures A.52 and A.53 in comparison to Figures A.26 and A.27].

The ray trace diagram for the down-slope ($\beta = -3°$), during the winter, is depicted in Figure 4.13. The convergence zone can be seen at ranges 35 - 42 km. The convergence zone in this case is about 2 km wider than the cross slope case. Accordingly, lower

transmission loss and good performance are expected at this region as depicted in Figures A.55 through A.63.

Although the bottom depth getting larger with range due to the slope the acoustic energy is still channeled within the upper water column. This suggests good performance at relatively large ranges due to a lower bottom interaction rate. On the other hand, high bottom interaction near the source introduces the bottom loss at short ranges. The bottom loss affects the transmission loss results throughout the 50 km range as shall be seen subsequently. In general, at short ranges the transmission loss is lower than in the cross-slope case, and at large ranges it is larger.

Figures A.55 through A.57 show the performance of the towed array for NB and BB processing. At f = 100 Hz, and 200 Hz, NB detection occurs for 150 m depth receiver continuously up to 48 km. The same is true for the 100 m depth except at ranges 24 - 29 km, where $FOM < H$. The 50 m receiver, performs poorer. It detects the NB signal at 0 - 17 km, then at 30 - 37 km, and 42 - 47 km. It should also be noted that at 35 km (at the convergence zone) the lower transmission loss is evident for 100 m depth when it is compared to 50 m and 150 m depths. The detection of BB signal by the towed array is again limited to the first 5 km. At 500 Hz the detection coverage by the towed array is reduced. The 50 m depth receiver can detect at 0 - 13 km, and 30 - 47 km. The 100 m depth receiver detects the NB signal at 0 - 20 km, and beyond 29 km. The 150 m depth receiver performs better and detects the target at 0 - 22 km, and beyond 28 km.

The performance of the hull mounted array is shown in Figures A.58 - A.60 for 500 Hz, 1 kHz, and 1.5 kHz respectively. At 500 Hz, the hull mounted array has 3 dB higher FOM than the towed array and therefore improved detection ranges are observed. For example, the 100 m depth receiver can now detect at 0 - 25 km (compare 0 - 20 km with the towed array.) From Figures A.58 - A.60, the BB signal can be detected only within 5 km from the target.

Figures A.61 through A.63 show the performance of the bow array. The bow array shows better performance as far as BB detection is concerned. In fact, the BB signal is

detected at about 0 - 7 km for the different receiver depths. The 100 m depth receiver is able to detect the target also at 34 - 36 km.

A.2.2   Summer Conditions

The performance of the various sonar systems during the summer are different from the winter due to the down refractive SVP structure near the surface (as discussed earlier) and due to the lower wave height. The latter creates less surface noise and less surface loss. Those two factors have a notable effect on the results described subsequently. The ray trace diagram for the up-slope ($\beta = 3°$), during the summer, is depicted in Figure 4.14. As true during the winter, a convergence zone is not formed and all the rays are at least bottom reflected. The performance results for this case are shown Figures A.64 through A.72.

Figures A.64 - A.66 show the performance of the towed array for NB and BB detection. It seems that, the NB component of the target at f = 100, 200, 500 Hz, can be detected by the towed array for the entire 30 km range. The BB component at 200 Hz can be detected by the towed array at 22 - 29 km for the 100 m and 150 m depth receivers. It can hardly be detected, however, at 50 m depth. At 500 Hz, the BB signal can be detected in 10 - 29 km at 100 m and 150 m depths. The 50 m depth receiver can detect the BB signal in 26 - 30 km. It must be noted that the transmission loss behavior looks quiet awkward as it decreases with range from 5 to 30 km. The reason for that is probably because of the high density of rays in this region which tends to compensate for the bottom loss at large ranges.

The hull mounted array, on the other hand, enables a detection of NB as well as BB for 0 - 30 km for the various depths (see Figures A.81 - A.83). This is also true for the BB signals at f = 1 kHz and 2 k Hz.

The performance of the bow array is depicted in Figures A.70 - A.72. The figures show good detection for the BB signals for the entire 30 km range due to high *FOM* (87 dB).

The ray trace diagram for the cross-slope ($\beta = 0°$), during the summer, is depicted in Figure 4.15. The convergence zone formed at ranges 29 - 36 km does not reach the surface. Accordingly, at 50 m depth poor performance is expected. The performance results for this case are shown in Figures A.73 through A.81.

The performance of the towed array can be seen in Figures A.73 - A.75. For f = 100, 200 Hz the towed array is capable of detecting NB signals at ranges 0 - 46 km at 100 m and 150 m depths. At 50 m depth the NB component can be detected in ranges of up to 25 km. At 500 Hz, the NB signal can be detected in ranges 0 - 48 km at 100 m and 150 m depths, and 0 - 31 km at 50 m depth. Figure A.75 shows in addition that BB detection occurs at the first few km for the various depths, and at 30 - 35 km only at 100 m and 150 m depths (the convergence zone cannot be seen at 50 m depth.)

The hull mounted array at 500 Hz, in addition to extended detection ranges for the NB component (compare to the towed array), allows detection of BB signal in ranges 10 - 22 km and 29 - 35 km at 100 m and 150 m depths (see Figure A.76). At f = 1 kHz, 1.5 kHz the BB signal can be detected in ranges 0 - 36 km at 100 m and 150 m depths, while it can be detected at 50 m depth only at 0 - 15 km (see Figure A.77 - A.78).

The performance of the bow array is shown in Figures A.79 - A.81. At f = 2 kHz and 3 kHz the BB detection ranges at 150 m depth are 0 - 37 km, at 100 m depth from 0 to 27 km, and 28 - 37 km, and at 50 m depth from 0 to 25 km and 32 - 35 km. At f = 5 kHz a 'shadow' zone is formed between 4 - 11 km for the various depths. The performance of the bow array outside the shadow zone is similar to the performance of the hull array.

The ray trace diagram for the down-slope case slope ($\beta = -3°$) for summer conditions is shown in Figure 4.16. As true for the cross-slope case, the convergence zone, at ranges 30 - 37 km, does not reach the surface, and therefore at 50 m depth poor performance are expected.

The performance of the various sonar systems for this case are depicted in Figures A.82 - A.90. The transmission loss structure resembles the one obtained for the cross-slope

case (see Figures A.73 - A.81). and therefore shall not be repeated in details. Some remarks must be written, however. The down-slope case introduces higher bottom loss and therefore higher transmission loss is observed except at short ranges where a lower H is observed. A lower transmission loss corresponds to shorter detection ranges. For the towed array (Figures A.82 - A.84) the detection ranges are 2 - 4 km shorter for NB, which is also true for the hull mounted array. For BB, however, there is an increase in the detection ranges at short distances. In fact, BB signal can be detected at ranges between 10 km to 20 km for the towed array at the various receiver depths.

The degradation of performance of the bow array are notable only at 50 m depth for 2 kHz and 3 kHz, where the BB signal may not be detected beyond 13 km. At 5 kHz, however, the BB signal may not be detected at all beyond 7 km for the 50 m receiver. It should be noted that in the down-slope case, there is an enormous impact due to receiver depth. In fact, the difference in transmission loss can reach even 20 dB in favor of the 150 m compare to 50 m beyond 7 km.

A.3   Third Location

The third location is analyzed here for the up-slope (β = 0.4°), cross-slope (β = 0°) and down-slope (β = -0.4°). The up-slope and down-slope are milder here than in the second location. Another important parameter is the averaged depth, which is 1200 m, at the center of the location. The depth along with the slope determine the angular spectrum of rays that are free from bottom interaction. This location is then, 500 m, shallower than location 2, and 1000 m shallower than location 1. The performance results for the third location and the corresponding *FOM* are shown in Figures A.91 through A.117 for the winter and A.118 through A.144 for the summer. For each season, the results are described first for the up-slope, then for the cross-slope, and lastly for the down-slope.

A.3.1 Winter Conditions

The ray trace diagram for the third location, up-slope case, during the winter season is depicted in Figure 4.17. The SVP is mostly down refractive with small gradient up to 400 m and then becomes upper refractive. In the upper tens of meters, however, there is a slight upper refractive gradient. The upper refractive part of the SVP, below 400 m, causes the rays to bend upwards and to form a convergence zone in the ranges 30 - 38 km. The convergence zone is clearly seen in the transmission loss results as shown in figures A.91 through A.117 that correspond to the third location during winter.

The performance of the towed array for the up-slope case is depicted in Figures A.91 through A.93. At f = 100 Hz, and 200 Hz NB signals can be detected by the towed array in ranges 0 - 50 km at 150 m depth, 0 - 44 km at 100 m depth, and 0 - 23 km and 27 - 39 km at 50 m depth. At 500 Hz NB detections occur at ranges 0 - 44 km at 150 m depth, 0 - 25 km and 27 - 41 km at 100 m depth, and 0 - 17 km and 28 - 36 km at 50 m depth. The BB detection is limited to 0 - 2 km for the towed array.

The hull mounted array at f = 500 Hz increases by 2 - 4 km the detection ranges form the corresponding ranges of the towed array at the same frequency due to an increases in the *FOM* by 3 dB (see Figure A.108). From Figures A.94 - A.96 the detection ranges for the BB signals using the hull mounted array are ranging from 4 - 7 km for the various receiver depths.

The bow array extends the detection ranges to 5 km, 7 km, and 9 km at 50 m depth, 100 m depth, and 150 m depth respectively (see Figures A.97 - A.99). In addition, BB detections occur at 35 - 39 km at 100 m depth, and in the vicinity of 33 km at 50 m and 150 m depths.

The cross-slope ray trace diagram is shown in Figure 4.18. Again, a convergence zone is identified at ranges 30 - 37 km. The performance results for this case are presented in Figures A.100 - A.108.

The results for the towed array (Figures A.100 - A.102) show basically similar performance for NB and BB when compared to the up-slope case. The same is also true for the hull mounted array and the bow array (Figures A.103 - A.108). For the bow array, however, a lower transmission loss can be observed at ranges 8 - 22 km compared to the up-slope case, but this fact does not change the performance in terms of detection ranges (Figures A.106 - A.108).

The ray trace diagram for the down-slope case is shown in Figure 4.19. The convergence zone is clearly seen at 30 - 37 km. The corresponding performance results are plotted in Figures A.109 - A.117.

When comparing the results for the towed array (Figures A.109 - A.111) to the cross-slope results or to the up-slope results, it is evident that the it suffers from higher transmission loss (in the order of 1 - 5 dB.)

It translates to a reduction in performance especially at 50 m depth for NB detection at frequencies 100 Hz and 200 Hz. The reduction in detection ranges are in the order of 2 - 4 km around 26 km and 40 km ranges from the target. At 500 Hz, the reduced NB performance is apparent at 100 m depth around 23 km from the target. The towed array performance at 150 m does not seem to suffer from the increase in H. The BB detection ranges, however, stays within the 2 - 3 km range from the target.

The hull mounted array at 500 Hz (Figure A.112) also shows reduced NB performance at 100 m depth around 23 km from the target when it is compared to the cross or up-slope cases. The BB performance stays the same with detection ranges of 4 km at 50 m depth to 7 km at 150 m depth for 500 Hz, 1 kHz, and 1.5 kHz (Figures A.112 - A.114).

No notable changes are present for the bow array when its performance is compared to the cross-slope or up-slope cases. It should be noted, however, that the bow array is capable of detecting BB signals between 30 - 40 km (at the convergence zone) while the hull mounted array cannot for all cases during the winter.

A.3.2 Summer Conditions

The first case to be considered is the up-slope case. The corresponding ray trace diagram is depicted in Figure 4.20. The diagram shows the maximum angular spectrum of the rays that do not hit the bottom before the convergence zone. The convergence zone does not reach the surface as was the case for the first two locations during the summer.

The performance results for the up-slope case are presented in Figures A.118 - A.126. The results for the towed array show good performance for NB detection (Figures A.118 - A.120). The towed array continuously detect the NB signals at 100 m and 150 m depths for 100 Hz, 200 Hz, and 500 Hz. At 50 m depth the towed array starts to loose the target around 40 km range for the above frequencies. The BB performance is different. At 100 Hz the towed array detects the BB signal within the first 2 km while at 200 Hz the towed array is capable of detecting the BB signal also around 30 km (convergence zone range) at 100 m depth. At 500 Hz, the BB signal can be detected in addition between 7 - 15 km.

Due to higher *FOM* the hull mounted array has better performance than the towed array at 500 Hz (Figure A.121). The NB signal can be detected at ranges exceeding 50 km for the various depths, and the BB signal can be detected at ranges 0 - 16 km at 50 m depth, 0 - 20 km, and 27 - 33 km at 100 m depth, and 0 - 33 km at 150 m depth.

At 1 kHz and 1.5 kHz, the hull mounted array can detect the BB signal between 0 - 17 km at 50 m depth, and 0 - 33 km at 100 m and 150 m depths (see Figures A.122 - A.123). Figures A.124 - A.126 show the same results for the bow array at frequencies 2 kHz, 3 kHz, and 5 kHz with minor differences.

Next, the cross-slope results are reviewed. The ray trace diagram for the cross-slope case is shown in Figure 4.21. The corresponding sonar performance results are presented in Figures A.127 - A.135. Note that the rays in the ray-trace diagram do not hit the bottom nor the surface. In other words, the sound is trapped in a sound channel. The summer conditions enable that effect by fixing the sound velocity at the surface to be higher than the

196

sound velocity at the bottom. In order to take advantage of this effect, the receiver must be placed below the minimum depth which is about 50 m as seen in Figure 4.21. This can happen, however, when the direction of propagation is a cross-slope or a down-slope.

The performance of the towed array is shown in Figures A.127 - A.129. The effect of a lower transmission loss than in the up-slope case can be seen for ranges beyond 35 km, and in particular around 43 km. There even at 50 m depth, a NB detection occurs for f = 100, 200 and 500 Hz. At 100 m and 150 m depths, the detection ranges exceed the 50 km. In addition, the towed array is able to detect BB signals in ranges 0 - 3 km and around 31 km at 100 m depth (f = 200 Hz), and 0 - 3 km, possibly between 7 - 15 km (for 50 m, 100 m, and 150 m), and 29 - 34 km (at 100 m, and 150 m) at 500 Hz. No improvement in BB detection ranges are seen for the cross-slope when it is compared to the up-slope.

As true in this study, the hull mounted array at 500 Hz has a 3dB higher *FOM* and therefore better performance than the towed array are expected. As can be seen in Figure A.130, However, both arrays perform equally well at 500 Hz for ranges 0 - 50 km and NB processing. For BB detection, no improved detection ranges are seen when comparing to the up-slope case. At 1 kHz, and 1.5 kHz, one should note that at 100 m the hull mounted array can loose the target occasionally in ranges 25 - 27 km, which is not the case for the up-slope results (see Figures A.131 - A.132). A possible detection may occur around 43 km however, for 100 m, and 150 m depths.

The results for the bow array are shown in Figures A.133 - A.135. The bow array extends the detection ranges set by the hull array, especially around 40, 43 km range where there is a definite detection at f = 2 kHz, and 3 kHz (for 100 m, and 150 m). This is not the case at 5 kHz, however, where the maximum detection ranges are 34 - 35 km at 100 m and 150 m, and 19 km at 50 m depth. The 50 m depth receiver may also detect near 31 km.

The last case to be considered is the down-slope case for the third location during the summer. The corresponding ray trace diagram is shown in Figure 4.22. The sonar performance results are shown in Figures A.136 - A.144.

the effect of the down slope can be observed clearly beyond 35 km when examining the transmission loss results and comparing it to the cross-slope results. The exact details are not repeated for this case, only main differences to the cross-slope results are mentioned. The performance results for the towed array are shown in Figures A.126 - A.128.

At 50 m the towed array looses NB detection beyond 35 km at 100 Hz - 500 Hz, which is also occasionally true for the 100 m depth. At 150 m depth, however, the array seems to be able to detect the NB almost continuously up to 49 km. At 200 Hz, the array detects the BB signal around 31 km in addition to the first 2 km when it is at 100 m depth. At 500 Hz it performs slightly better and can detect the BB signal between 7 - 10 km and 30 - 34 km at 100 m depth.

The hull mounted array at 500 Hz performs even better, extending the NB detection ranges, and enabling detection of BB signal between 0 - 15 km at the various depths, and 29 - 34 for the receivers at 100 m and 150 m depth (see Figure A.139). No substantial differences in the performance of the hull mounted array between the cross-slope and the down-slope results are notable at 1 kHz and 1.5 kHz as can be seen in Figures A.140 - A.141.

From Figures A.142 - A144, the bow array seems to loose the BB signal beyond 35 km at the various depths giving rise to a better performance at the cross-slope case at frequencies 2 kHz and 3 kHz.

As a general remark, one should note the differences in H as a function of depth especially during the summer especially around the convergence zone region. In fact, the 15 - 20dB difference is observed between 50 m depth and 100 m depth.

loc. 1, up-slope, winter, towed-array, f= 100Hz

loc. 1, up-slope, winter, towed-array, f= 200Hz
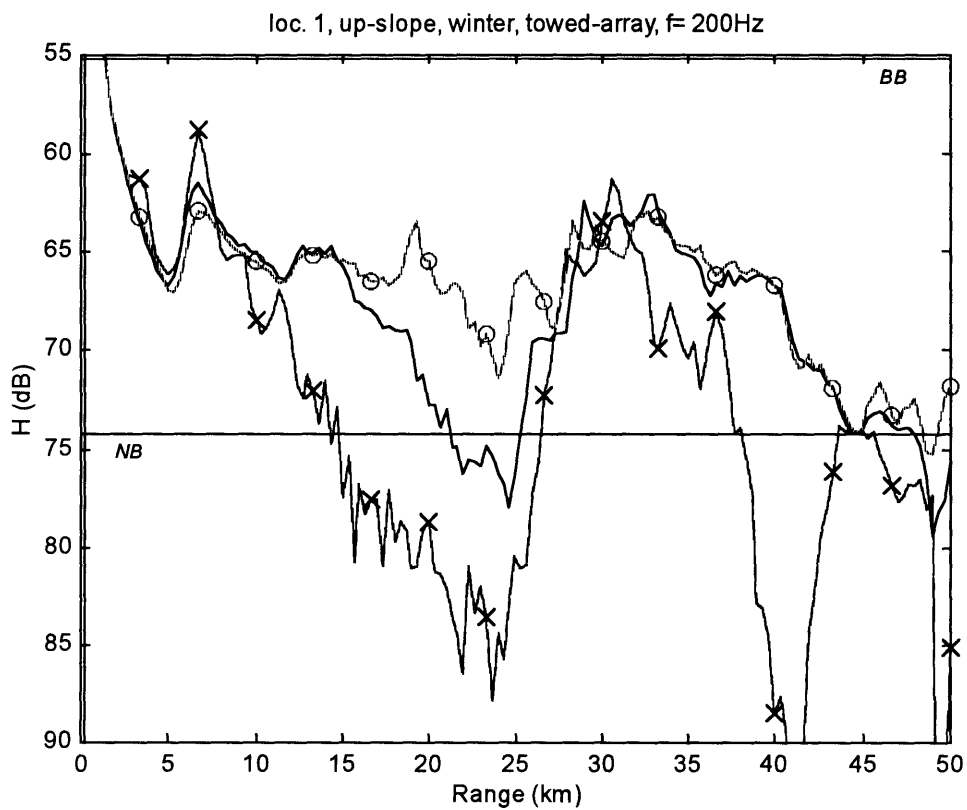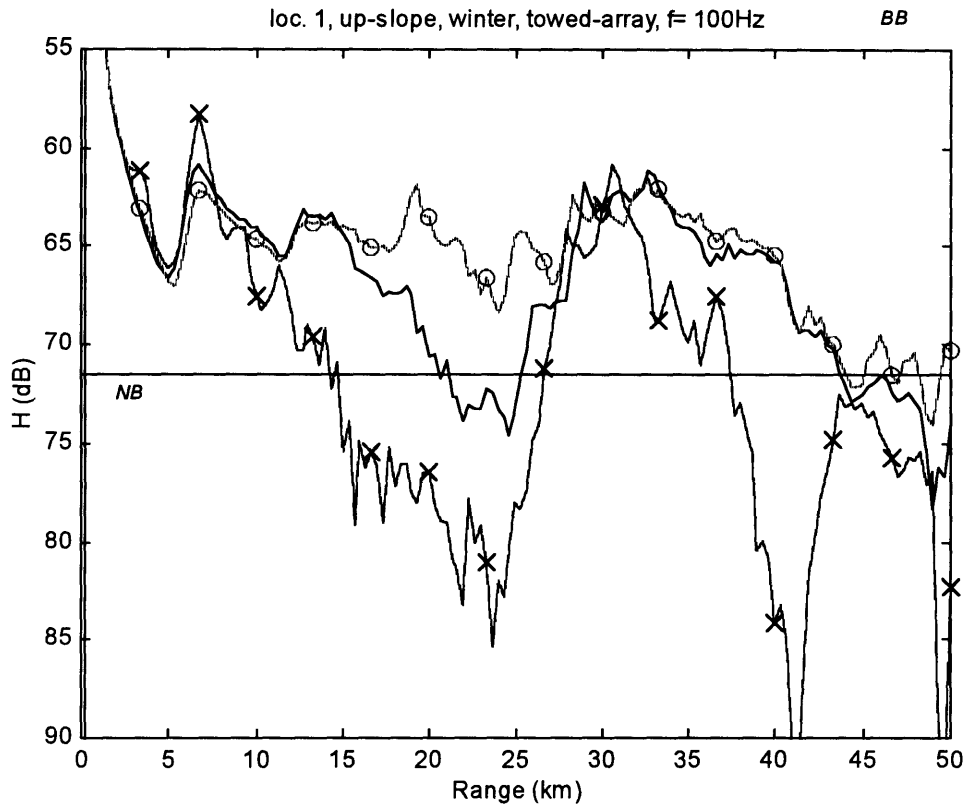
Figure A.1 (upper) & Figure A.2 (lower): Sonar performance, 1st location.

loc. 1, up-slope, winter, towed-array, f= 500Hz
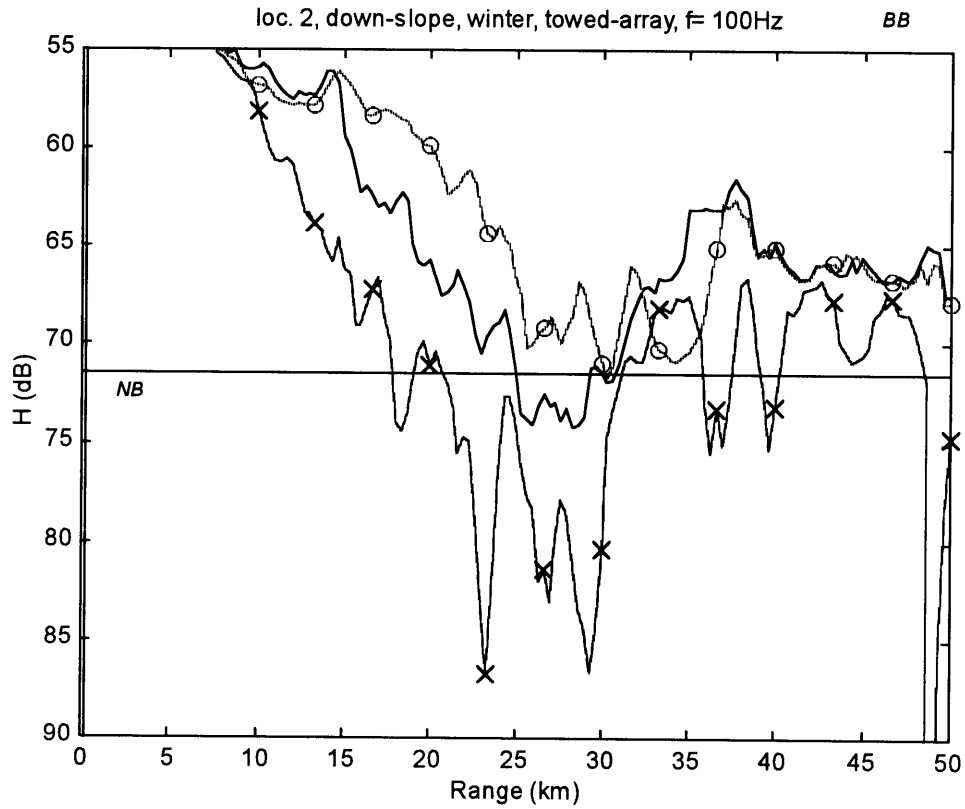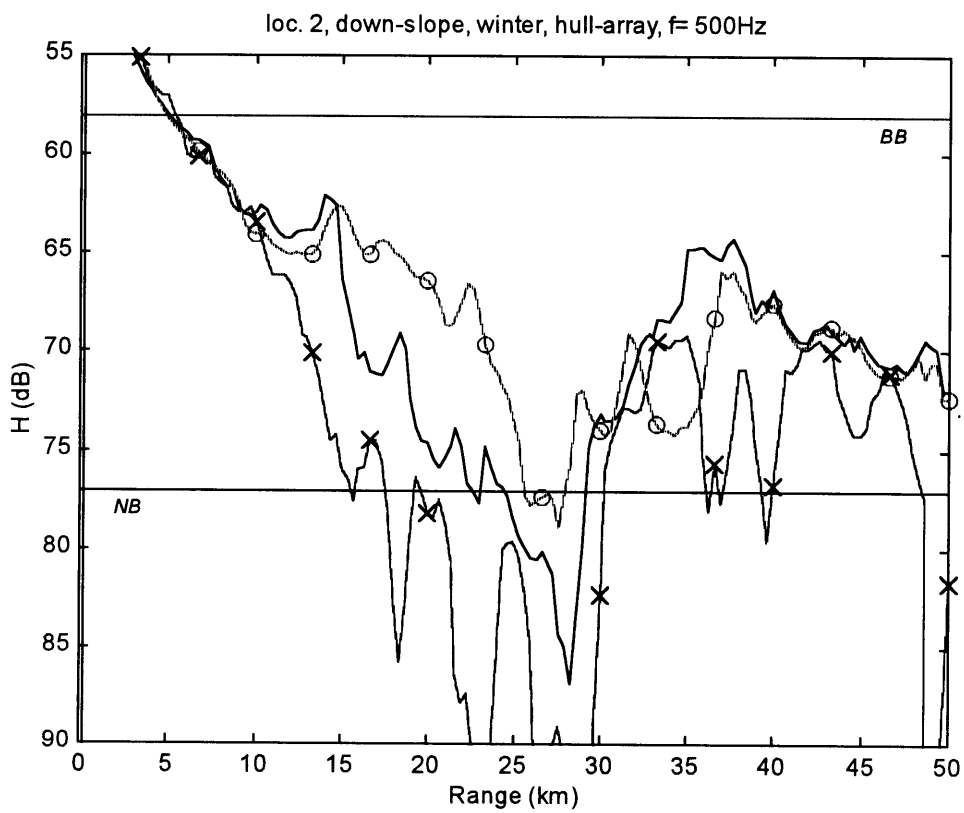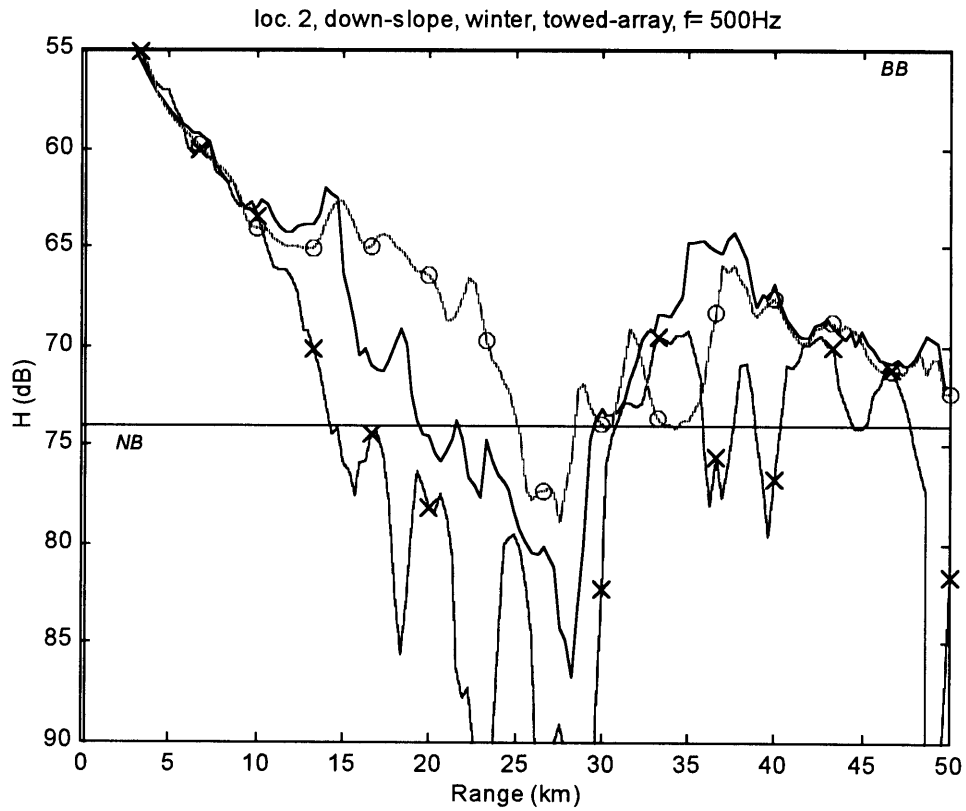

loc. 1, up-slope, winter, hull-array, f= 500Hz
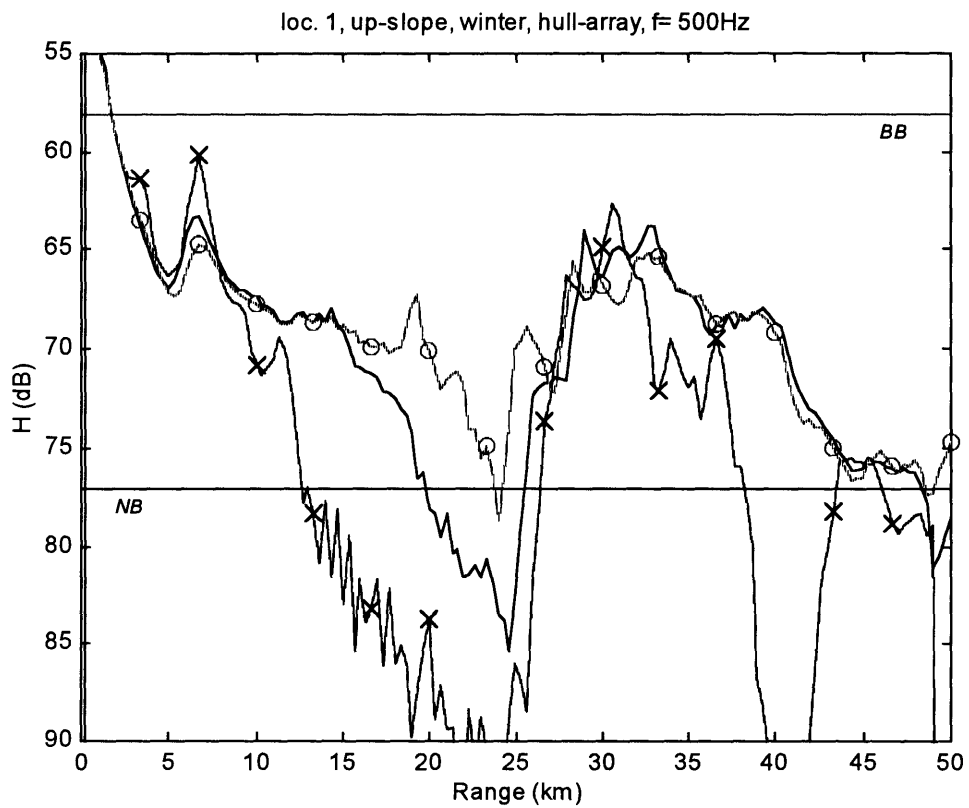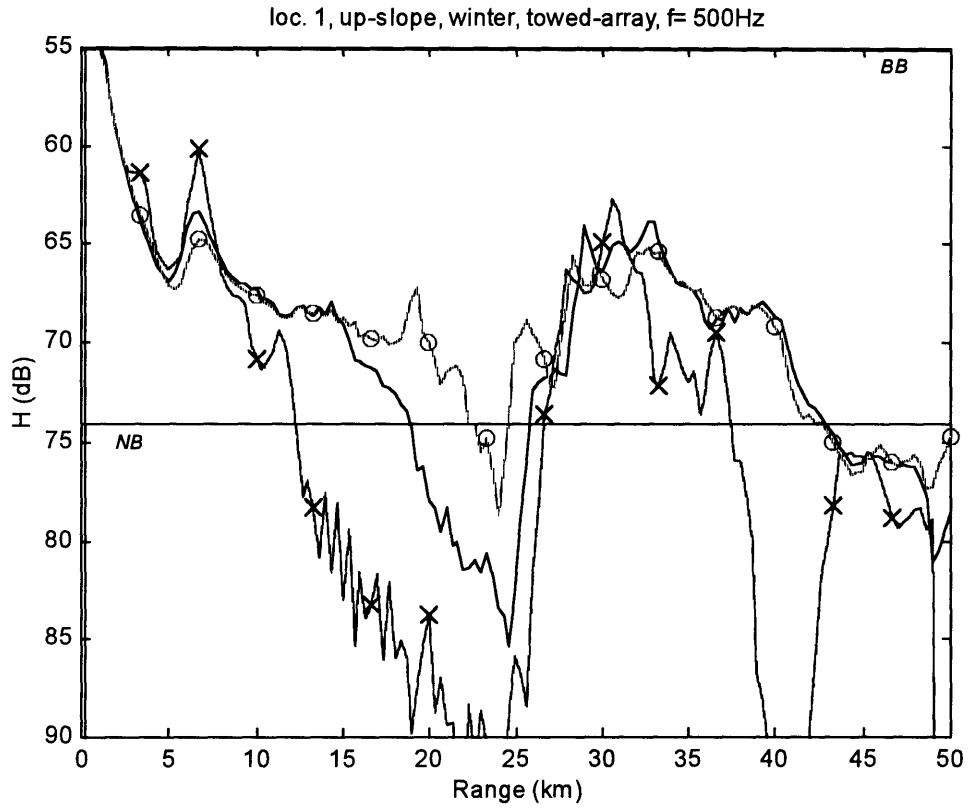
Figure A.3 (upper) & Figure A.4 (lower): Sonar performance, 1st location.
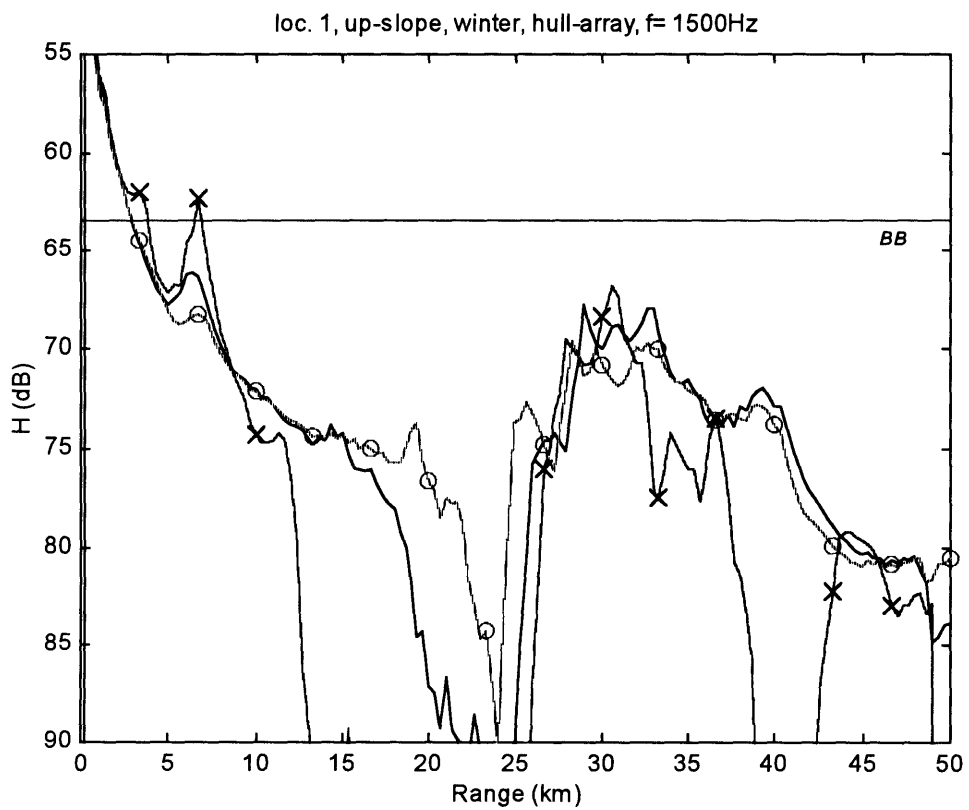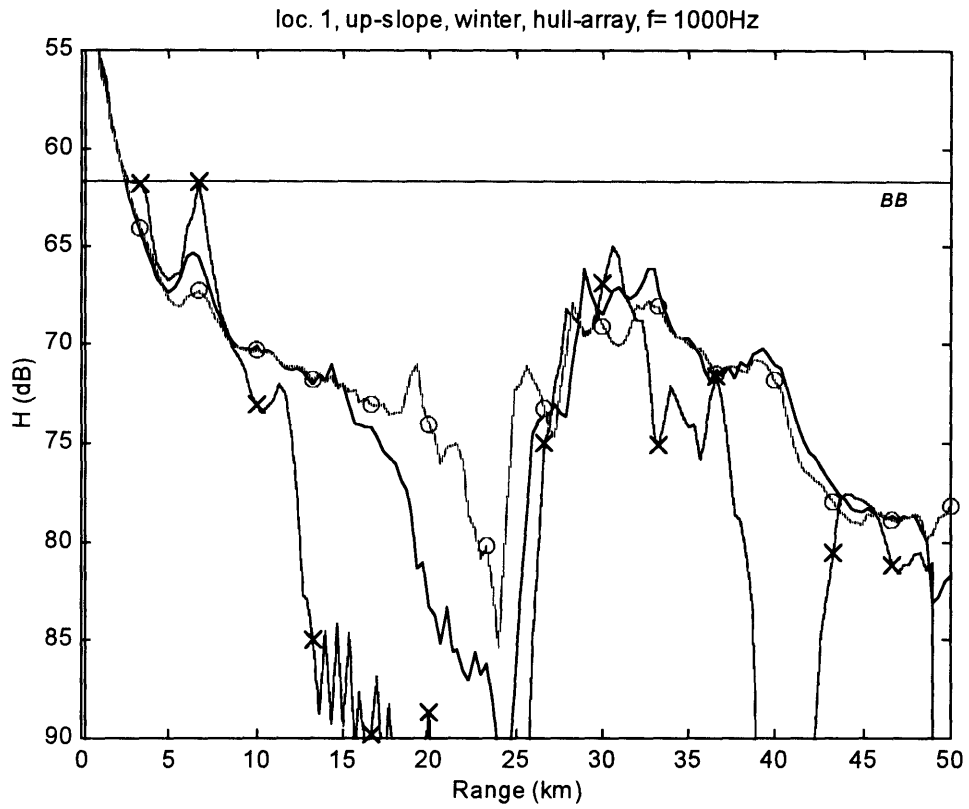
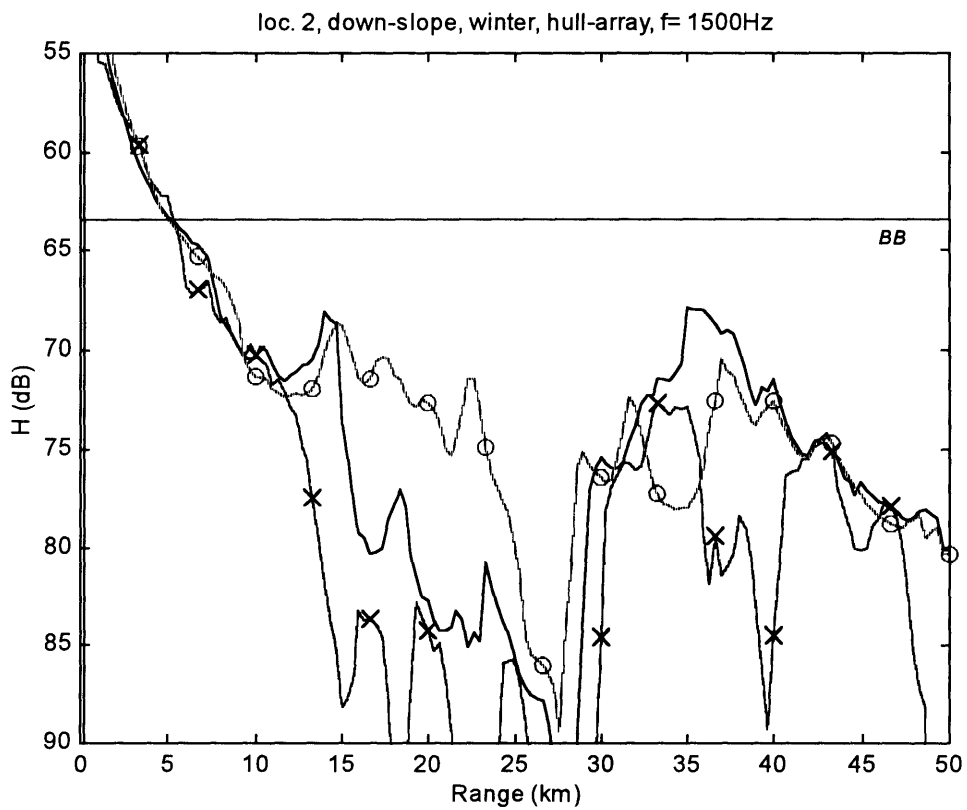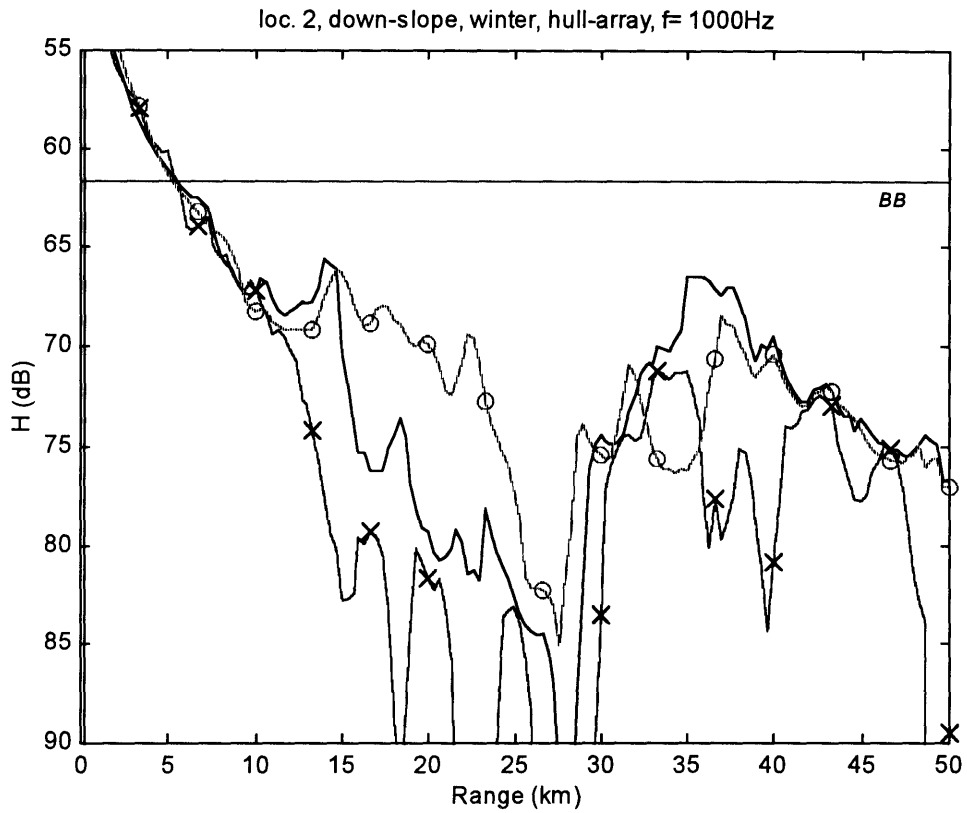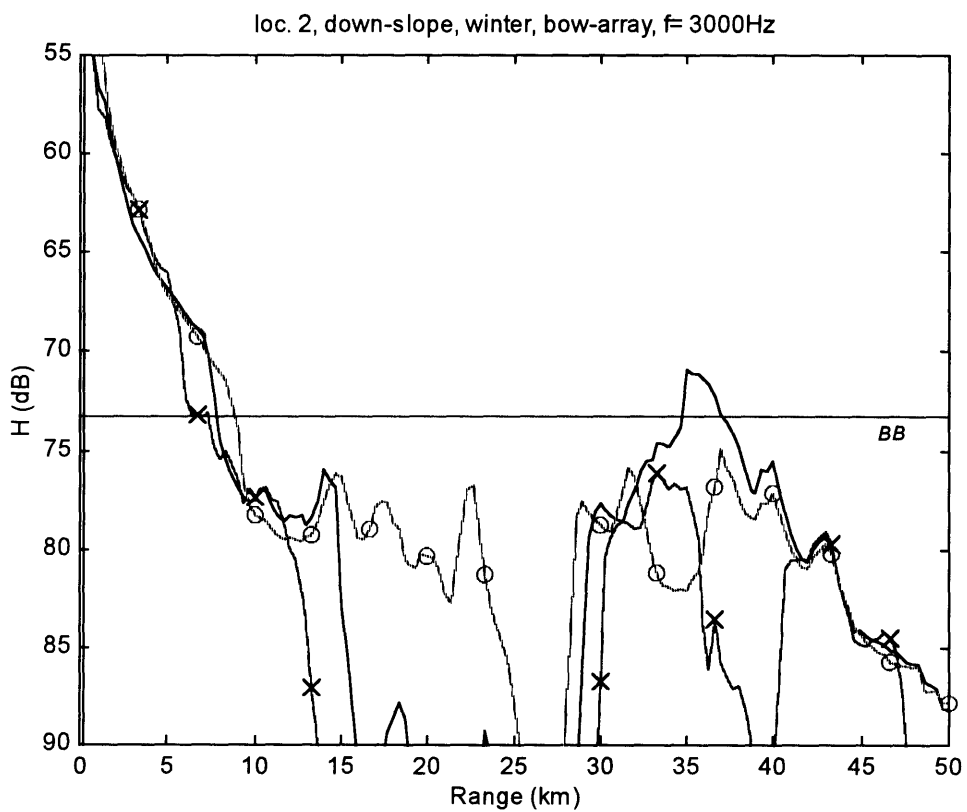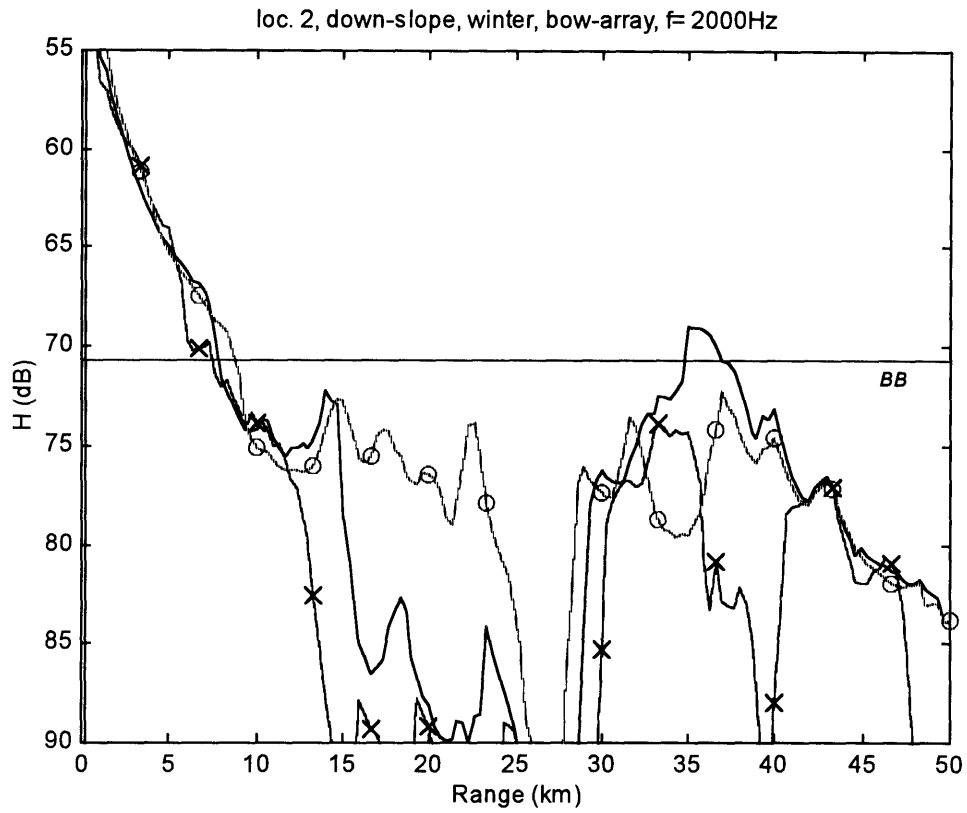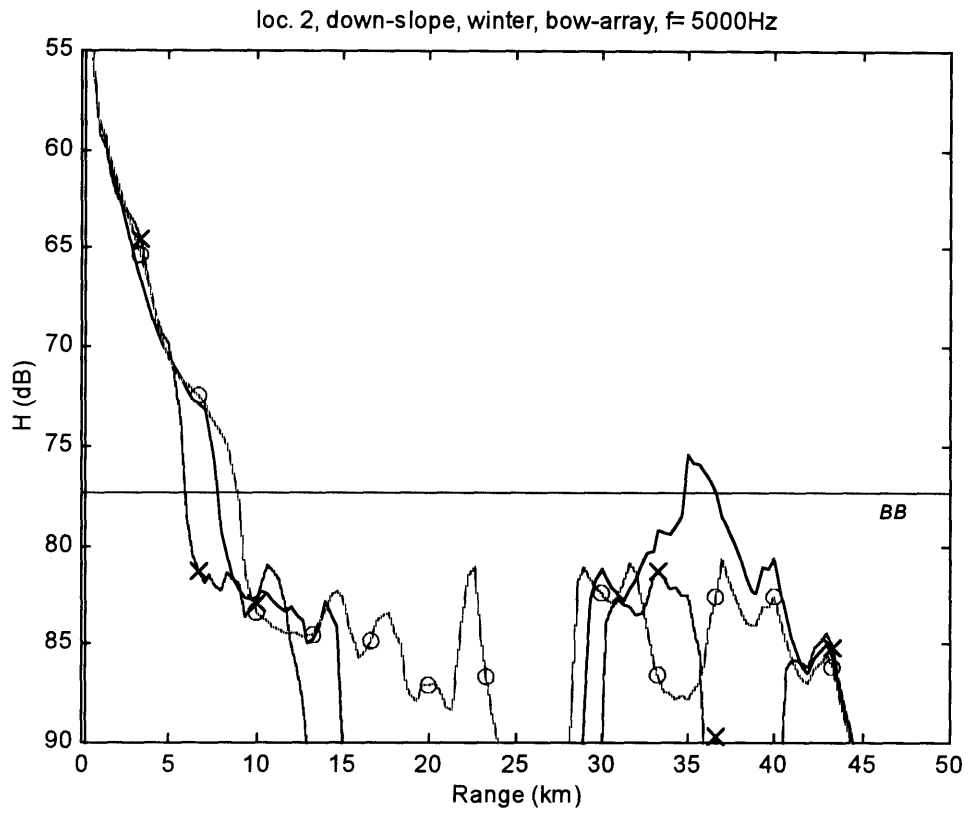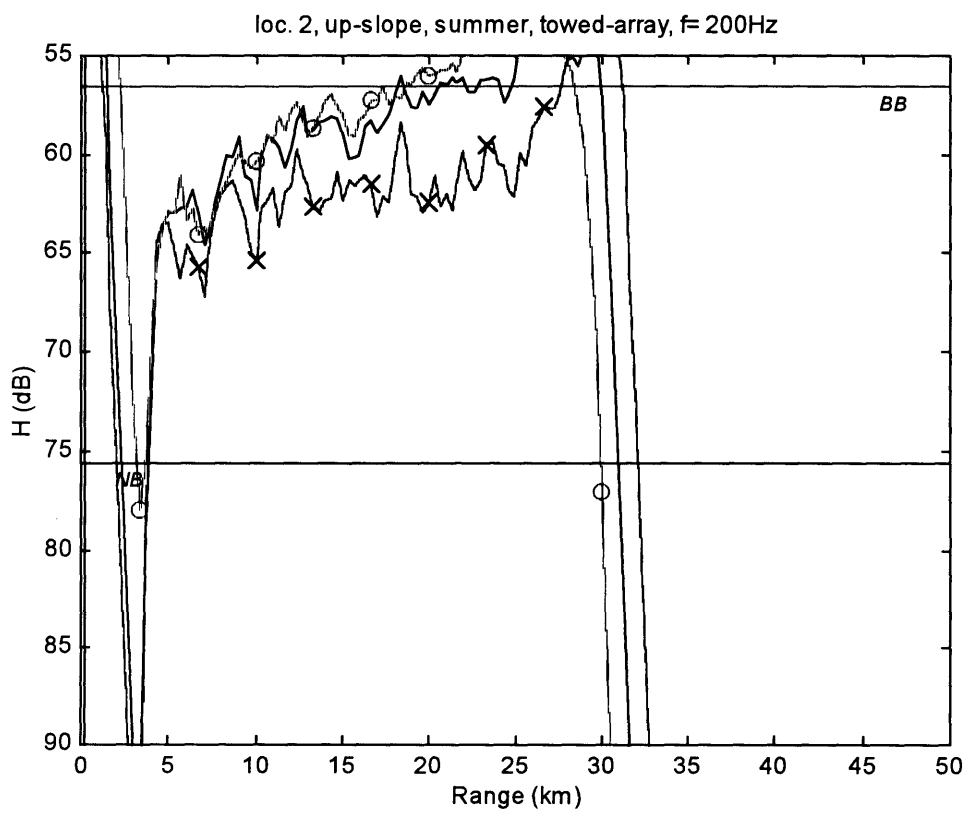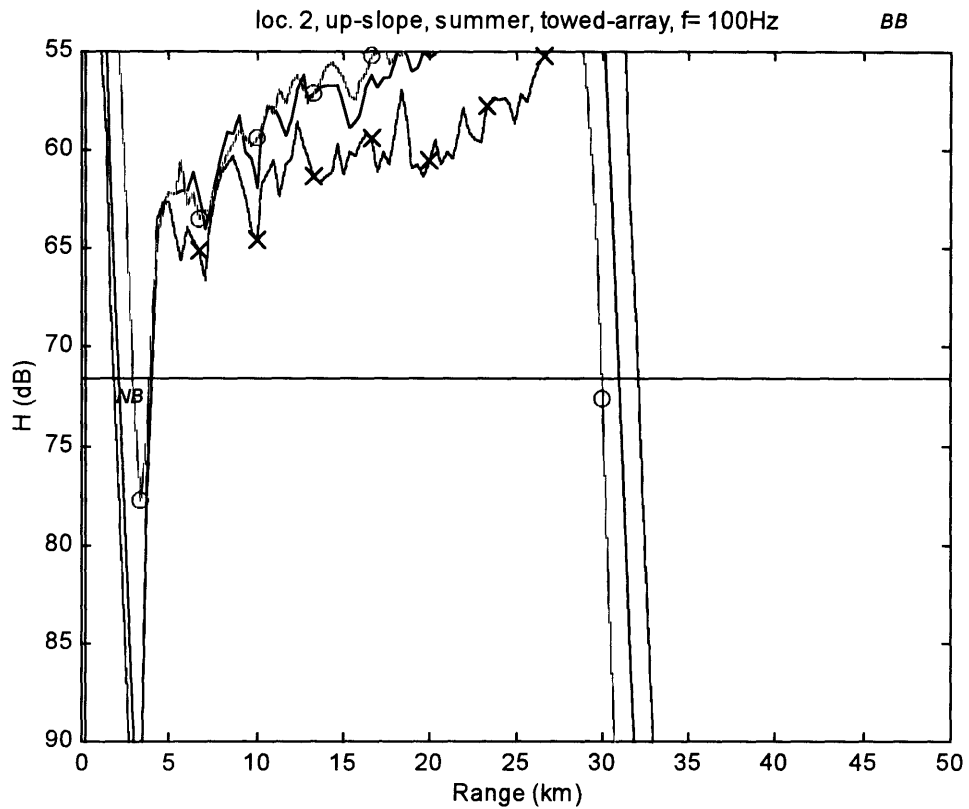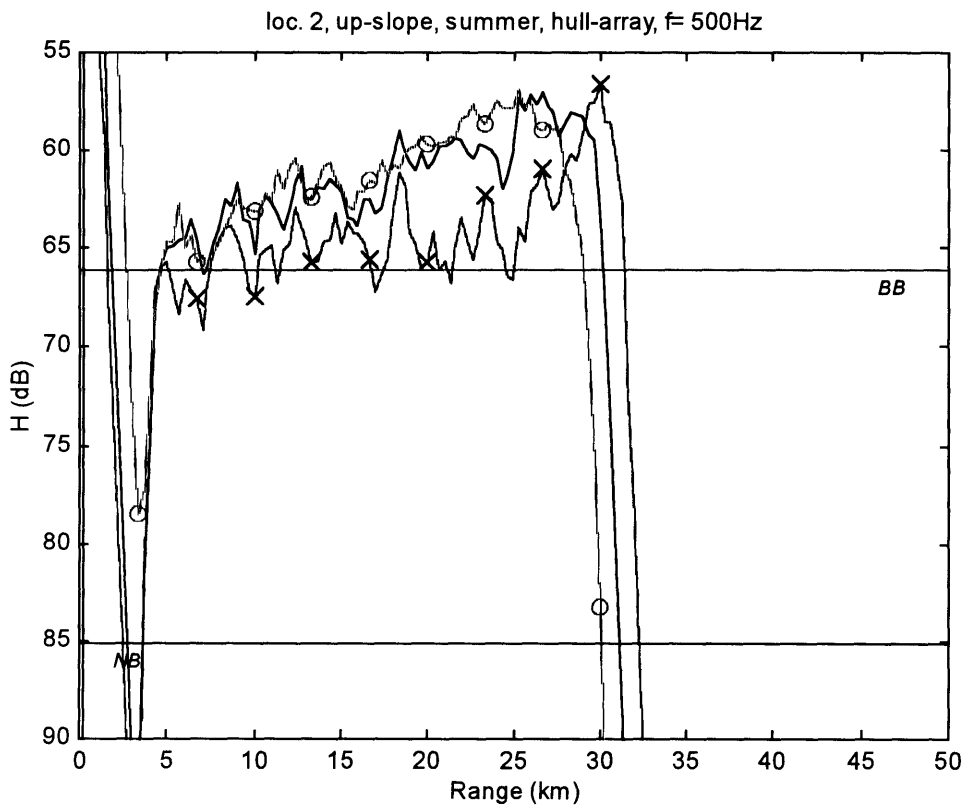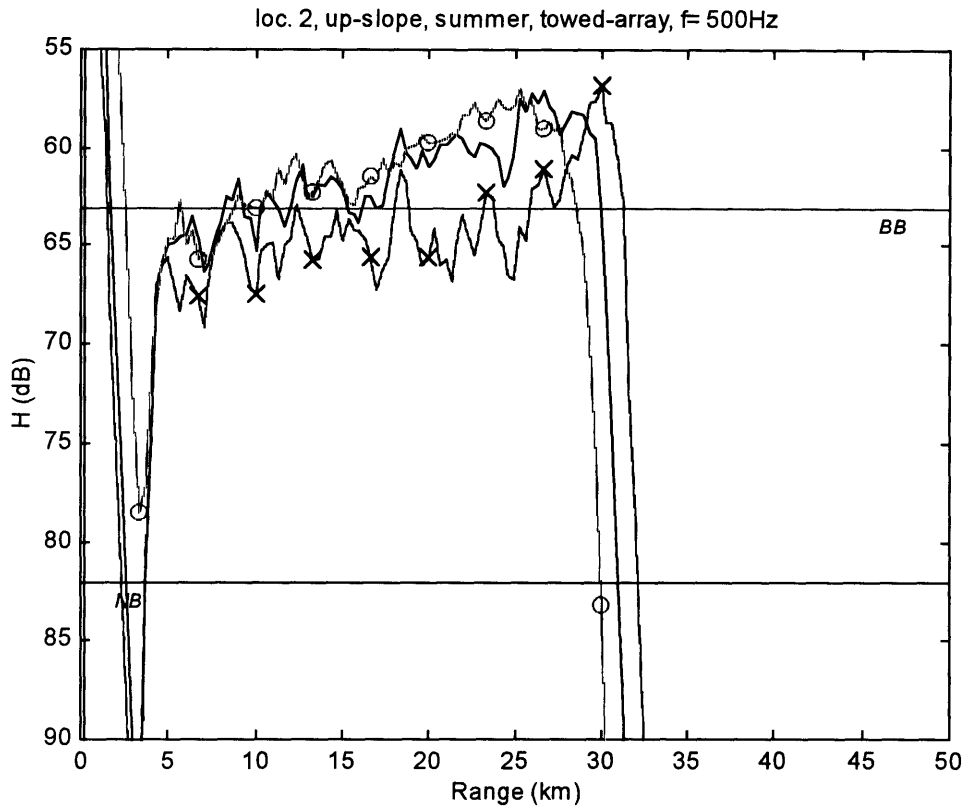Figure A.5 (upper) & Figure A.6 (lower): Sonar performance, 1st location.

loc. 1, up-slope, winter, bow-array, f= 2000Hz

loc. 1, up-slope, winter, bow-array, f= 3000Hz
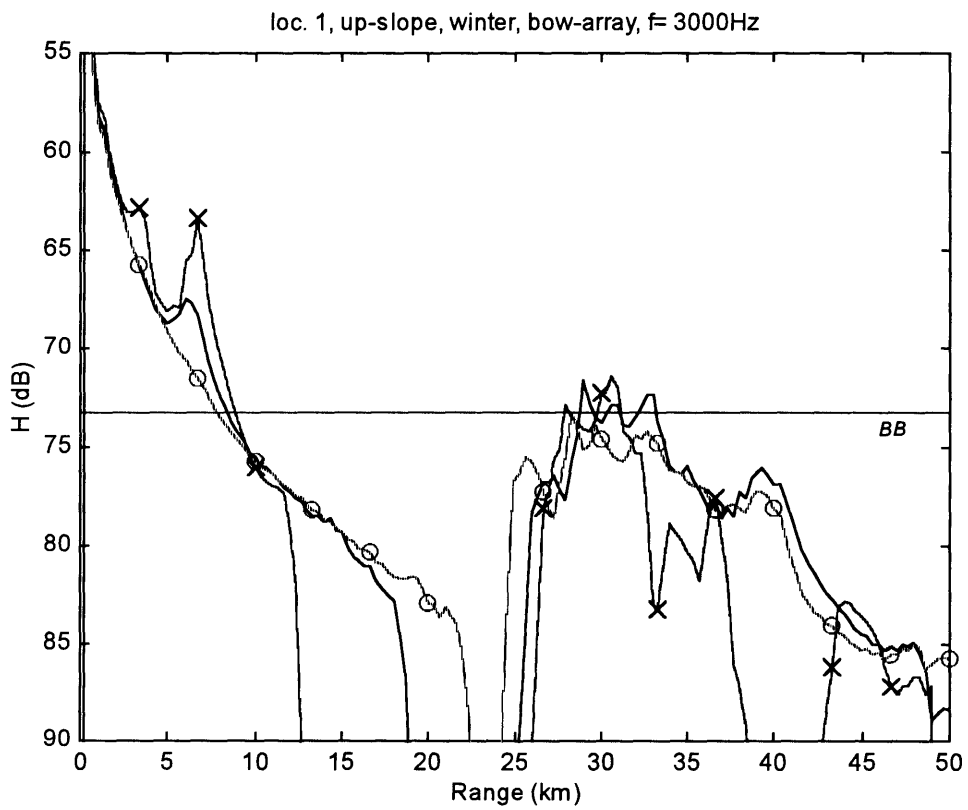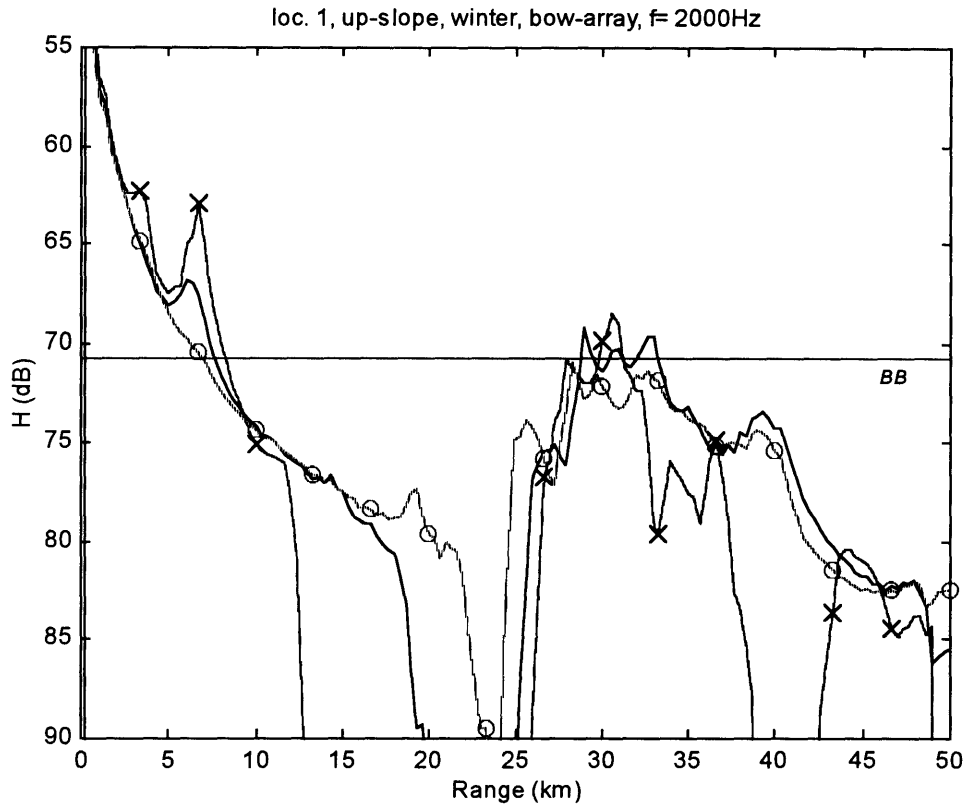
Figure A.7 (upper) & Figure A.8 (lower): Sonar performance, 1st location.

loc. 1, up-slope, winter, bow-array, f= 5000Hz
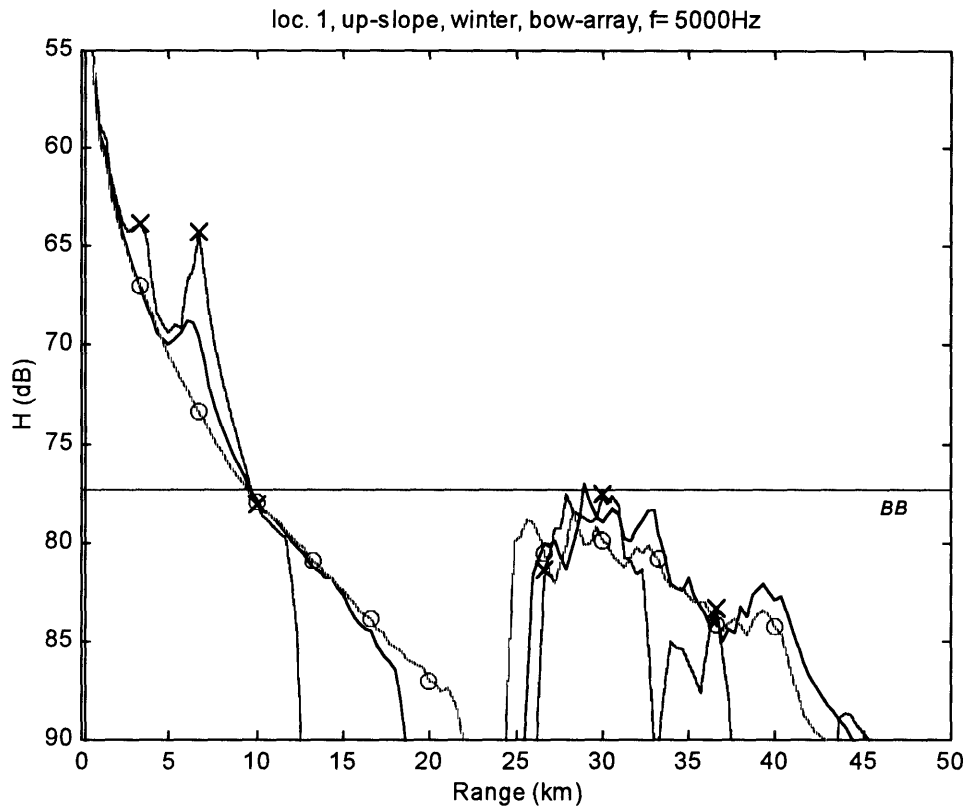
Figure A.9: Sonar performance, 1st location.
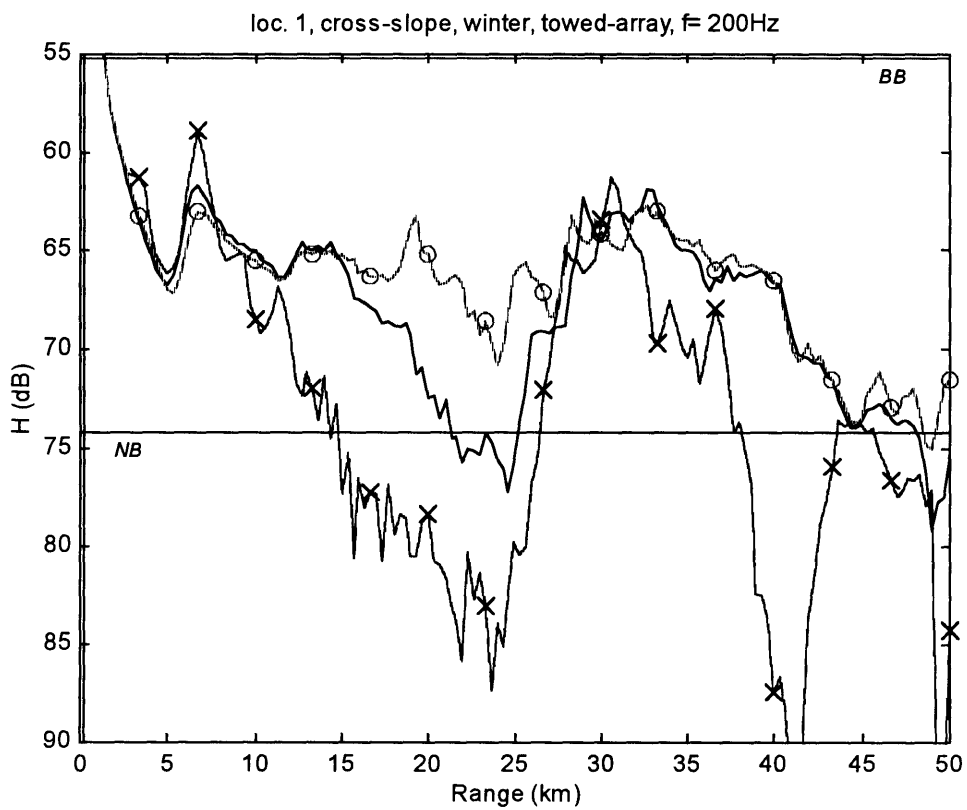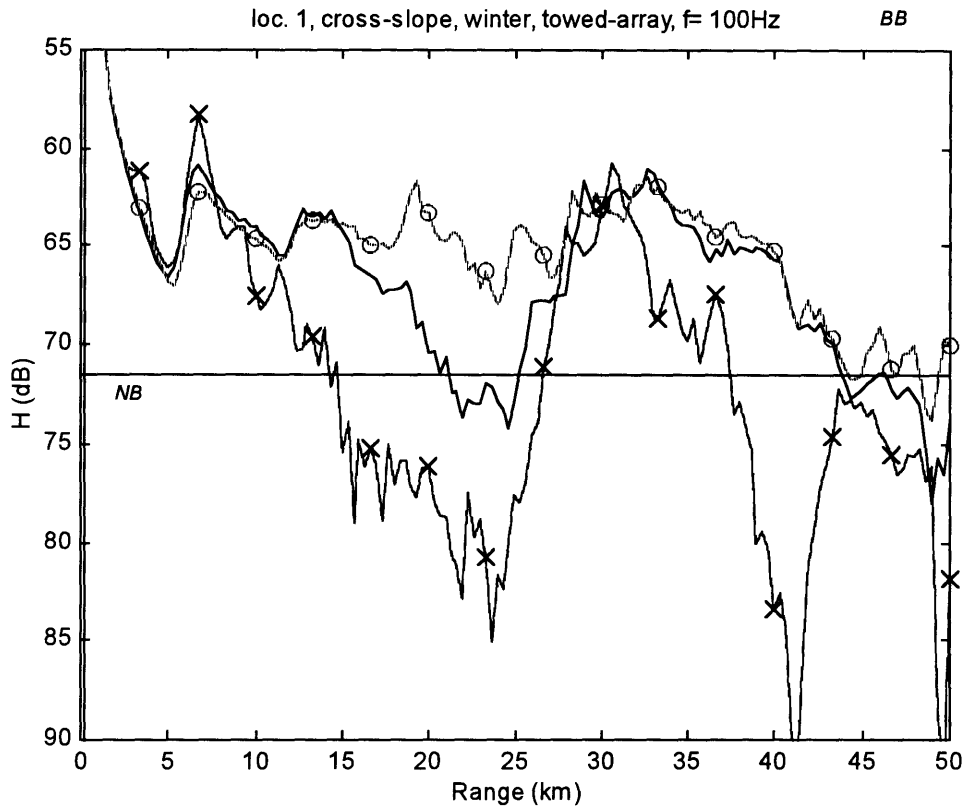
Figure A.10 (upper) & Figure A.11 (lower): Sonar performance, 1st location.

loc. 1, cross-slope, winter, towed-array, f= 500Hz

loc. 1, cross-slope, winter, hull-array, f= 500Hz
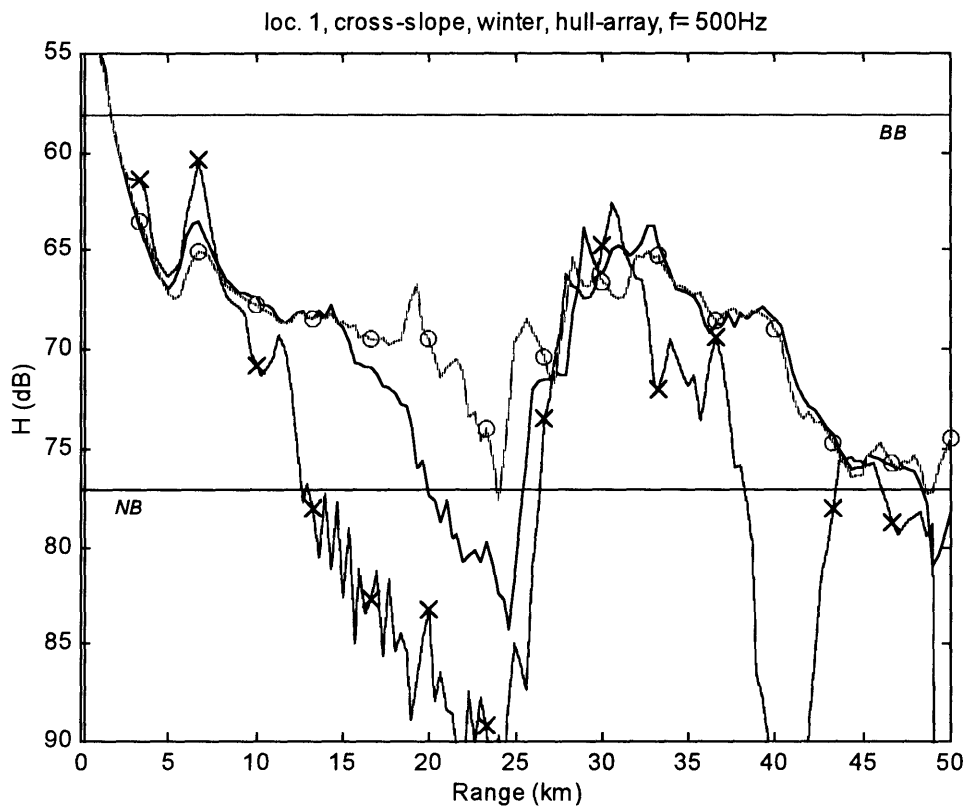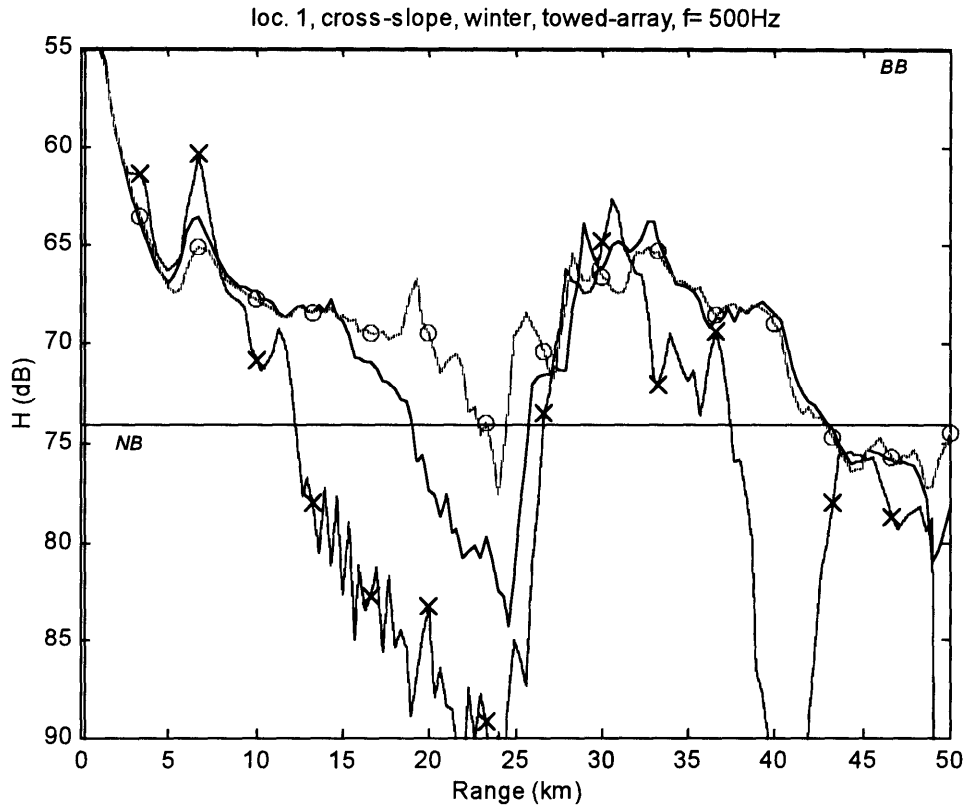
Figure A.12 (upper) & Figure A.13 (lower): Sonar performance, 1st location.
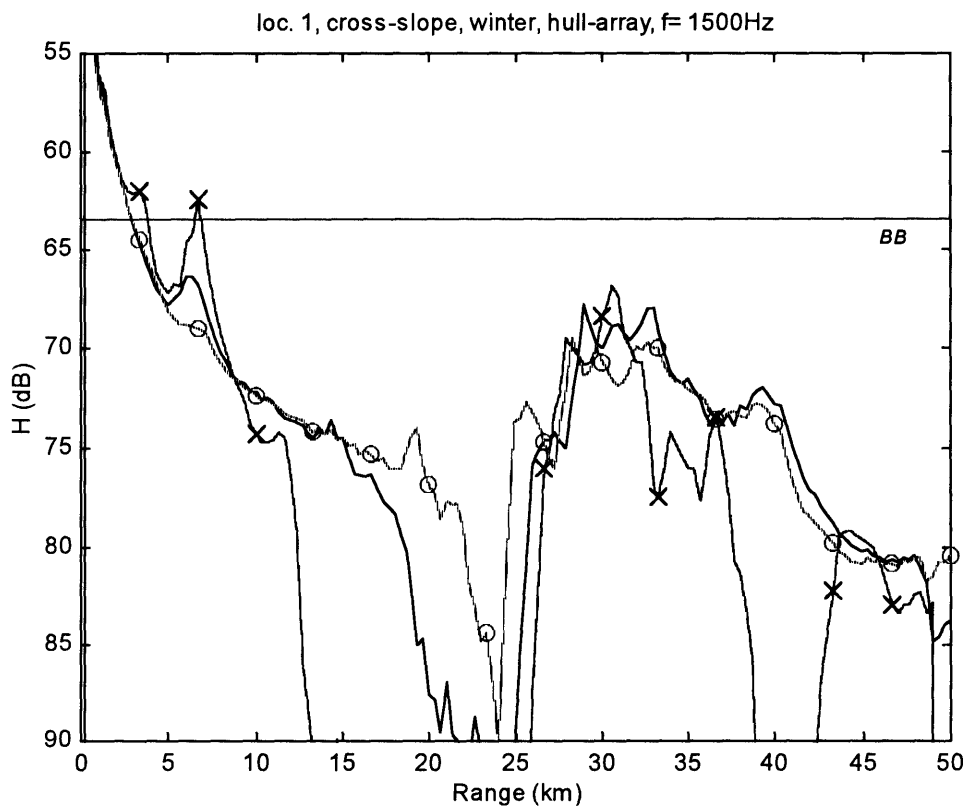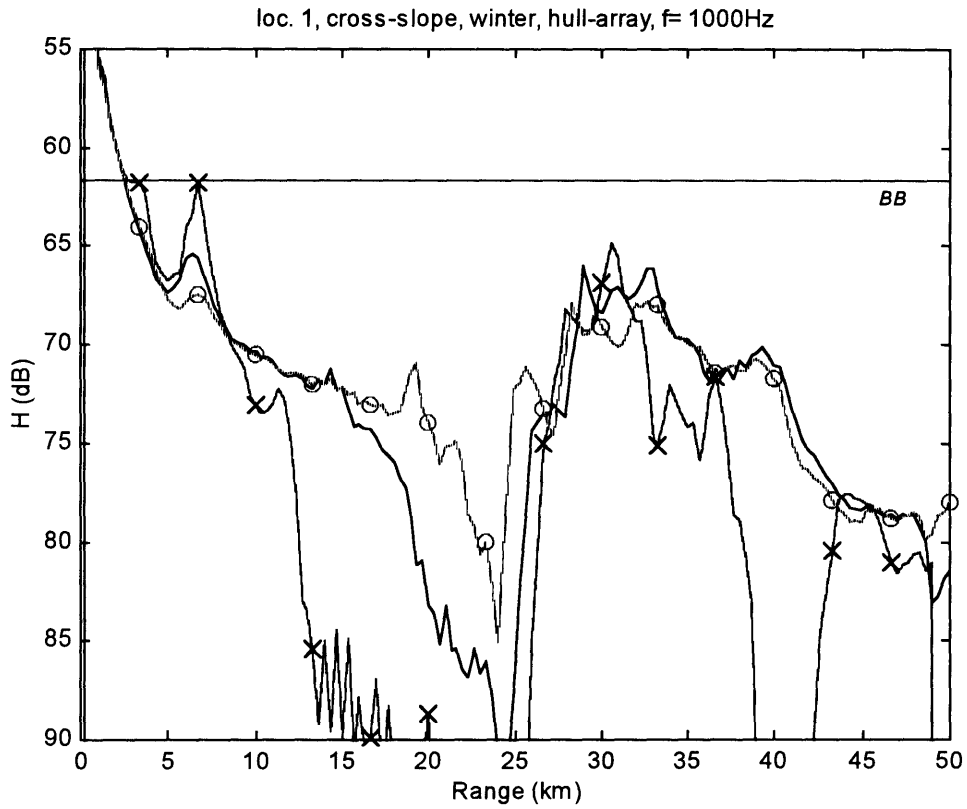
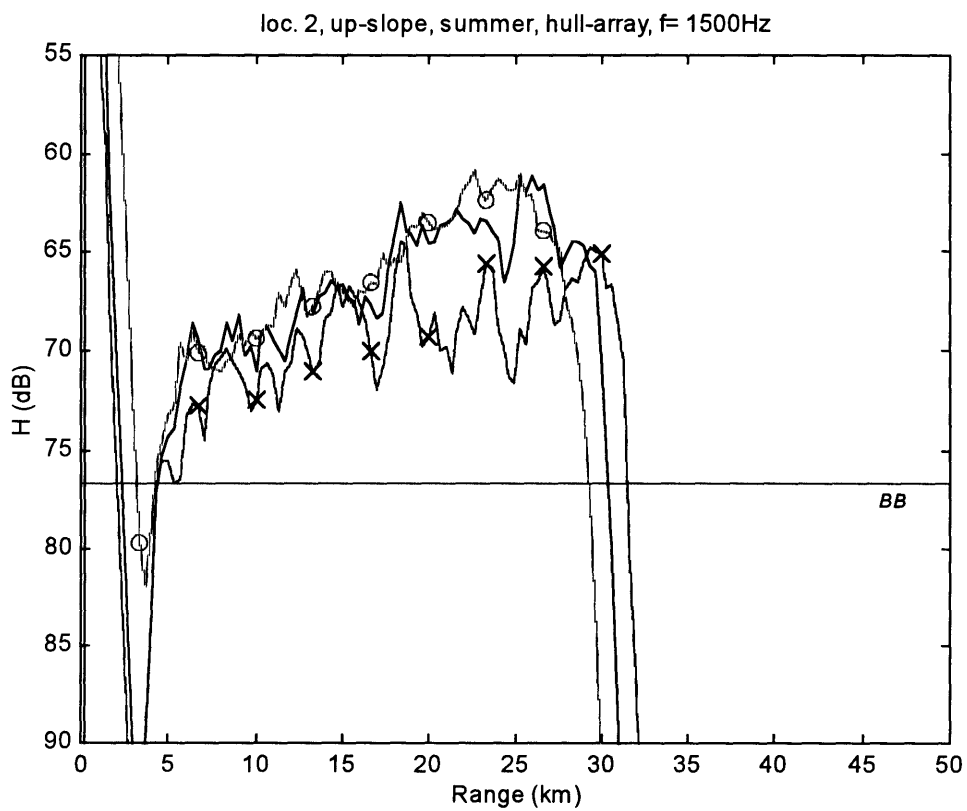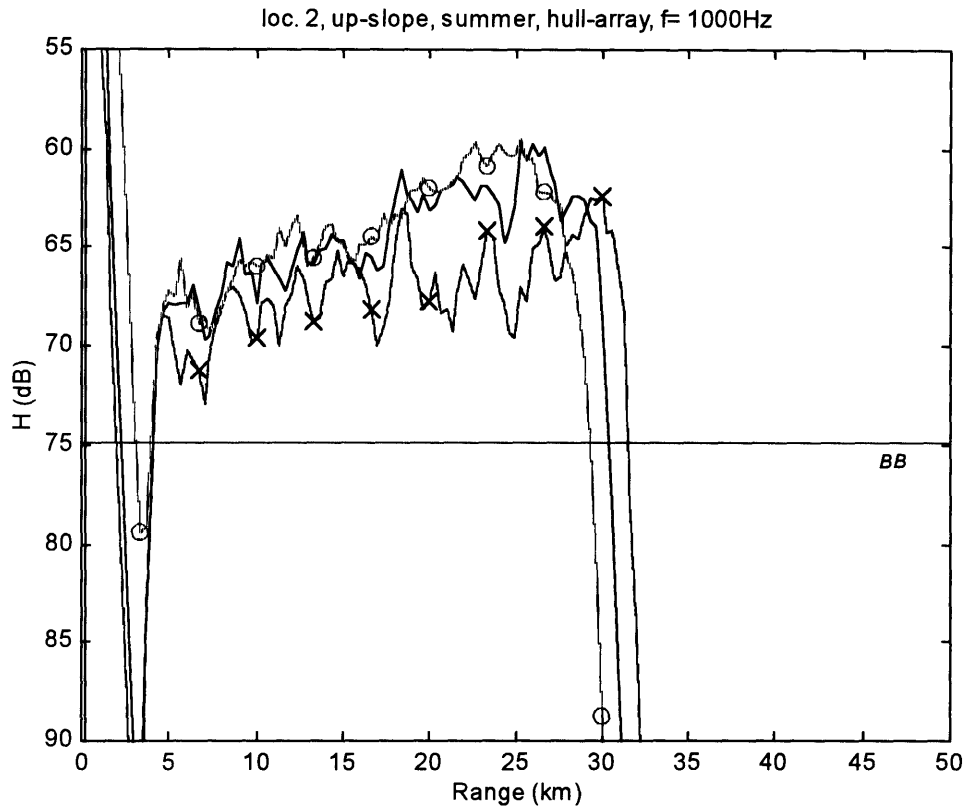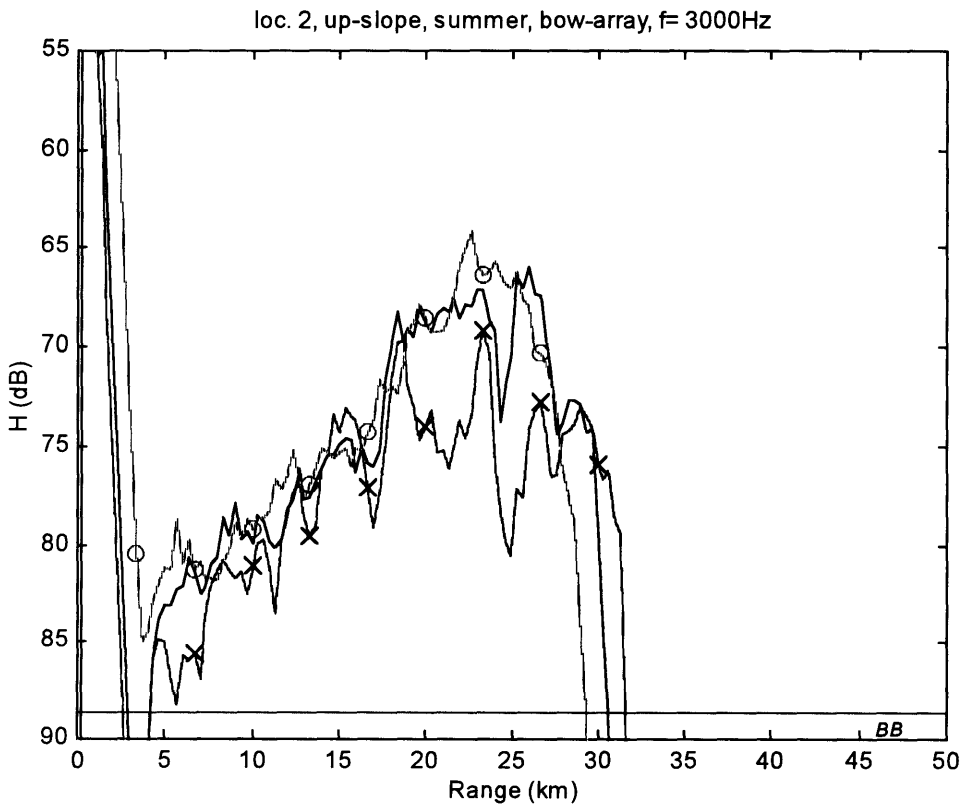Figure A.14 (upper) & Figure A.15 (lower): Sonar performance, 1st location.

loc. 1, cross-slope, winter, bow-array, f= 2000Hz

loc. 1, cross-slope, winter, bow-array, f= 3000Hz
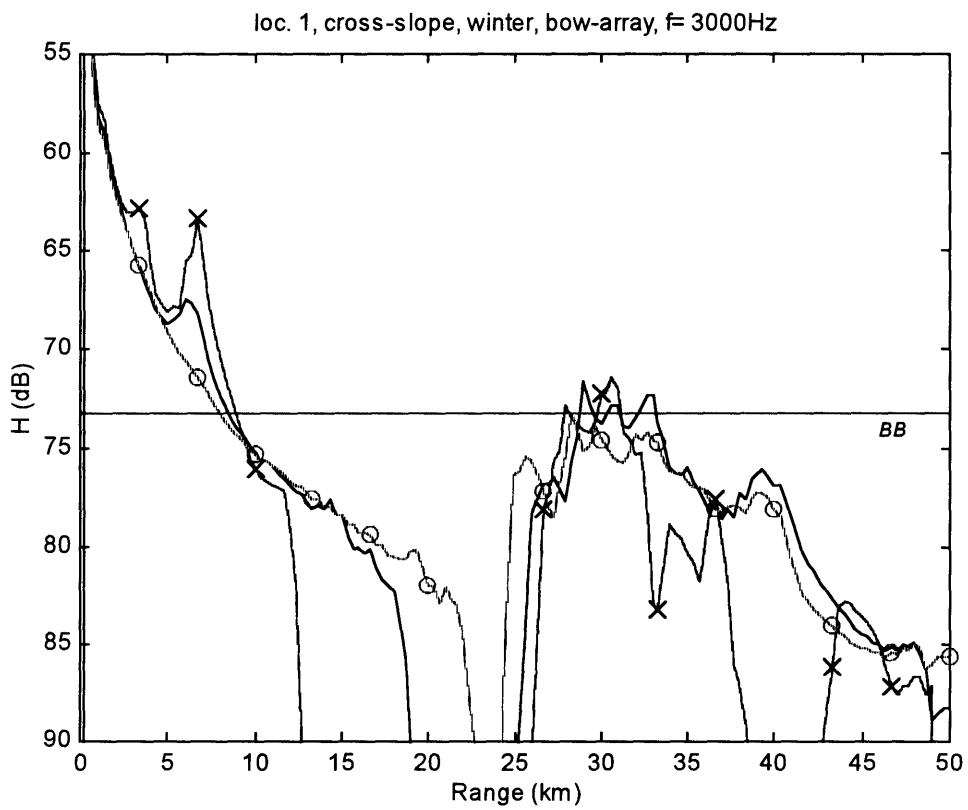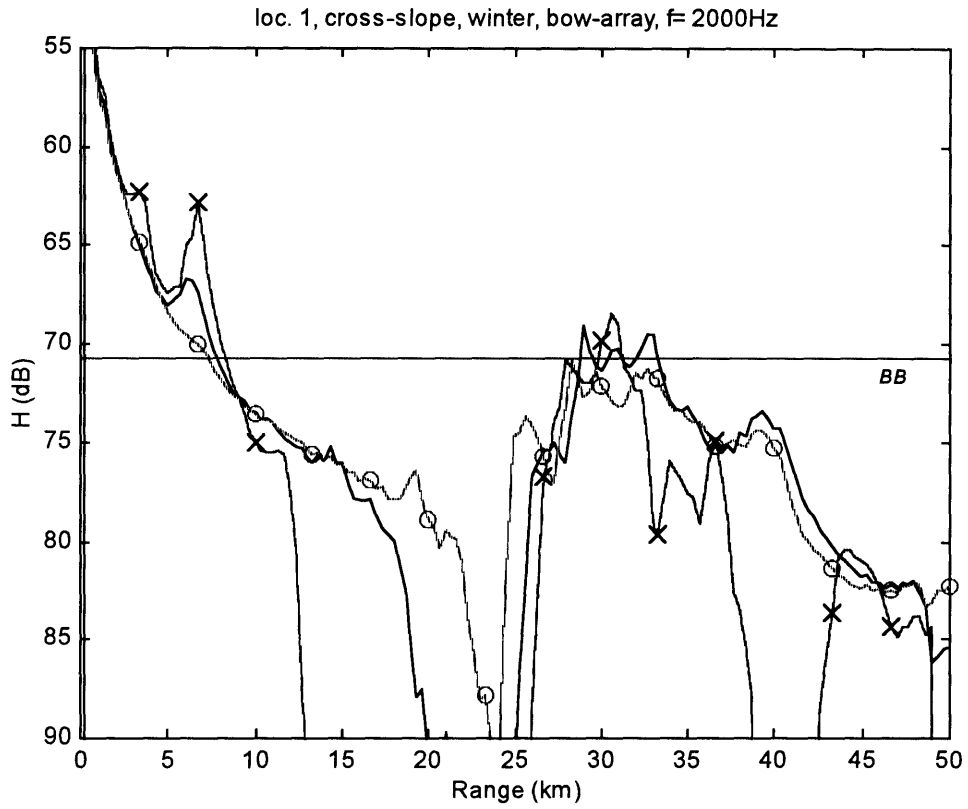
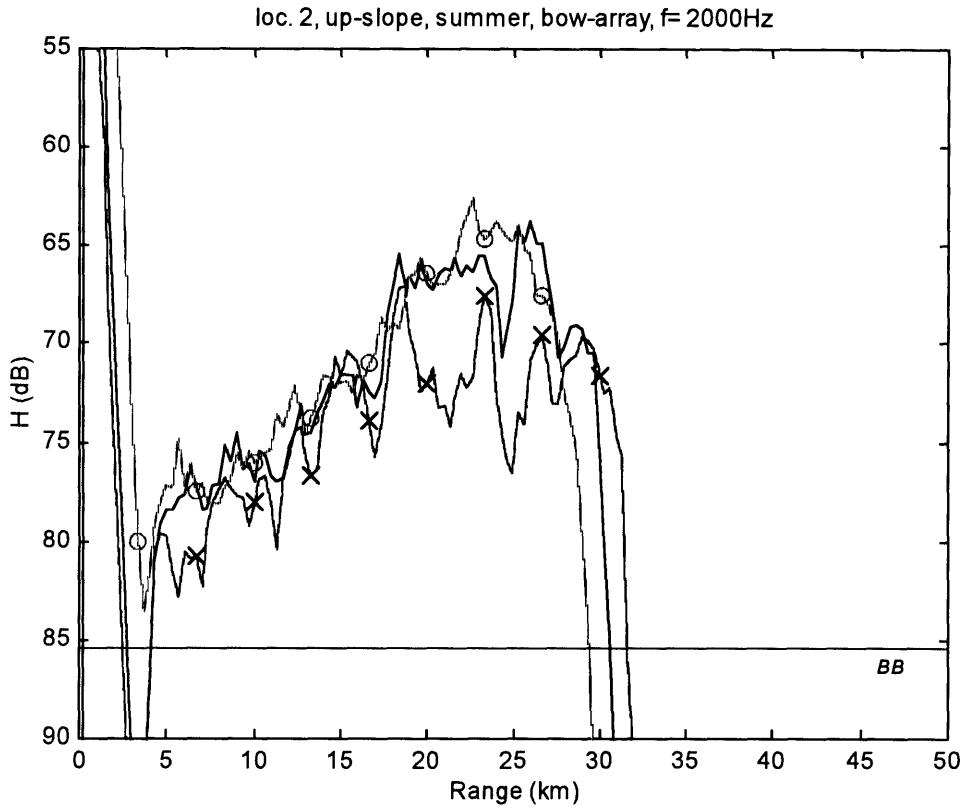Figure A.16 (upper) & Figure A.17 (lower): Sonar performance, 1st location.

loc. 1, cross-slope, winter, bow-array, f= 5000Hz
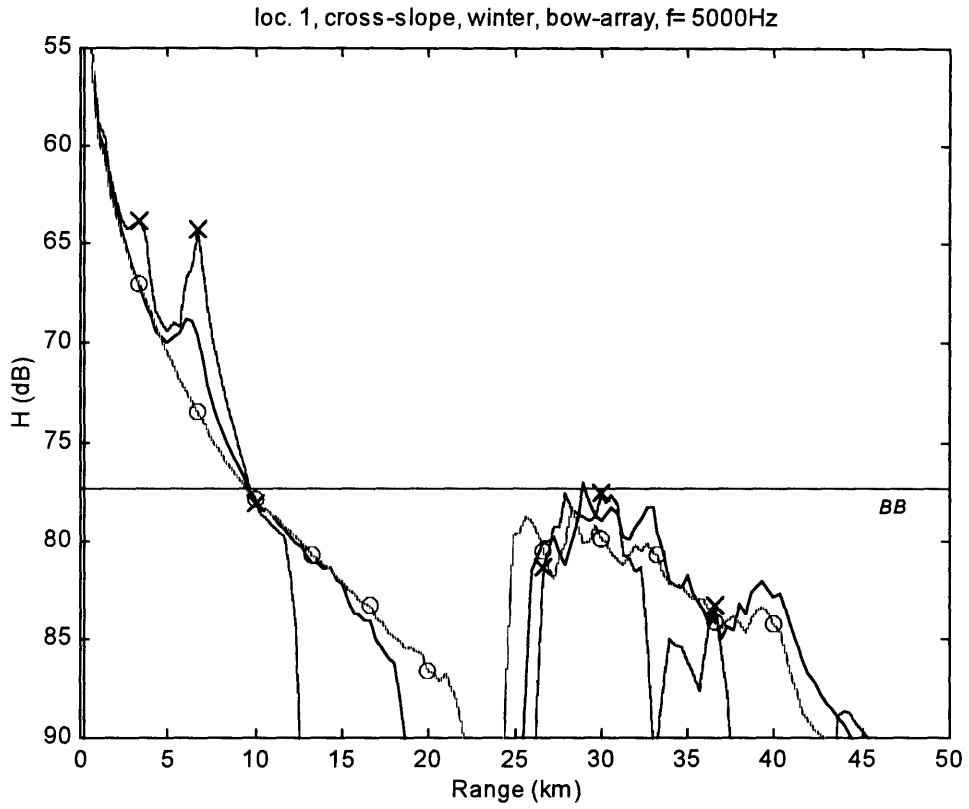
Figure A.18: Sonar performance, 1st location.

loc. 1, up-slope, summer, towed-array, f= 100Hz

loc. 1, up-slope, summer, towed-array, f= 200Hz
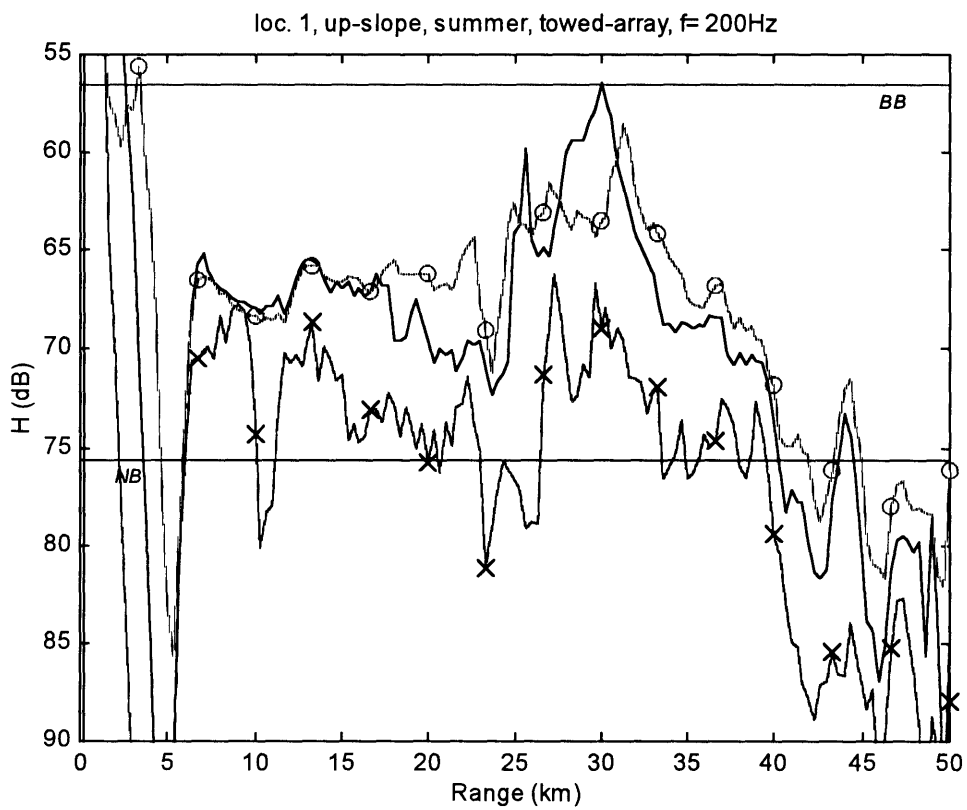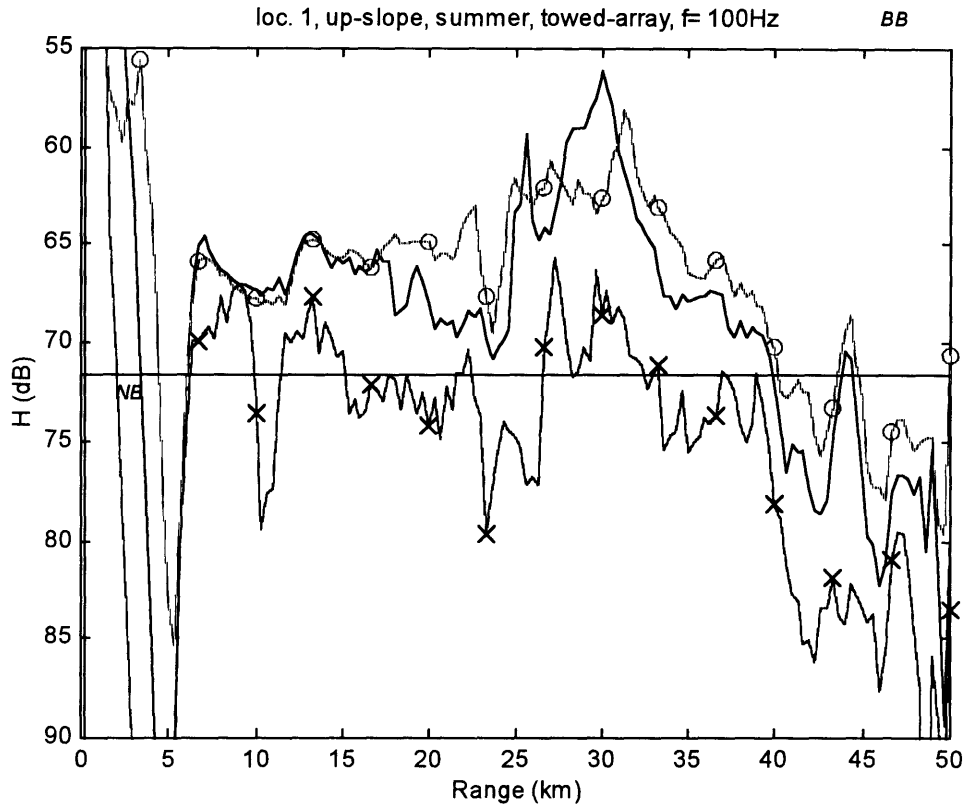
Figure A.19 (upper) & Figure A.20 (lower): Sonar performance, 1st location.
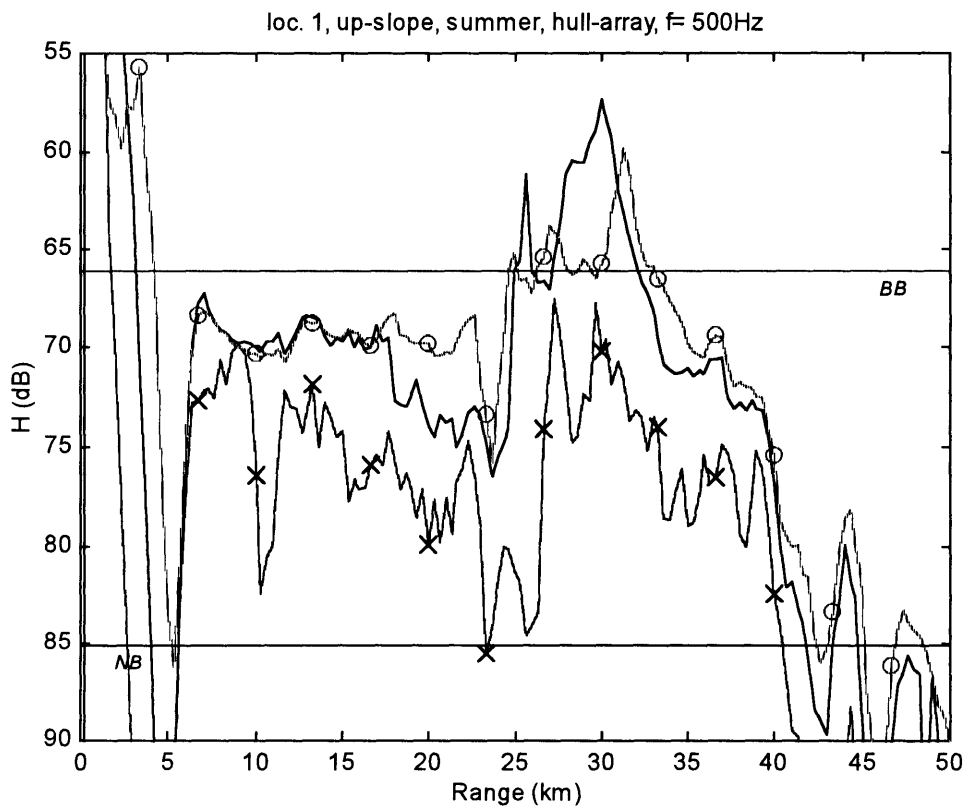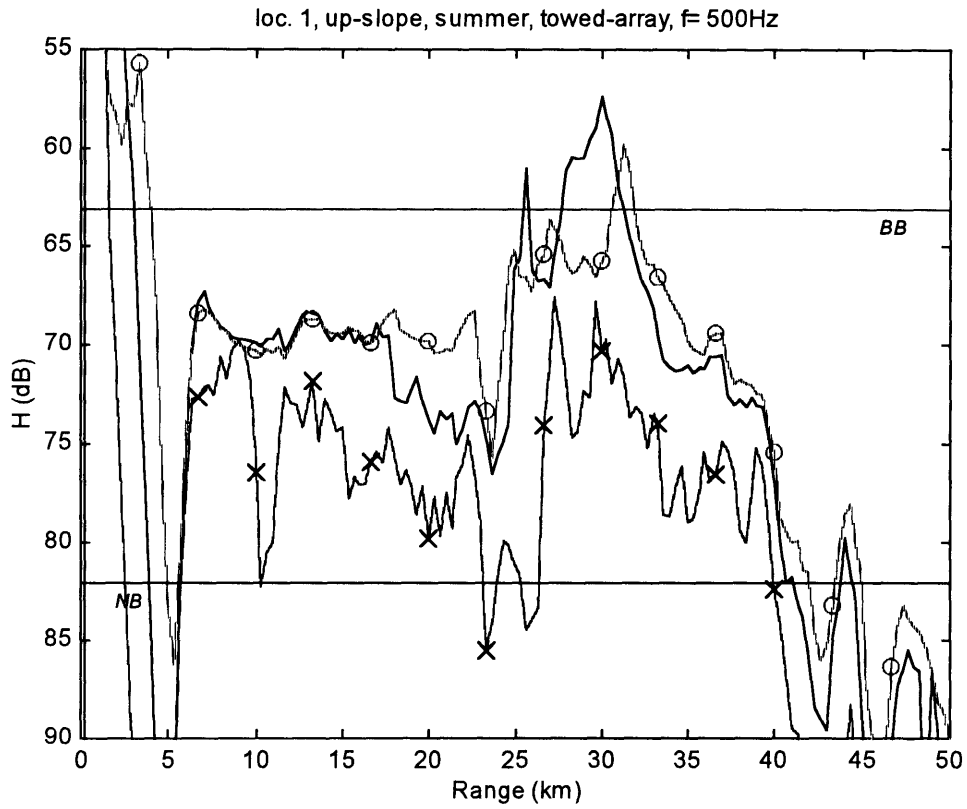
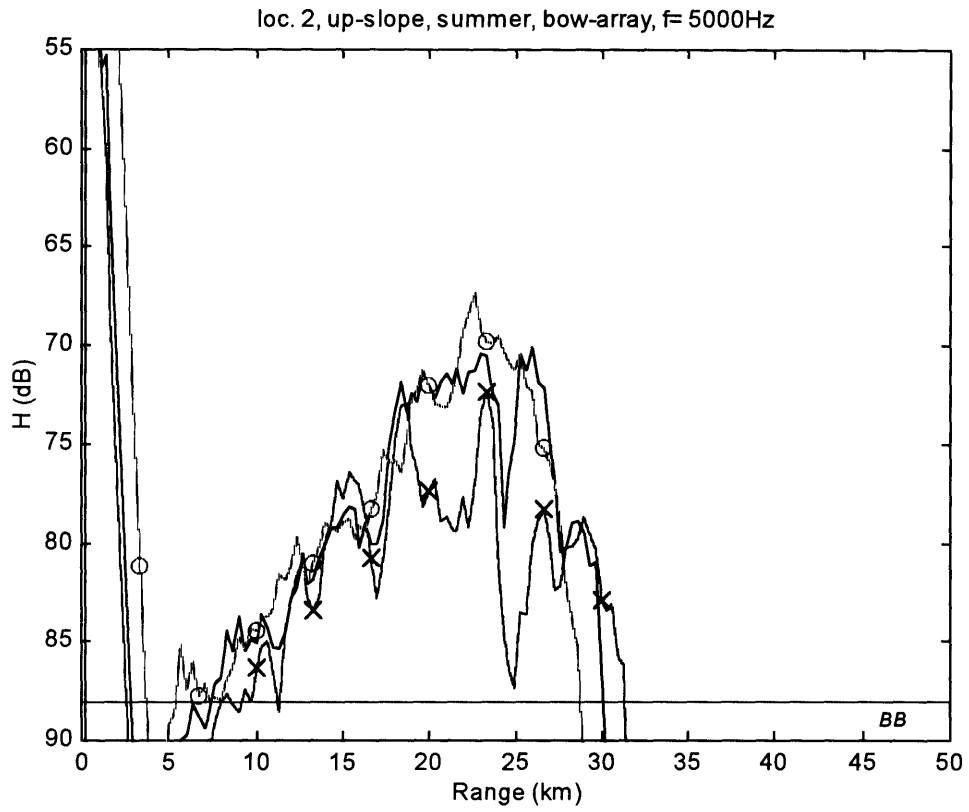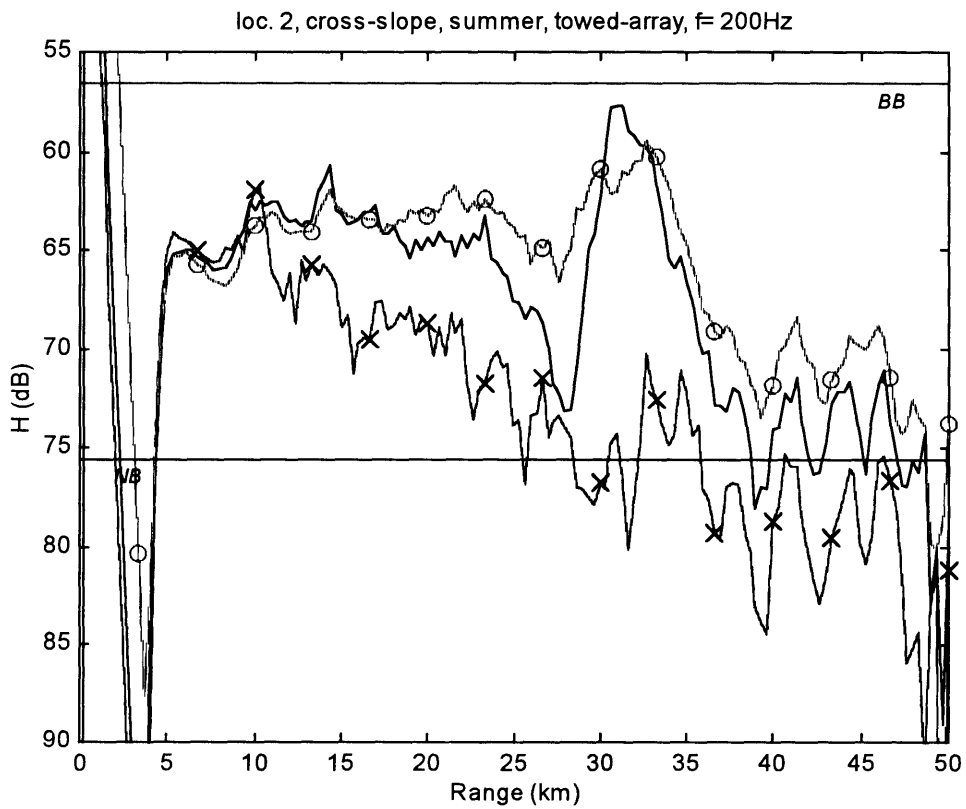Figure A.21 (upper) & Figure A.22 (lower): Sonar performance, 1st location.
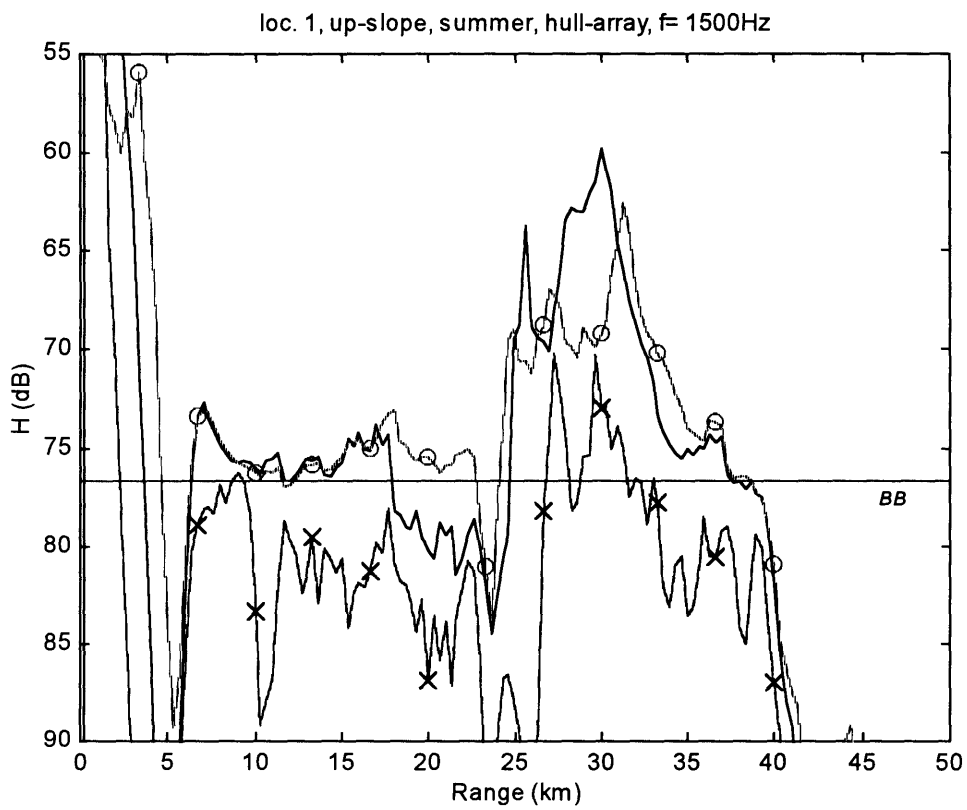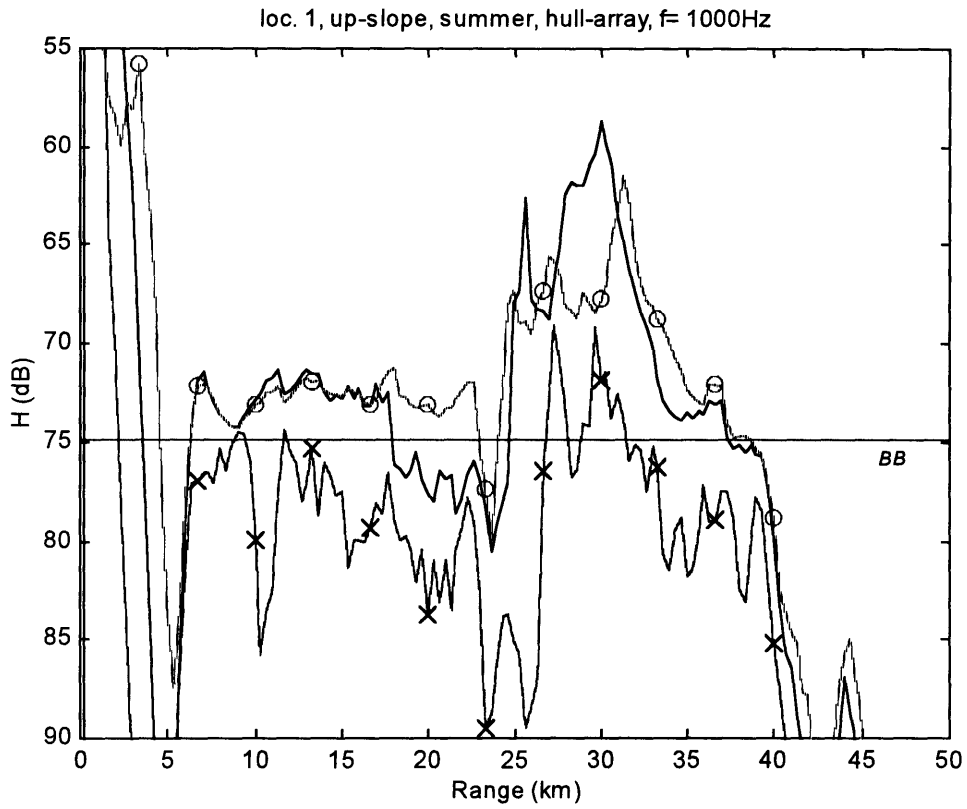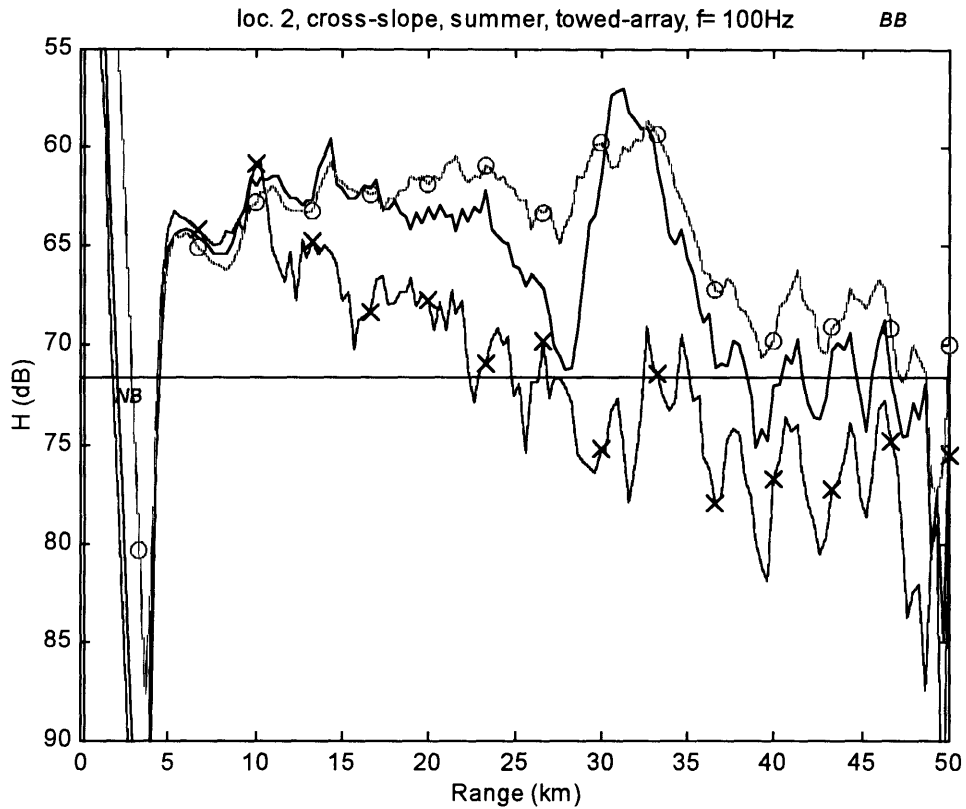
Figure A.23 (upper) & Figure A.24 (lower): Sonar performance, 1st location.
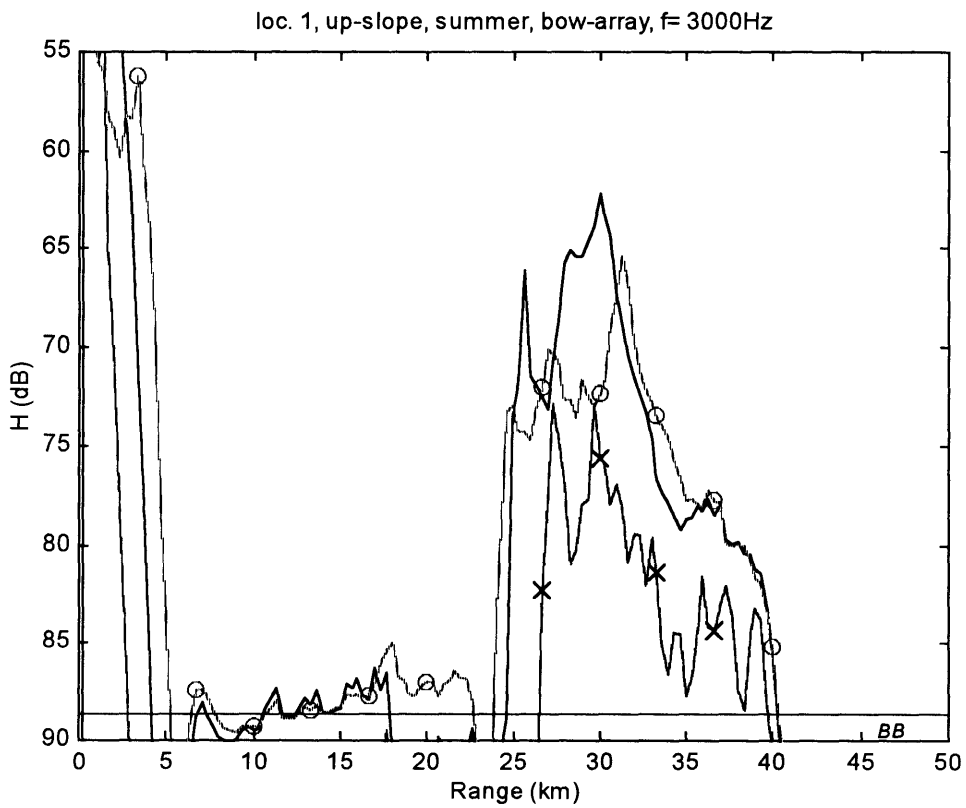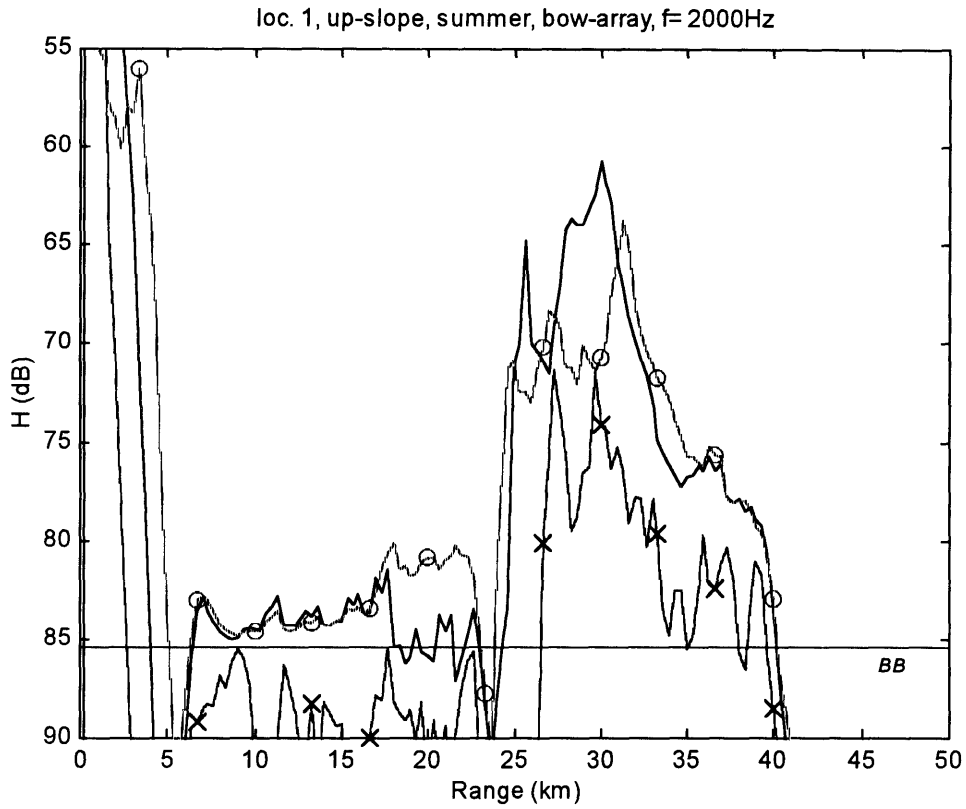
Figure A.25 (upper) & Figure A.26 (lower): Sonar performance, 1st location.

loc. 1, up-slope, summer, bow-array, f= 5000Hz
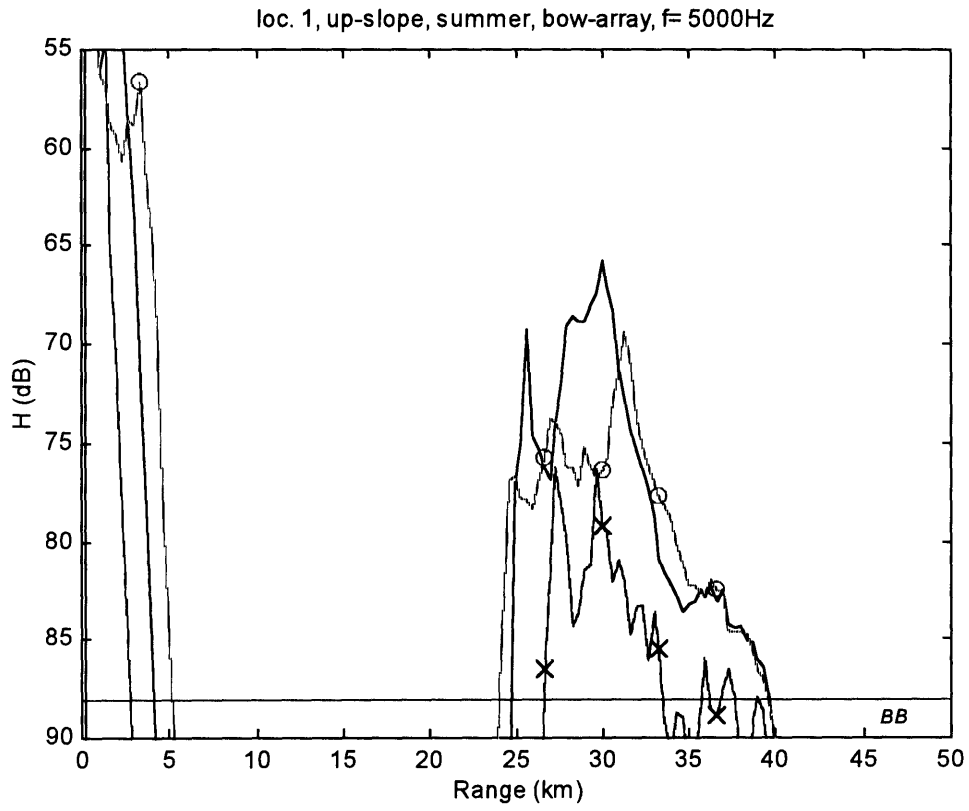
Figure A.27: Sonar performance, 1st location.

loc. 1, cross-slope, summer, towed-array, f= 100Hz

loc. 1, cross-slope, summer, towed-array, f= 200Hz
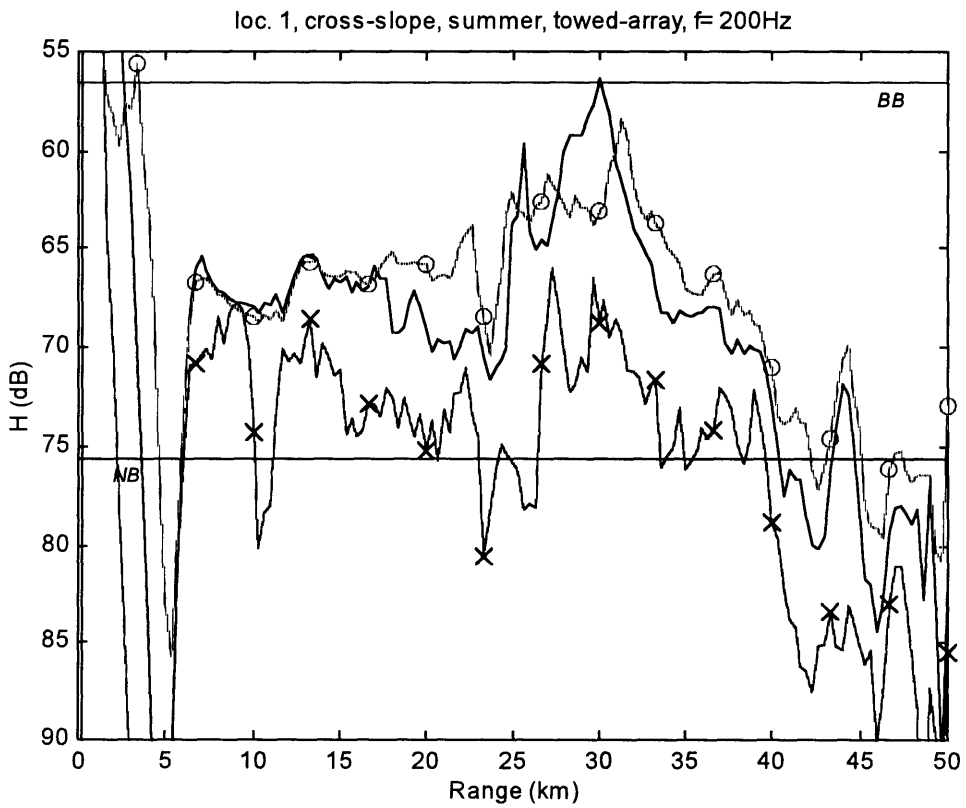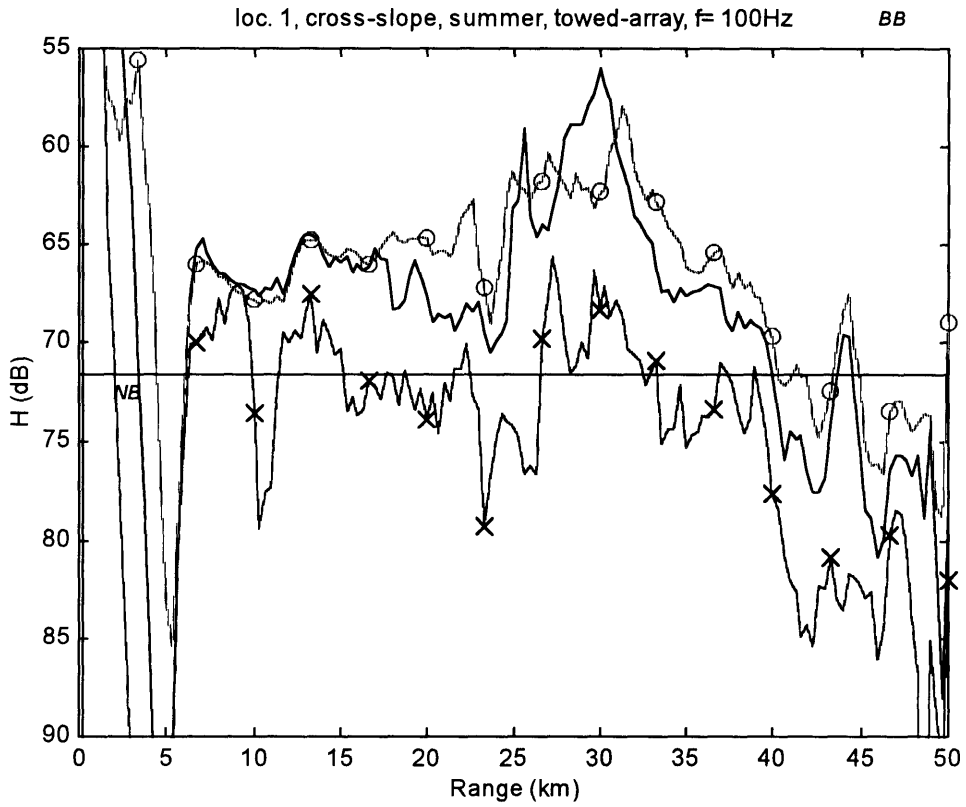
Figure A.28 (upper) & Figure A.29 (lower): Sonar performance, 1st location.

loc. 1, cross-slope, summer, towed-array, f= 500Hz

loc. 1, cross-slope, summer, hull-array, f= 500Hz
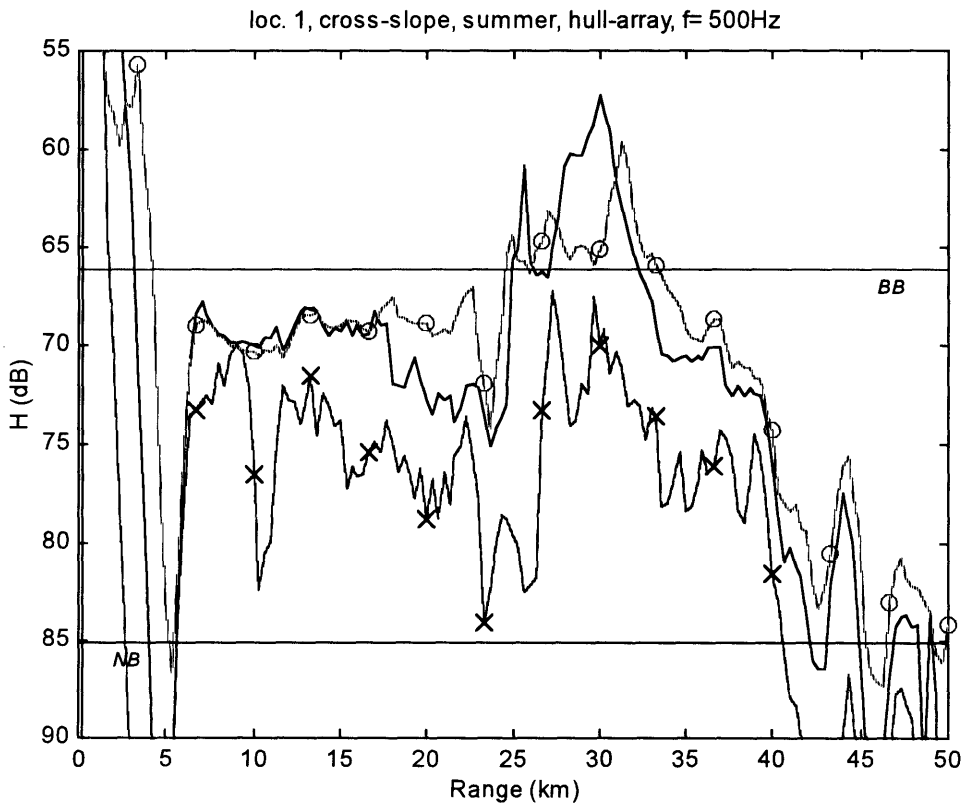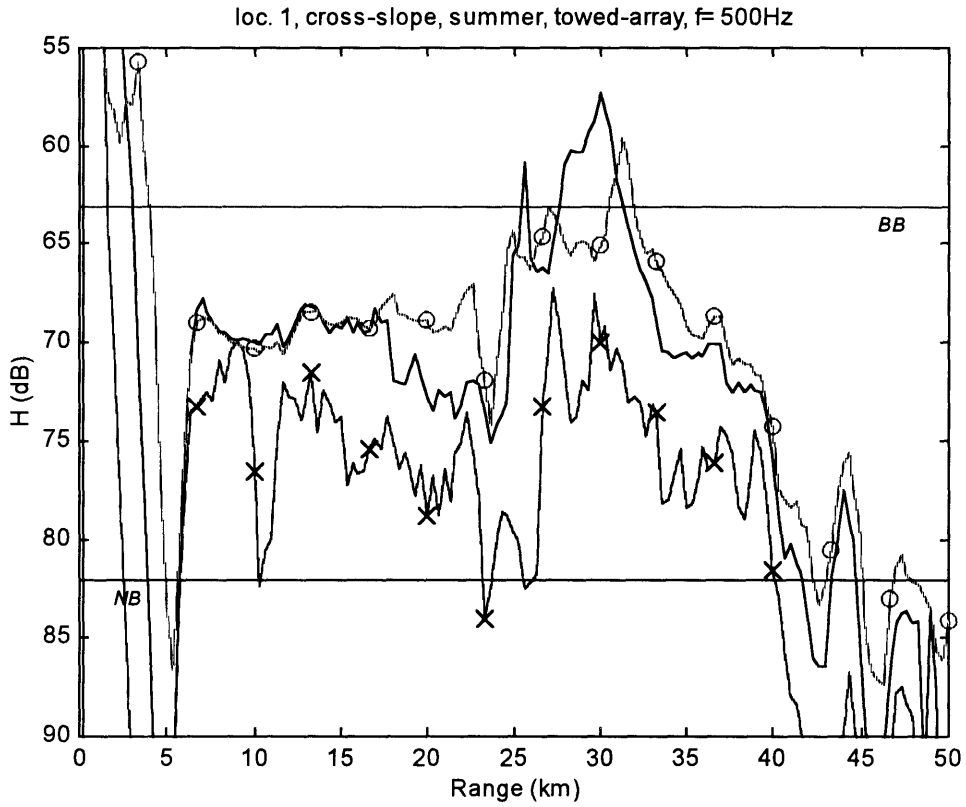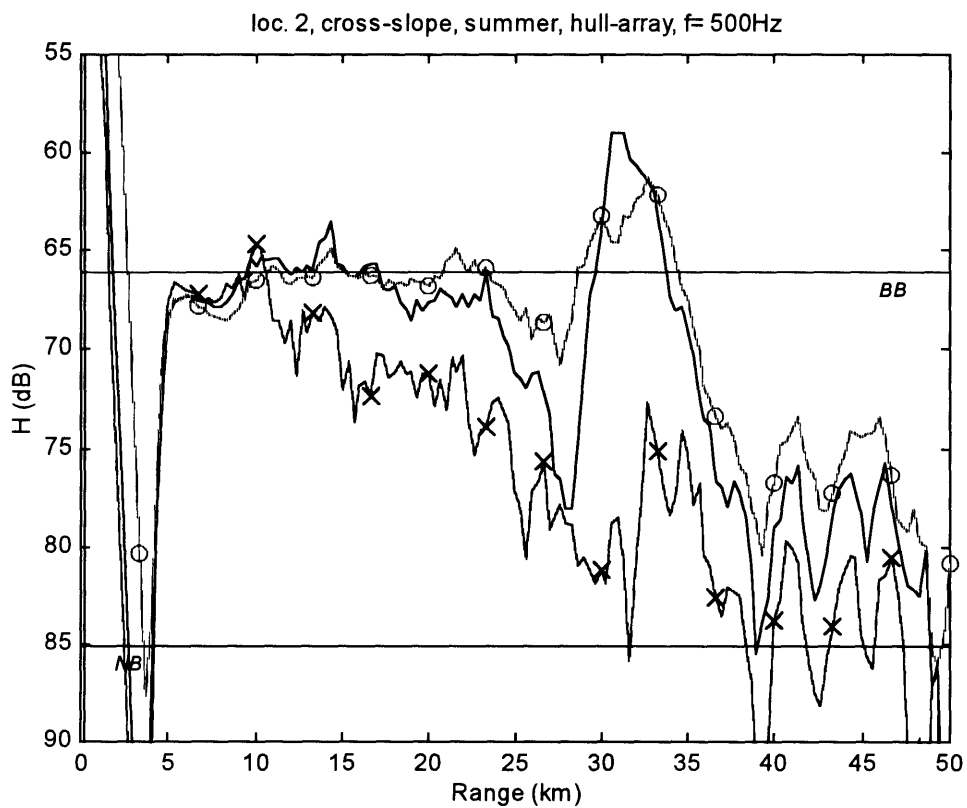
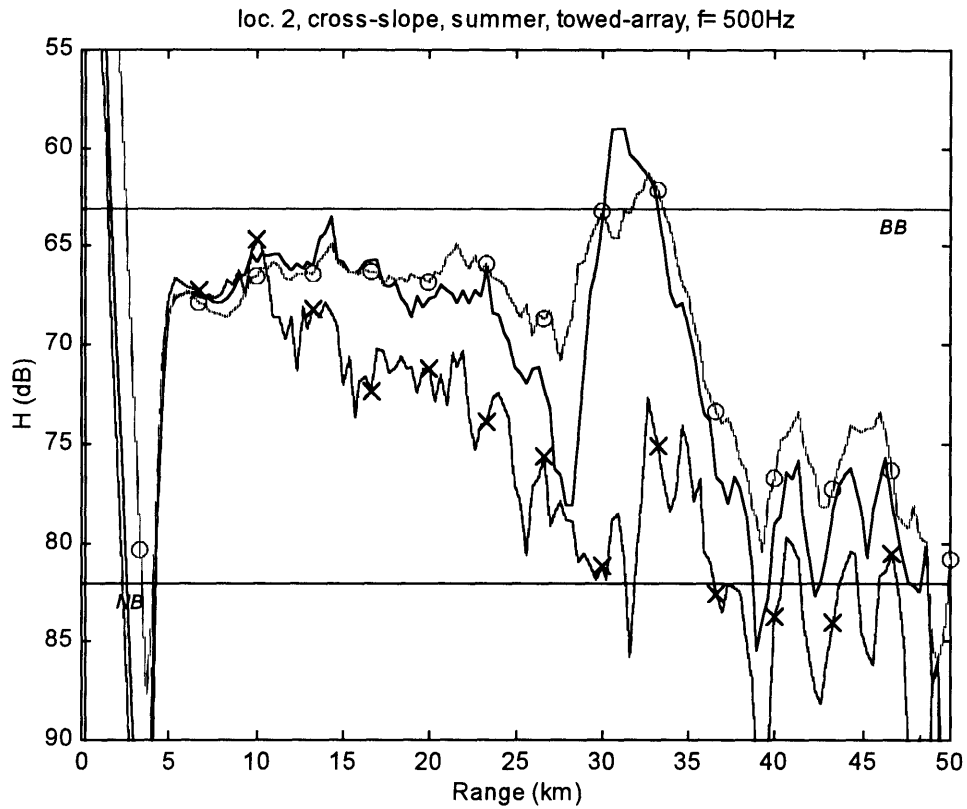Figure A.30 (upper) & Figure A.31 (lower): Sonar performance, 1st location.

loc. 1, cross-slope, summer, hull-array, f= 1000Hz

loc. 1, cross-slope, summer, hull-array, f= 1500Hz
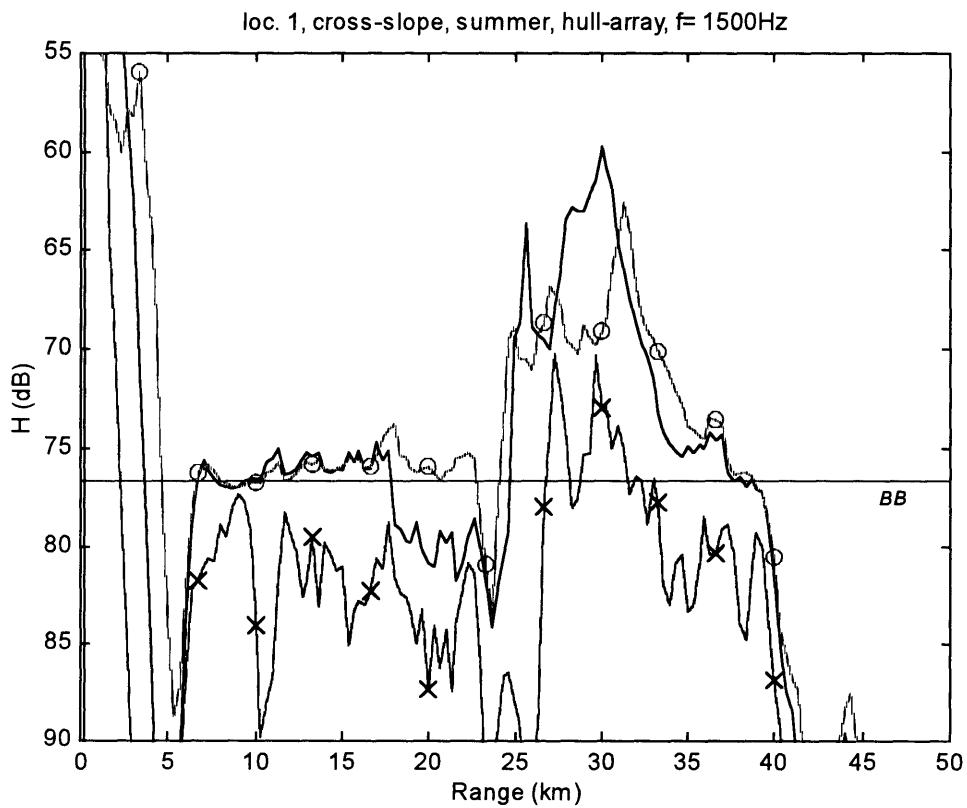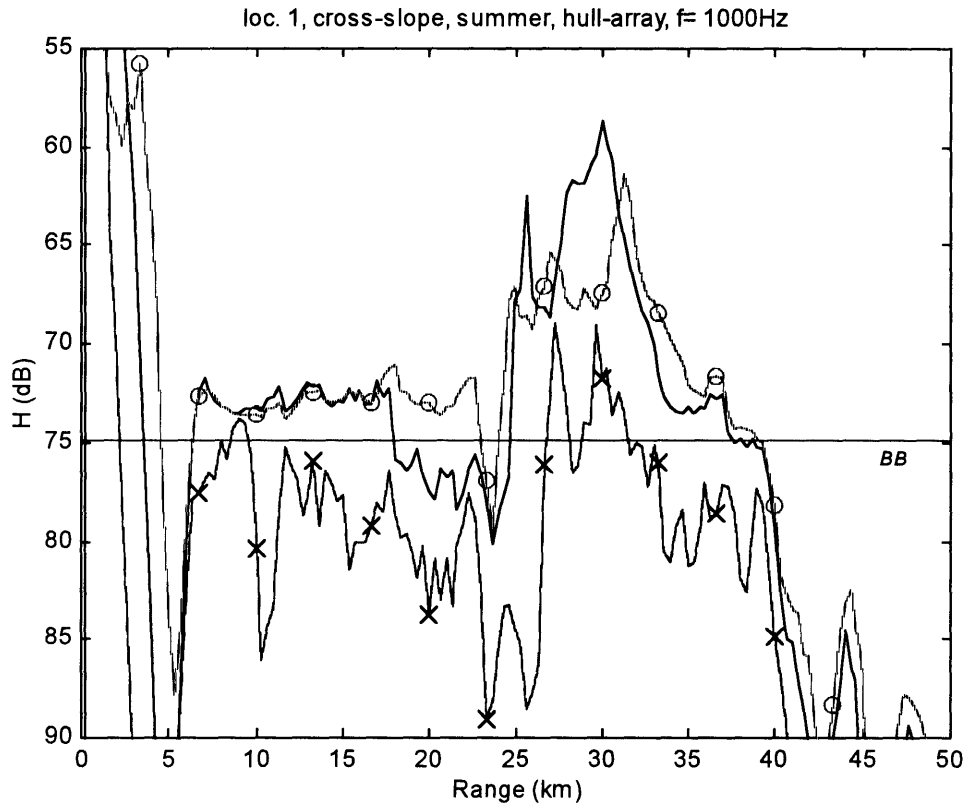
Figure A.32 (upper) & Figure A.33 (lower): Sonar performance, 1st location.

loc. 1, cross-slope, summer, bow-array, f= 2000Hz

loc. 1, cross-slope, summer, bow-array, f= 3000Hz
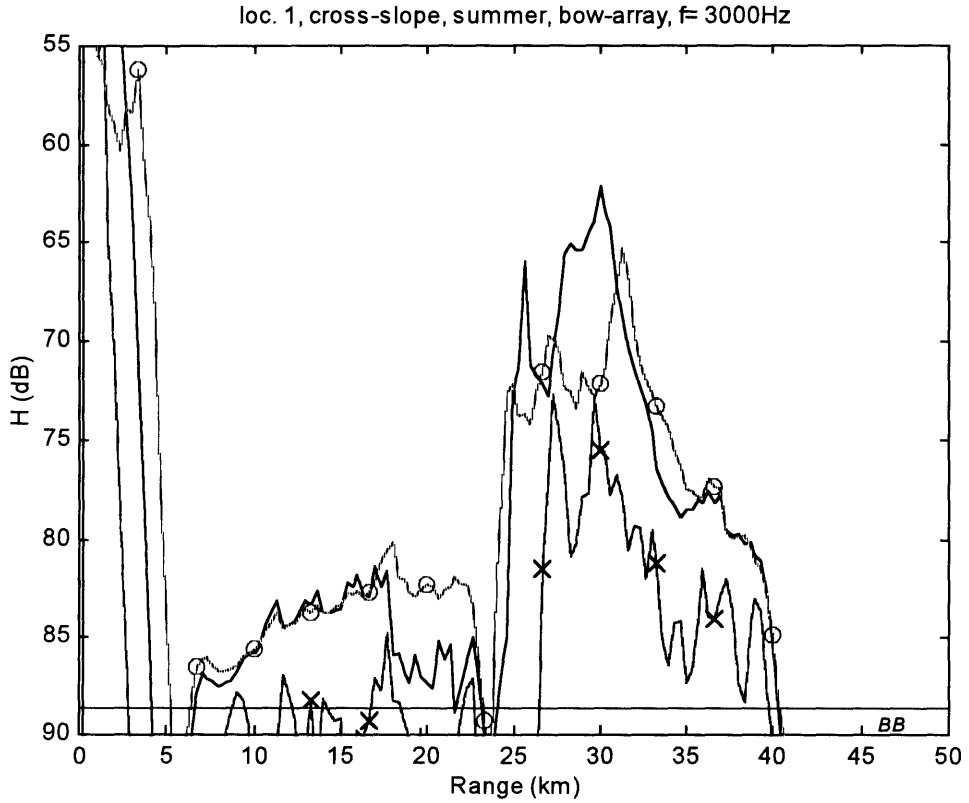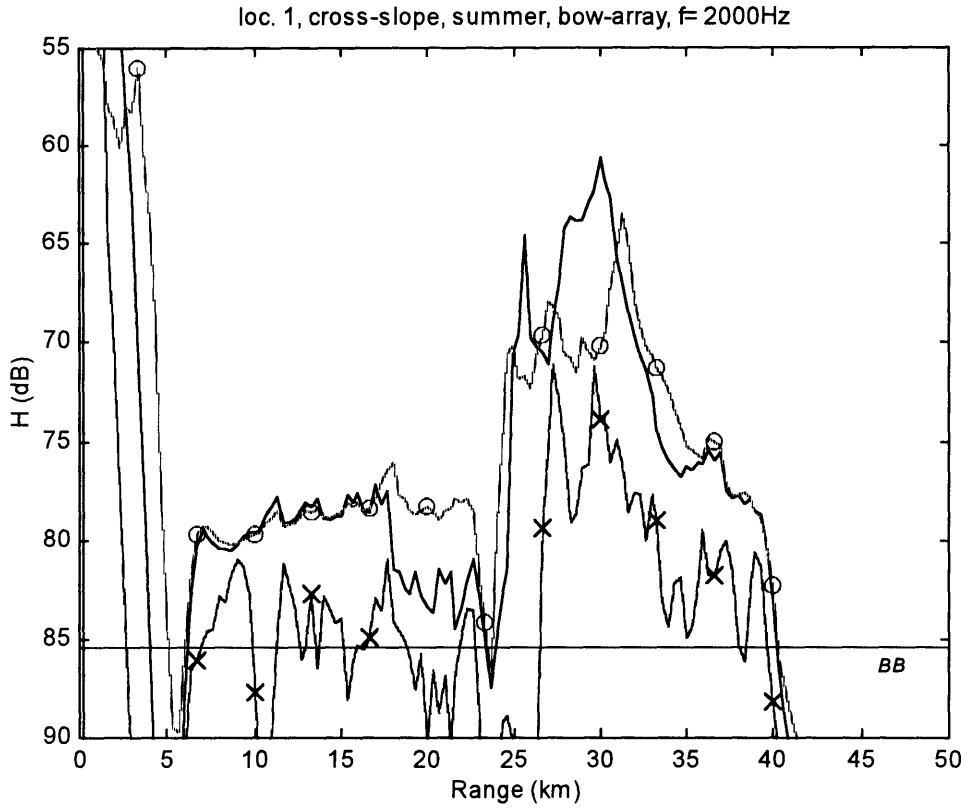
Figure A.34 (upper) & Figure A.35 (lower): Sonar performance, 1st location.

loc. 1, cross-slope, summer, bow-array, f= 5000Hz
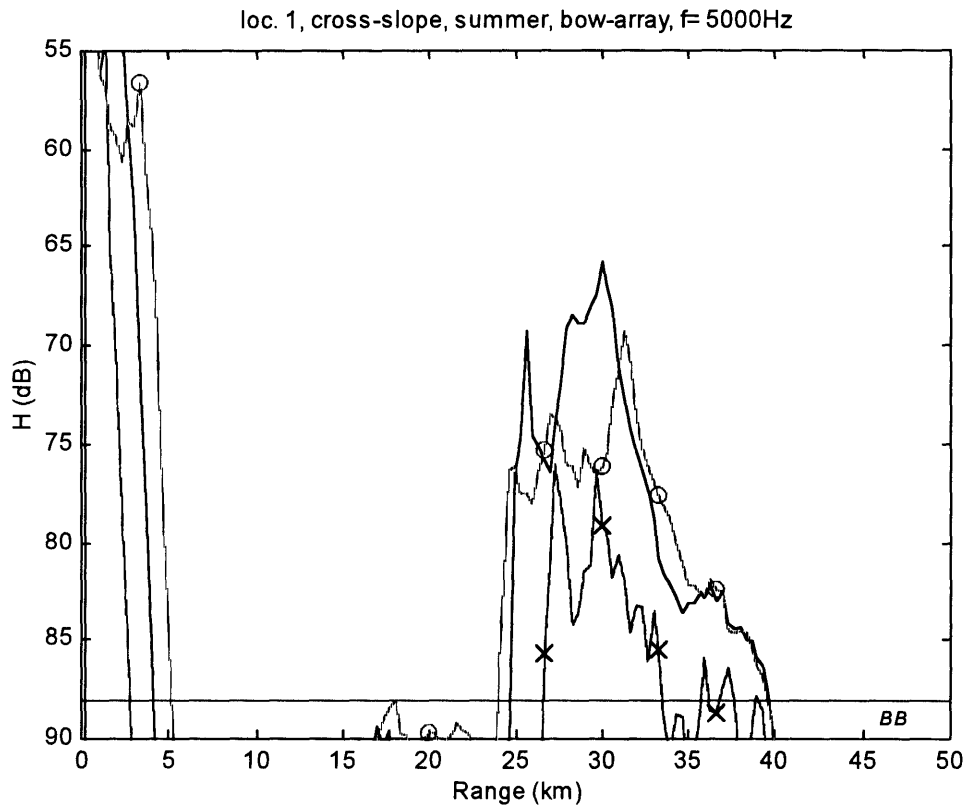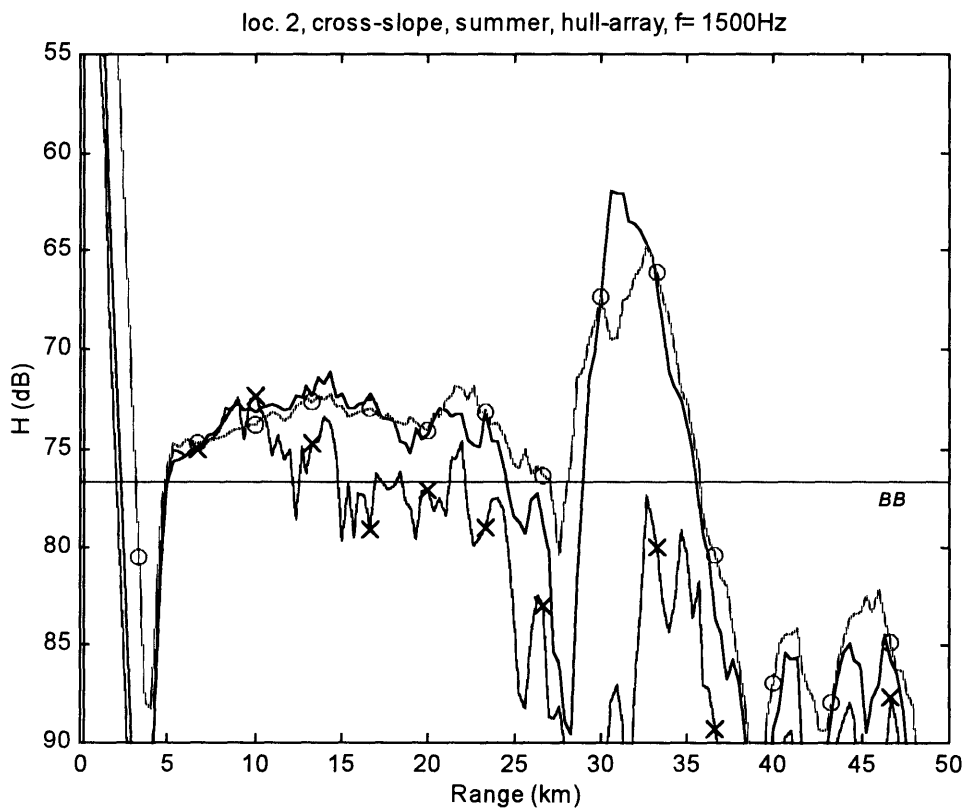
Figure A.36: Sonar performance, 1st location.
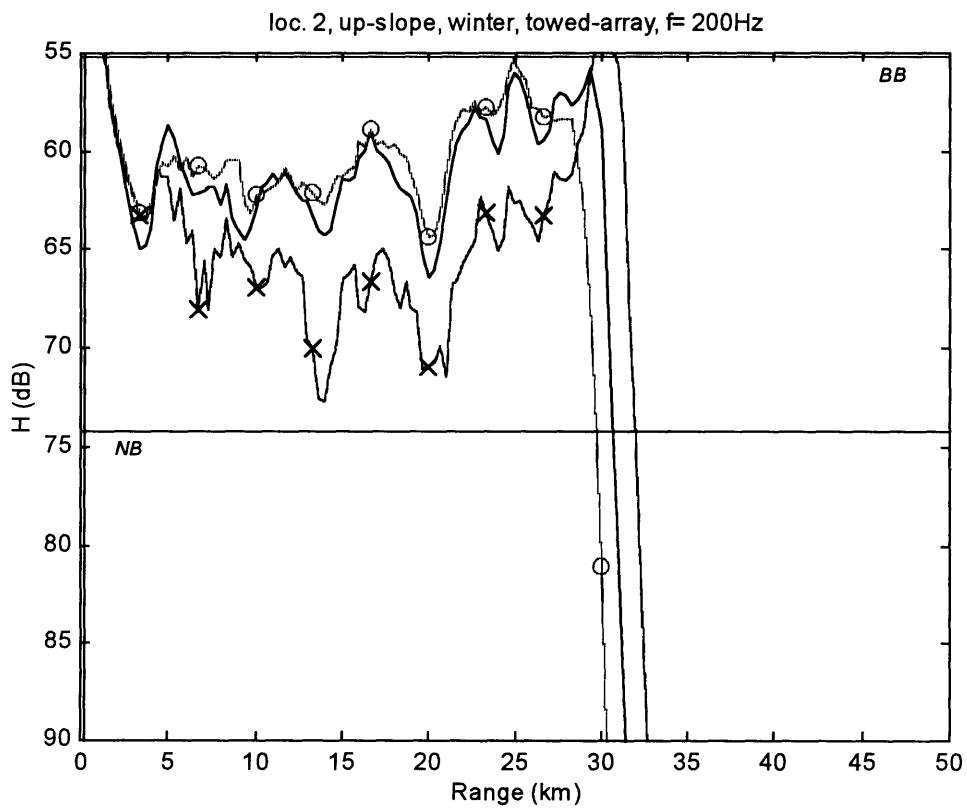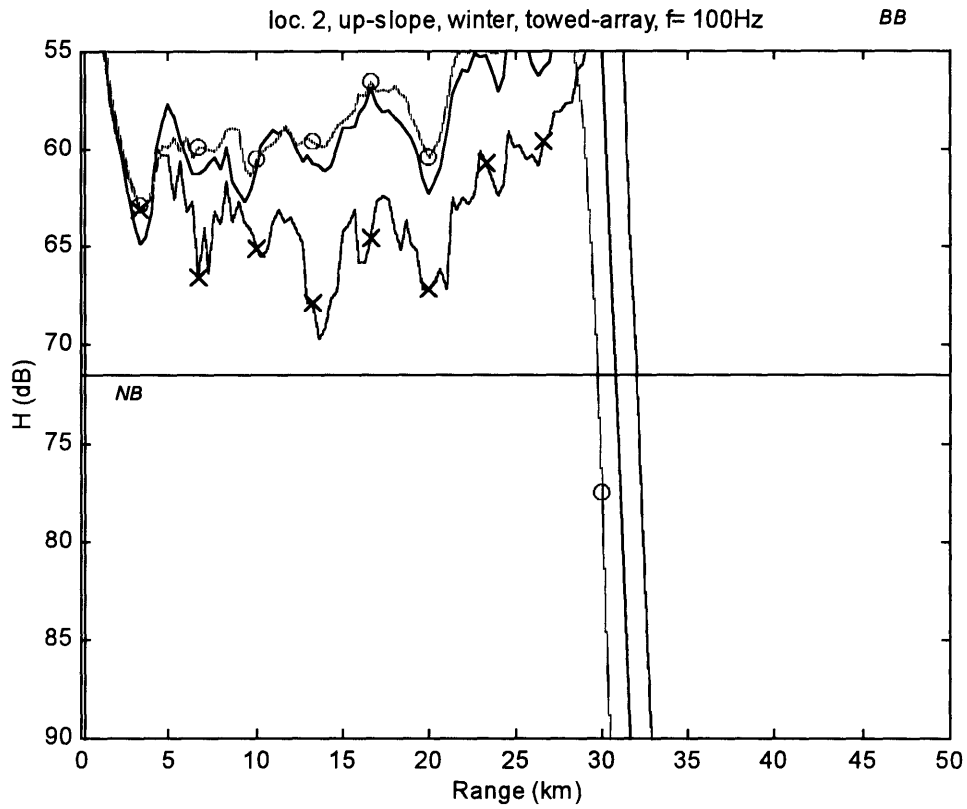
Figure A.37 (upper) & Figure A.38 (lower): Sonar performance, 2nd location.

loc. 2, up-slope, winter, towed-array, f= 500Hz

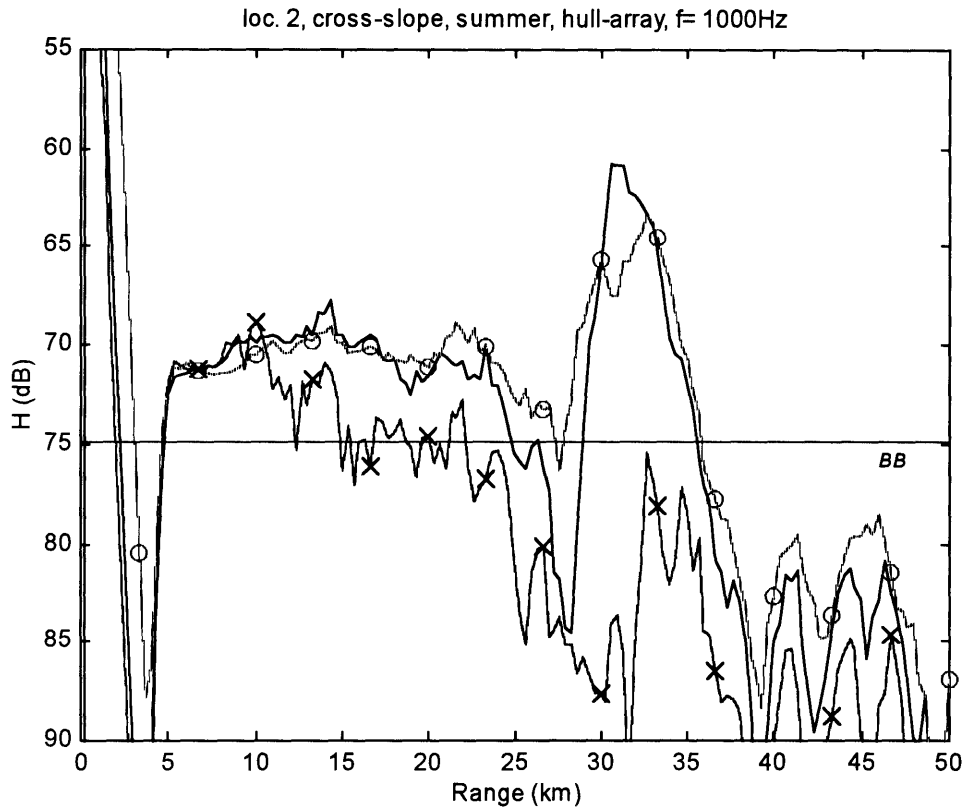loc. 2, up-slope, winter, hull-array, f= 500Hz
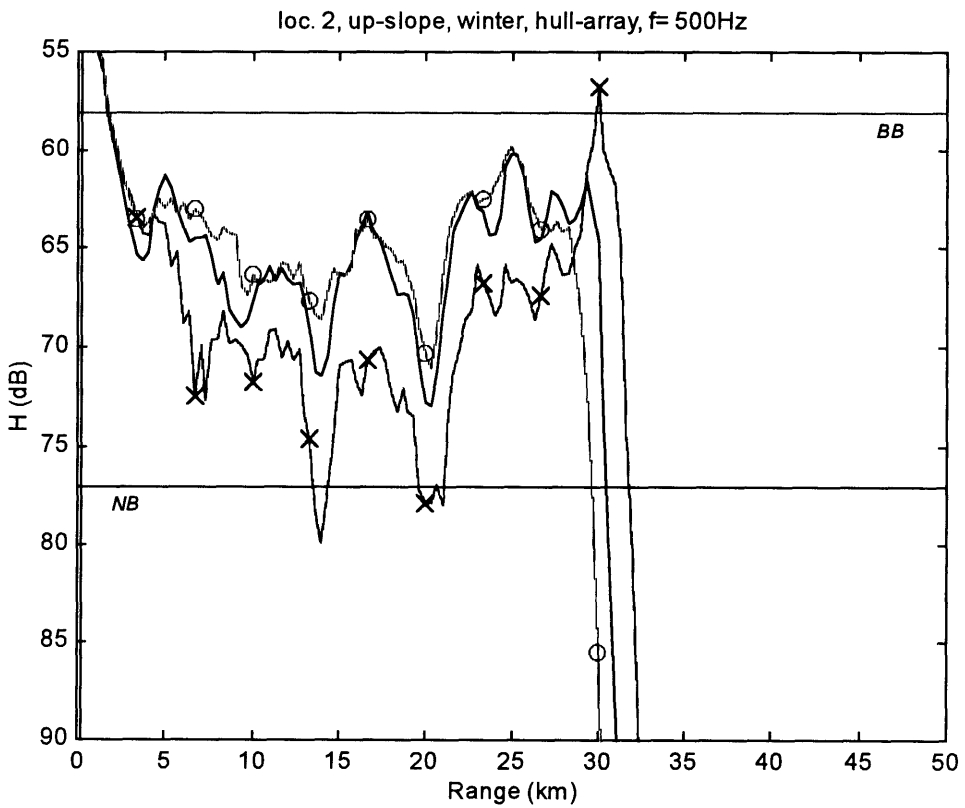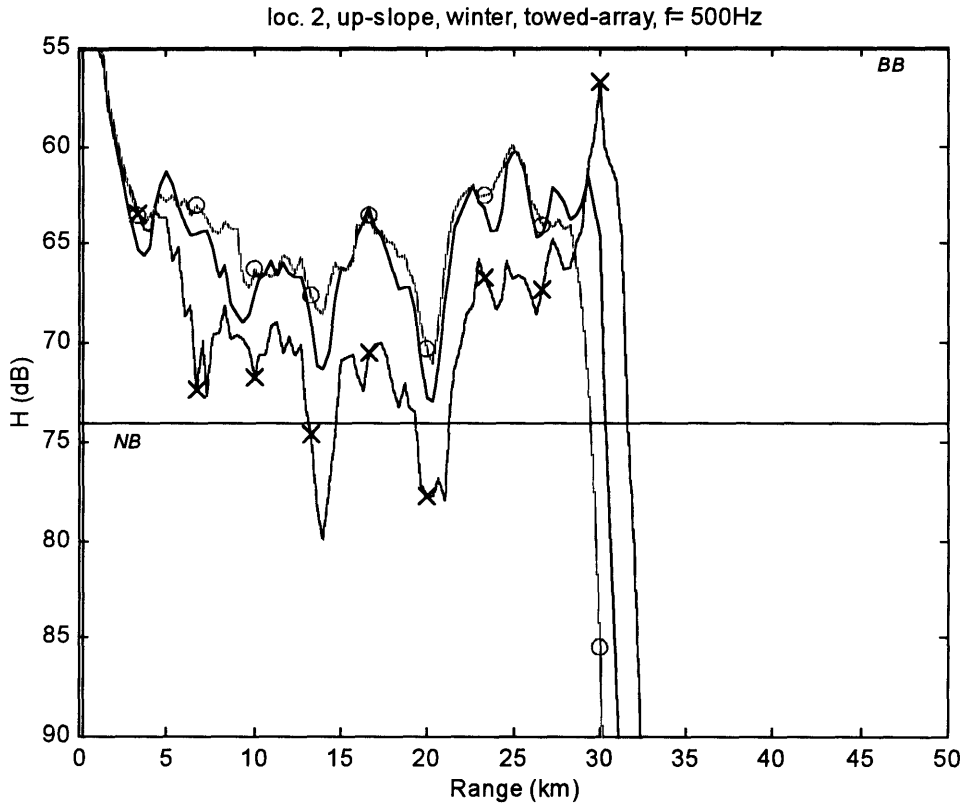
Figure A.39 (upper) & Figure A.40 (lower): Sonar performance, 2nd location.
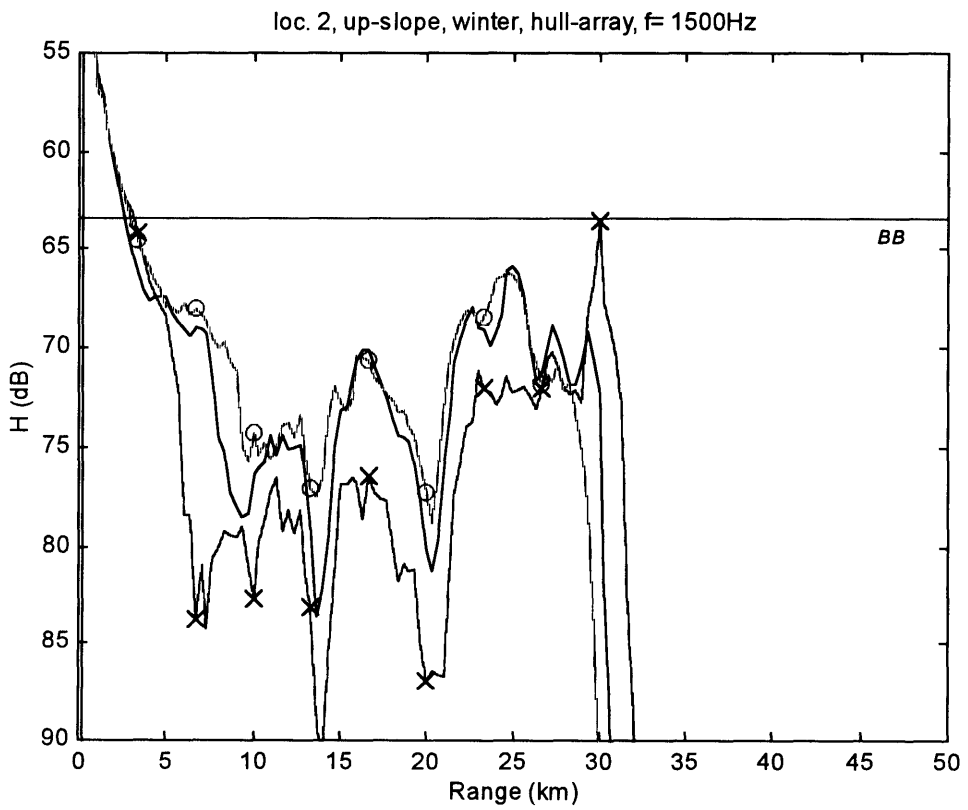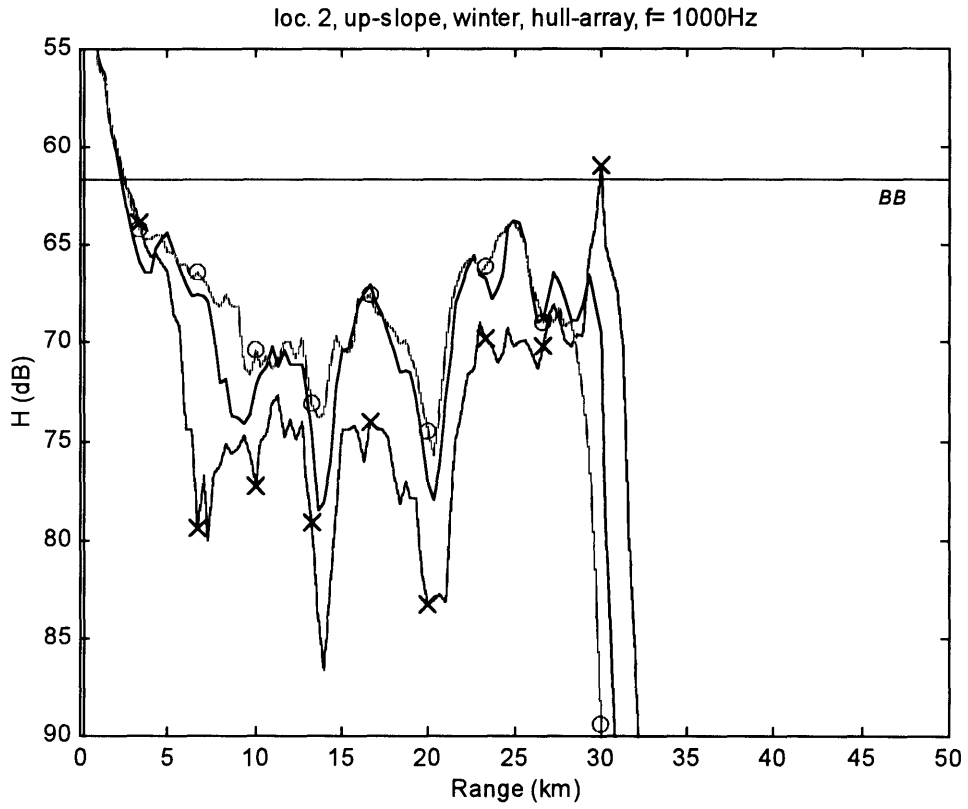
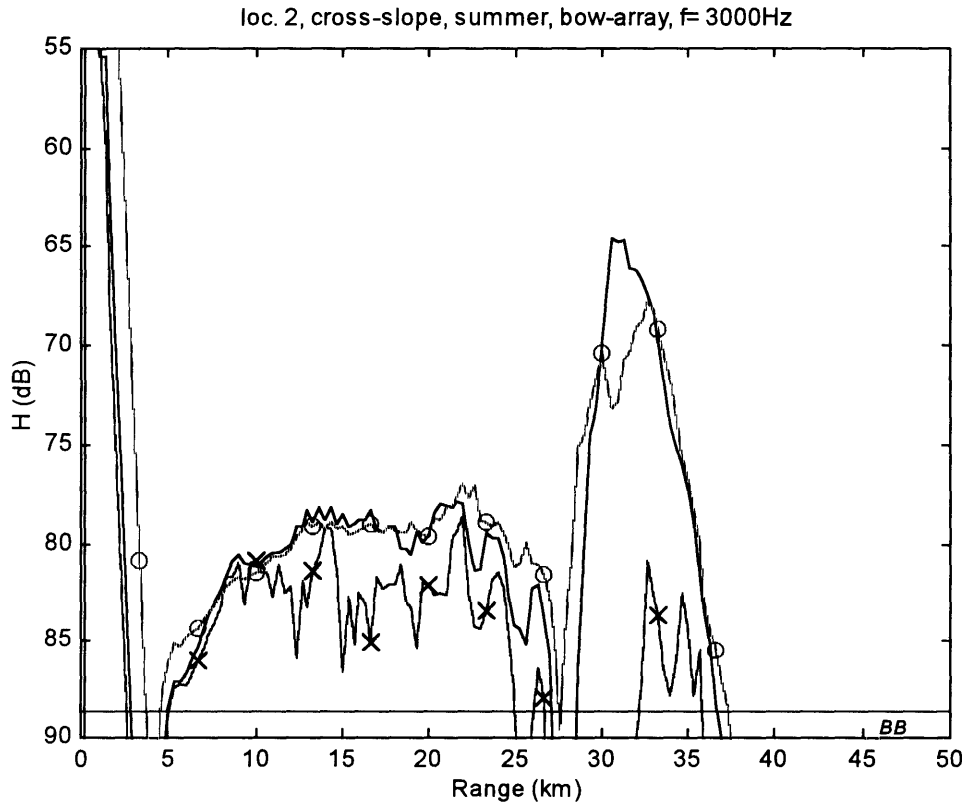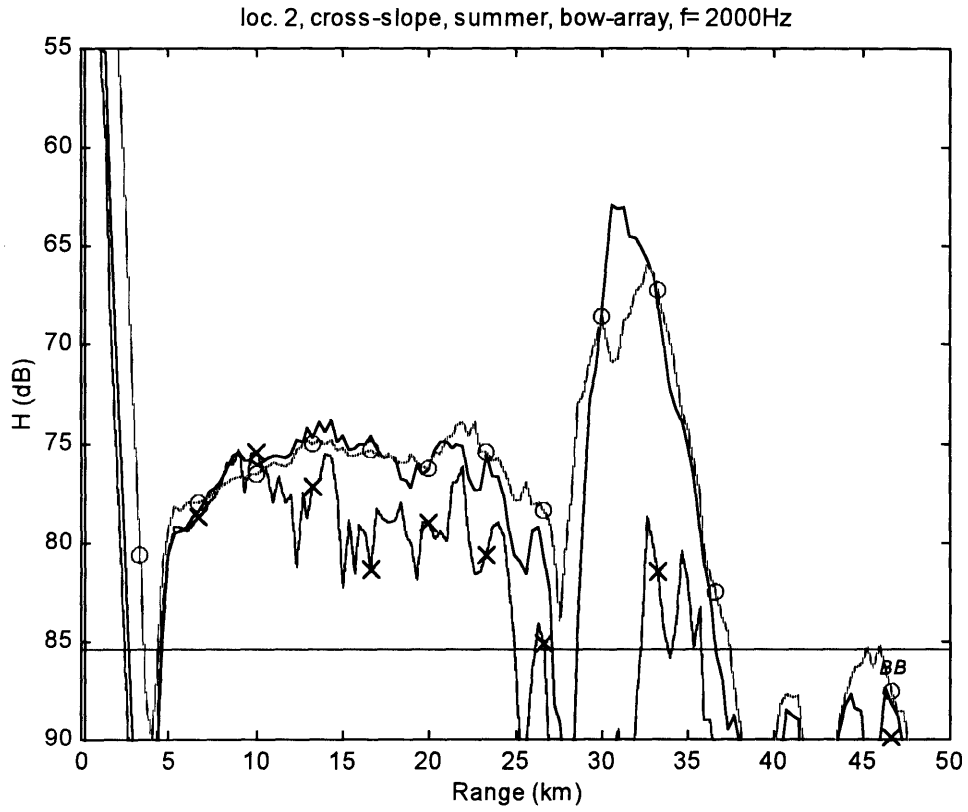Figure A.41 (upper) & Figure A.42 (lower): Sonar performance, 2nd location.
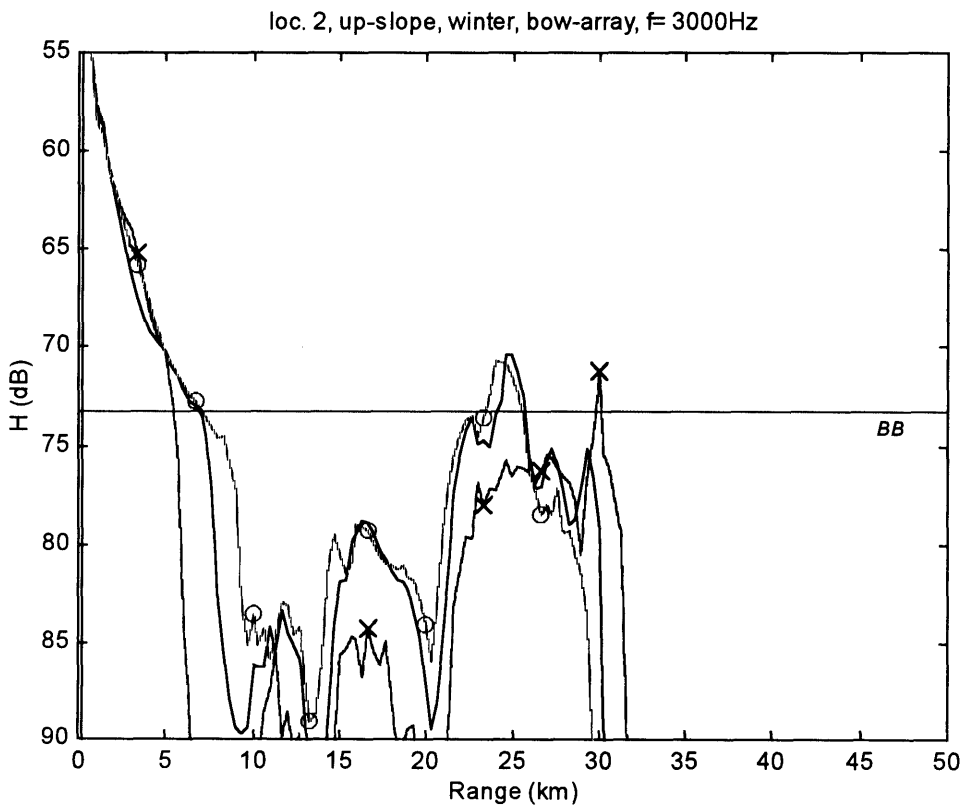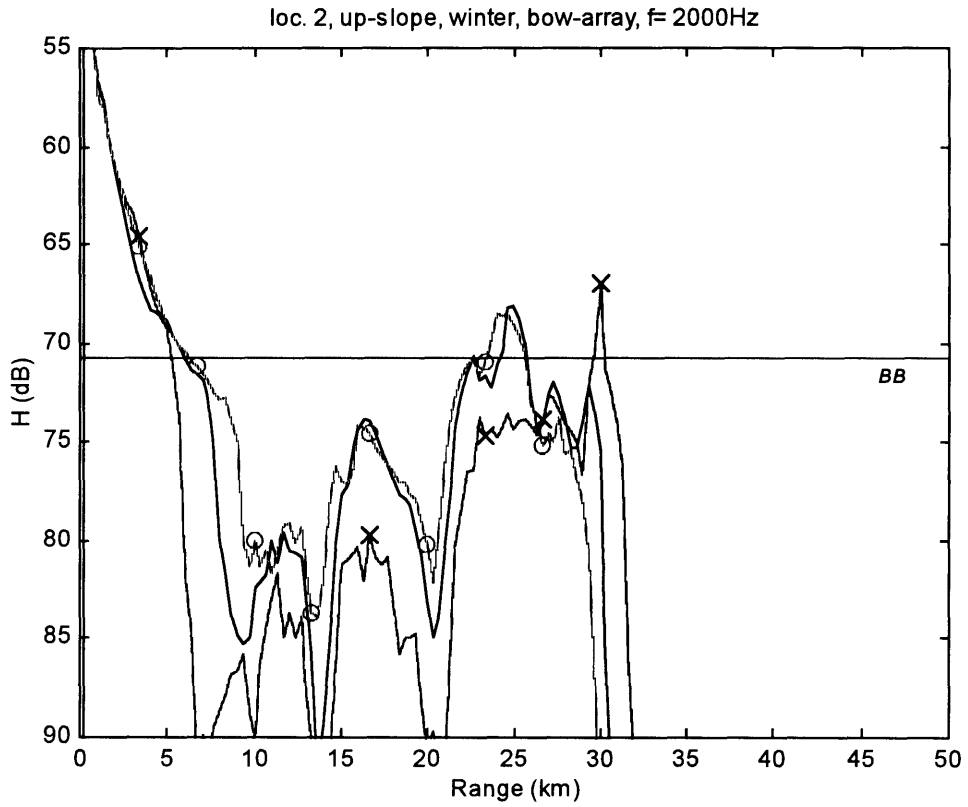
Figure A.43 (upper) & Figure A.44 (lower): Sonar performance, 2nd location.
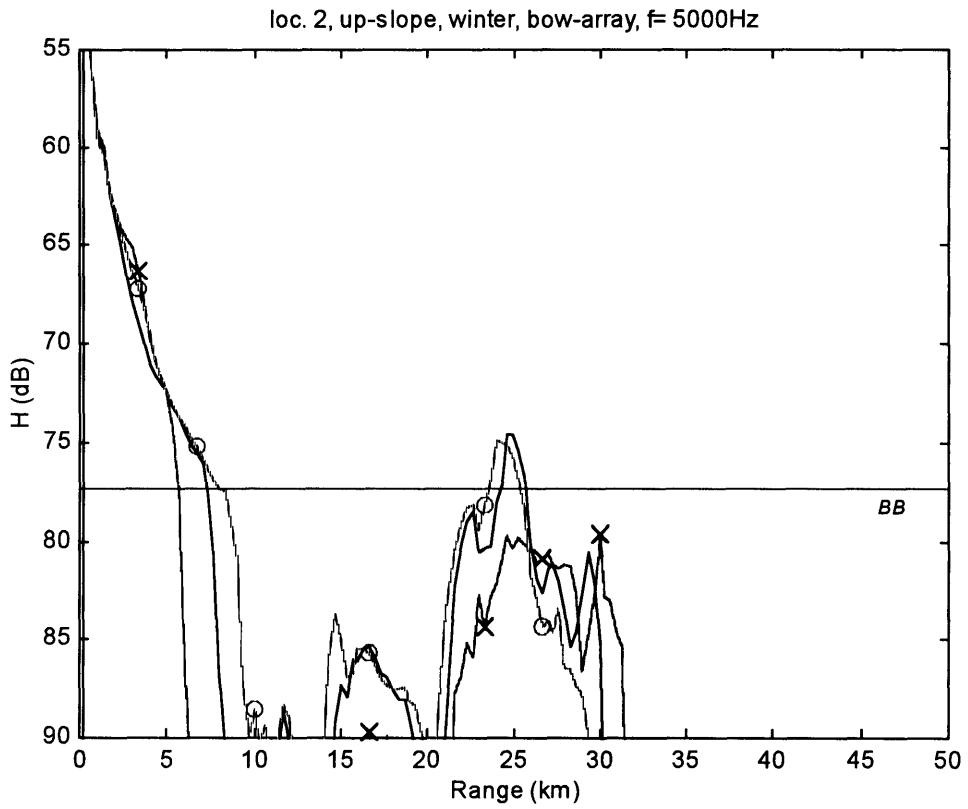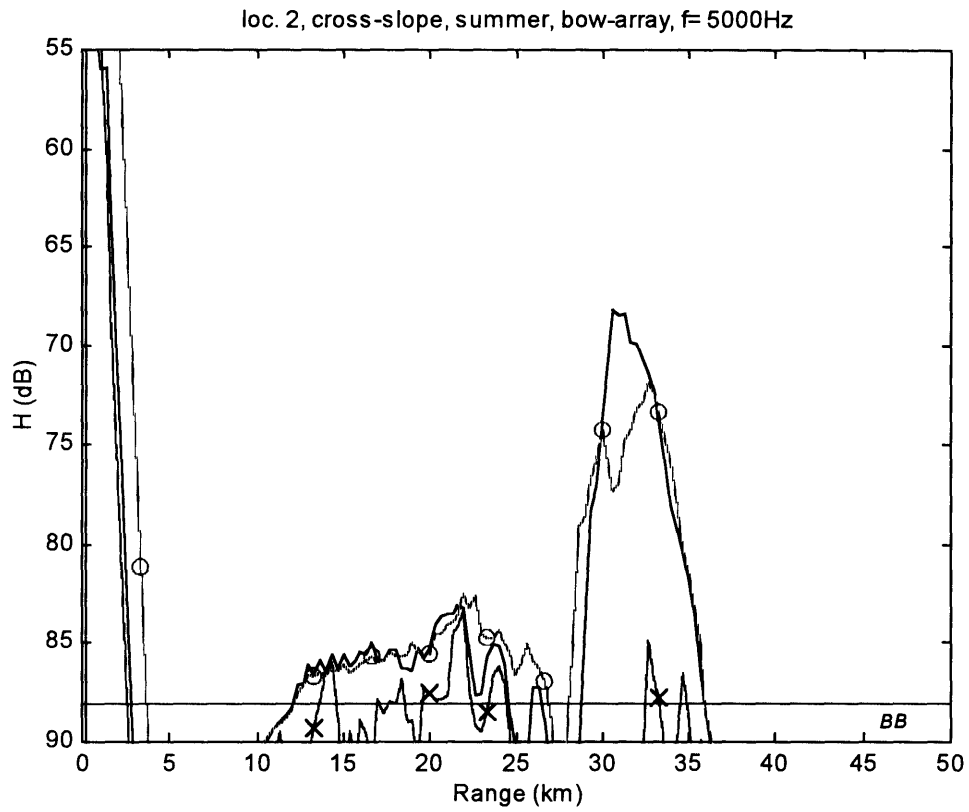
Figure A.45: Sonar performance, 2nd location.
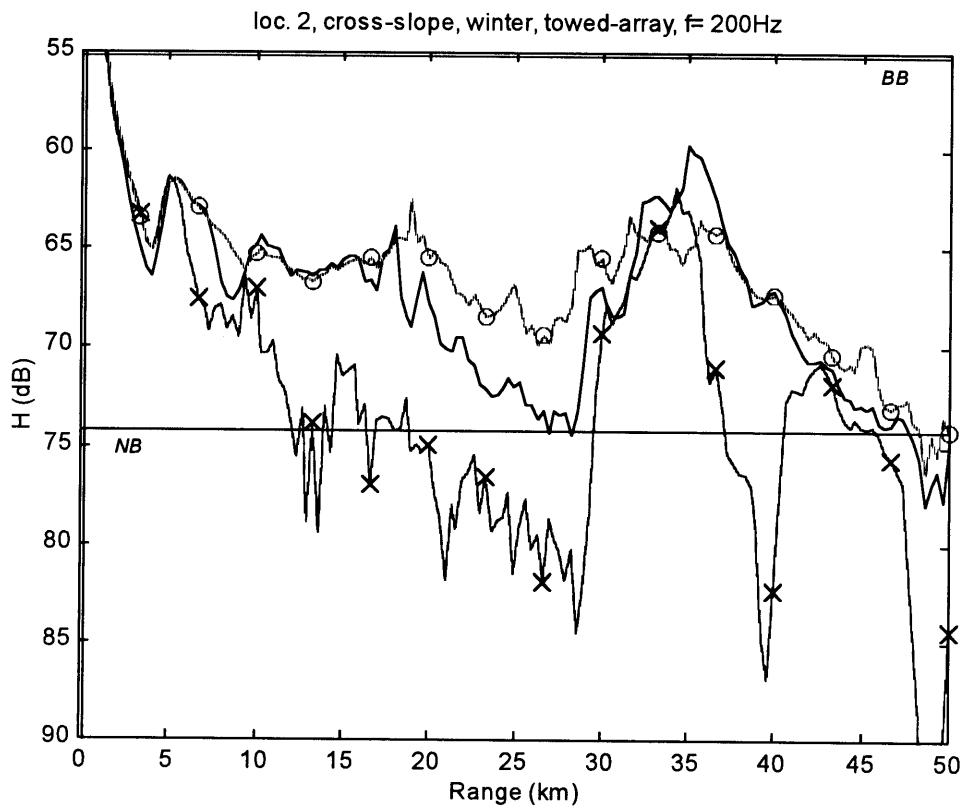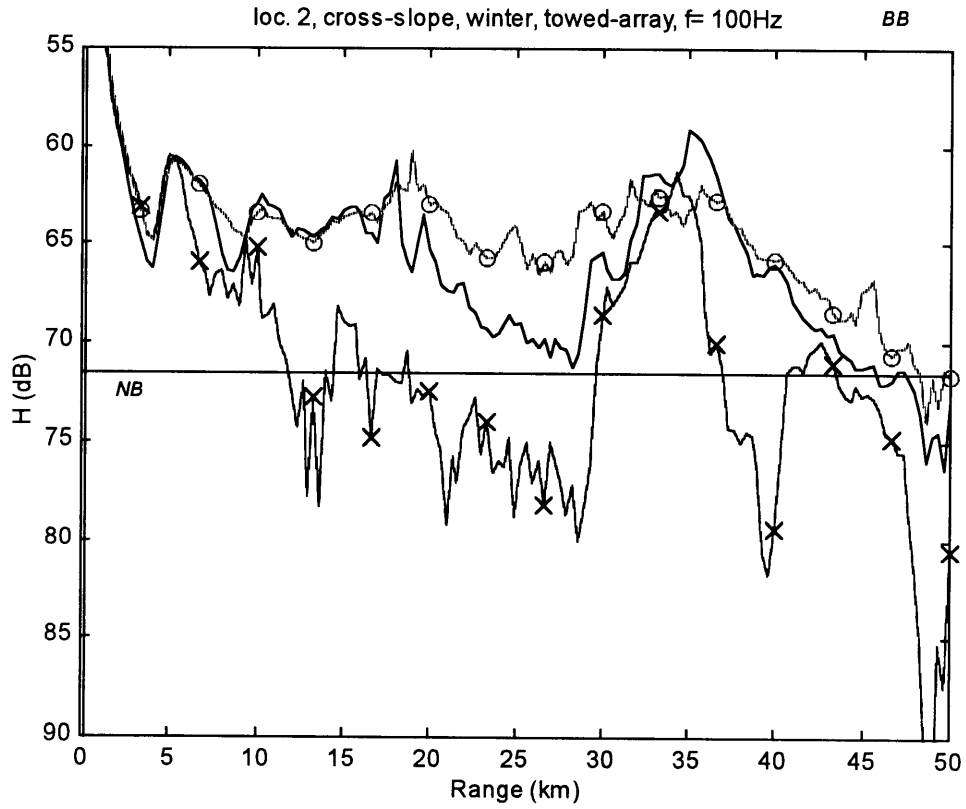
Figure A.46 (upper) & Figure A.47 (lower): Sonar performance, 2nd location.

loc. 2, cross-slope, winter, towed-array, f= 500Hz
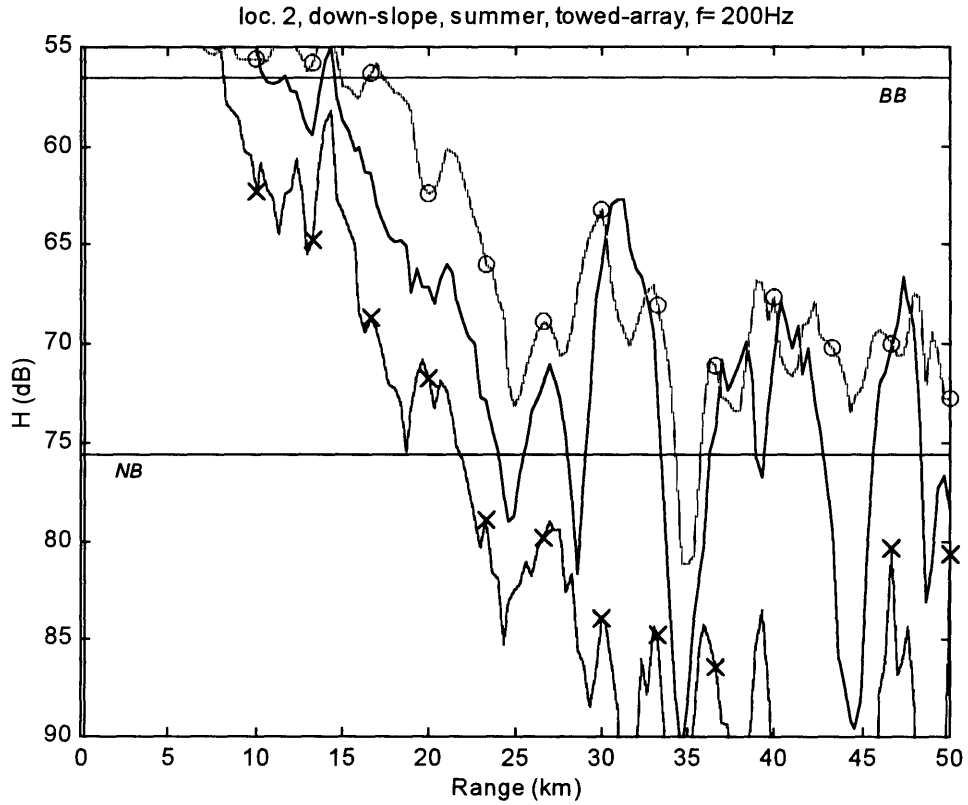
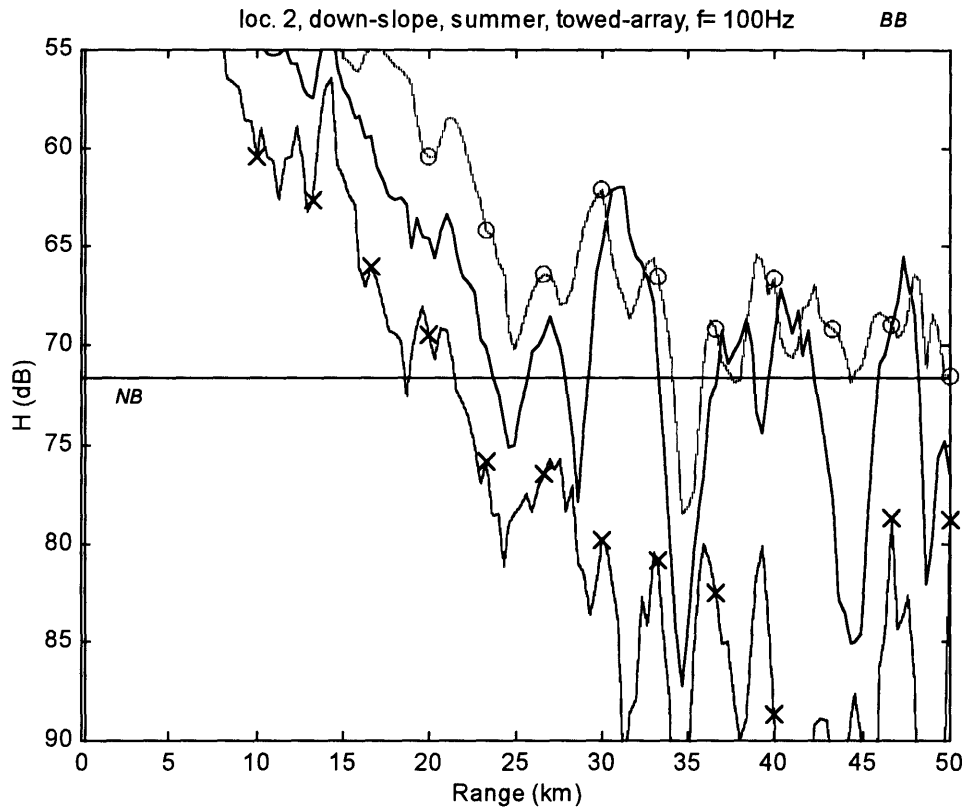loc. 2, cross-slope, winter, hull-array, f= 500Hz
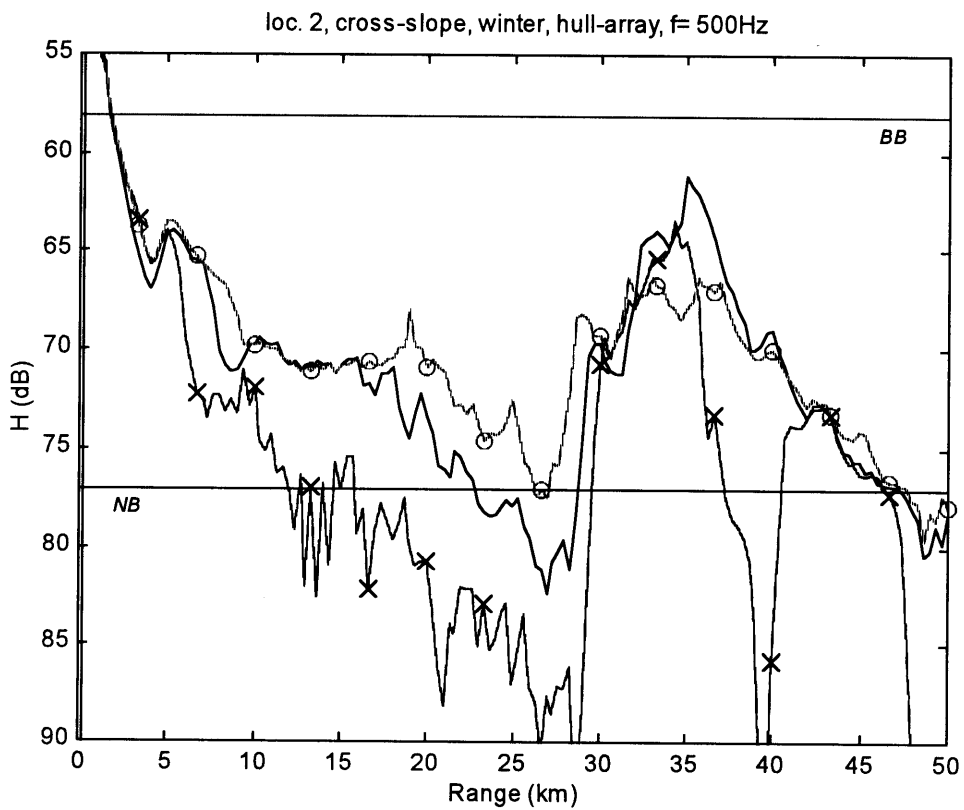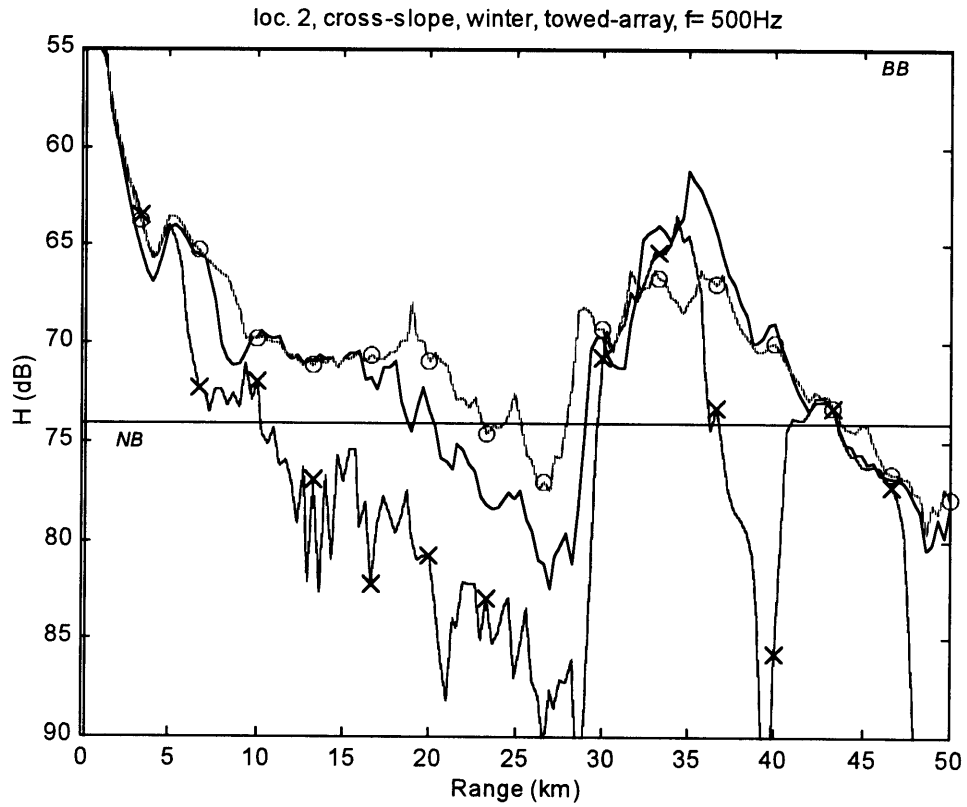
Figure A.48 (upper) & Figure A.49 (lower): Sonar performance, 2nd location.
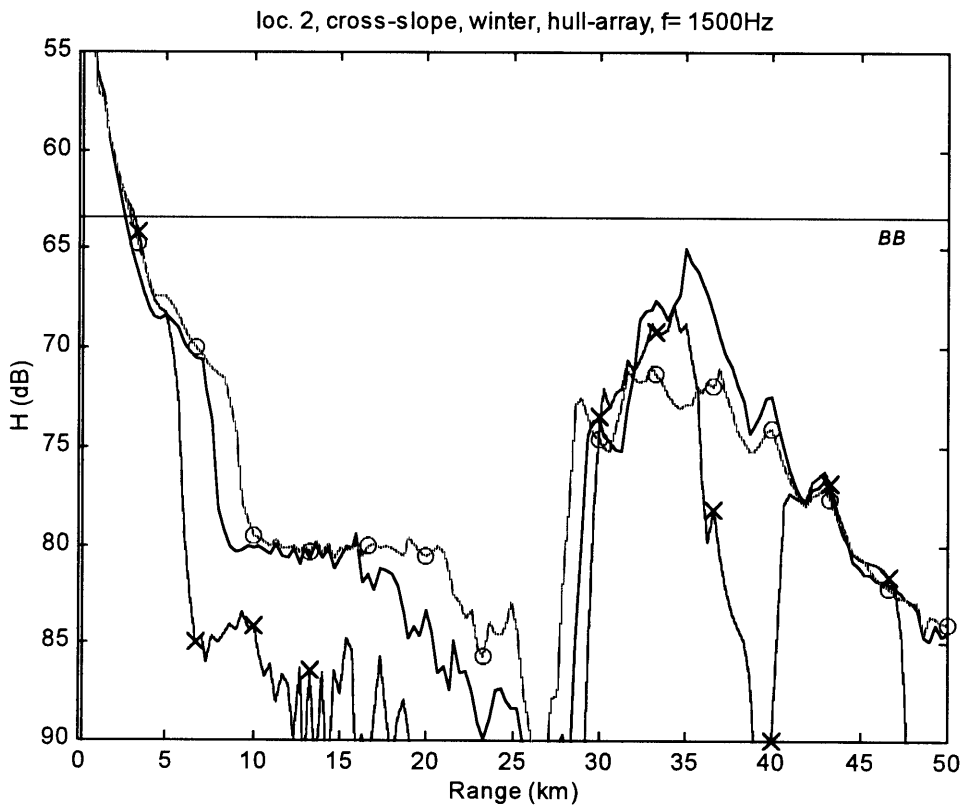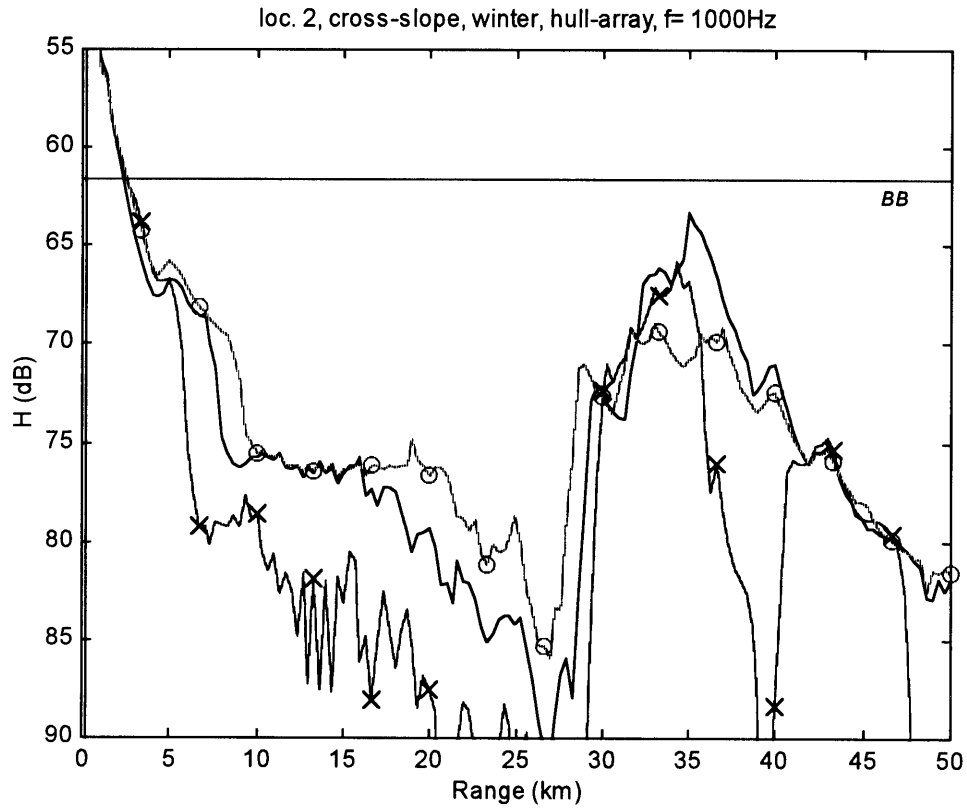
Figure A.50 (upper) & Figure A.51 (lower): Sonar performance, 2nd location.

loc. 2, cross-slope, winter, bow-array, f= 2000Hz
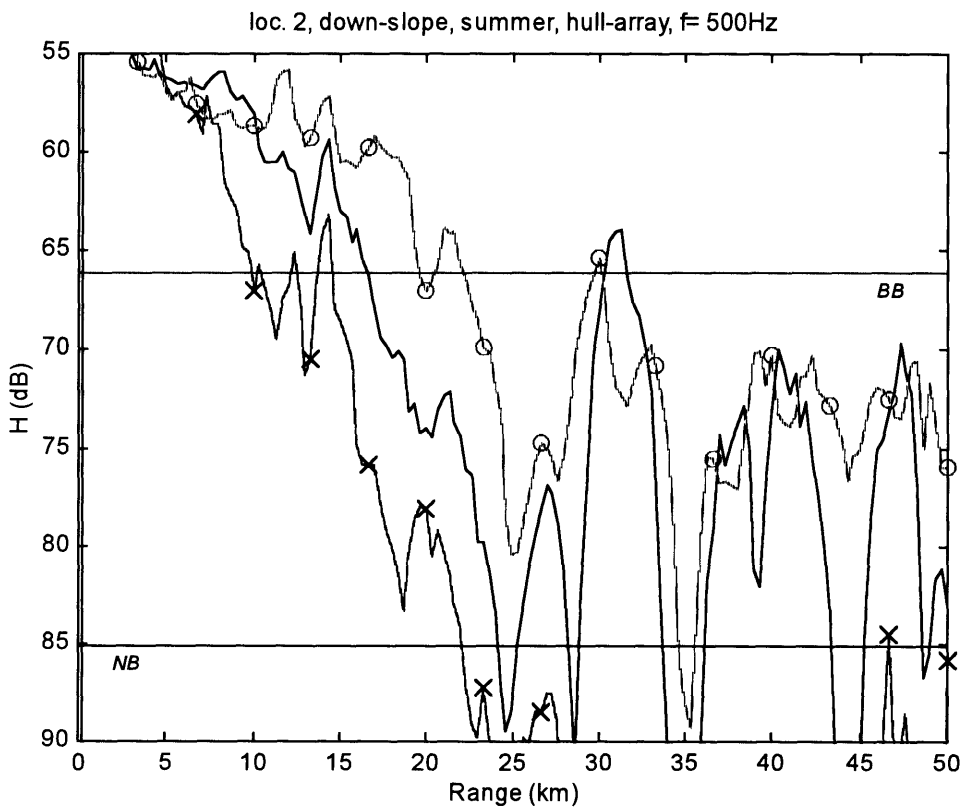
loc. 2, cross-slope, winter, bow-array, f= 3000Hz
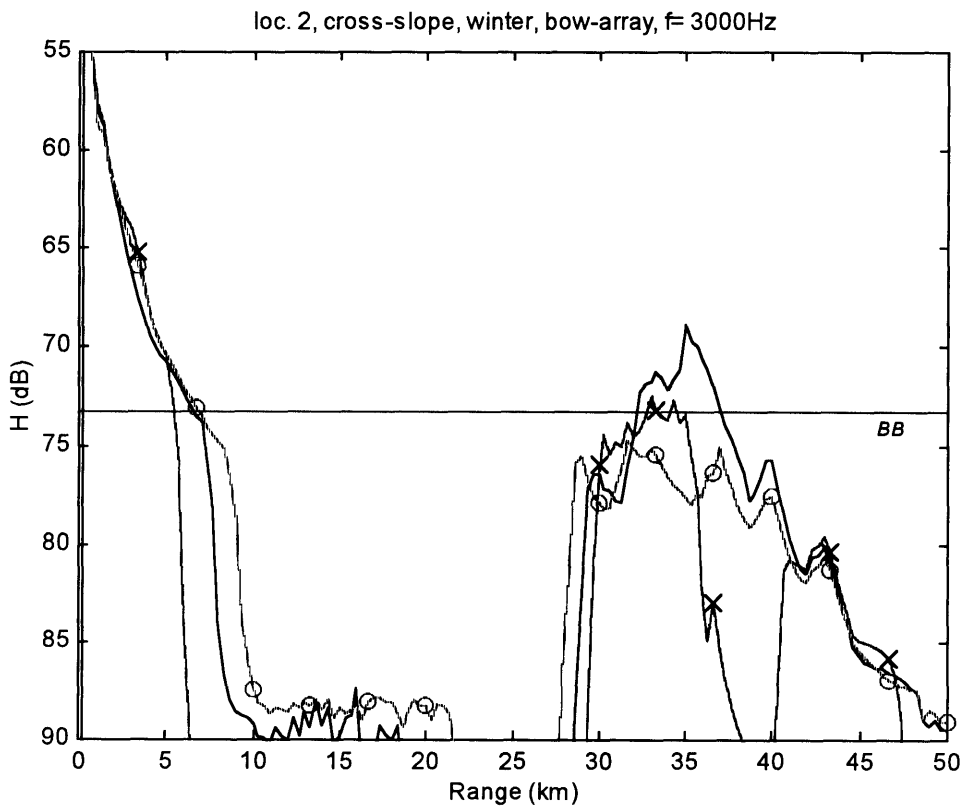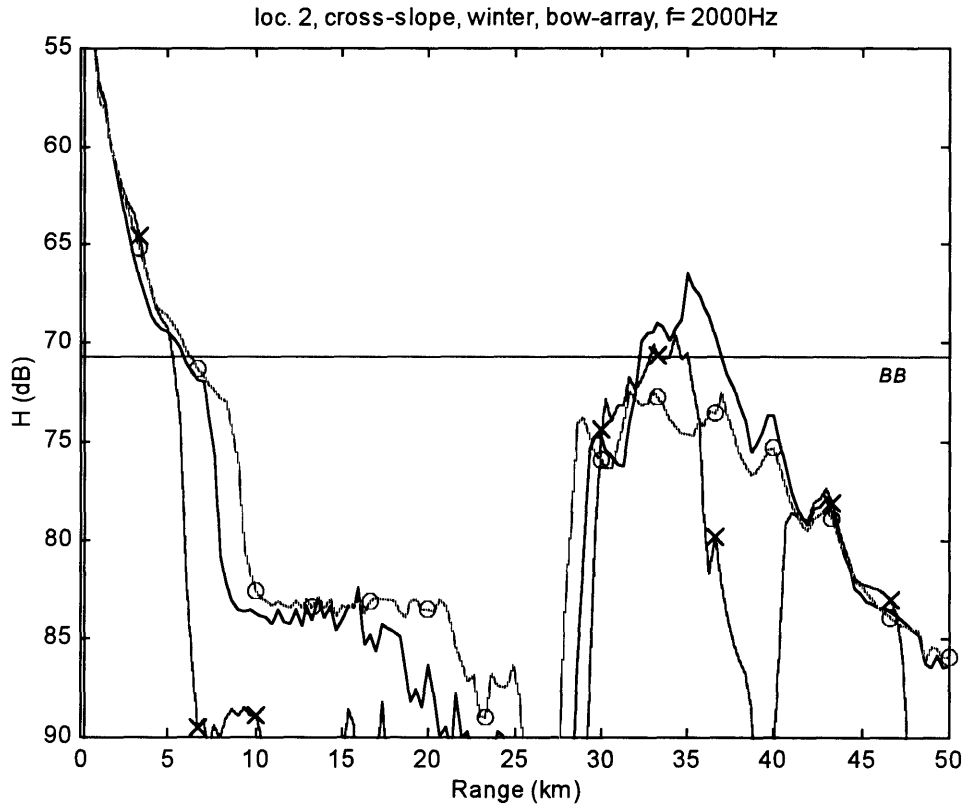
Figure A.52 (upper) & Figure A.53 (lower): Sonar performance, 2nd location.

loc. 2, cross-slope, winter, bow-array, f= 5000Hz
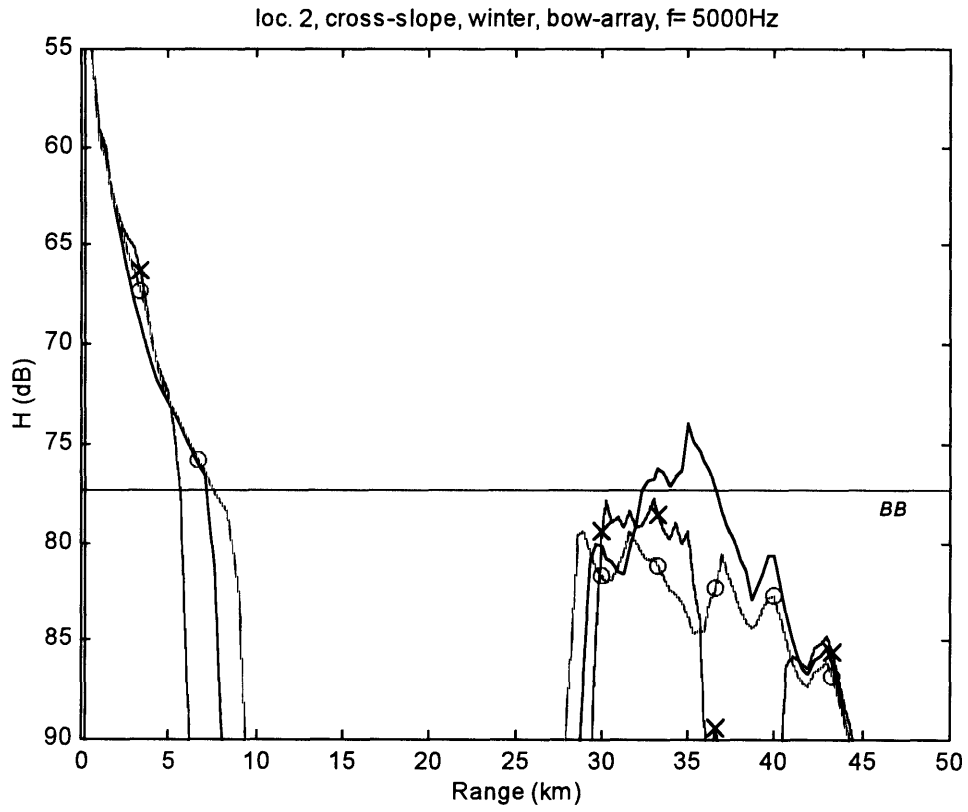
Figure A.54: Sonar performance, 2nd location.

loc. 2, down-slope, winter, towed-array, f= 100Hz   *BB*

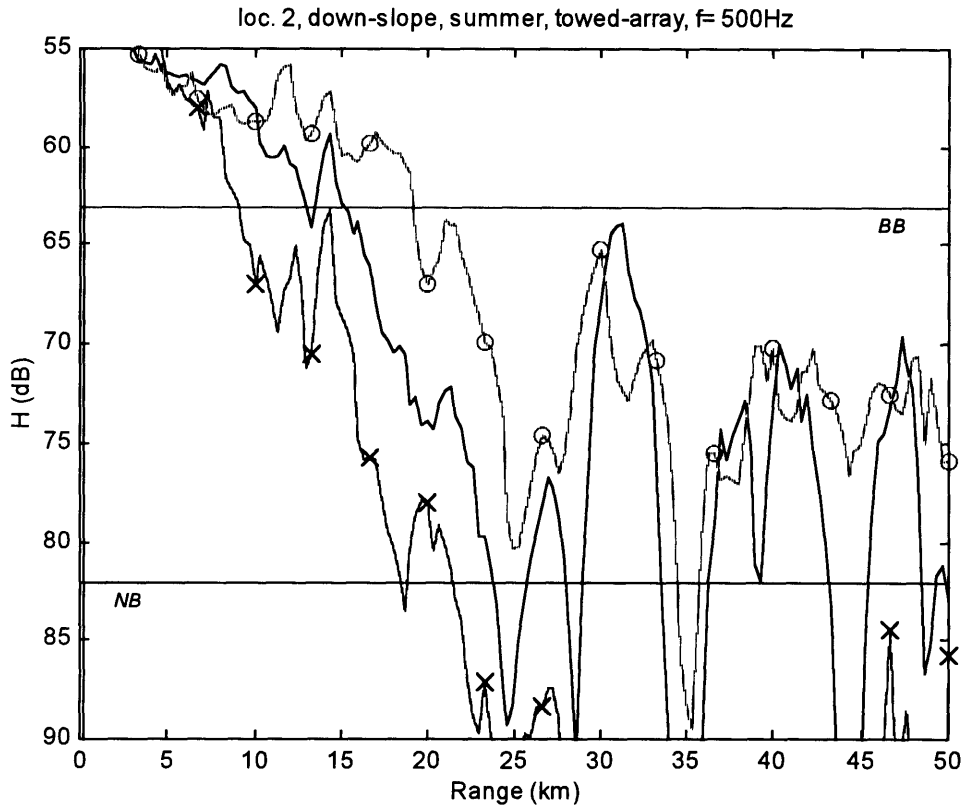loc. 2, down-slope, winter, towed-array, f= 200Hz
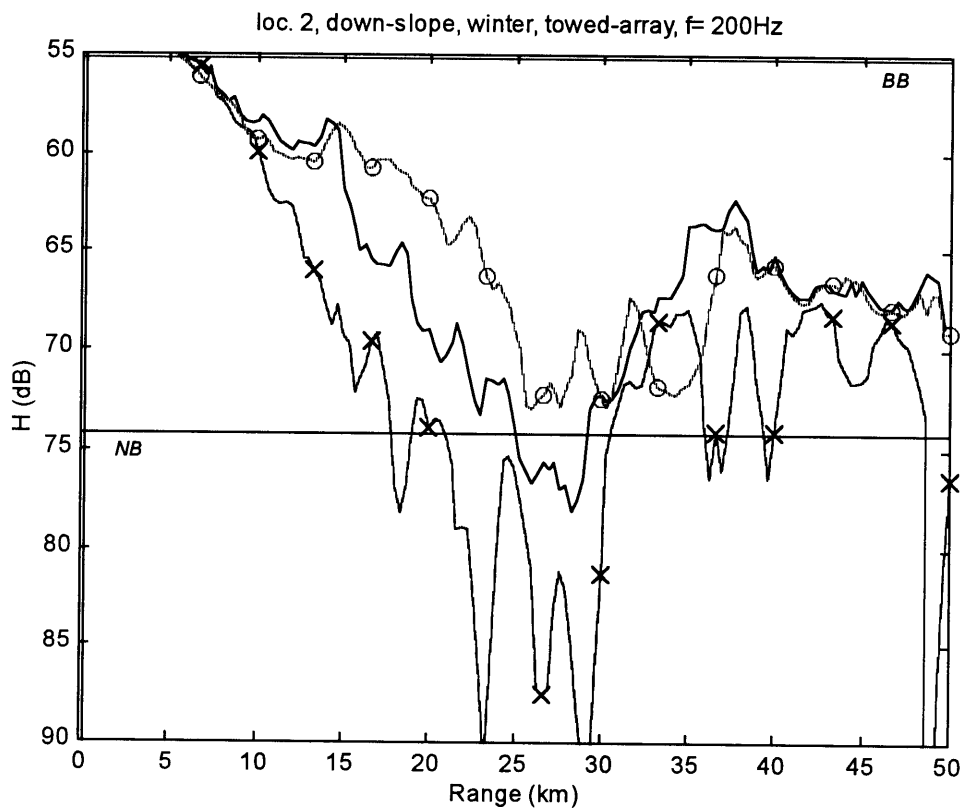
Figure A.55 (upper) & Figure A.56 (lower): Sonar performance, 2nd location.

Figure A.57 (upper) & Figure A.58 (lower): Sonar performance, 2nd location.
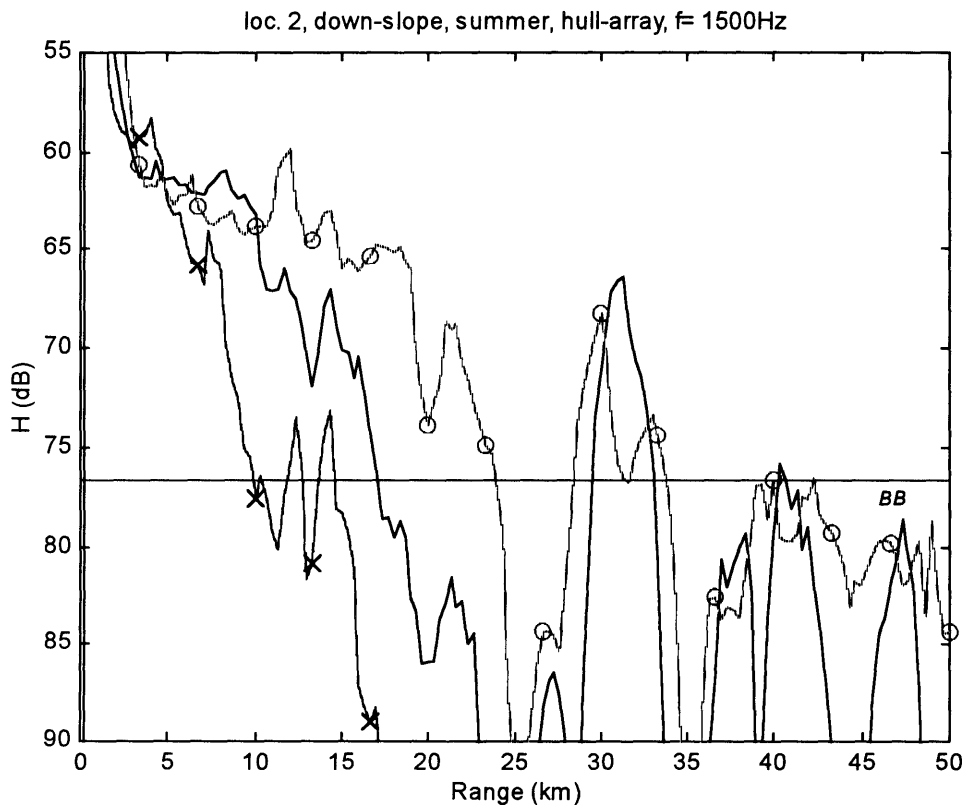
loc. 2, down-slope, winter, hull-array, f= 1000Hz

loc. 2, down-slope, winter, hull-array, f= 1500Hz

Figure A.59 (upper) & Figure A.60 (lower): Sonar performance, 2nd location.

loc. 2, down-slope, winter, bow-array, f= 2000Hz

loc. 2, down-slope, winter, bow-array, f= 3000Hz

Figure A.61 (upper) & Figure A.62 (lower): Sonar performance, 2nd location.

Figure A.63: Sonar performance, 2nd location.

loc. 2, up-slope, summer, towed-array, f= 100Hz   *BB*

loc. 2, up-slope, summer, towed-array, f= 200Hz

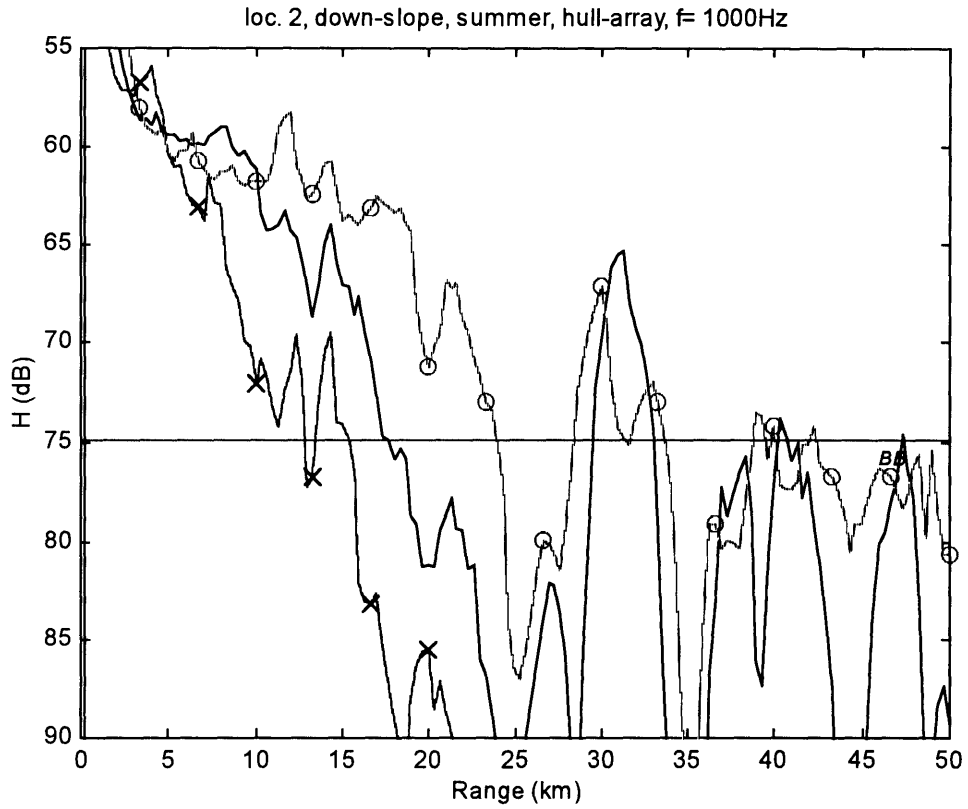Figure A.64 (upper) & Figure A.65 (lower): Sonar performance, 2nd location.

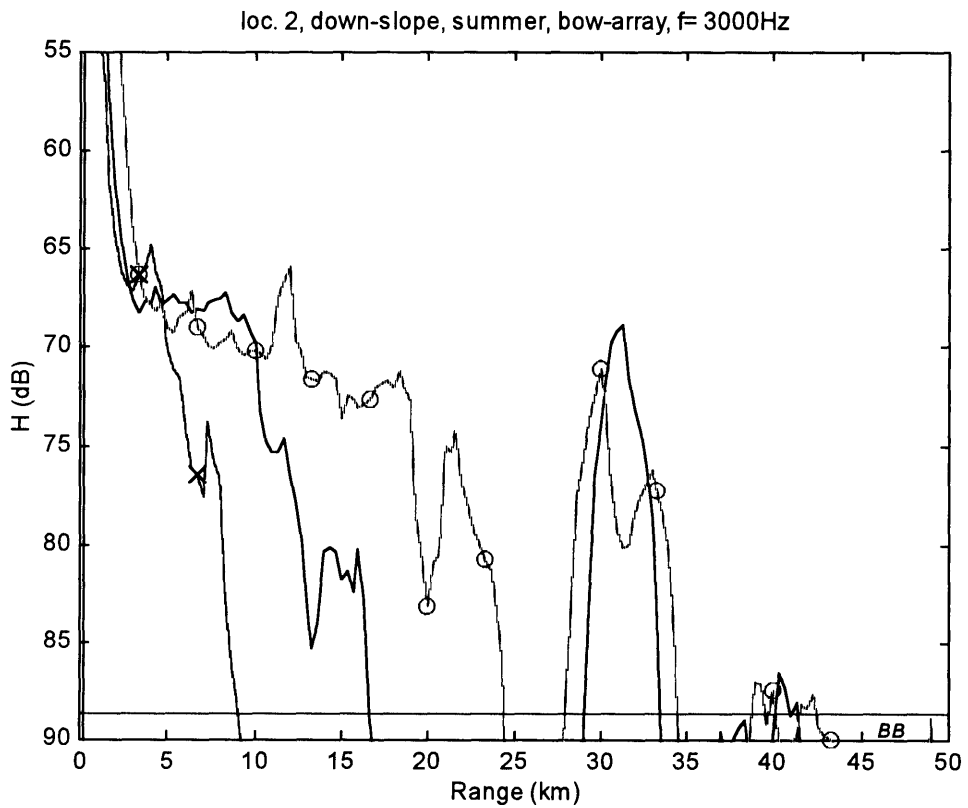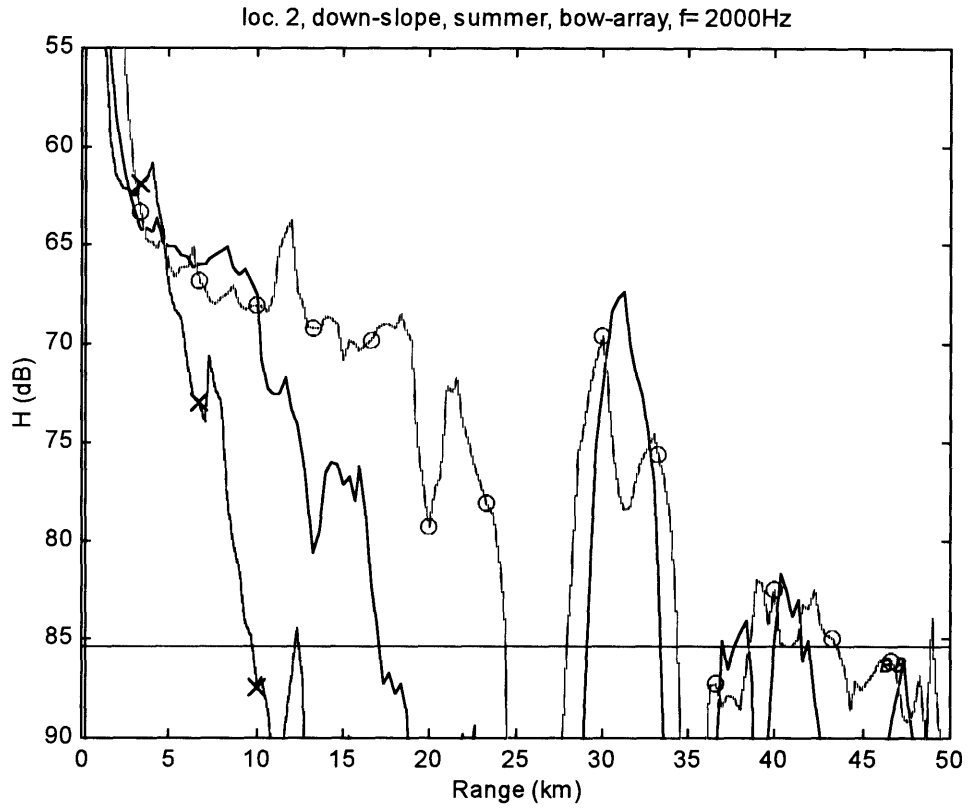Figure A.66 (upper) & Figure A.67 (lower): Sonar performance, 2nd location.

Figure A.68 (upper) & Figure A.69 (lower): Sonar performance, 2nd location.
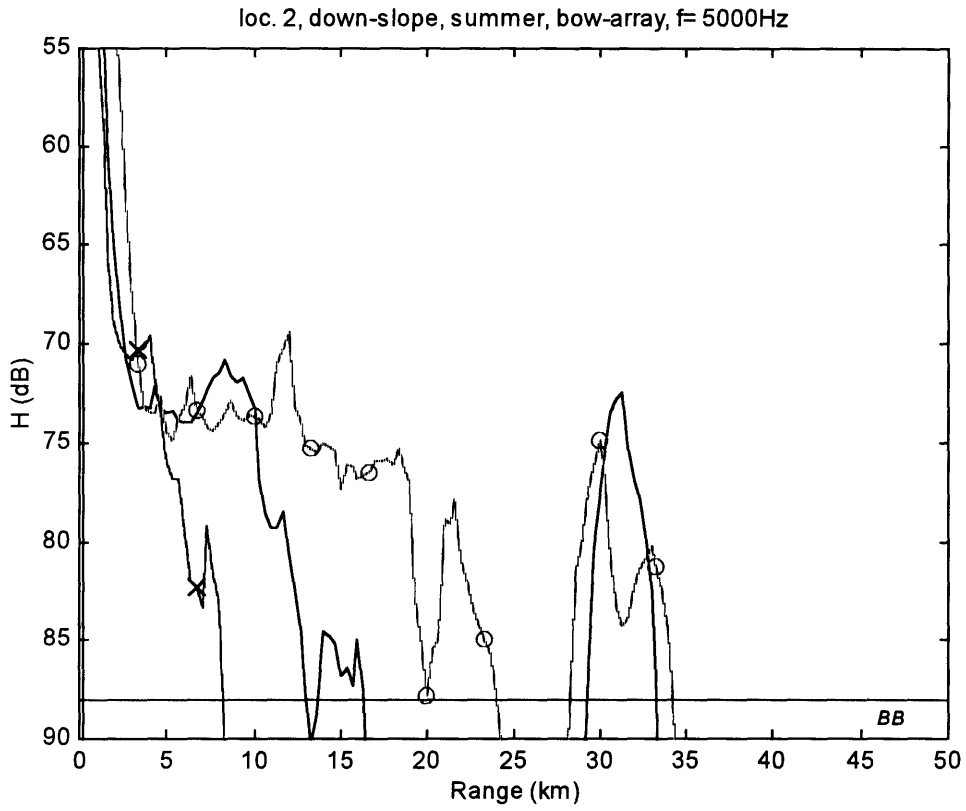
loc. 2, up-slope, summer, bow-array, f= 2000Hz

loc. 2, up-slope, summer, bow-array, f= 3000Hz

Figure A.70 (upper) & Figure A.71 (lower): Sonar performance, 2nd location.

loc. 2, up-slope, summer, bow-array, f= 5000Hz

Figure A.72: Sonar performance, 2nd location.

loc. 2, cross-slope, summer, towed-array, f= 100Hz   *BB*
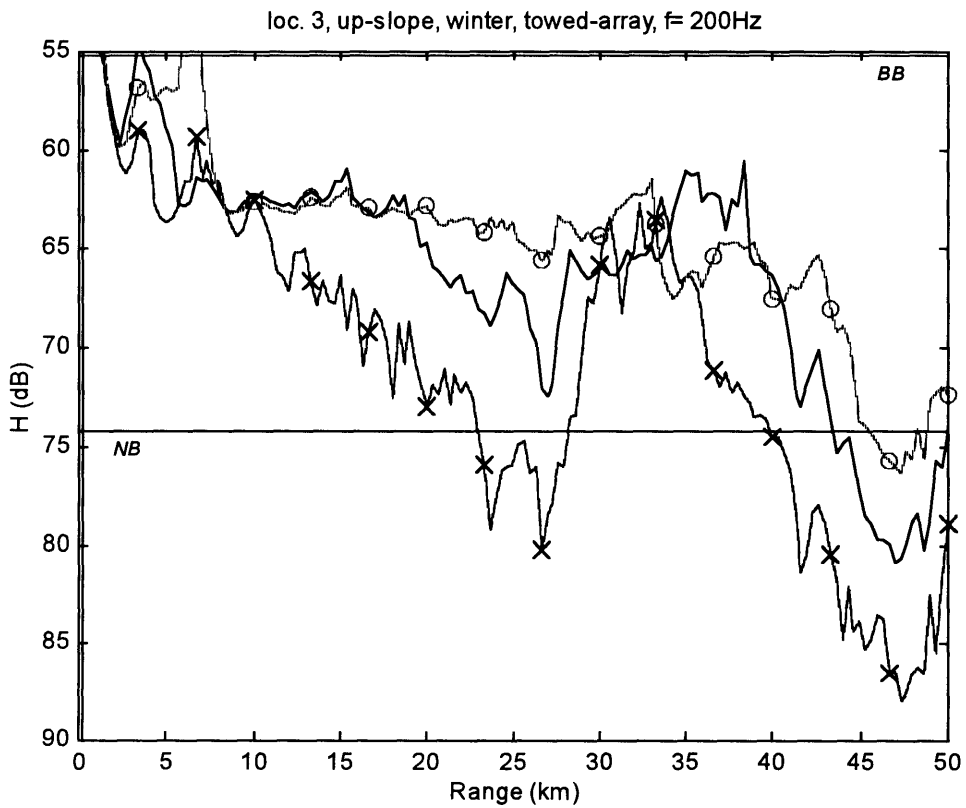
loc. 2, cross-slope, summer, towed-array, f= 200Hz

Figure A.73 (upper) & Figure A.74 (lower): Sonar performance, 2nd location.

loc. 2, cross-slope, summer, towed-array, f= 500Hz

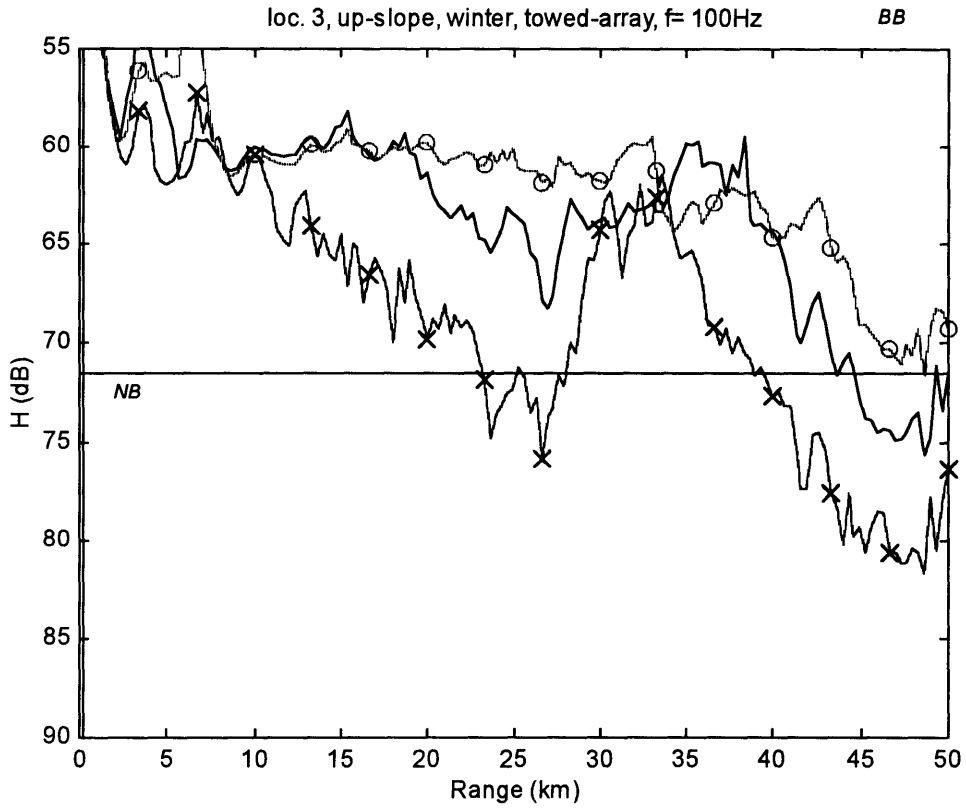loc. 2, cross-slope, summer, hull-array, f= 500Hz

Figure A.75 (upper) & Figure A.76 (lower): Sonar performance, 2nd location.

Figure A.77 (upper) & Figure A.78 (lower): Sonar performance, 2nd location.

loc. 2, cross-slope, summer, bow-array, f= 2000Hz

loc. 2, cross-slope, summer, bow-array, f= 3000Hz

Figure A.79 (upper) & Figure A.80 (lower): Sonar performance, 2nd location.

loc. 2, cross-slope, summer, bow-array, f= 5000Hz
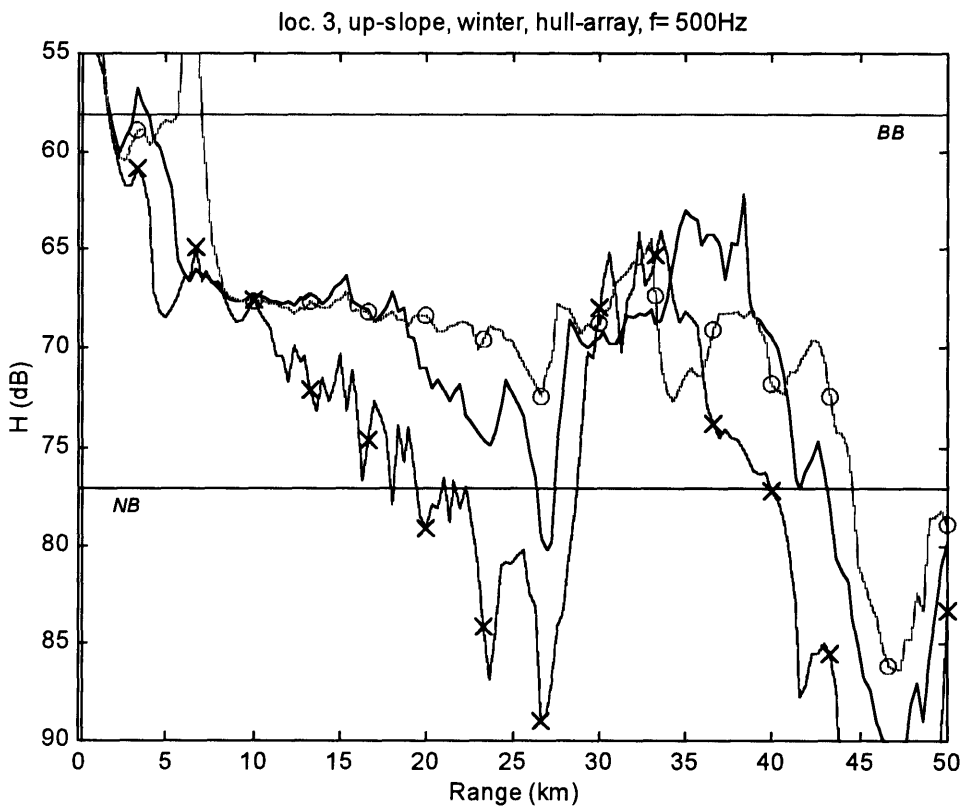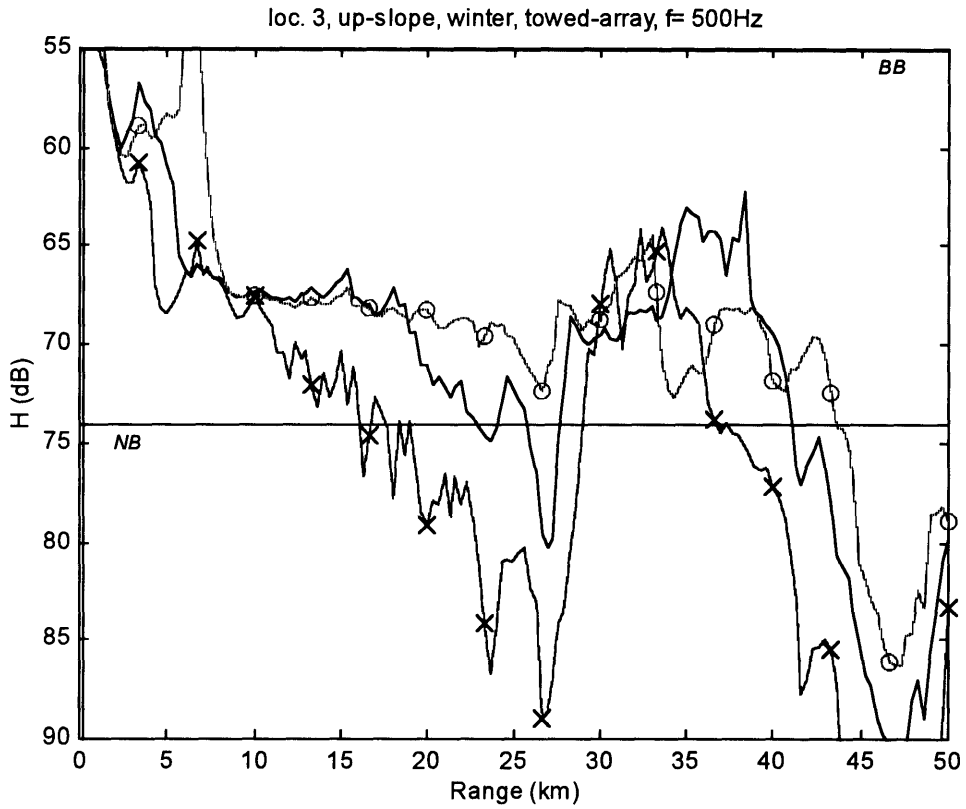
Figure A.81: Sonar performance, 2nd location.

Figure A.82 (upper) & Figure A.83 (lower): Sonar performance, 2nd location.

loc. 2, down-slope, summer, towed-array, f= 500Hz

BB

NB

H (dB)

Range (km)

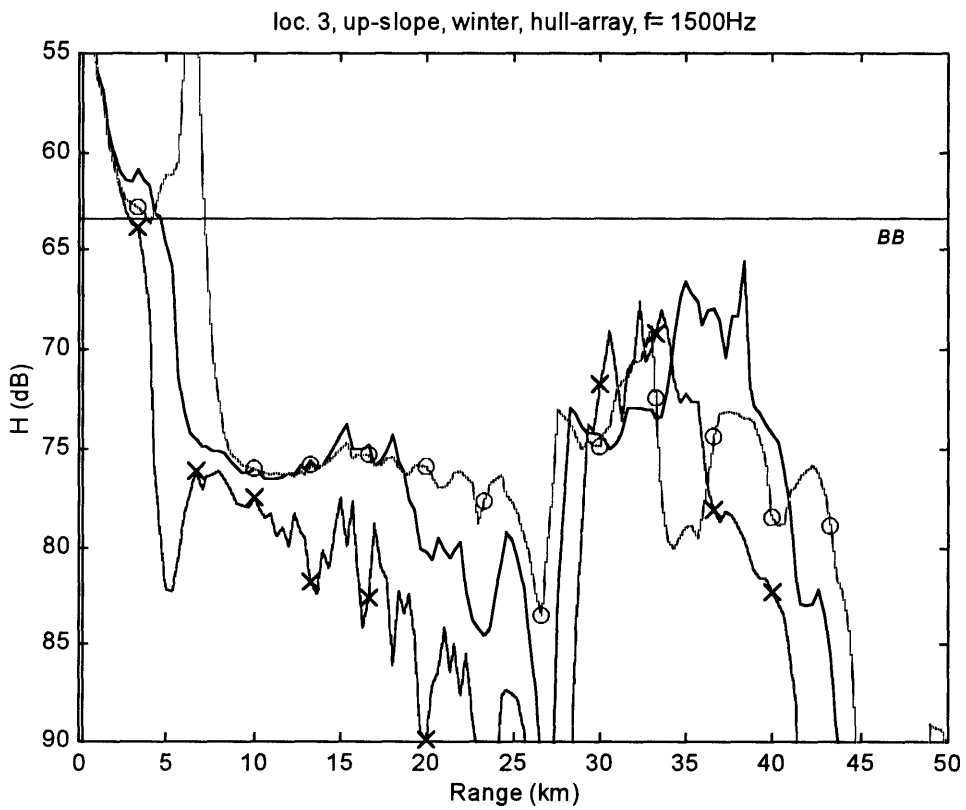loc. 2, down-slope, summer, hull-array, f= 500Hz

BB

NB

H (dB)

Range (km)

Figure A.84 (upper) & Figure A.85 (lower): Sonar performance, 2nd location.

loc. 2, down-slope, summer, hull-array, f= 1000Hz

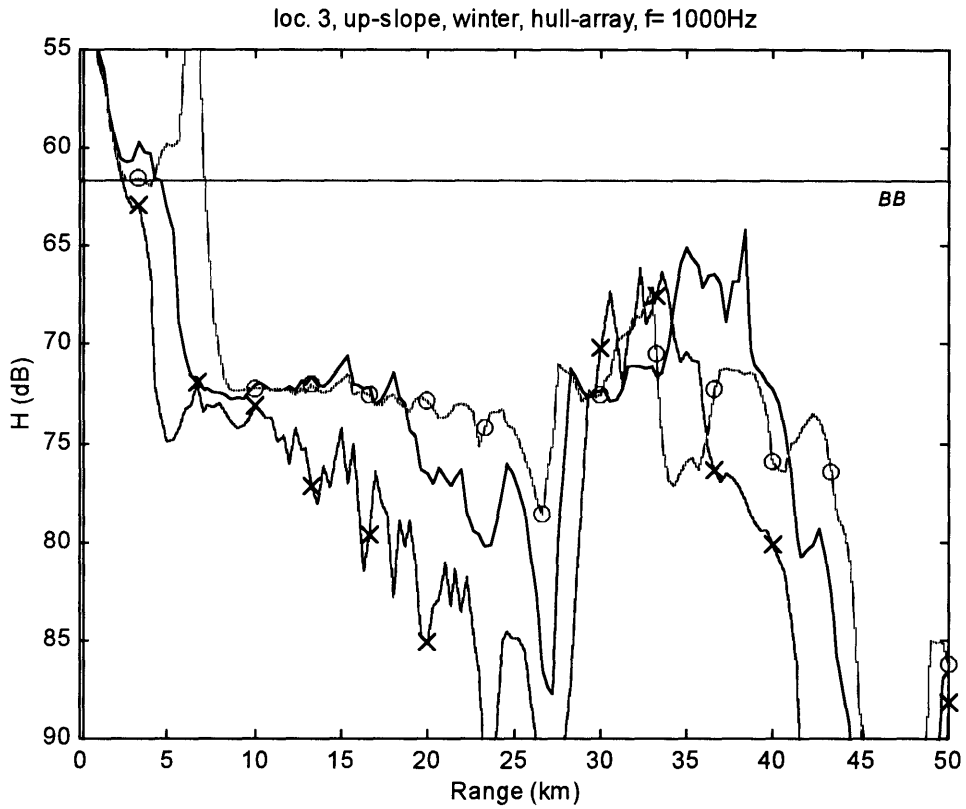loc. 2, down-slope, summer, hull-array, f= 1500Hz

Figure A.86 (upper) & Figure A.87 (lower): Sonar performance, 2nd location.

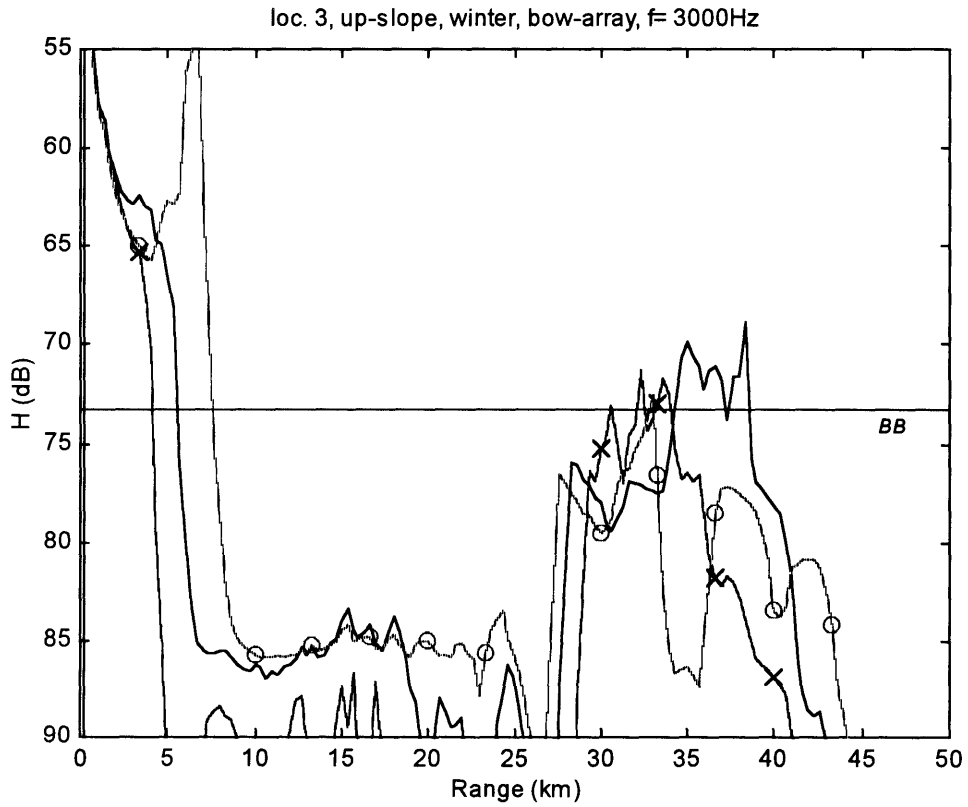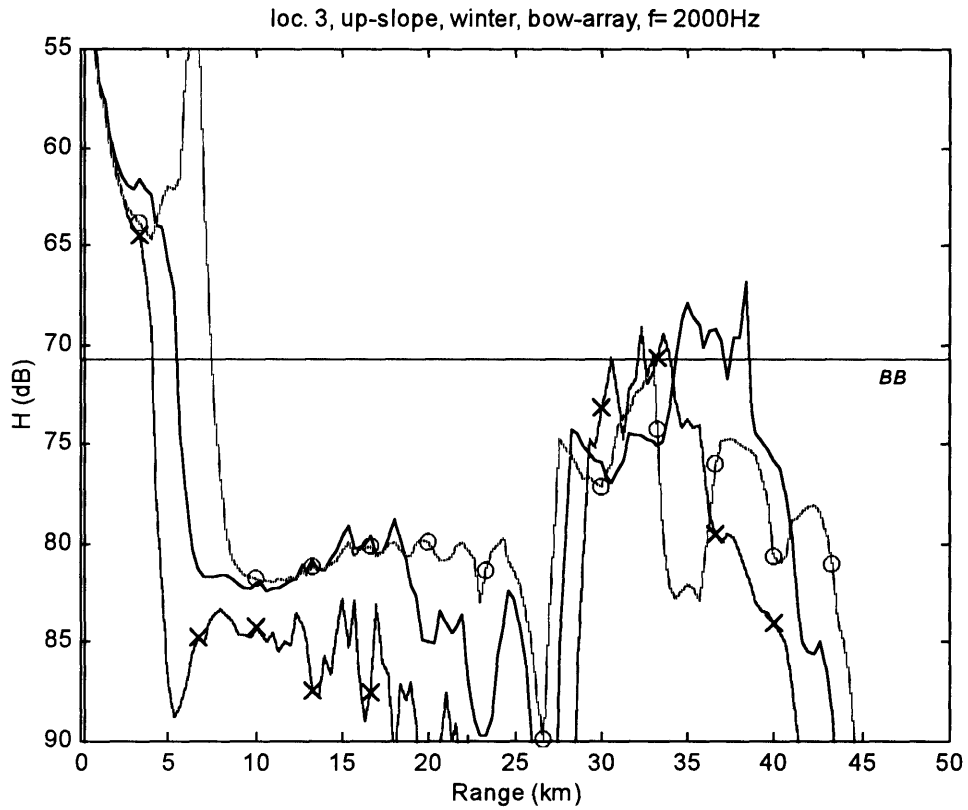Figure A.88 (upper) & Figure A.89 (lower): Sonar performance, 2nd location.

loc. 2, down-slope, summer, bow-array, f= 5000Hz

Figure A.90: Sonar performance, 2nd location.

loc. 3, up-slope, winter, towed-array, f= 100Hz

loc. 3, up-slope, winter, towed-array, f= 200Hz

Figure A.91 (upper) & Figure A.92 (lower): Sonar performance, 3rd location.

loc. 3, up-slope, winter, towed-array, f= 500Hz

BB

NB

H (dB)

Range (km)

loc. 3, up-slope, winter, hull-array, f= 500Hz

BB

NB

H (dB)

Range (km)

Figure A.93 (upper) & Figure A.94 (lower): Sonar performance, 3rd location.

Figure A.95 (upper) & Figure A.96 (lower): Sonar performance, 3rd location.

Figure A.98 (upper) & Figure A.99 (lower): Sonar performance, 3rd location.
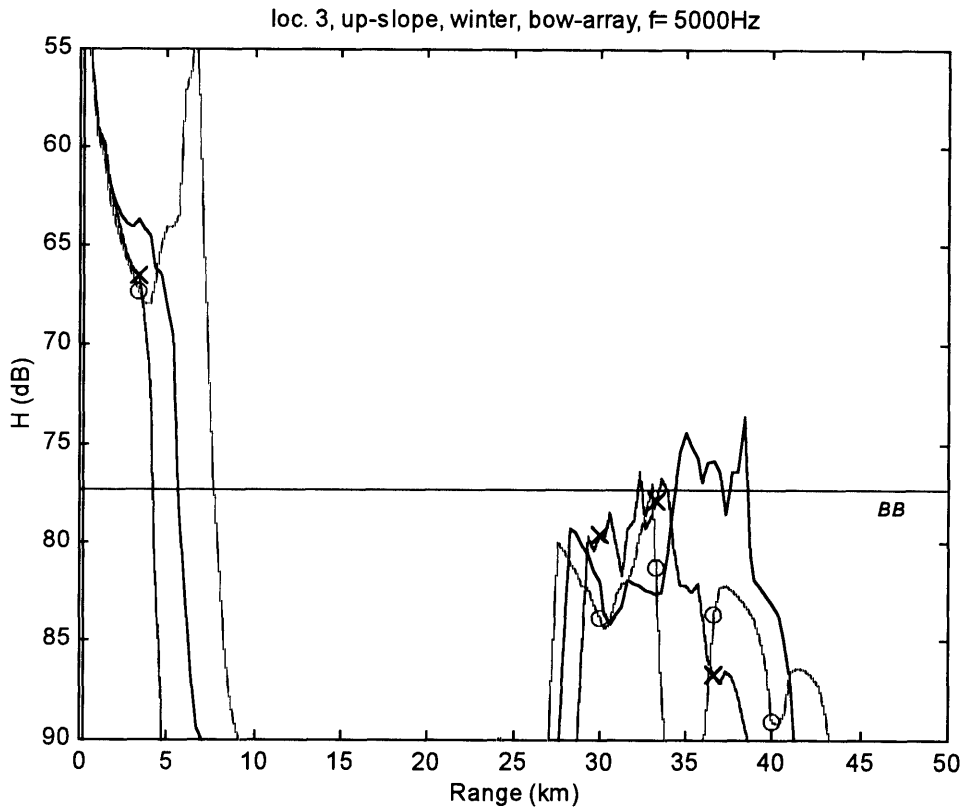
loc. 3, up-slope, winter, bow-array, f= 5000Hz

Figure A.100: Sonar performance, 3rd location.

loc. 3, cross-slope, winter, towed-array, f= 100Hz
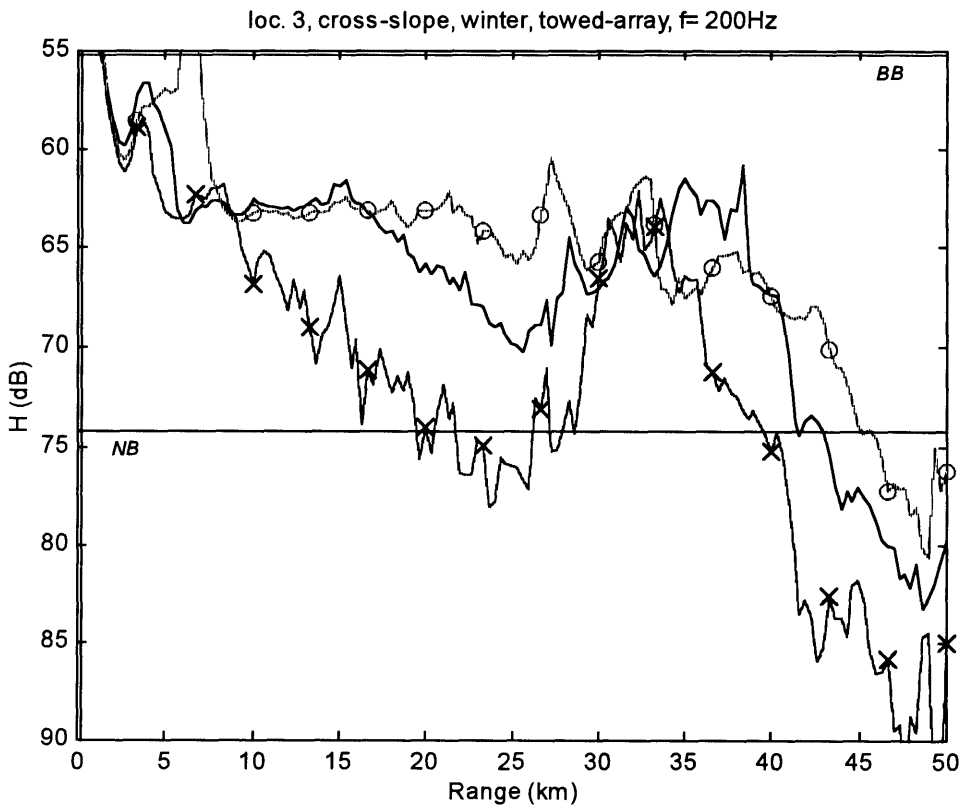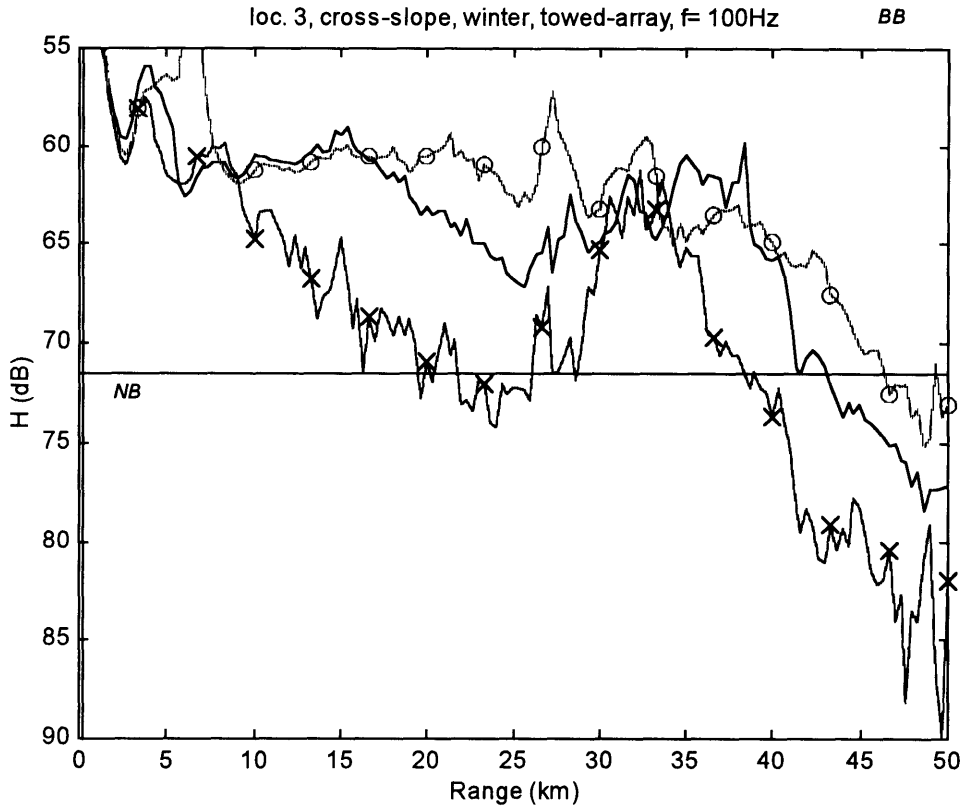
loc. 3, cross-slope, winter, towed-array, f= 200Hz

Figure A.101 (upper) & Figure A.102 (lower): Sonar performance, 3rd location.

loc. 3, cross-slope, winter, towed-array, f= 500Hz

loc. 3, cross-slope, winter, hull-array, f= 500Hz
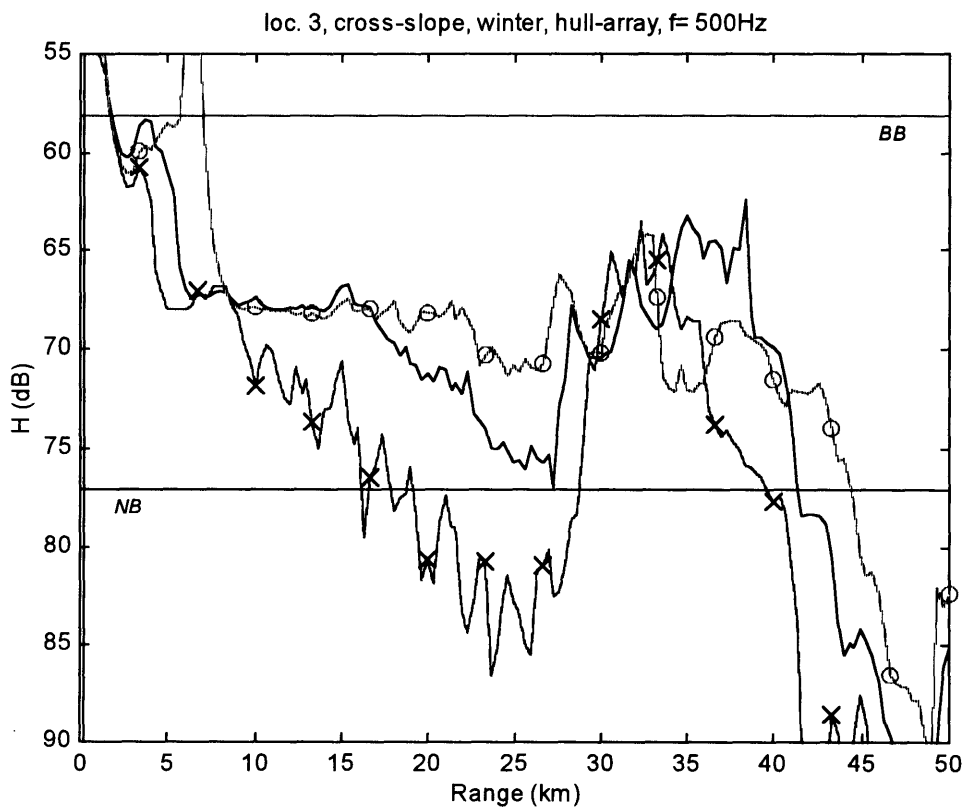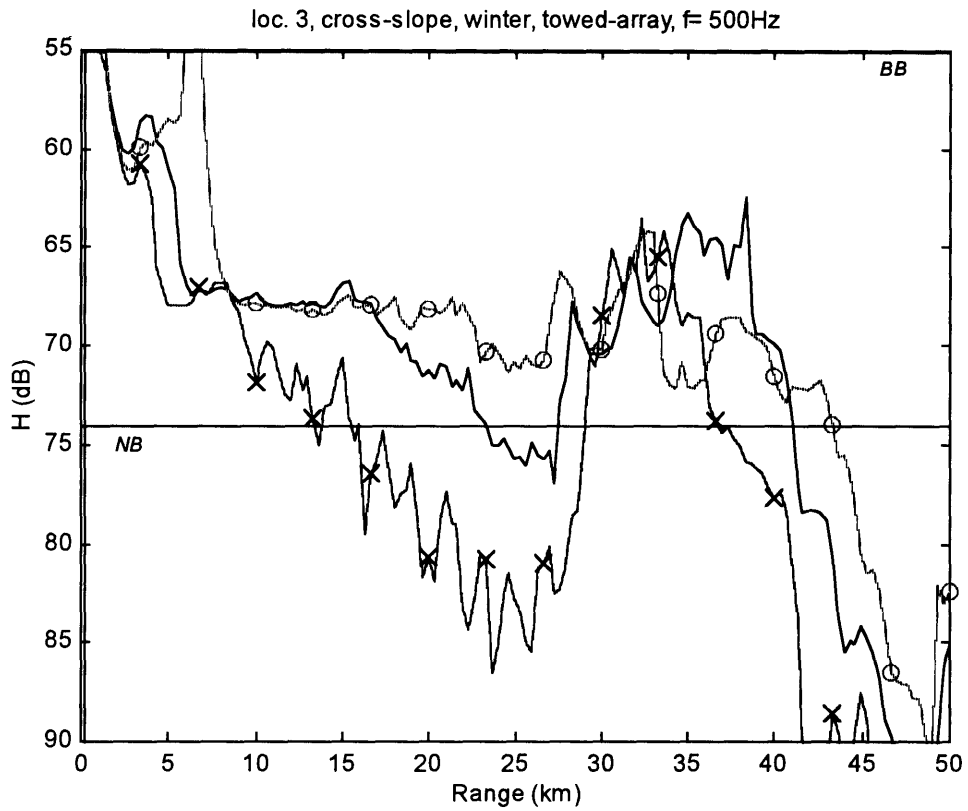
Figure A.102 (upper) & Figure A.103 (lower): Sonar performance, 3rd location.

loc. 3, cross-slope, winter, hull-array, f= 1000Hz

loc. 3, cross-slope, winter, hull-array, f= 1500Hz
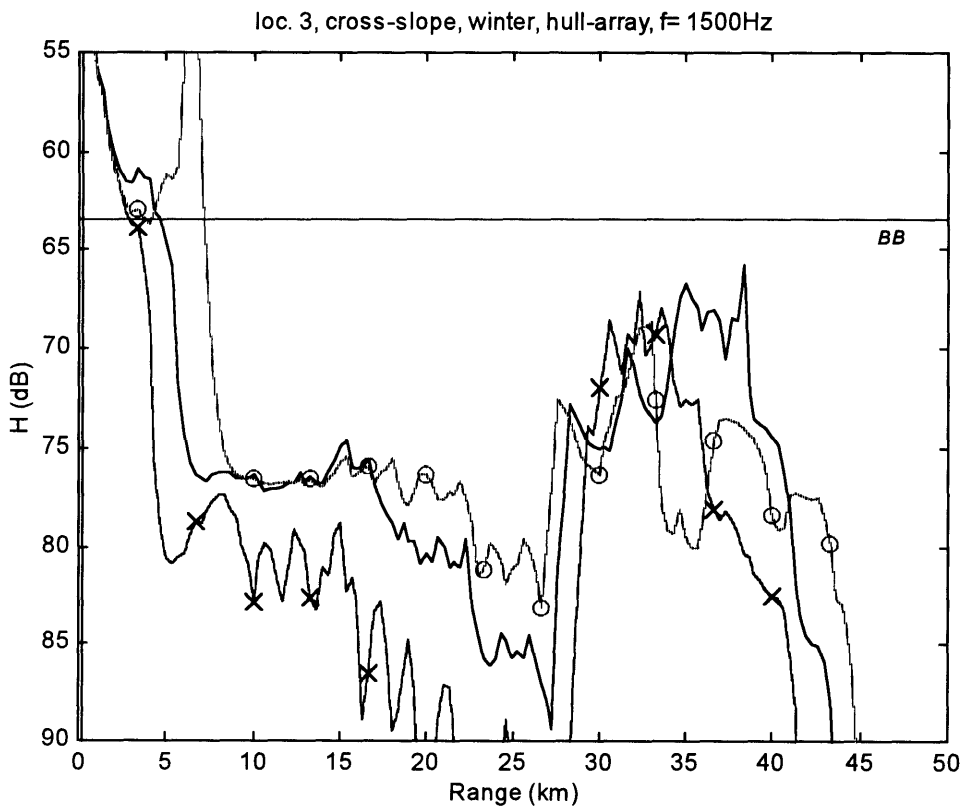

Figure A.104 (upper) & Figure A.105 (lower): Sonar performance, 3rd location.

loc. 3, cross-slope, winter, bow-array, f= 2000Hz

loc. 3, cross-slope, winter, bow-array, f= 3000Hz

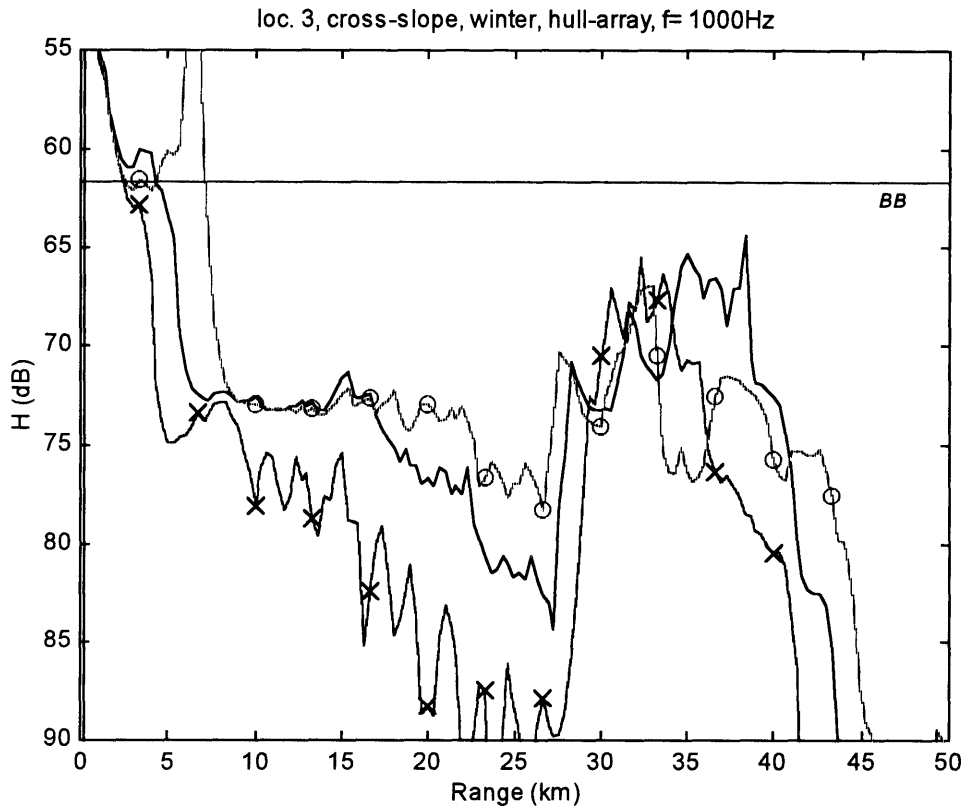Figure A.106 (upper) & Figure A.107 (lower): Sonar performance, 3rd location.

loc. 3, cross-slope, winter, bow-array, f= 5000Hz

Figure A.108: Sonar performance, 3rd location.

loc. 3, down-slope, winter, towed-array, f= 100Hz

loc. 3, down-slope, winter, towed-array, f= 200Hz

Figure A.109 (upper) & Figure A.110 (lower): Sonar performance, 3rd location.

Figure A.111 (upper) & Figure A.112 (lower): Sonar performance, 3rd location.
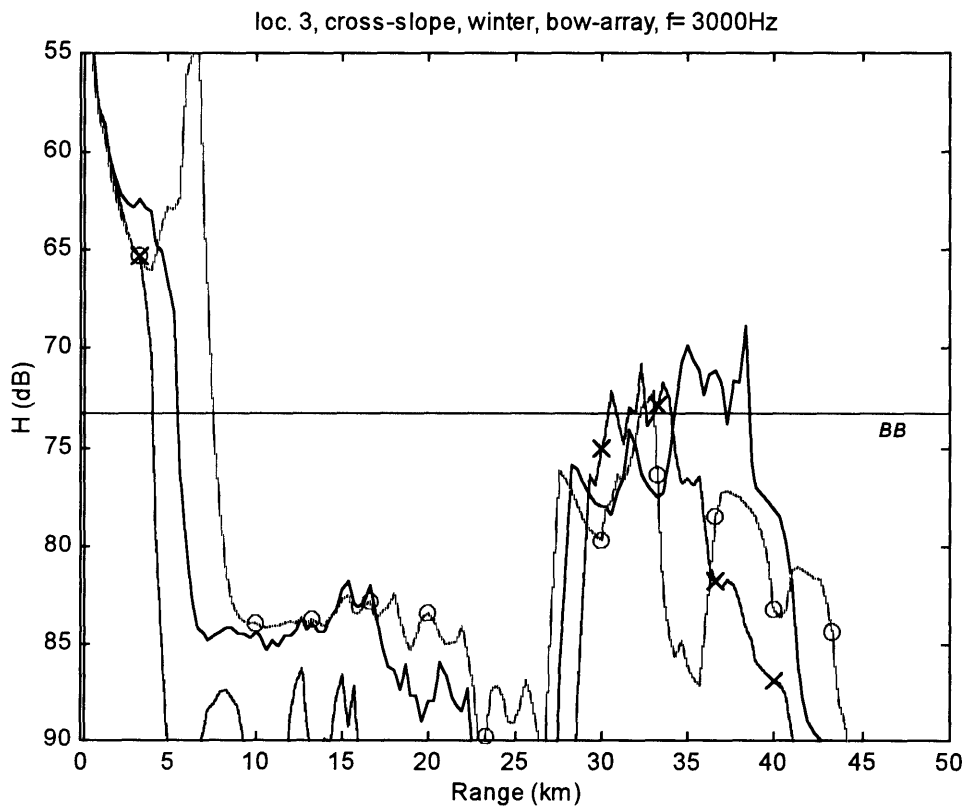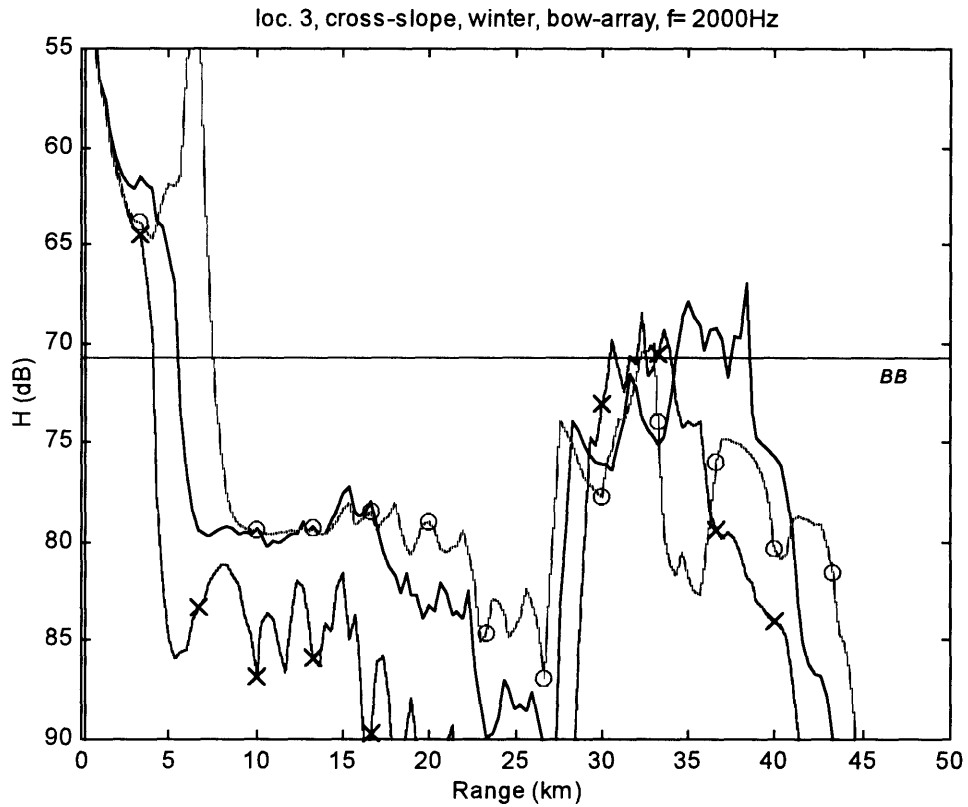
loc. 3, down-slope, winter, hull-array, f= 1000Hz

loc. 3, down-slope, winter, hull-array, f= 1500Hz

Figure A.113 (upper) & Figure A.114 (lower): Sonar performance, 3rd location.

Figure A.115 (upper) & Figure A.116 (lower): Sonar performance, 3rd location.
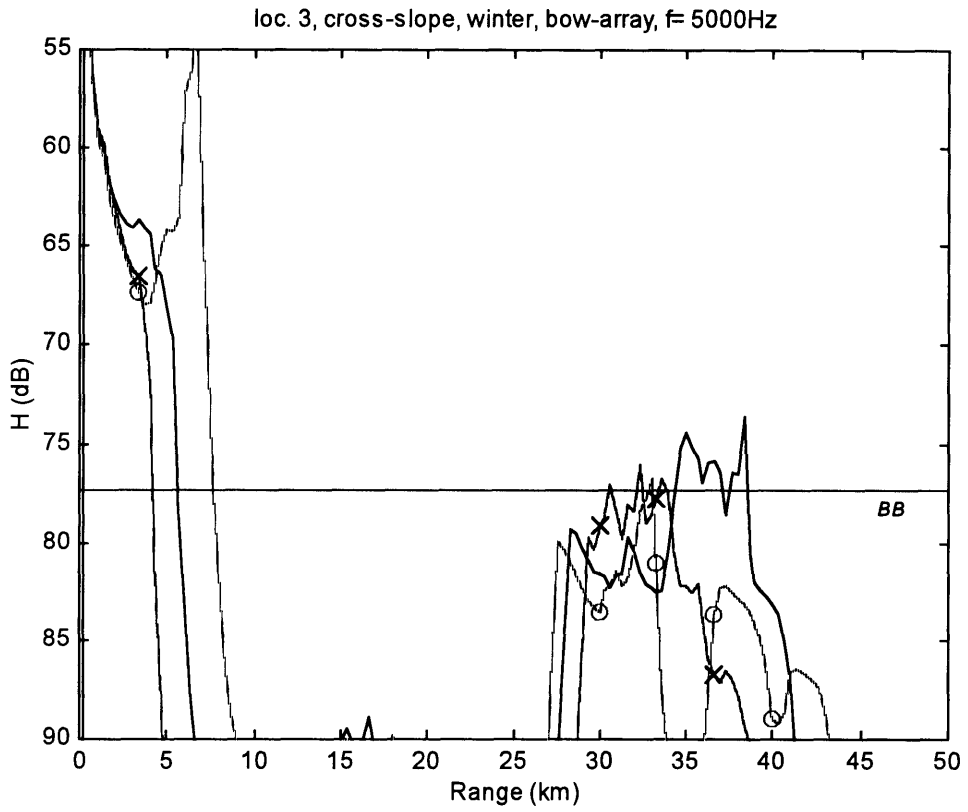
loc. 3, down-slope, winter, bow-array, f= 5000Hz

Figure A.117: Sonar performance, 3rd location.

Figure A.118 (upper) & Figure A.119 (lower): Sonar performance, 3rd location.

loc. 3, up-slope, summer, towed-array, f= 500Hz
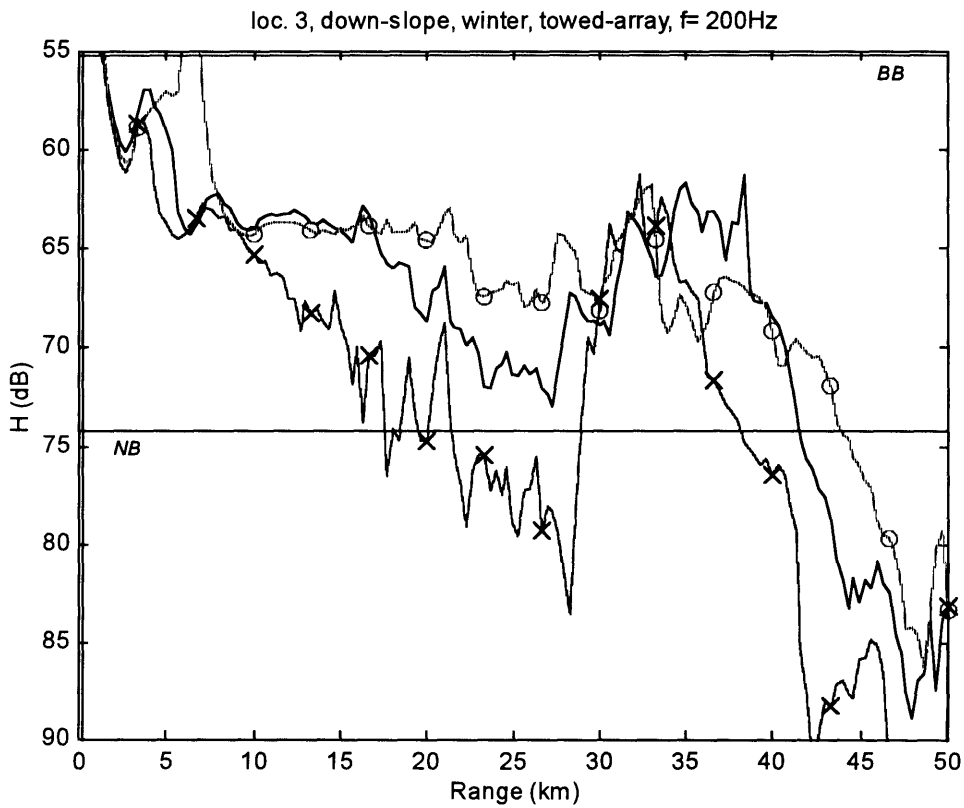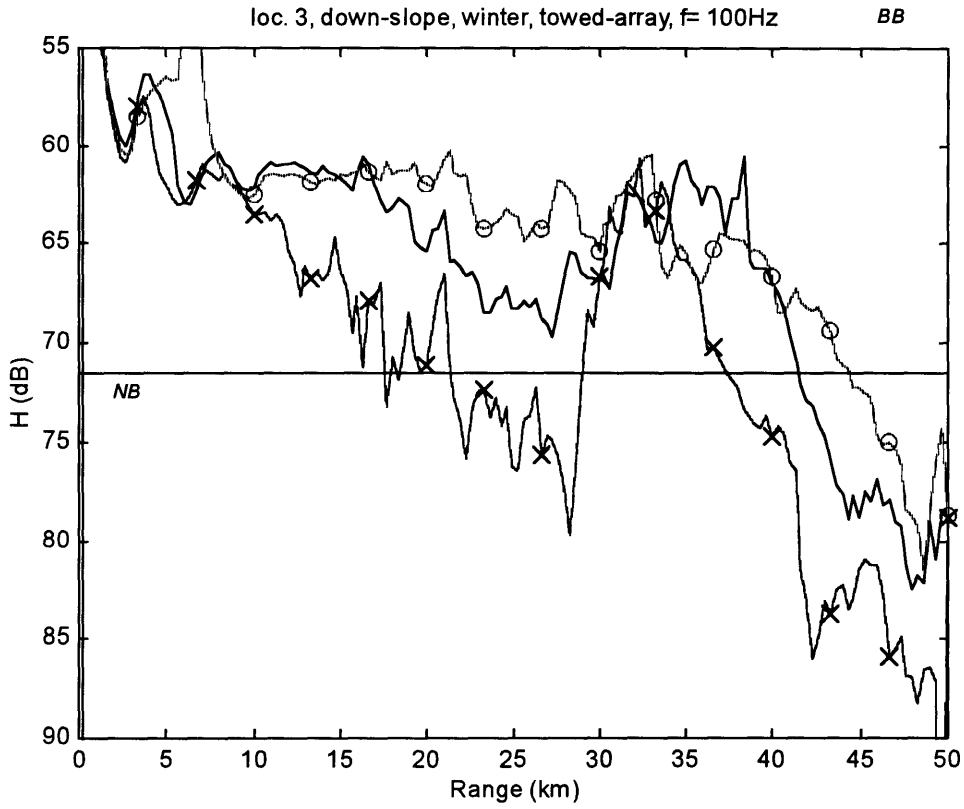

loc. 3, up-slope, summer, hull-array, f= 500Hz
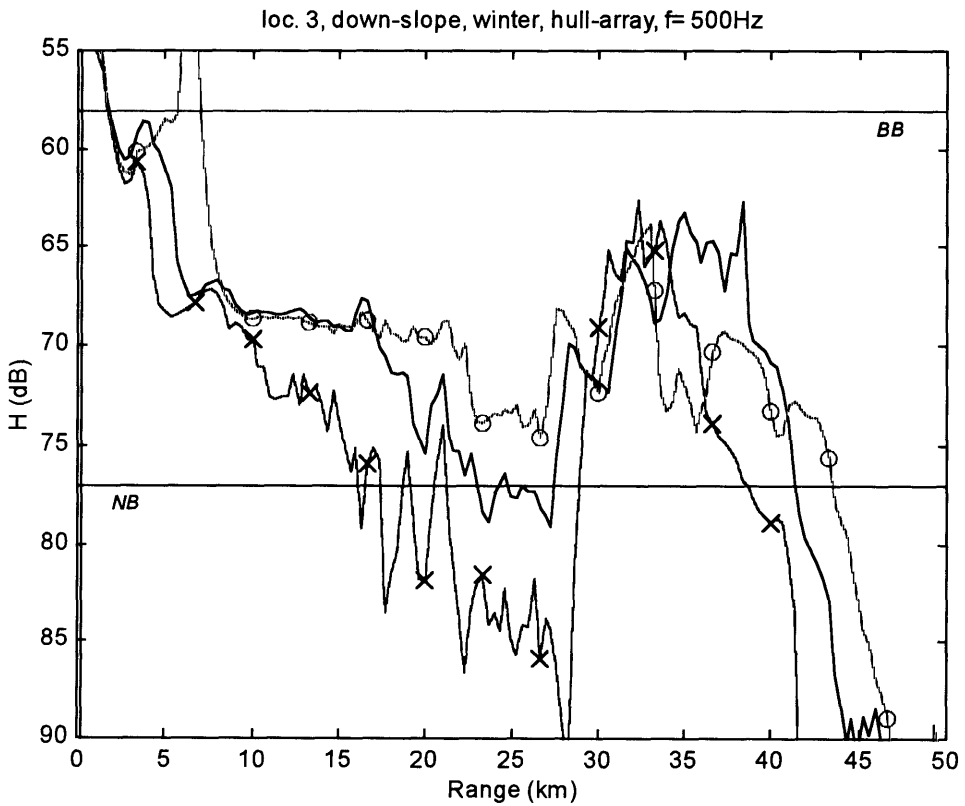
Figure A.120 (upper) & Figure A.121 (lower): Sonar performance, 3rd location.

loc. 3, up-slope, summer, hull-array, f= 1000Hz

loc. 3, up-slope, summer, hull-array, f= 1500Hz

Figure A.122 (upper) & Figure A.123 (lower): Sonar performance, 3rd location.

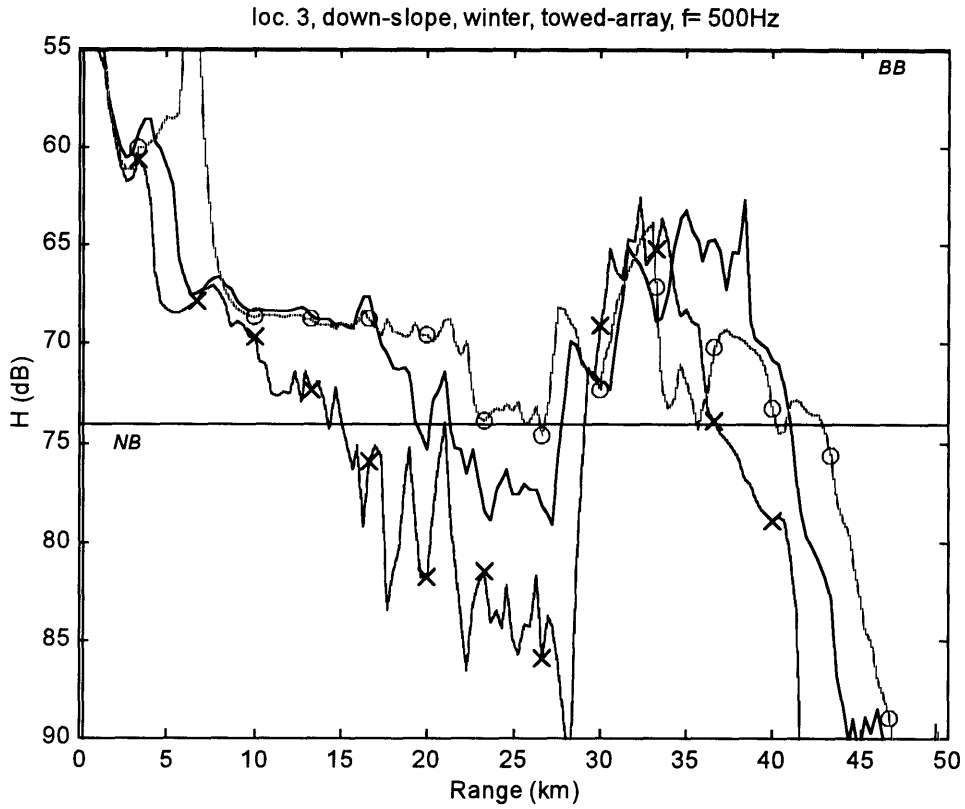loc. 3, up-slope, summer, bow-array, f= 2000Hz

loc. 3, up-slope, summer, bow-array, f= 3000Hz
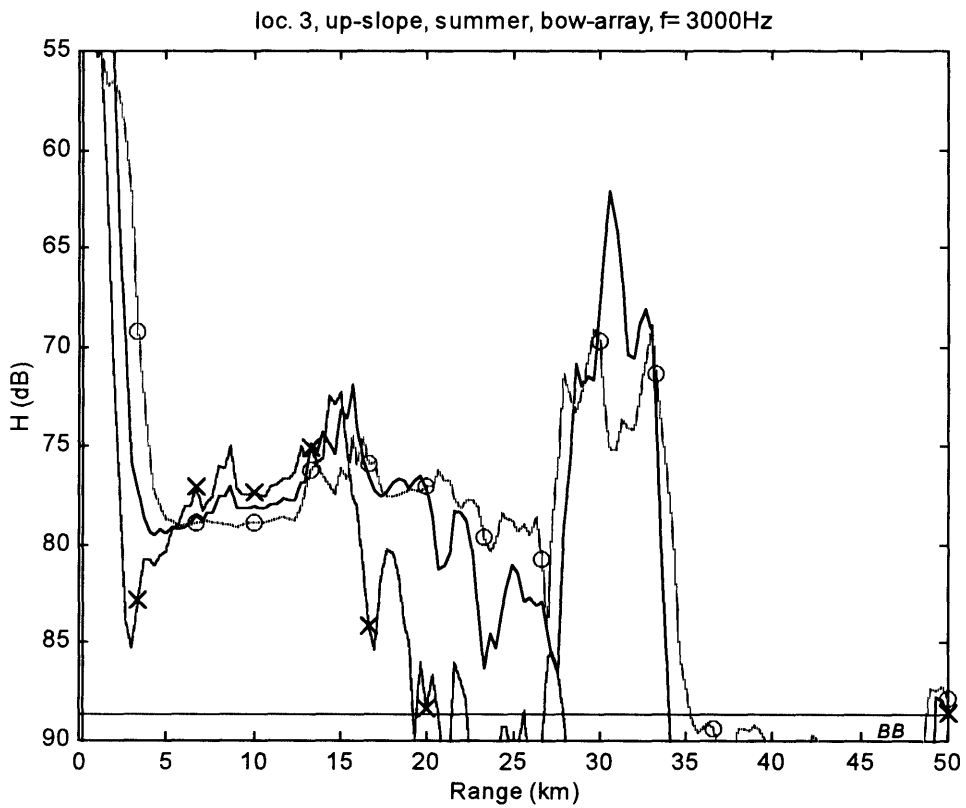
Figure A.124 (upper) & Figure A.125 (lower): Sonar performance, 3rd location.

loc. 3, up-slope, summer, bow-array, f= 5000Hz
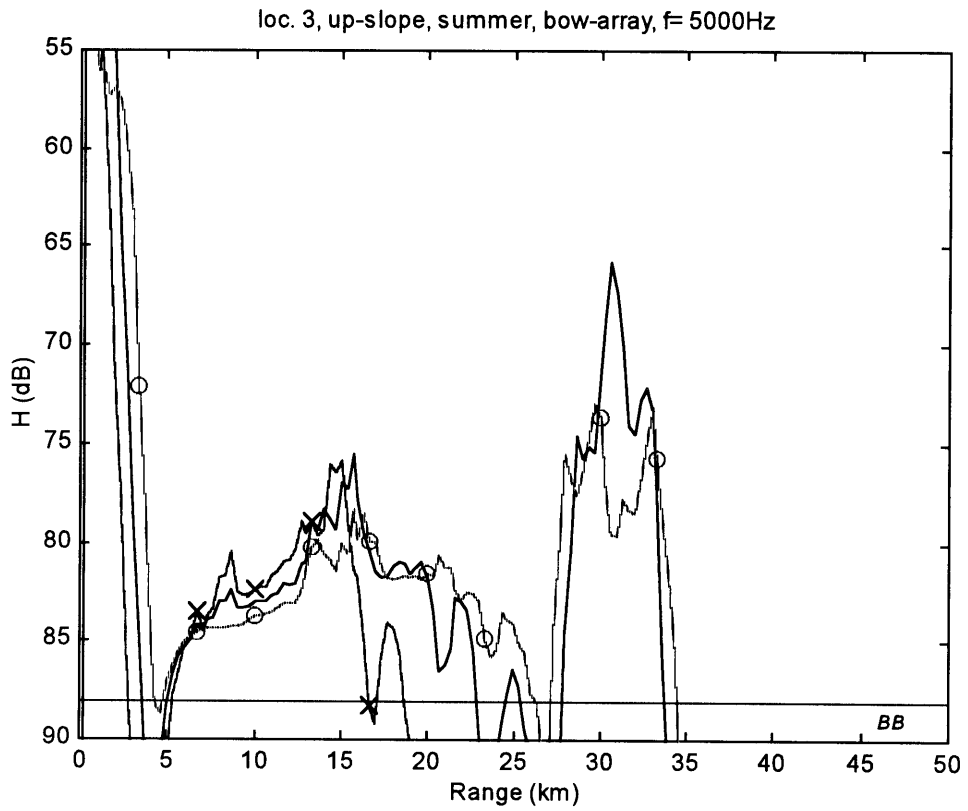
Figure A.126: Sonar performance, 3rd location.

loc. 3, cross-slope, summer, towed-array, f= 100Hz   *BB*

loc. 3, cross-slope, summer, towed-array, f= 200Hz
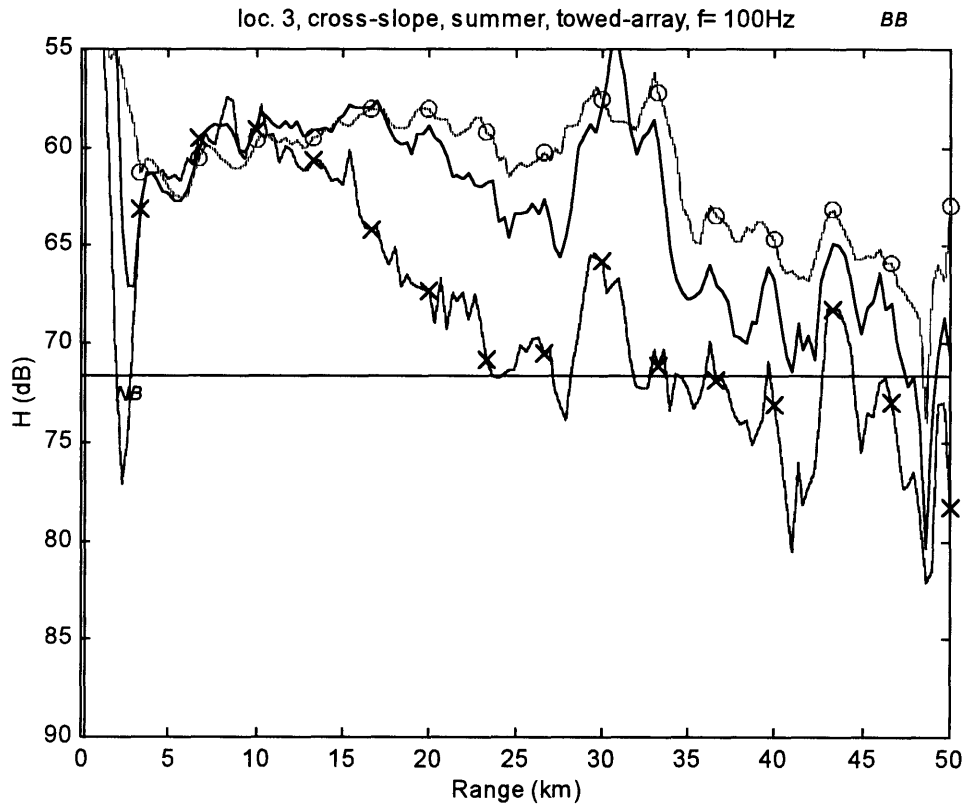
Figure A.127 (upper) & Figure A.128 (lower): Sonar performance, 3rd location.

loc. 3, cross-slope, summer, towed-array, f= 500Hz

loc. 3, cross-slope, summer, hull-array, f= 500Hz

Figure A.129 (upper) & Figure A.130 (lower): Sonar performance, 3rd location.
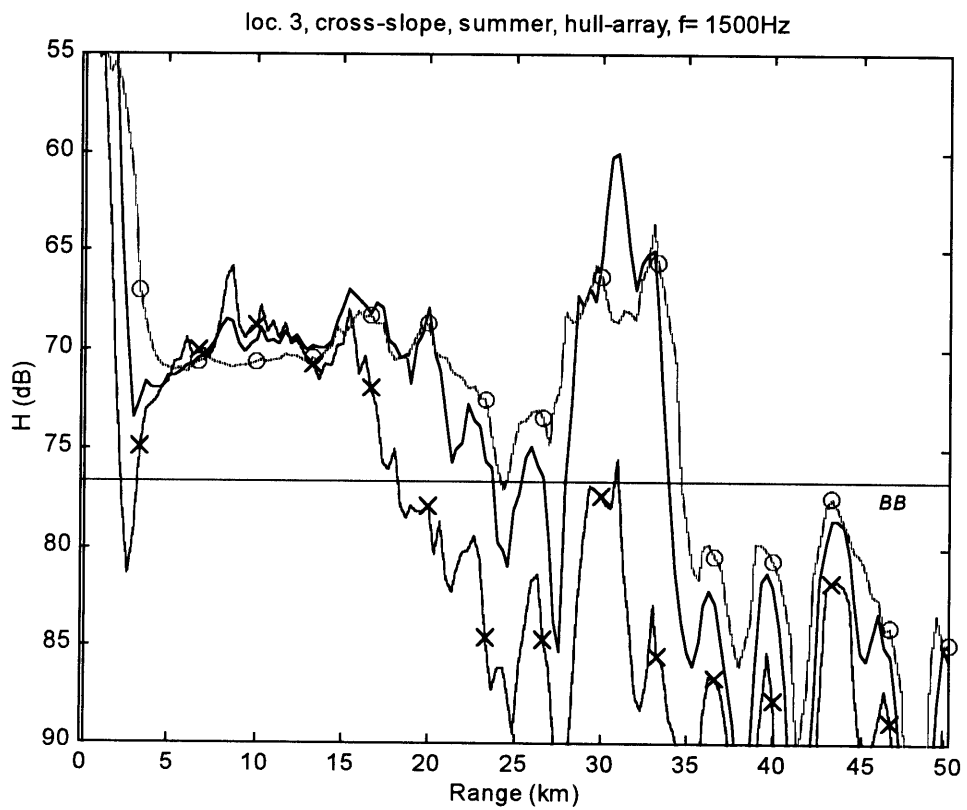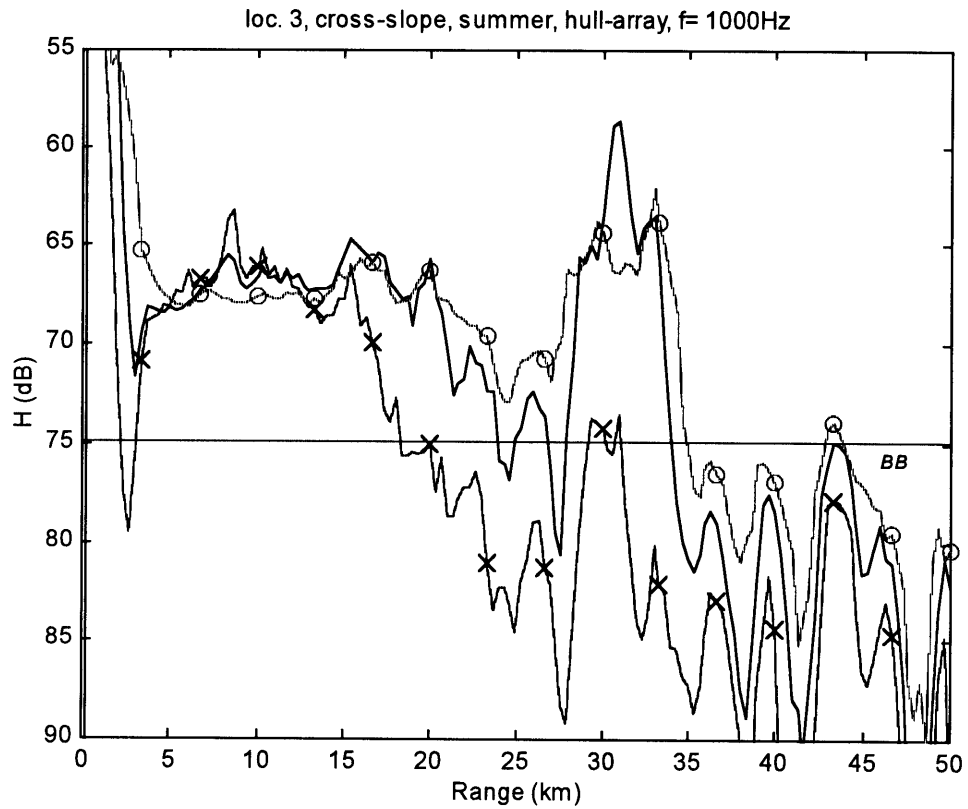
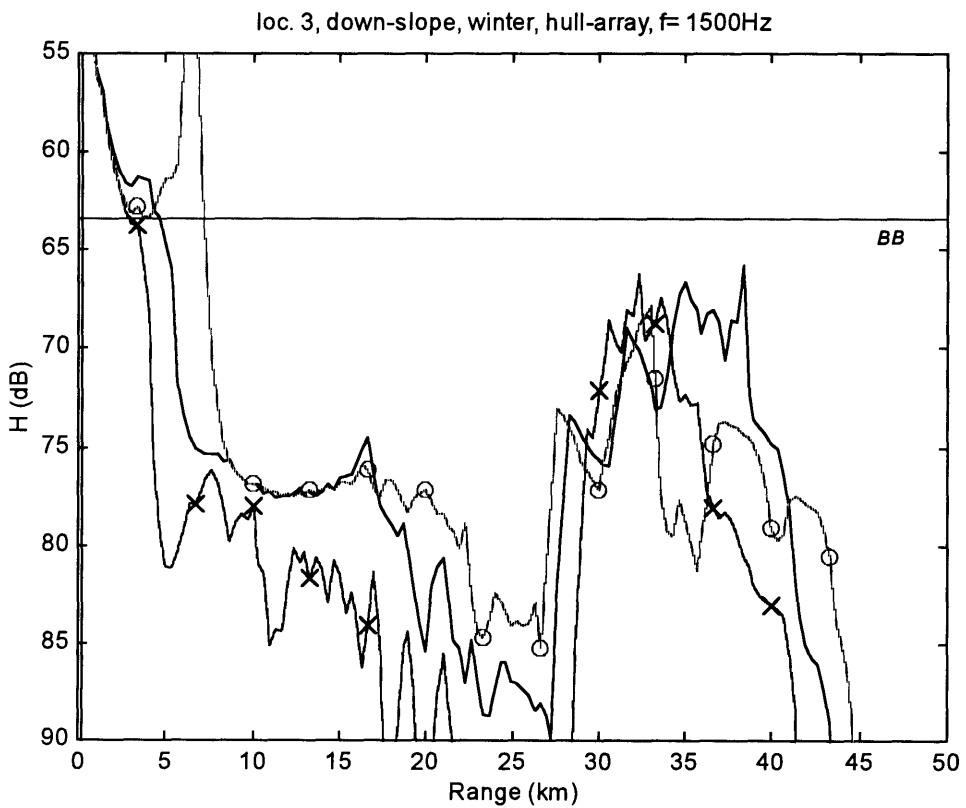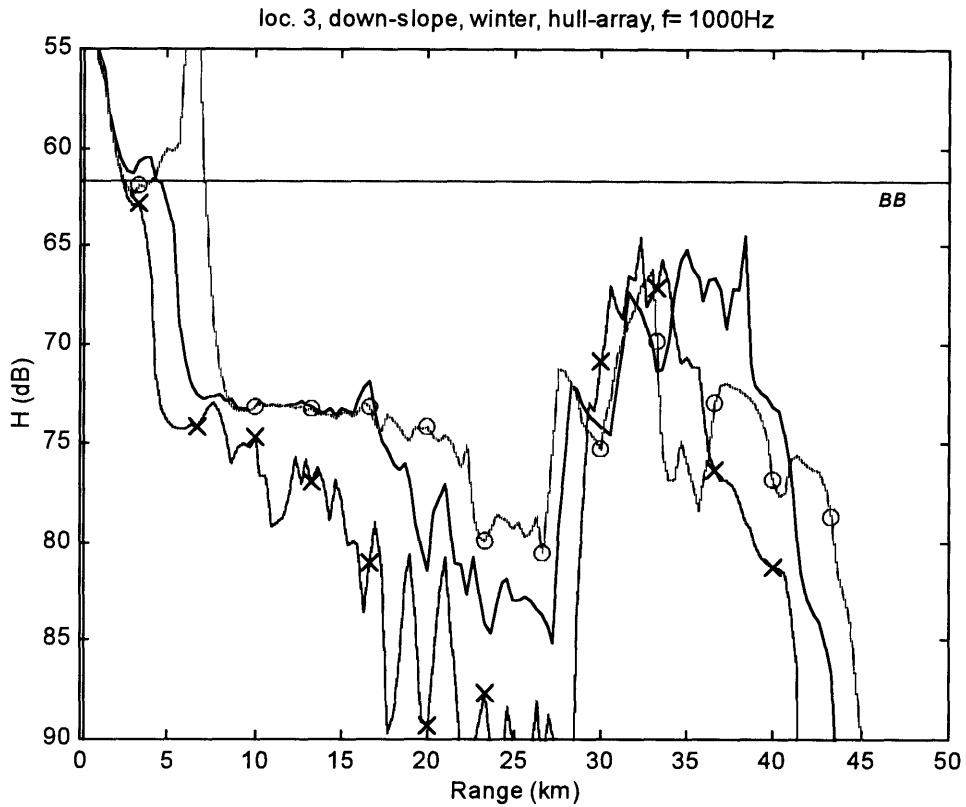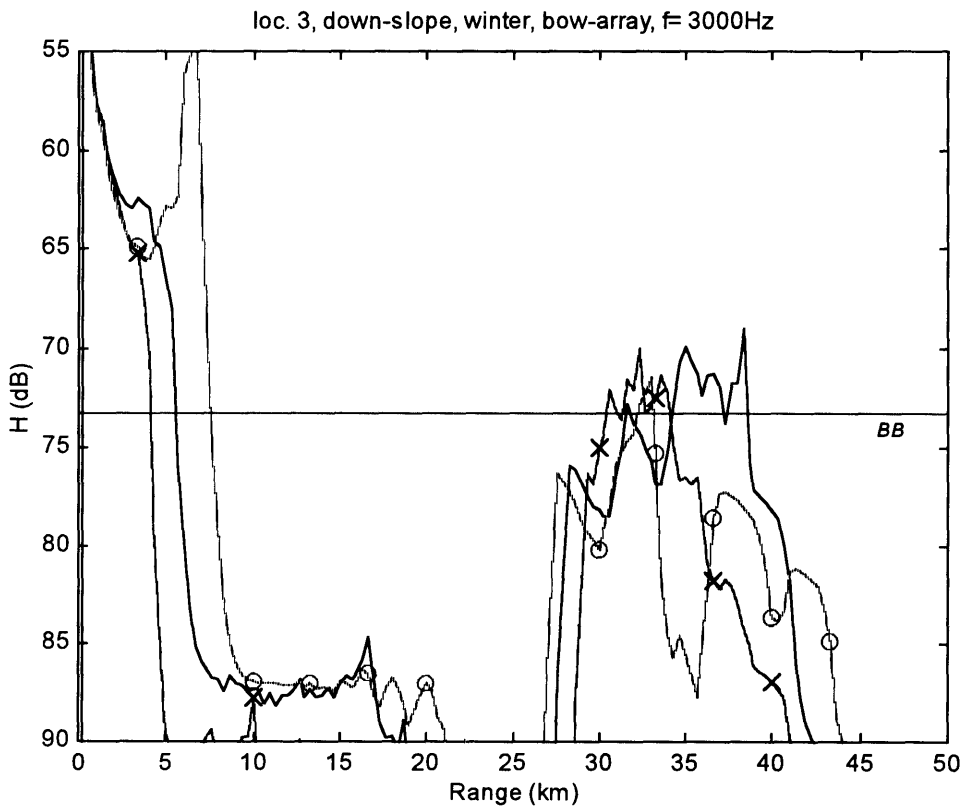Figure A.131 (upper) & Figure A.132 (lower): Sonar performance, 3rd location.

loc. 3, cross-slope, summer, bow-array, f= 2000Hz

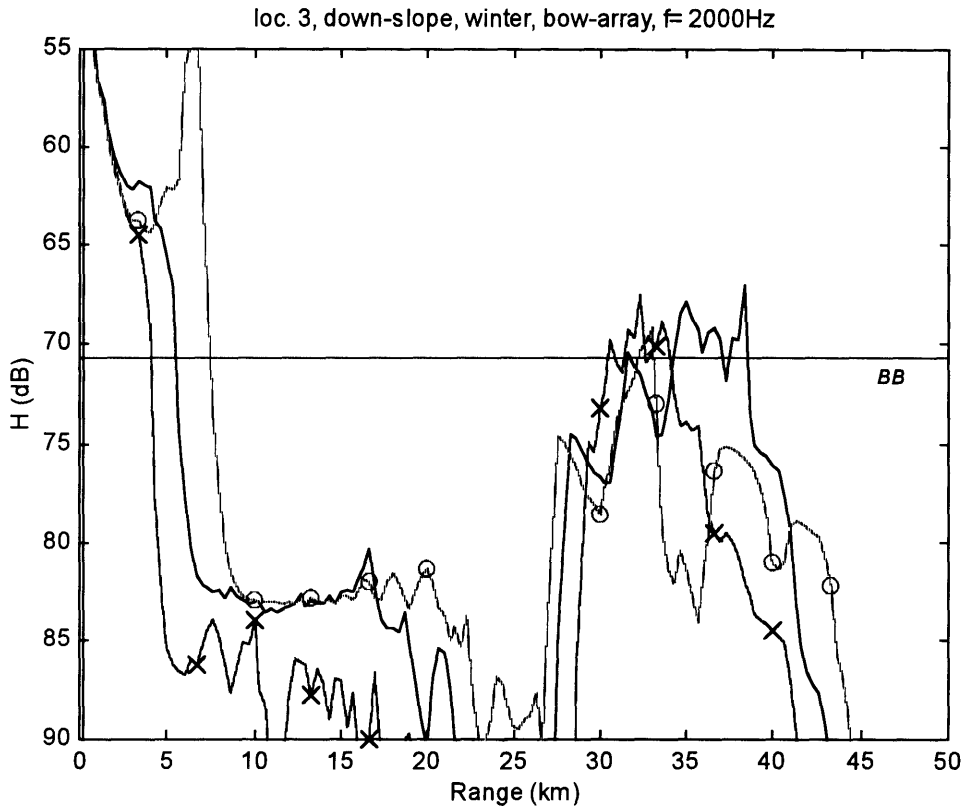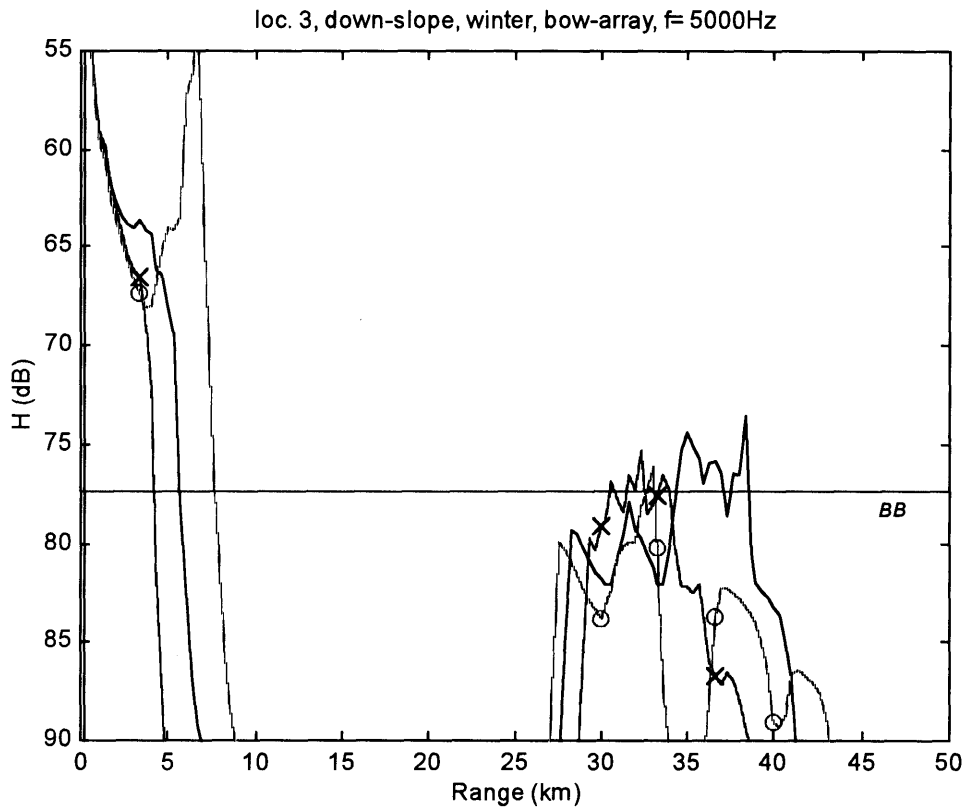loc. 3, cross-slope, summer, bow-array, f= 3000Hz
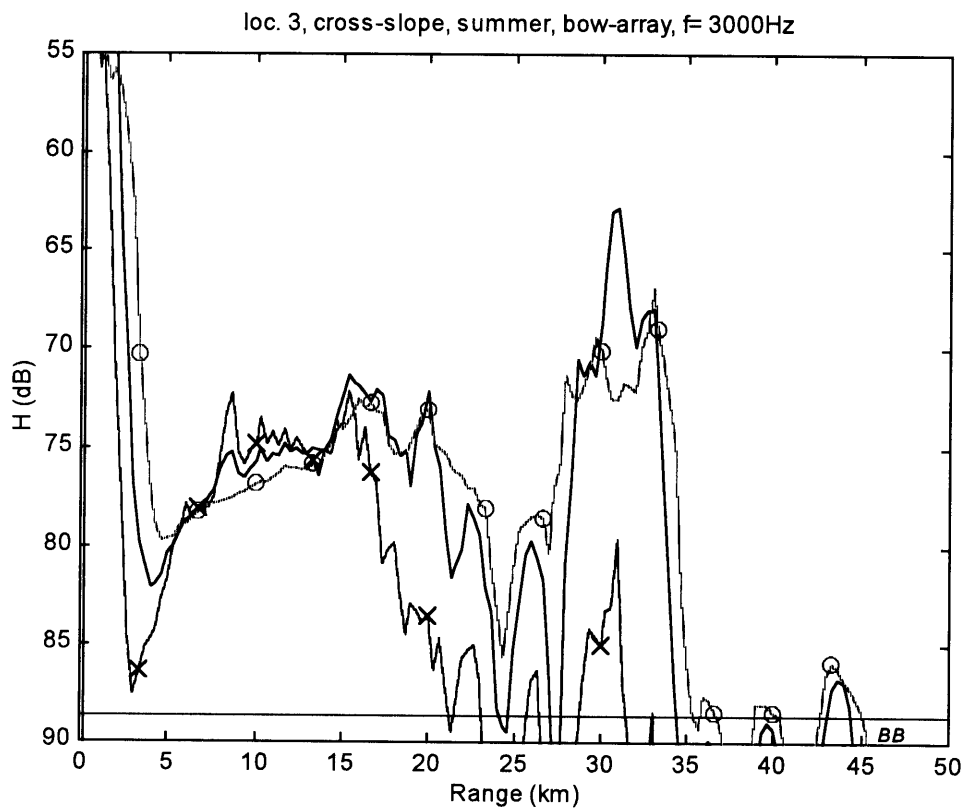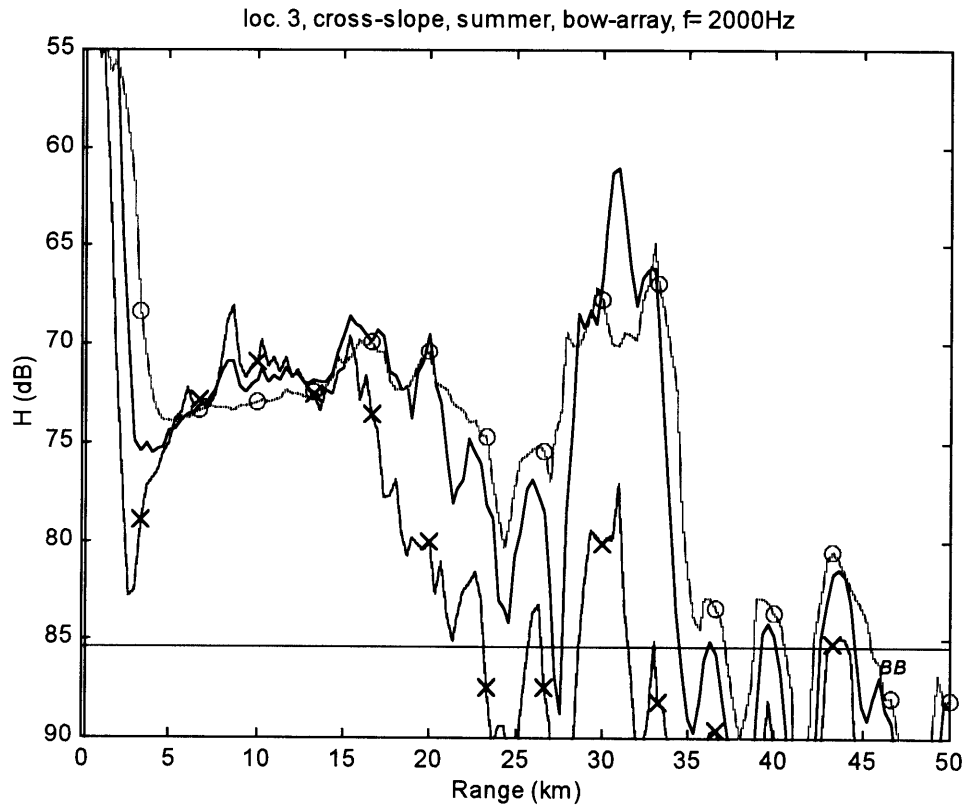
Figure A.133 (upper) & Figure A.134 (lower): Sonar performance, 3rd location.
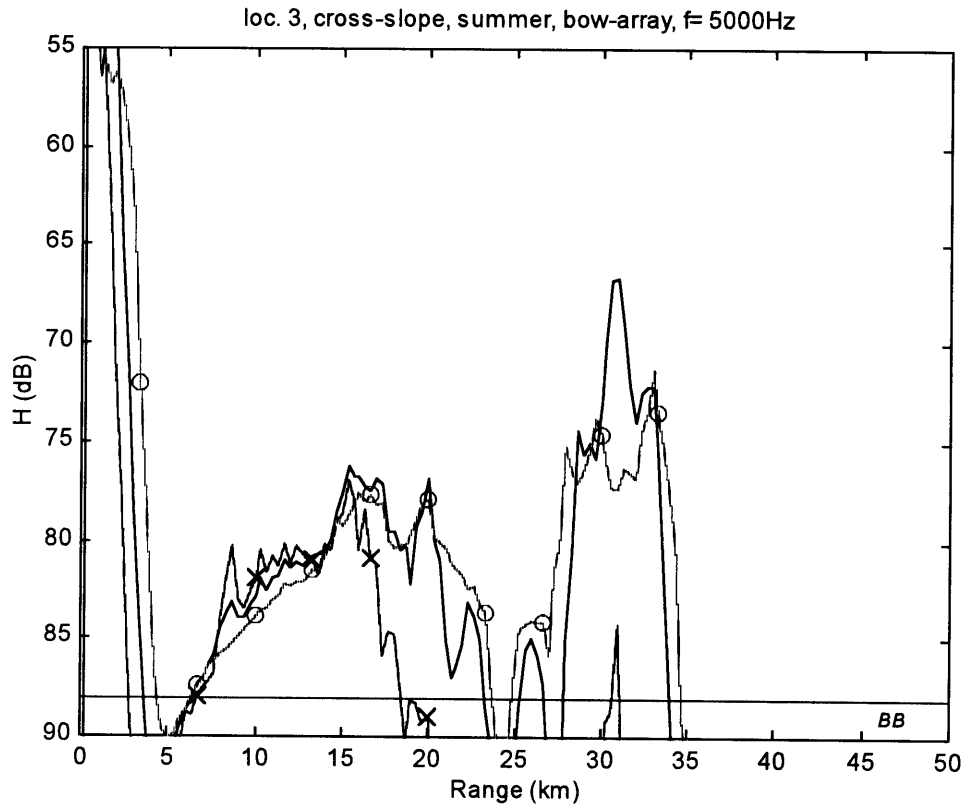
Figure A.135: Sonar performance, 3rd location.

loc. 3, down-slope, summer, towed-array, f= 100Hz   *BB*

loc. 3, down-slope, summer, towed-array, f= 200Hz
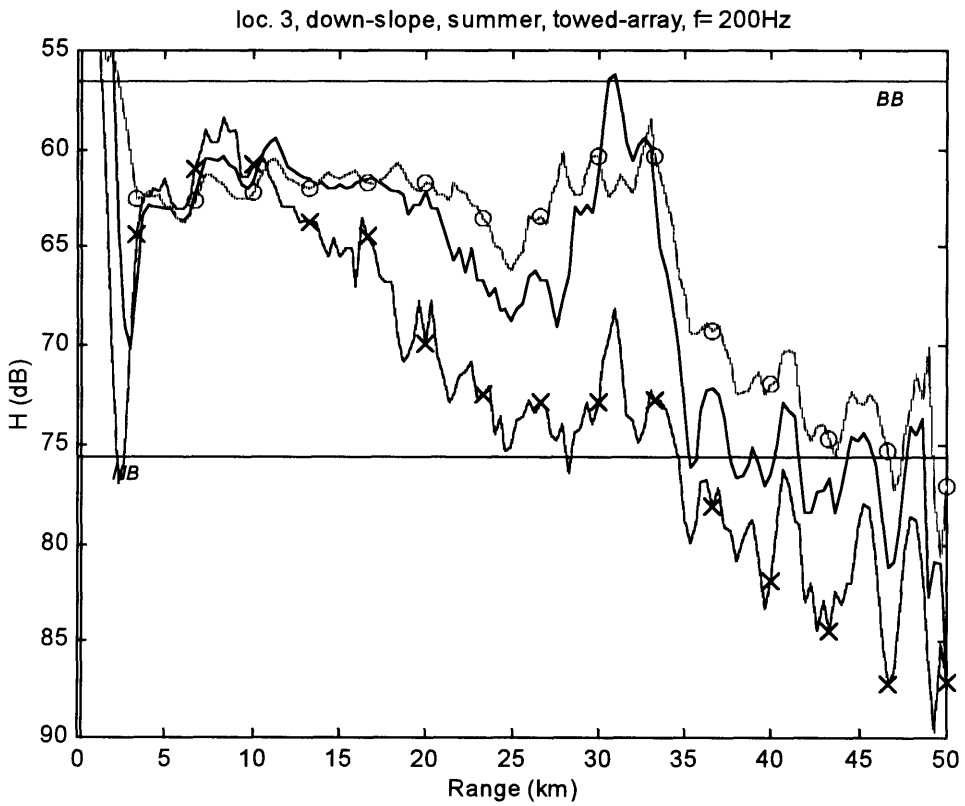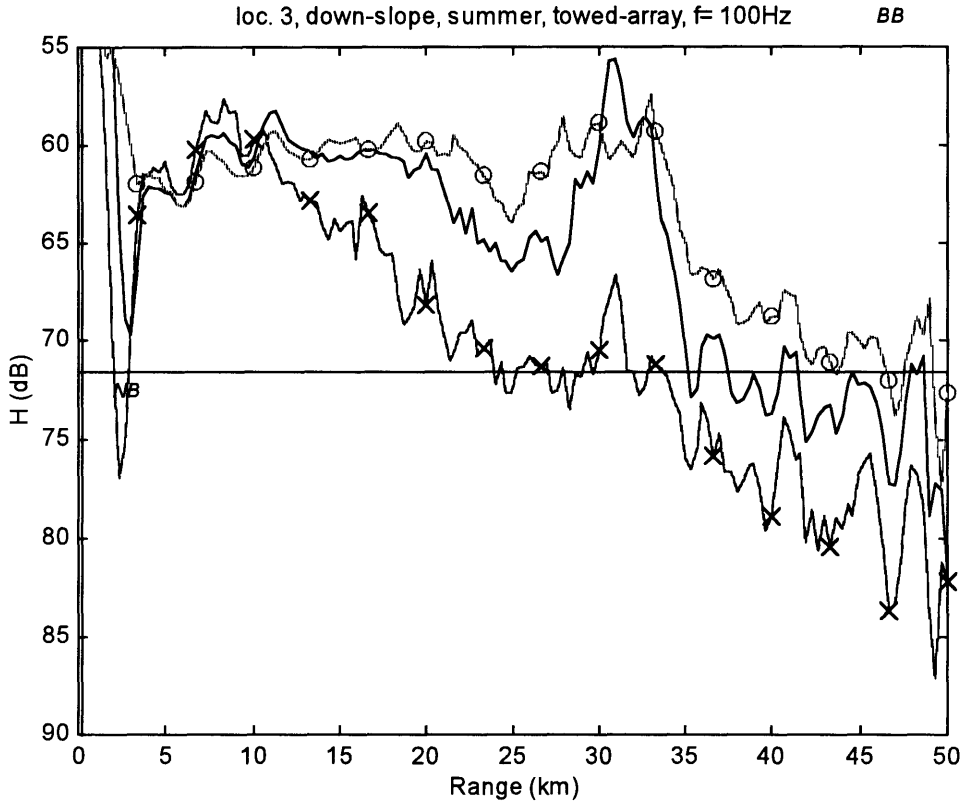
Figure A.136 (upper) & Figure A.137 (lower): Sonar performance, 3rd location.

loc. 3, down-slope, summer, towed-array, f= 500Hz

loc. 3, down-slope, summer, hull-array, f= 500Hz
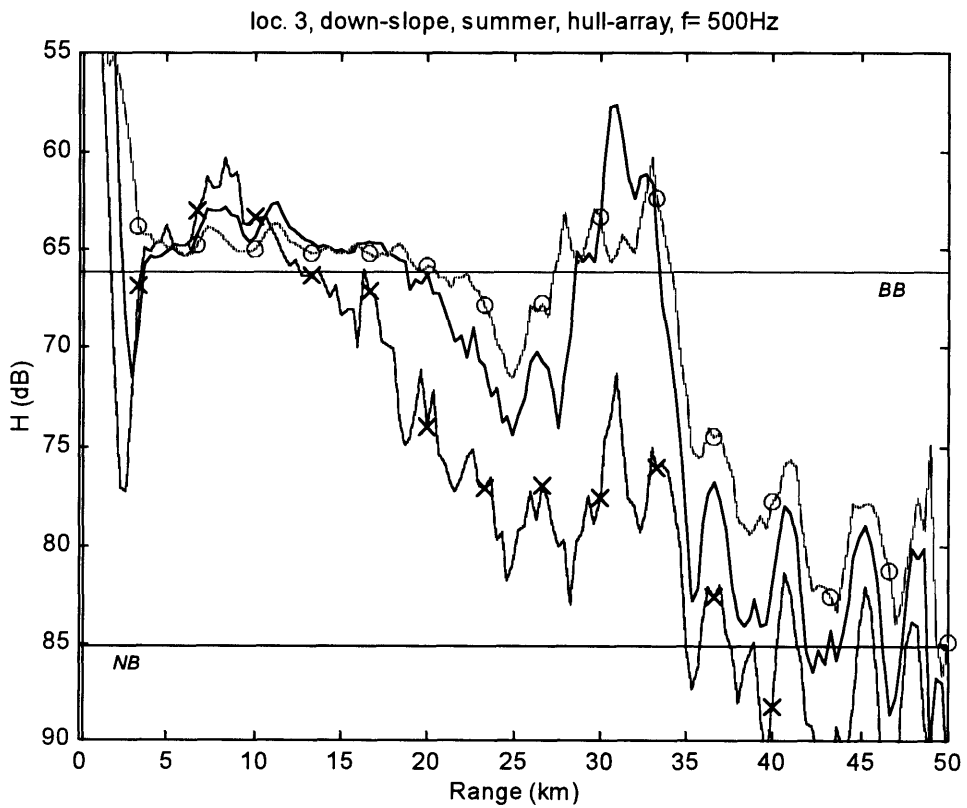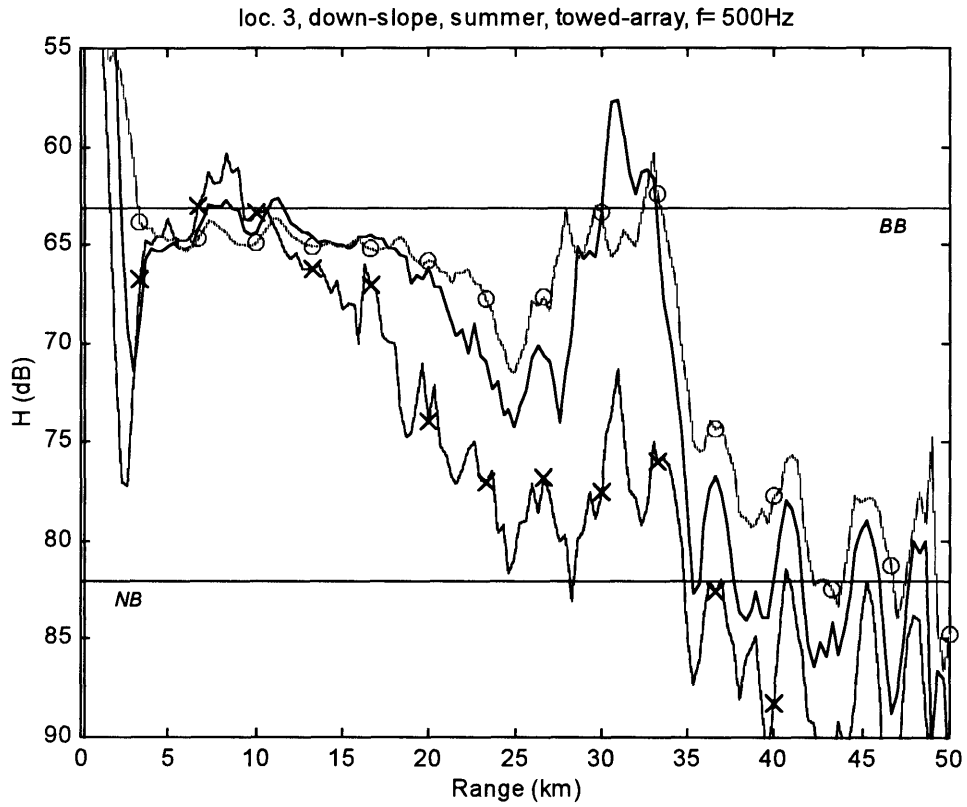
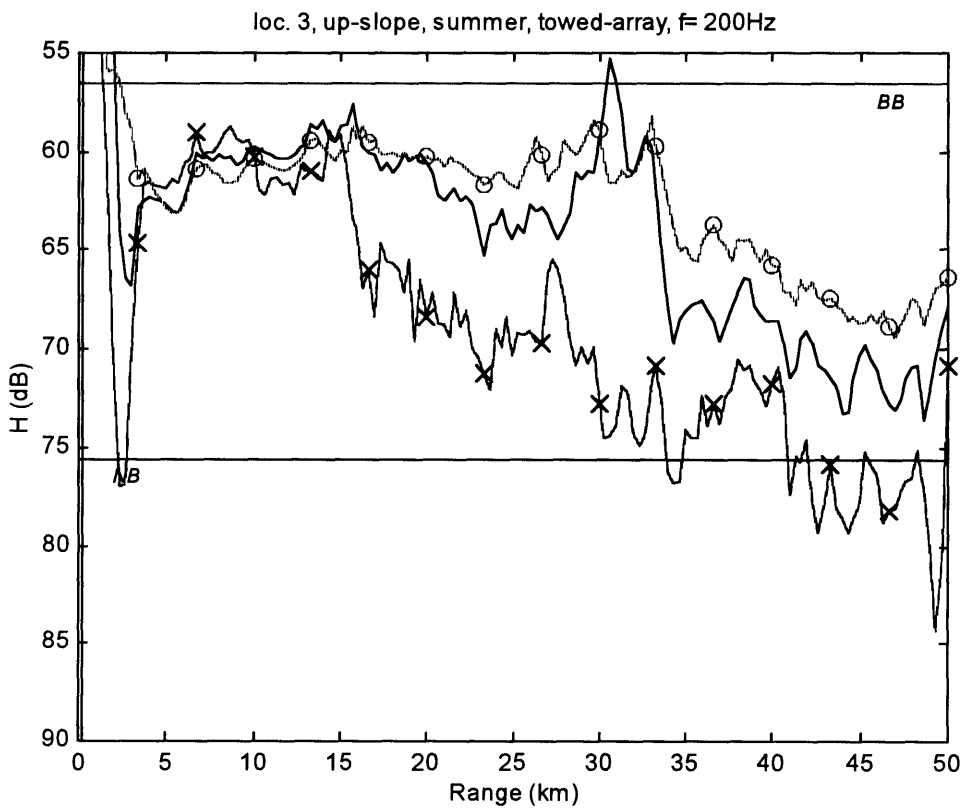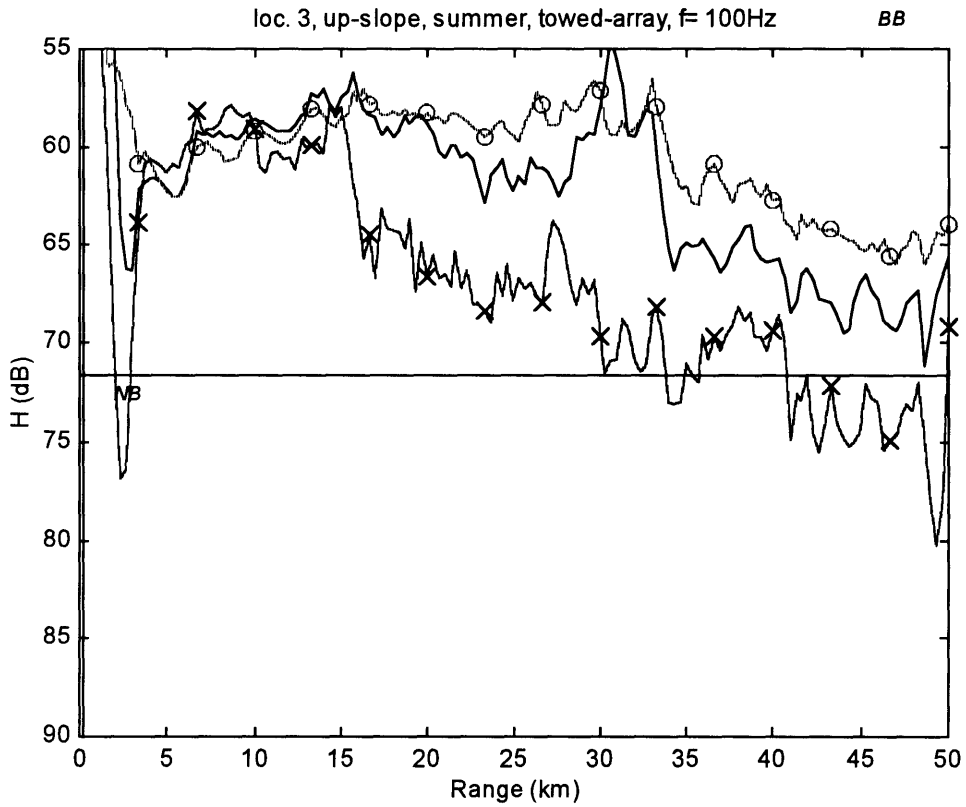Figure A.138 (upper) & Figure A.139 (lower): Sonar performance, 3rd location.

loc. 3, down-slope, summer, hull-array, f= 1000Hz

loc. 3, down-slope, summer, hull-array, f= 1500Hz
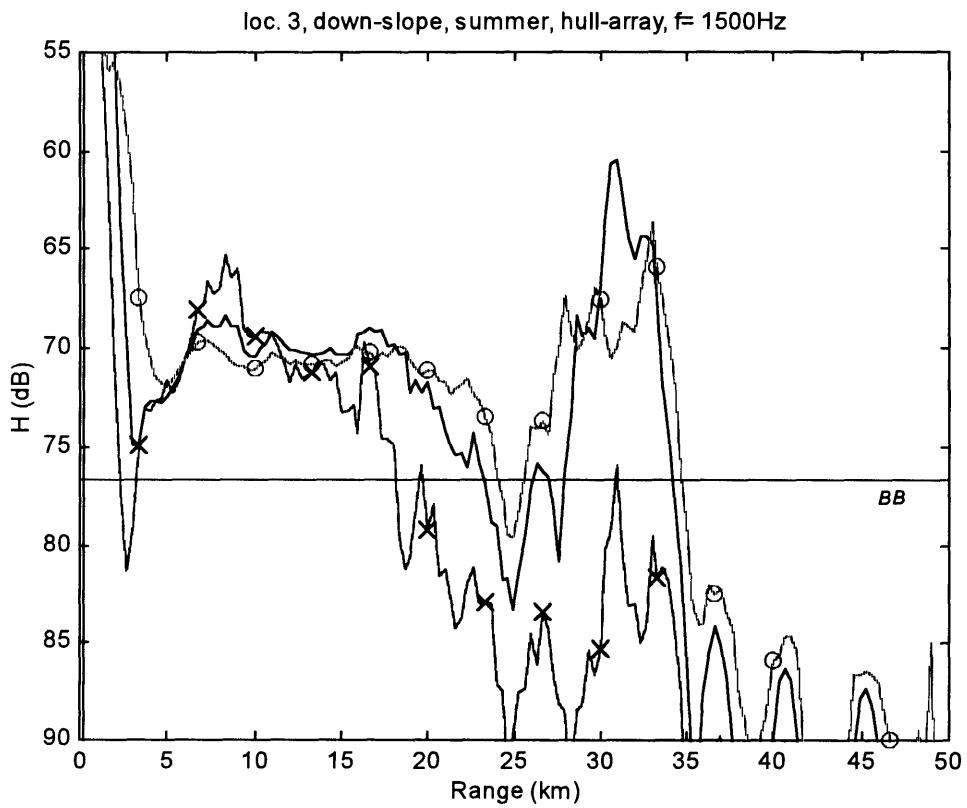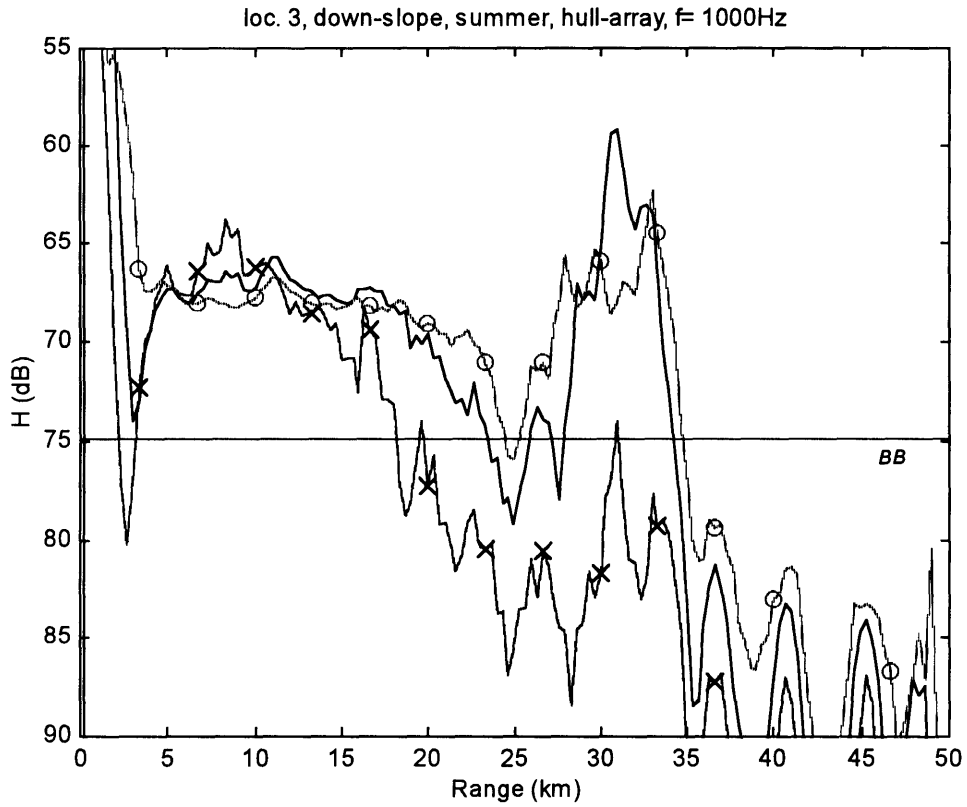
Figure A.140 (upper) & Figure A.141 (lower): Sonar performance, 3rd location.

loc. 3, down-slope, summer, bow-array, f= 2000Hz

loc. 3, down-slope, summer, bow-array, f= 3000Hz
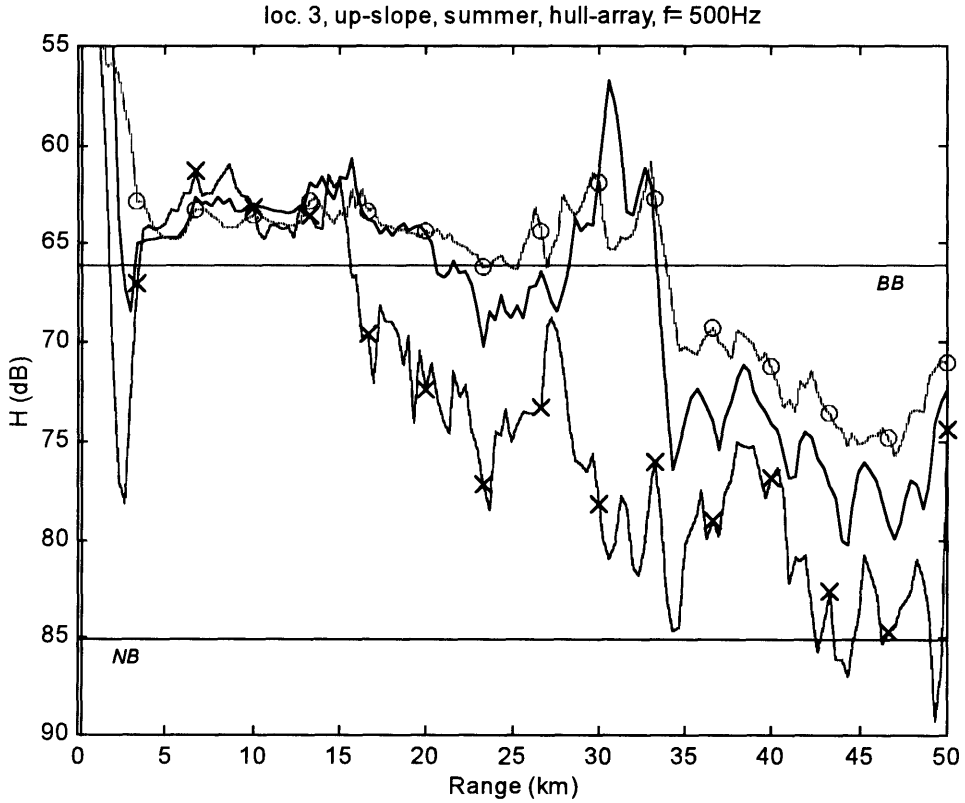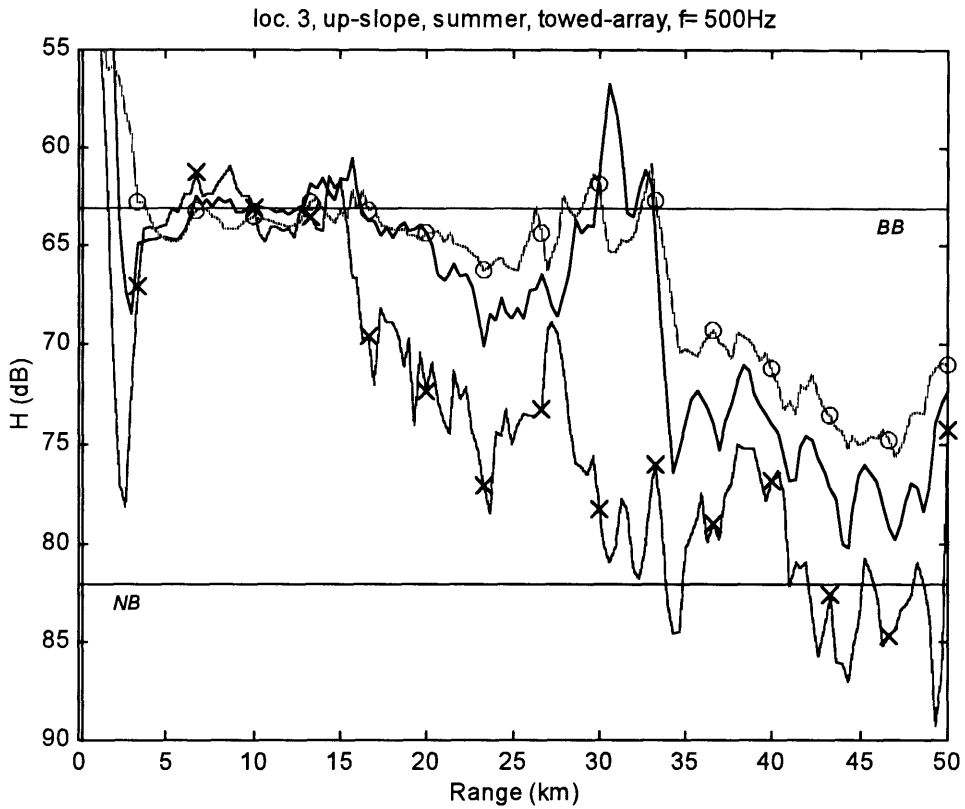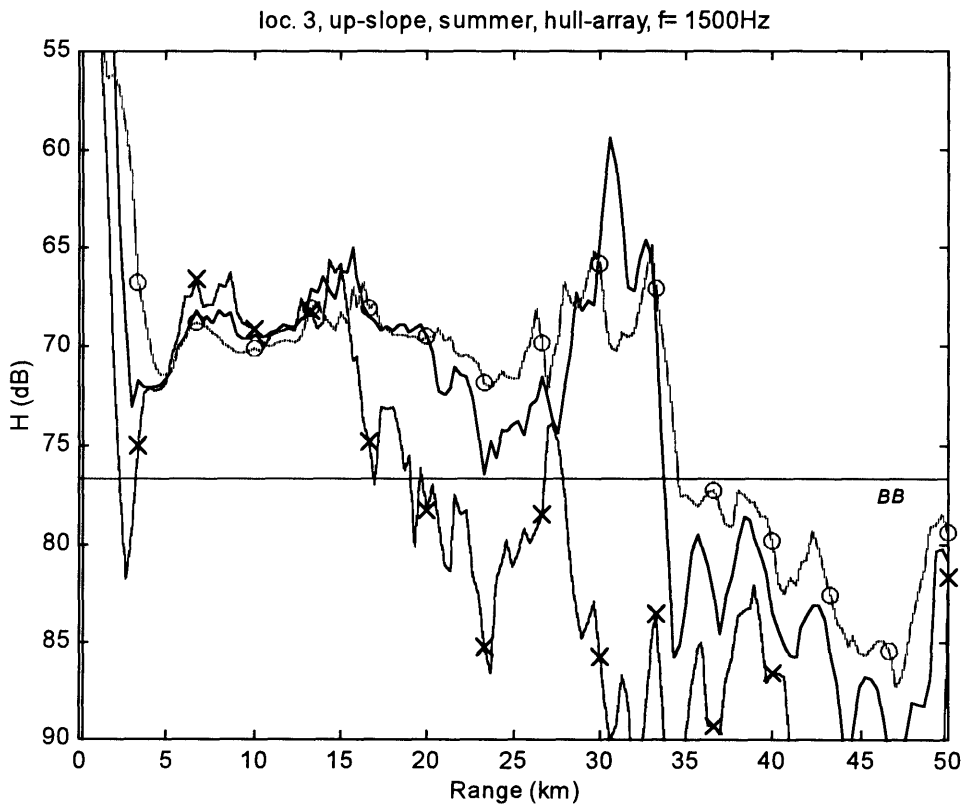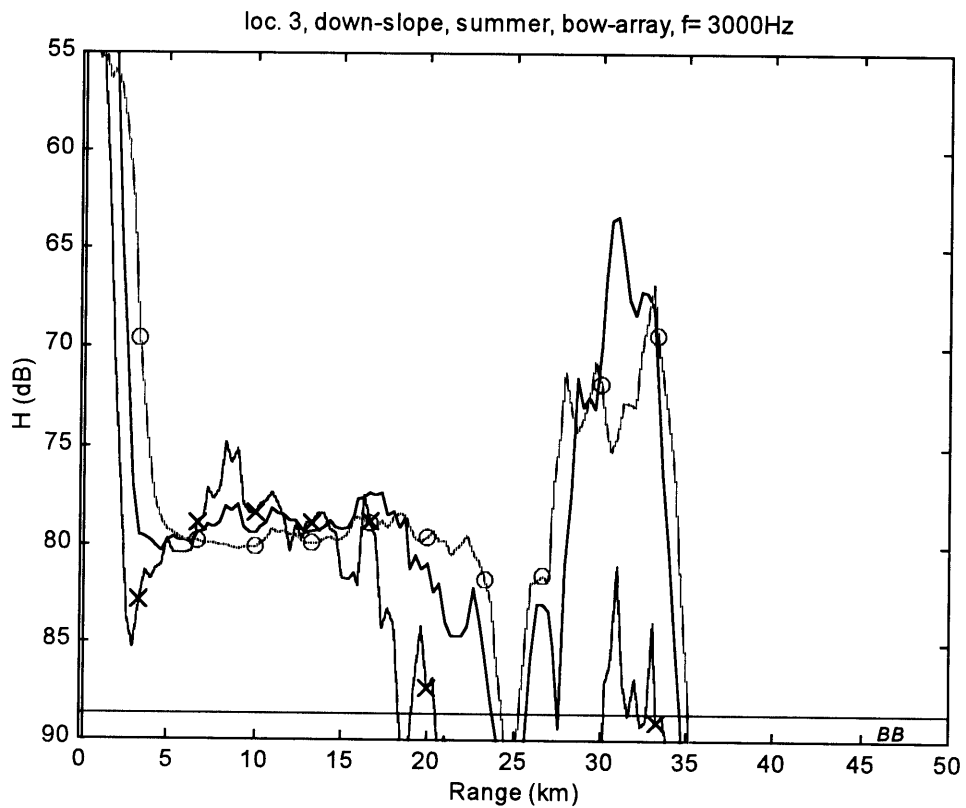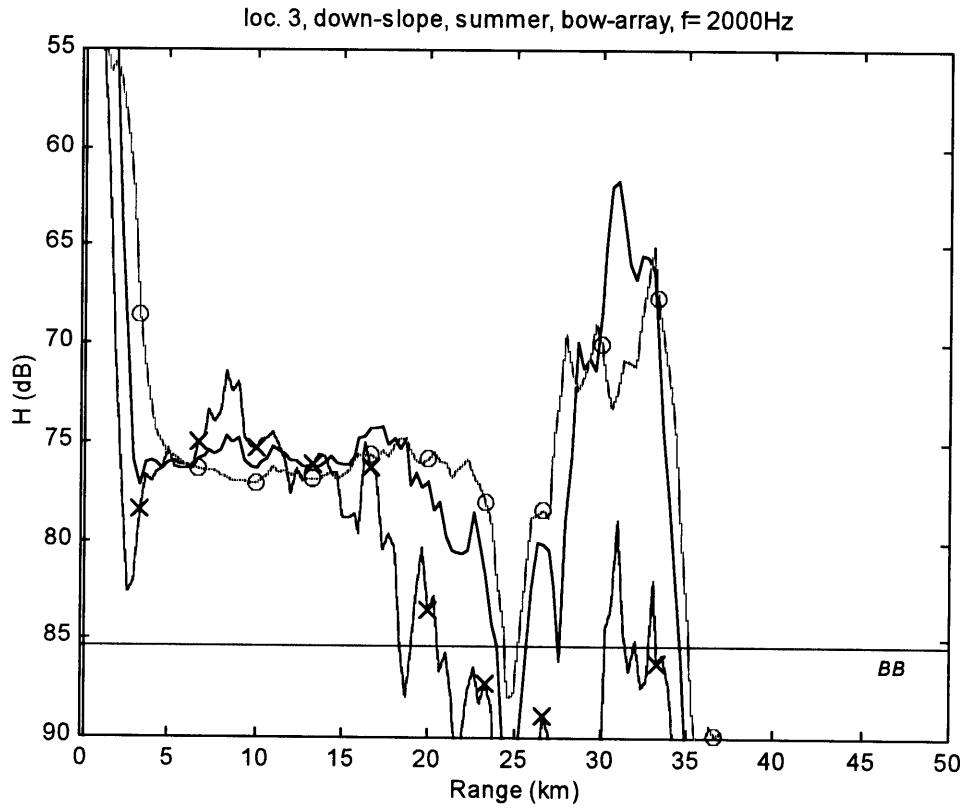
Figure A.142 (upper) & Figure A.143 (lower): Sonar performance, 3rd location.

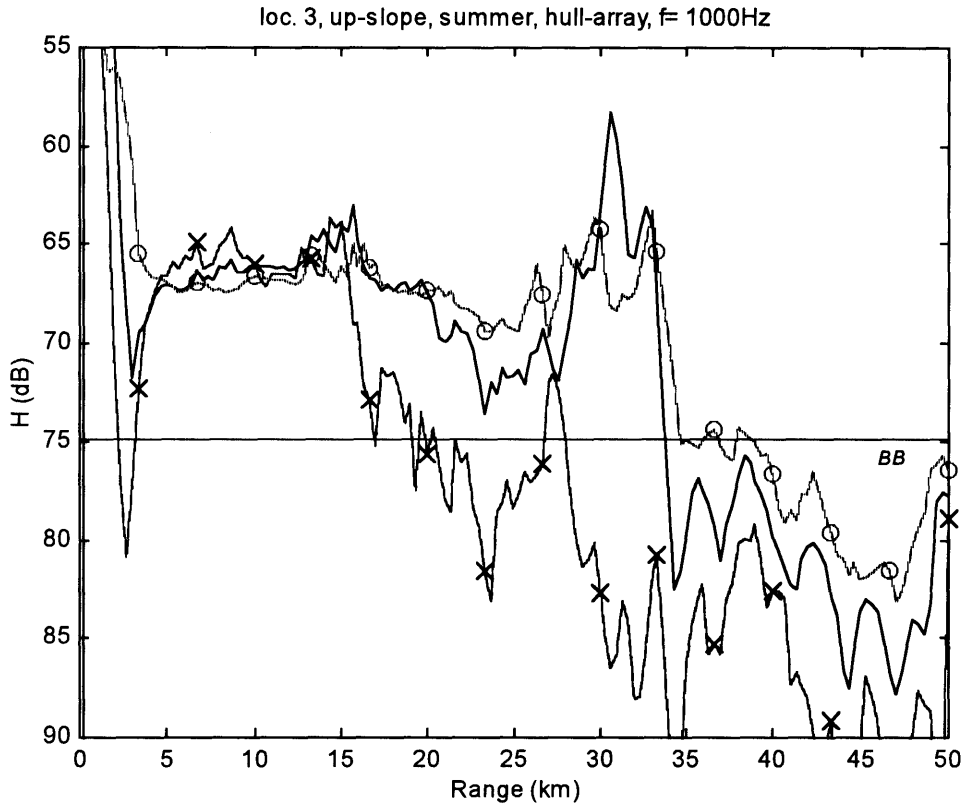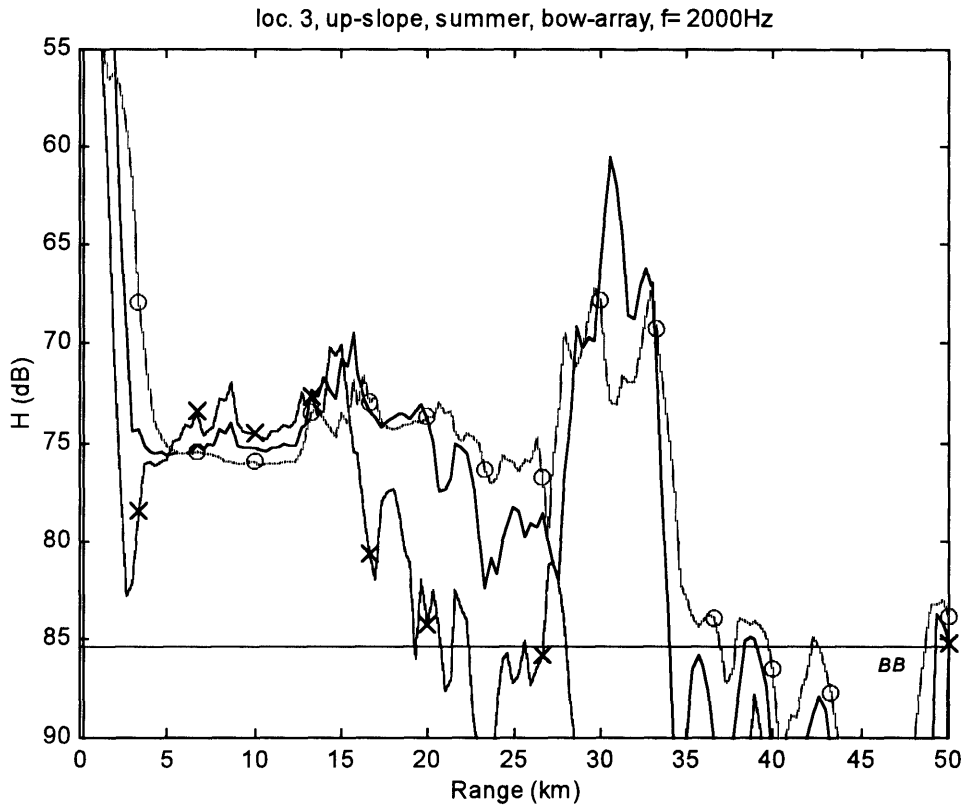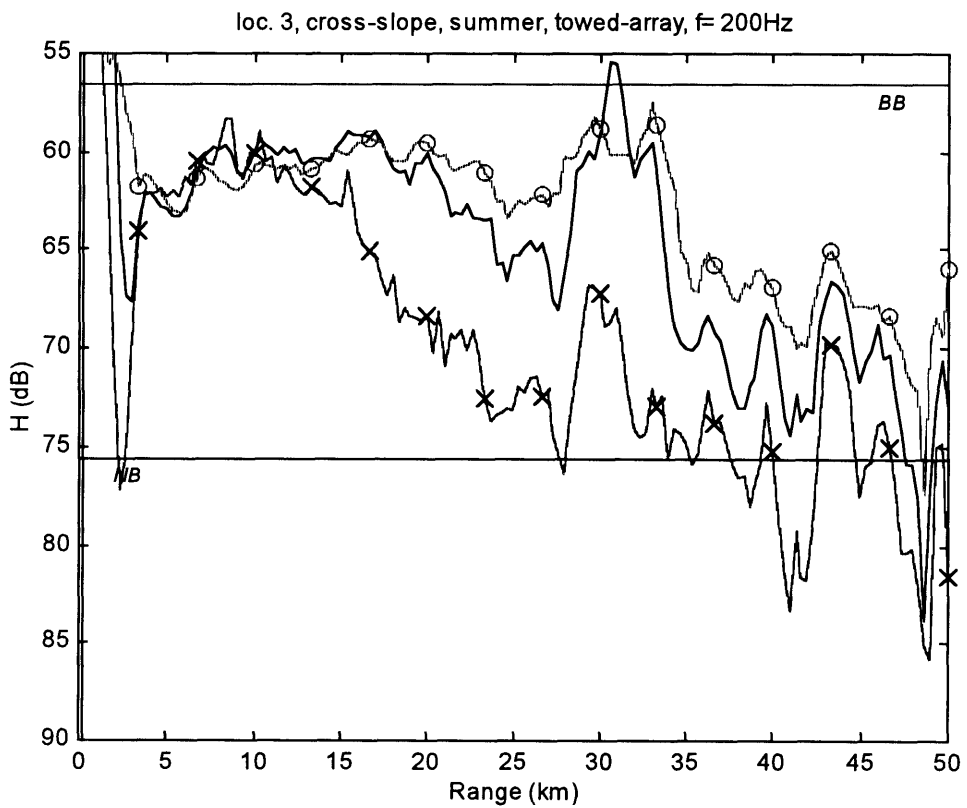loc. 3, down-slope, summer, bow-array, f= 5000Hz
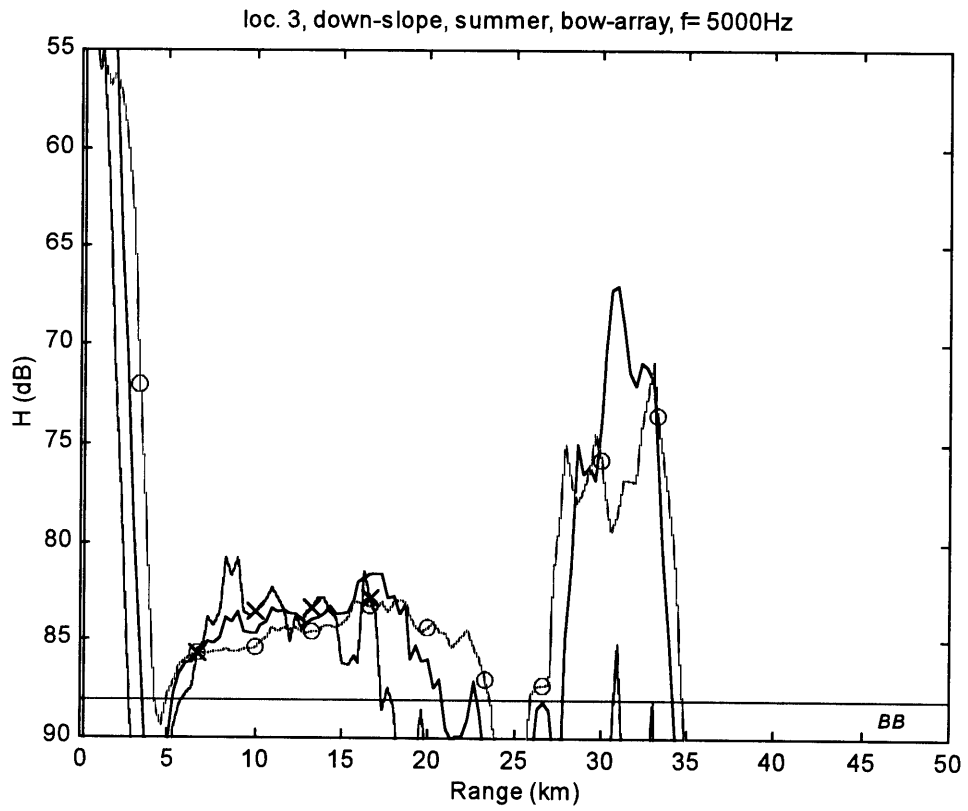
Figure A.144: Sonar performance, 3rd location.

Appendix B

A Note on Horizontal Refraction

Many numerical and analytical acoustics models, especially those which involve full wave solution, handle only horizontally stratified layers in the water column as well as in the bottom. The reason for that is the absence of a fully range dependent algorithm that can take into account an arbitrary bottom shape. The problem becomes even more severe when one would like to solve the wave equation in a 3–D environment. The latter case is more realistic and at the same time much more difficult to deal with. Here the propagation problem is not limited to the plane connecting source and receiver (as an ordinary 2–D problem) but includes other paths that exist due to bottom slopes that are greater than zero. This effect becomes more substantial as the number of bottom interactions increases. This phenomenon is called 'horizontal refraction' of sound. The receiver, in this case, may receive the source signal from different directions, and may interpret those signals as different sources. When sonar systems are concerned those signals should be considered as noise. Horizontal refraction is ignored in this study due to its complexity , however, the next paragraph provides some physical insight to this effect in view of its importance.
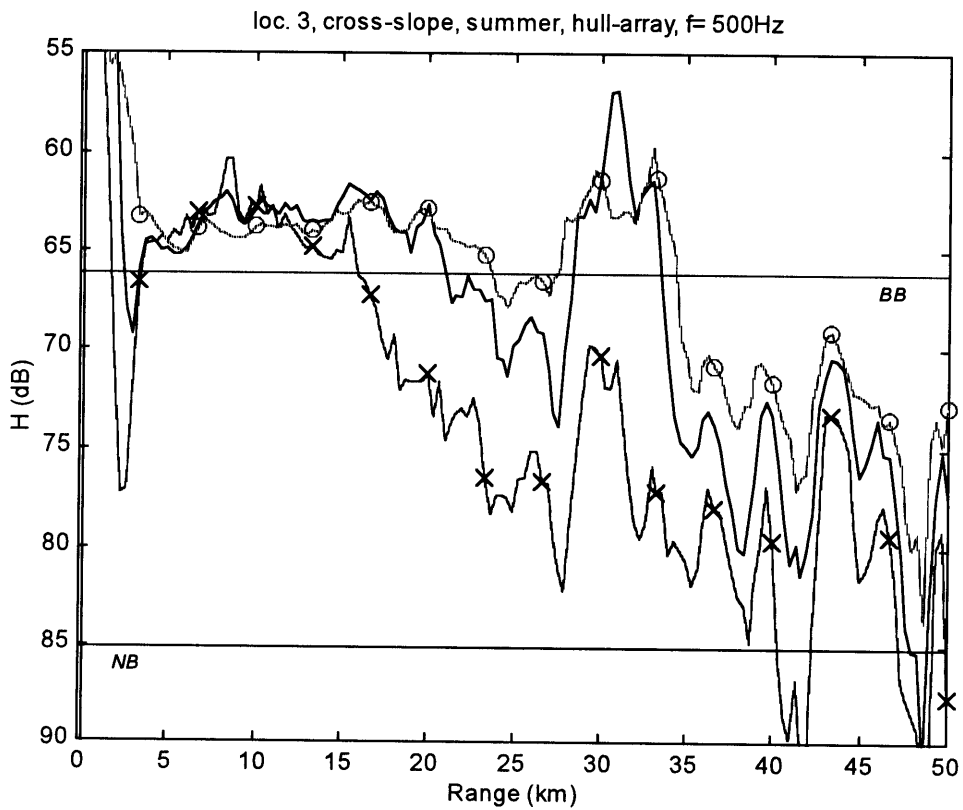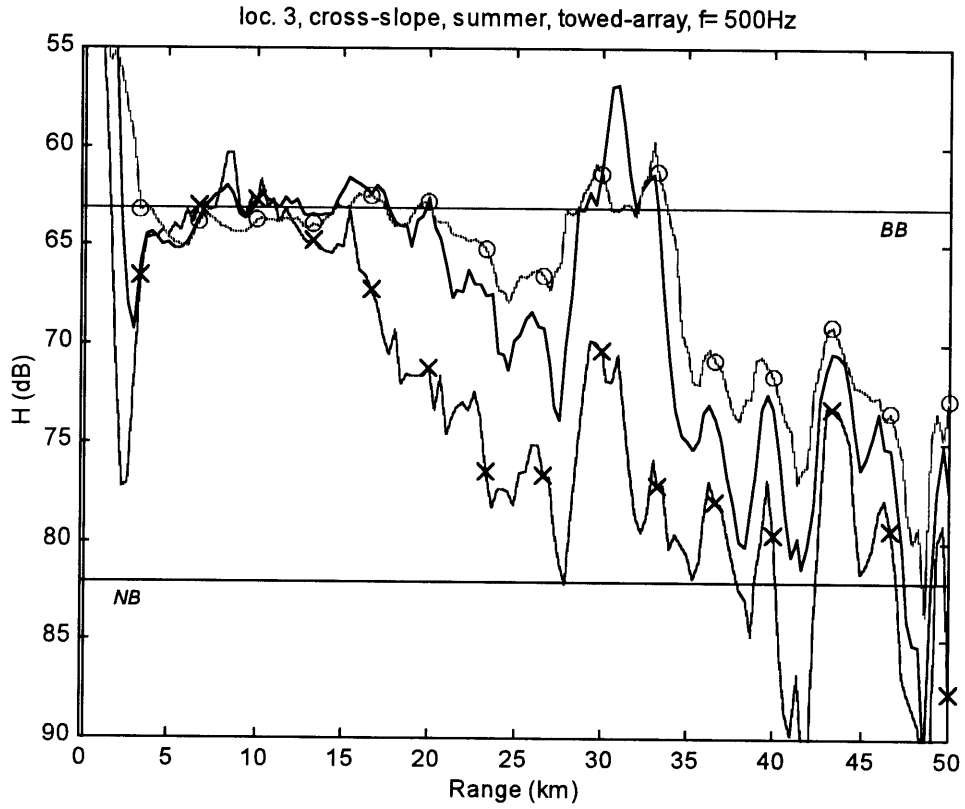
Horizontal refraction is well covered in the literature. It was first dealt with by Weston [1, 2], and further investigated by Milder [3], Harisson [4], and Tolstoy *et al* [5]. Reflections from sloping bottom is hard to visualize but can be derived using spherical trigonometry. The relations between incident ray and reflected ray [2]

$$\sin\theta_2 = \cos 2\gamma \sin\theta_1 + \sin\theta_1 \cos\theta_1 \cos\phi_1 \qquad (\text{B.1})$$

$$\cos\theta_2 \sin\phi_2 = \cos\theta_1 \sin\phi_1 \qquad\qquad\qquad (B.2)$$

where θ_1, ϕ_1 are incident ray elevation and azimuth angles respectively, θ_2, ϕ_2 are the corresponding reflected ray angles, and γ is the bottom slope aligned with the y axis as seen in Figure. If the medium is bounded by a plane upper surface and bottom of low slope it can be shown [4] that the elevation angle in the vertical plane can be written as

$$\sin\theta_n = (H_0/H_n)\sin\theta_0 \qquad\qquad\qquad (B.3)$$

where θ_n is the new elevation angle, θ_0 is the initial elevation angle, and H_0 and H_n are the initial and final water depths respectively. Since Equation (B.2) is true always it is considered an invariant of the ray and for the nth reflection from the bottom this equation becomes
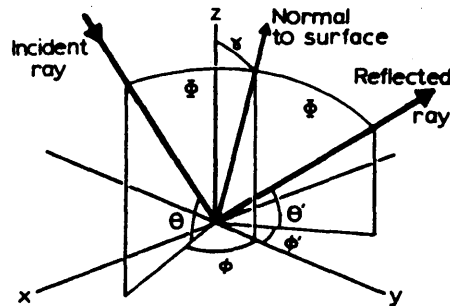
Figure 1: Ray geometry for a single reflection off sloping bottom [4].

$$\cos\theta_n \sin\phi_n = \cos\theta_0 \sin\phi_0 . \qquad (B.4)$$

Combining Equation(B.3) and Equation (B.4), assuming the horizontal projection of the ray approaches continuous curve, result a relation between the azimuth angle ϕ as a function of the initial parameters and final depth. It can be shown that for a trough case this relation is

$$\sin\phi = H(H^2 - H_0^2 \sin^2\theta_0)^{-1/2} \sin\phi_0 \cos\theta_0 \qquad (B.5)$$

and the corresponding travel distance along the trough is therefore

$$x = \int dy \tan\phi = \int \frac{\sin\phi_0 \cos\theta_0}{\left[\left(1 - \sin^2\phi_0 \cos^2\theta_0\right) - \left(H_0^2 / H^2\right)\sin^2\theta_0\right]^{1/2}} . \qquad (B.6)$$

Once the depth can be represented as a function of y the above integral can be solved and thus the ray path, y(x), can be determined. For circular mounts or basins the derivation should take advantage of the polar coordinates and the results are a bit different. It should be noted that the refraction due to changes in the sound velocity has not been included in the derivation and therefore the results are perfectly true for constant sound velocity profile. For other profiles the above results are only an approximation.

The validity of this approximation is examined in [6] but it is reasonable to state that when horizontal refraction is created after many bottom – surface reflections the vertical angles are relatively steep and thus making the ray curvature in the vertical plane less significant. In addition, one should investigate further and take into account the reflection coefficient for those steep angles as well. In order to illustrate this phenomenon, I present three cases of horizontal refraction in Figure B.2.

Horizontal refraction is only one among other phenomena that has an effect on the propagation of sound. In fact, A 1-D approximation of the bottom, like it is done in this study, might not be enough, especially near complex bottom shapes, as true for many parts in the Mediterranean sea and other ocean basins around the world. A deeper look into this topic, however, requires a separate attention.
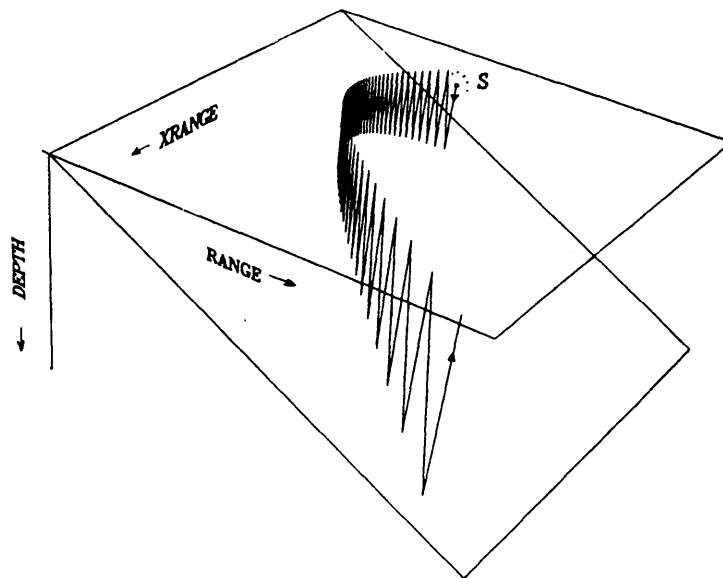
Figure 2: Examples of horizontal refraction of rays [5]

Appendix C

Sea-States Table

Table C-1: Relations between wind speed, wave height, and sea state [12].

Sea criteria	Beau-fort scale	Wind speed Range knots (m/sec)	Mean knots (m/sec)	12-h wind Wave height[a,b] ft (m)	Fully arisen sea Wave height[a,b] ft (m)	Duration[b,c] h	Fetch[b,c] naut. miles (km)	Sea-state scale
Mirror-like	0	<1 (<0.5)						0
Ripples	1	1-3 (0.5-1.7)	2 (1.1)					½
Small wavelets	2	4-6 (1.8-3.3)	5 (2.5)	<1 (<0.30)	<1 (<0.30)			1
Large wavelets, scattered whitecaps	3	7-10 (3.4-5.4)	8½ (4.4)	1-2 (0.30-0.61)	1-2 (0.30-0.61)	<2.5	<10 (<19)	2
Small waves, frequent whitecaps	4	11-16 (5.5-8.4)	13½ (6.9)	2-5 (0.61-1.5)	2-6 (0.61-1.8)	2.5-6.5	10-40 (19-74)	3
Moderate waves, many whitecaps	5	17-21 (8.5-11.1)	19 (9.8)	5-8 (1.5-2.4)	6-10 (1.8-3.0)	6.5-11	40-100 (74-185)	4
Large waves, whitecaps every-where, spray	6	22-27 (11.2-14.1)	24½ (12.6)	8-12 (2.4-3.7)	10-17 (3.0-5.2)	11-18	100-200 (185-370)	5
Heaped-up sea, blown spray, streaks	7	28-33 (14.2-17.2)	30½ (15.7)	12-17 (3.7-5.2)	17-26 (5.2-7.9)	18-29	200-400 (370-740)	6
Moderately high, long waves, spindrift	8	34-40 (17.3-20.8)	37 (19.0)	17-24 (5.2-7.3)	26-39 (7.9-11.9)	29-42	400-700 (740-1300)	7

[a] The average height of the highest one-third of the waves (significant wave height).
[b] Estimated from data given in U. S. Navy Hydrographic Office (Washington. D. C.) publications HO 604 (1951) and HO 603 (1955).
[c] The minimum fetch and duration of the wind needed to generate a fully arisen sea.

Appendix D

Matlab Code

The following code generates the ray trajectories and amplitude associated with the rays for the first location as an example. This m-file uses the m-file raytrace.m which is also attached.

```
%       FILE NAME: WINRAY1.M
%       ----------------------
%
%       THIS M-FILE GENERATES RAY TRACE DIAGRAM
%       AROUND THE FIRST LOCATION (31 Long, 35 Lat)
%       FOR WINTER TIME. THIS M-FILE USES THE FILE
%       RAYTRACE.M THAT ACTUALLY GENERATES THE
%       RAY DIAGRAM.
%       RAYTRACE.M MUST HAVE THE FOLLOWING VARIABLES
%       DEFINED:
%               C - SOUND VELOCITIES Vs. DEPTH [M/S]
%               z - DEPTH MEASUREMENT POINTS [M]
%               Sdepth - SOURCE DEPTH [M]
%               Sdis - SOURCE DISTANCE FROM CENTER [M]
%               theta - RAY LAUNCH ANGLES [RAD]
%               BotSlp - BOTTOM SLOPE [DEG]
%               BotDpt - BOTTOM DEPTH (CENTER) [M]
%
%       NOTE THAT RAYTRACE.M USES INTERSVP.M TO GENERATE
%       THE INTERPOLATED SOUND VELOCITY AT EACH
%       DEPTH THAT LIES BETWEEN THE SURFACE AND
%       THE BOTTOM. INTERSVP.M CAN INTERPOLATE THE DATA
%       LINEARLY OR USING MATLAB SPLINE TECHNIQUE.
%
%       Source Location
%       ----------------
%
Sdepth = 100;           % Source Depth
Sdis = 0;            % Source Distance from center point
f=250;                  % Source Freq
%
```

```
%       Sound Velocity Profile for Location #1
%       ----------------------------------------
%
cd data;            % Loading svp for Summer time
load winsvp.mat;    % Path may be different !
cd ..
%
C=winSVP1; C=[C(1) C];
z=bdpt; z=[0 z];
%
%       Bottom Depth
%       ------------
%
BotDpt = 2200;
%
%       Bottom Slope
%       ------------
%
BotSlp = 0.1;
%
%       Launch Angles
%       -------------
%
theta=linspace(-pi/5,0,60);
theta=[theta , -theta(length(theta)-1:-1:1)];
%
%       Calling RAYTRACE.M
%       ------------------
%
raytrace
figure(2), title('Ray Trace - Loc. 1 - winter');
figure(1); title('SVP - Loc. 1 - winter'),
axis([1510 1550 0 2500]);
%%%%%%%%%%%%%%%%%%%%%%%%%%%%%%%%%%%%%%%%%%%%%%%%%%%%
%       FILE NAME: RAYTRACE.M
%       ---------------------
%
%       THIS M-FILE GENERATES RAY TRACE DIAGRAM
%       AROUND THE LOCATIONS OF INTERESTS GIVEN
%       SVP. ALSO, IT IS ASSUMED THAT THE RANGE
%       DEPENDENCY OF THE SVP CAN BE IGNORED.
%       THE SEA SURFACE IS TAKEN TO BE HORIZONTALLY
%       FLAT AND THE BOTTOM IS CONSIDERED TO BE FLAT
%       WITH A SPECIFIC SLOPE.
%       THE AMPLITUDE OF EACH RAY TUBE IS ALSO
%       CALCULATED.
%
%       VARIABLES THAT MUST BE DEFINED:
%               C - SOUND VELOCITIES Vs. DEPTH [M/S]
%               z - DEPTH MEASUREMENT POINTS [M]
%               Sdepth - SOURCE DEPTH [M]
%               Sdis - SOURCE DISTANCE FROM CENTER [M]
%               theta - RAY LAUNCH ANGLES [RAD]
%               BotSlp - BOTTOM SLOPE [DEG]
%               BotDpt - BOTTOM DEPTH (CENTER) [M]
```

```
%              f - Source Frequency
%
%
%       Setting Initial Conditions
%       --------------------------
%
Rcoor(1)=Sdis; Zcoor(1)=Sdepth; B=BotSlp*pi/180;% Initial coordinates
[Svel,dcdz,dcdr]=intersvp(z,C,Sdepth,Sdis);     % Initial sound velocity
Tr_Time(1)=0;                                    % Initial travel time
Freq=f; omega=2*pi*Freq;                         % Source frequency
Cos_Theta(1)=cos(theta(1));                      % Initial angle
SR(1)=0; m(1)=0; Ai=0+1i;                        % # of surface reflections
RayPhase(1)=1;                                   % Initial Phase
AO(1)=1;                                % Initial Amplitude
d_z(1)=0;                               % Initial d_z
figure(1), clf,
plot(C,z), axis('ij');
title('Sound Speed Profile'), xlabel('C [m/s]'), ylabel('Depth [m]');
%
%       Begining of Main Program
%       ------------------------
%
h=1;                                    % integration step
RM=50000;
%
%       Main Loop
%       ---------
%
for j=1:length(theta),
    j
    SR(1)=0;
    xsi(1)=cos(theta(j))/Svel(1); zi(1)=sin(theta(j))/Svel(1);
%
%       Second Loop (marching in range and depth)
%       -----------
%
    i=1;
    while Rcoor(i)<RM
       [Svel(i),dcdz(i),dcdr]=intersvp(z,C,Zcoor(i),Rcoor(i));
       xsi(i+1)=xsi(i)-h*dcdr/((Svel(i))^2); % in our case dcdr=0
       zi(i+1)=zi(i)-h*dcdz(i)/((Svel(i))^2);
       Rcoor(i+1)=Rcoor(i)+h*Svel(i)*xsi(i);
       Zcoor(i+1)=Zcoor(i)+h*Svel(i)*zi(i);
       Tr_Time(i+1)=Tr_Time(i)+h/Svel(i);
       Cos_Theta(i+1)=xsi(i+1)*Svel(i);
%
%          Acount for reflections
%          ----------------------
%          --> from the surface:
%          ----------------------
%
         if (Zcoor(i+1)<=0),
          zi(i+1)=-zi(i+1);
          Zcoor(i+1)=Zcoor(i)-h*Svel(i)*zi(i);
          SR=1;
```

286

```
%
%           -->  from the bottom:.
% ---------------------
%
    elseif (Zcoor(i+1)>=BotDpt-Rcoor(i)*(tan(BotSlp*pi/180))),
        tmptheta=asin(abs(zi(i+1))*Svel(i))+B;
        zi(i+1)=-sin(tmptheta)/Svel(i);
    if (BotDpt-Rcoor(i)*tan(B)<=1),
        Zcoor(i+1)=0;
        Rcoor(i+1)=50000;
        zi(i+1)=0; Rcoor=real(Rcoor); Zcoor=real(Zcoor); end;
    end;
    if (Rcoor(i+1)>50000),
        Rcoor(i+1)=50000; Zcoor(i+1)=Zcoor(i);
        Svel(i)=inf;
    end;
%
% Intensity Calculations
% ---------------------
%
    if (j>=2),
        d_theta=theta(j-1)-theta(j);
        Ind=max( find( TTlast<=Tr_Time(i+1) )) ;
        d_z(i+1)=Zlast(Ind)-Zcoor(i+1);
        if (abs(d_z(i+1))<0.001), d_z(i+1)=1e-3; end;
        Jacobian=Rcoor(i+1)/Cos_Theta(i+1)*d_z(i+1)/d_theta;
        if ( sign(d_z(i+1))~=sign(d_z(i)) ), m=(m+1)*sign(i-1);   end;

AO(i+1)=1/4/pi*sqrt(abs(Svel(i)*cos(theta(j))/Svel(1)/Jacobian));
        end;
    if Zcoor(i)<60,   h=5;
        elseif Zcoor(i)>300, h=30;
        else h=20; end;
        i=i+1;
    end; % of while
    TTlast=real(Tr_Time); Zlast=Zcoor; mind=length(Rcoor);Svel(i)=Svel(i-
1);
Rres=fix(RM/150); R1=1:Rres:RM;
Z(j,:)=(interp1(Rcoor,Zcoor,R1))';
SV(j,:)=(interp1(Rcoor,real(Svel),R1))';
if (j>=2),
        if (j==2), A(1,:)=(interp1(Rcoor,AO,R1))'; end;
        A(j,:)=(interp1(Rcoor,AO,R1))'; end; m=0; i=1; Rcoor=1;
Zcoor=Sdepth; Svel=Svel(1);
        AO=AO(1); Tr_Time=Tr_Time(1);
    end;
end;
%
%       Plot Ray Trace Diagram
%       ---------------------
%
figure(2), clf;
axes('position',[0.1 0.2 0.1 0.7]);
plot(C,z,'w'), grid, axis('ij'); set(gca,'FontSize',8),
axis([1510 1550 0 BotDpt+300]);
```

```
title('Sound Speed Profile'), xlabel('C [m/s]'), ylabel('Depth [m]');
axes('position',[0.25,0.2,0.65,0.7]);
plot(R1./1e3,Z','w'), axis([0 RM/1000 0 BotDpt+300]);
r=linspace(1,50,100);
BotCrv=BotDpt-r.*tan(BotSlp*pi/180)*1e3;
hold on
plot(r',BotCrv','.w'), axis ij, hold off; set(gca,'FontSize',8);
title('Ray Trace - loc#? - win/sum'), xlabel('Range [km]');
end;
%%%%%%%%%%%%%%%%%%%%%%%%%%%%%%%%%%%%%%%%%%%%%%%%%%%%%%%%%%%%%%%%%%%%%%%
```

The next files generate the pressure field using the ray trajectories and other parameters that were defined in the previous code.

```
%%%%%%%%%%%%%%%%%%%%%%%%%%%%%%%%%%%%%%%%%%%%%%%%%%%%%%%%%%%%%%%%%%%%%%%
%load ray path data for any location and season
SONAR = 'bow-array, ';
slp = 'down-slope, ';
f=5000;
Location=3;
season='summer, ';
%error;
As = smooth2(A);    %       smoothing the amplitude
                    %       add bottom and surface losses
Al = getloss(As,Z,R1,f,season,SV,theta,SONAR,slp);
tl_ray;             %       generate pressure field
load c:\thesis\data\tp.mat
TPw=[TPw(:,1), TPw];
TPs=[TPs(:,1), TPs];
if season(1:3)=='win'
      TP=TPw(Location,:);
else
      TP=TPs(Location,:);
end;
TL=volabs(Tr_Loss,Depth,R,f,TP,z);% add volumetric absorption
plotl(TL,Range,f,Location,slp,season,SONAR);%plotting
end;
%%%%%%%%%%%%%%%%%%%%%%%%%%%%%%%%%%%%%%%%%%%%%%%%%%%%%%%%%%%%%%%%%%%%%%
function As = smooth (A);
% Smooth
%
%       USAGE: As = smooth (A, Z, R1, f, season, SV, theta, sonar, slp)
%       A:      unsmoothed amplitude
%
%       As:     Smoothed
%
disp('--->>>> smoothing amplitude <<<<----');
[M,N] = size( A );
% M: number of rays
% N: number of points on each ray
for i = 1:M
```

```
%       disp(['ray #',num2str(i)]);
        for j = 5:N-5
        if A(i,j)>A(i,j-1)
             x1 = 0.2*A(i,j-1) + 0.2*A(i,j+1);
             x2 = 0.1*A(i,j-2) + 0.2*A(i,j+2);

             A(i,j)=0.4*A(i,j)+x1+x2;
        end;
        end;
end;
As=A;
end;
%%%%%%%%%%%%%%%%%%%%%%%%%%%%%%%%%%%%%%%%%%%%%%%%%%%%%%%%%%%%%
function Aloss = getloss (A, Z, R1, f, season, SV, theta, sonar, slp)
% GETLOSS generates the amplitude of the rays with bottom/
%       surface loss using Fresnel forward scatter model.
%
%       USAGE: Aloss = getloss (A, Z, R1, f, season, SV, theta, sonar, slp)
%       A
%       Z
%       R1
%       f
%       season
%       SV
%       theta
%       sonar: 'towed' or 'hull' or 'bow'
%       slp: 'cros' or 'up' or 'down'
%
%       Aloss:       Amplitude with loss
%
disp('--->>>> applying bottom loss and surface loss <<<<---');
[M,N] = size( A );
Loss = 1;
New_Loss = 1;
if (sonar(1:2)=='to')
        bw = 0.1
elseif (sonar(1:2)=='hu')
        bw = 1535/f/30
elseif (sonar(1:2)=='bo')
        bw = 1672.5/f/pi
end;
%pause;
for i = 1:M
%       disp(['ray #',num2str(i)]);
        x1 = Z(i,2) - Z(i,1);
        for j = 2:N-1
                %disp(j);
                x2 = Z(i,j+1) - Z(i,j);
                if (x2*x1 < 0)
                        sigma = cos( theta(i) ) / SV(i,1);
                        if (x1 > 0)
                                %disp(['bottom', num2str(j)]);
                                New_Loss =
        bottml(f,season,SV(i,j),SV(i,j)*sigma,R1(j),bw,slp);
                        else
```

```
                                   %disp(['surface', num2str(j)]);
                                   New_Loss = surfac( f, season, SV(i,j),
SV(i,j)*sigma );
                         end;
                  Loss = Loss * New_Loss; %disp([New_Loss,Loss]);
                  end;
                  A(i,j) = A(i,j) * Loss;
                  x1 = x2;
         end;
         A(i,N) = A(i,N-1);
         Loss = 1;
end;
Aloss=A;
end;
%%%%%%%%%%%%%%%%%%%%%%%%%%%%%%%%%%%%%%%%%%%%%%%%%%%%%%%%%%%%%%%%%%%%%%%%
%        File Name: TL_RAY.m
%
%        Transmission Loss Calculation
%        Based on Ray theory and linear
%          Interpolation Technique.
%        ------------------------------------
%
%        Generating new matrices representing
%        Amplitude, Phase, Range, and Depth
%        ------------------------------------
%
%        Setting the Pressure matriz dimentions and resolution
%        ------------------------------------------------------
Vres=10;
%Hres=200;
Depth=0:Vres:BotDpt+500;
Range=R1;
%omega=Freq*2*pi;
temp1=0; temp2=0; Ai=0+1i;
Pressure=zeros(length(Depth),length(Range))+1e-20;
%
%        Creating the matrices in (r,z)
%        ------------------------------
%
Zray=Z';
Amp=Al';
%
%        Main Loop - # of Ray Tubes
%        --------------------------
%
for i=1:length(theta)-1
%
%        Generate pressure field for each ray tube
%        -----------------------------------------
%
for k=1:length(Range)
     Zmin=min(Zray(k,i),Zray(k,i+1));
     Zmax=max(Zray(k,i),Zray(k,i+1));
     Lmin=Vres*ceil(Zmin/Vres);
     Lmax=Vres*floor(Zmax/Vres);
```

```
%for l=Lmin:Vres:Lmax
    if Lmax<Lmin, Lmax=Lmin; end;
    l=Lmin:Vres:Lmax;
        if (l(1)>Zray(k,i) & l(1)<Zray(k,i+1)) | (l(1)>Zray(k,i+1) &
l(1)<Zray(k,i)),
            temp1=interp1(Zray(k,i:i+1),Amp(k,i:i+1),l);
        end;

        LocalPr=4*pi*temp1; %.*exp(Ai*(omega*temp2));
        Pressure(l./Vres+1,k)=Pressure(l./Vres+1,k)+LocalPr;
        temp1=0; temp2=0;
end;
i
end;
Tr_Loss=-20*log10(abs(Pressure));
freemem; clear Amp; clear Zray; clear Pressure;
%
%        Plotting TL
%        -----------
%
map=[0.6 0.4 0; 0.9 0.5 0;1 1 0;0 0.8 0;0 0.7 1;0 0 0.7];
figure(1);
pcolor(Range./1e3,Depth,Tr_Loss), axis ij, shading flat,
caxis([50 110]), colormap(map), colorbar,
xlabel('Range [km]'), ylabel('Depth [m]'), title('Transmission Loss');
figure(2);
subplot(3,1,1);
plot(Range./1e3,Tr_Loss(6,:)), axis ij, axis([0 50 50 120])
title('H, SD=100m, RD=50m, Freq=250Hz, winter, Loc#1');
ylabel('Loss [dB]');
subplot(3,1,2);
plot(Range./1e3,Tr_Loss(11,:)), axis ij, axis([0 50 50 120])
title('H, SD=100m, RD=100m, Freq=250Hz, winter, Loc#1');
ylabel('Loss [dB]');
subplot(3,1,3);
plot(Range./1e3,Tr_Loss(15,:)), axis ij, axis([0 50 50 120])
title('H, SD=100m, RD=150m, Freq=250Hz, winter, Loc#1');
xlabel('Range [km]'), ylabel('Loss [dB]');
R=Range/1e3;
figure(3)
H=[Tr_Loss(6,:);Tr_Loss(11,:);Tr_Loss(16,:)]';
plot(R,H(:,1),'w',R,H(:,2),'--w',R,H(:,3),':w'), axis ij, axis([0 50 50
100])
title('Loc , slope, winter, num2str(f), array');
xlabel('Range (km)')
ylabel('H (dB)')
end;
%%%%%%%%%%%%%%%%%%%%%%%%%%%%%%%%%%%%%%%%%%%%%%%%%%%%%%%%%%%%%%%%%%%%%%%%
function TL = volabs (Tr, D, R, F, TP, TPdepth)
% VOLABS CALCULATES THE VOLUMETRIC ABSORPTION DUE
% TO RELAXATION MECHANISMS IN SEA WATER.
%
%        USAGE:        TL = volabs(Tr,D,R,F,TP);
%        Tr:    Transmission loss from ray theory
```

```
%       D:      depth vector
%       R:      Range vector in km
%       F:      Frequency in Hz
%       TP:     Temperature Profile in c
%       TPdepth:Corresponding depths of TP
%
[M, N] = size( Tr );
T = interp1(TPdepth, TP, D);
for i=1:M % loop on number of dpeths
        alfa = absorp (T(i), D(i), F/1000);
        alfaR = alfa * R;
        TL(i,:) = Tr(i,:) + (alfaR);
end;
%%%%%%%%%%%%%%%%%%%%%%%%%%%%%%%%%%%%%%%%%%%%%%%%%%%%%%%%%%%%%%%%%%%%%%%%%
function L = bottml(f,season,c,cos_theta,R,dphi,slope)
% BOTTML generates the bottom loss (5kzsin(th))
%
%       USAGE: L = bottml(f,season,c,cos_theta,R,dphi,slope);
%       f
%       season
%       c
%       cos_theta
%       R
%       dphi: beamwidth in radians
%       slope: 'cros' or 'up' or 'down'
%
%       L = the loss (not in dB)
%
k = 2 * pi * f / c;
sin_theta = real(sqrt( 1 - cos_theta^2 ));
T=0.31; % integration time
L=obscl(c,T,cos_theta,R,dphi,slope); % observation scale
%[L,R,cos_theta]
if (L>=250)
        z=0.023*L^0.5;
else
        z=0.008*0.35*L;
end;
%disp(['RMS roughness hieght =' num2str(z)]);
tmp = 5 / 20 * k * z * sin_theta;
L = 1 / 10^tmp;
%disp(['Loss (dB) = ' num2str(20*log10(L))]);
%pause;
if imag(L)~=0,
        cos_theta
        sin_theta
        c
        tmp
        pause;
end;
end;
%%%%%%%%%%%%%%%%%%%%%%%%%%%%%%%%%%%%%%%%%%%%%%%%%%%%%%%%%%%%%%%%%%%%%%%%%
function L = surfac(f,season,c,cos_theta)
% SURFACE generates the surface loss (5kzsin(th))
%
```

```
%      USAGE:  L = surfac(f,season,c,cos_theta);
%      f
%      season
%      c
%      cos_theta
%
%      L = the loss (not in dB)
%
k = 2 * pi * f / c;
sin_theta = real(sqrt( 1 - cos_theta^2 ));
if (season(1:3) == 'win')
      z = 1;
else  z = 0.2;
end;
tmp = 5 / 20 * k * z * sin_theta;
L = 1 / 10^tmp;
end;
%%%%%%%%%%%%%%%%%%%%%%%%%%%%%%%%%%%%%%%%%%%%%%%%%%%%%%%%%%%%%
function alfa = absorp( Temp,depth,freq )
% ALFA GENERATES THE ABSORPTION COEFFICIENT GIVEN
% TEMPERAUTE, DEPTH, AND FREQUENCY. THE FORMULAS
% ARE TAKEN FROM DYER [7]
%
%      USAGE:        alfa = absorp ( Temp, depth, freq );
%      Temp: Temperature in C
%      depth:        depth in m
%      freq: frequency in kHz
%
%      alfa: absorption coefficient
%
S = 39;
P = (depth/10 +1);
T = Temp+273;
f = freq;
f3 = 1.55*1e4*T*exp(-3052/T);
f4 = 1.32*T*exp(-1700/T);
alfa2 = 2.94*1e-2*freq^2/f3;
tm = 2.03*(1e-2)*f3*((f/f3)^2)/(1+(f/f3)^2);
alfa3 = S*(1-6.54*(1e-4*P))*tm;
alfa4 = 1.1*1e-1*f4*(f/f4)^2/(1+(f/f4)^2);
alfa = alfa2+alfa3+alfa4;
end;
%%%%%%%%%%%%%%%%%%%%%%%%%%%%%%%%%%%%%%%%%%%%%%%%%%%%%%%%%%%%%
function Lamda=obscl(c,T,cos_theta,R,dphi,slope);
% OBSCL CALCULATES THE OBSERVATION SCALE, LAMDA.
%
%      Usage: Lamda = obscl(c,T,cos_theta,T,dphi,slope);
%      c
%      cos_theta
%      R
%      dphi
%      slope
%
%      Lamda: observation scale in m
%
```

```
Lamdai=c*T/cos_theta;
Lamdaj=R*dphi;
tmp=Lamdai/Lamdaj;
if (tmp>5) | (tmp<0.2)
      Lamdaj=sqrt(Lamdai*Lamdaj);
end;
if (slope(1:2)=='cr')
      Lamda=Lamdai;
%       disp(['cross slope ',num2str(Lamda)]);
%       pause
else  Lamda=Lamdaj;
%       disp(['up/down slope ',num2str(Lamda)]);
%       pause
end;
end;
%%%%%%%%%%%%%%%%%%%%%%%%%%%%%%%%%%%%%%%%%%%%%%%%%%%%%%%%%%%%%%%%%%%
%%%%%%%%%%%%%%%%%%%%%%%%%%%%%%%%%%%%%%%%%%%%%%%%%%%%%%%%%%%%%%%%%%%
```

Bibliography

[1] D.E. Weston. "Guided propagation in a slowly varying medium." *Proc. Phys. Soc. London*, 73: 365 – 384, 1959.

[2] D.E. Weston. "Horizontal refraction in a three-dimensional medium of variable stratification." *Proc. Phys. Soc. London*, Vol. 78, pp. 46–52, 1961.

[3] D. M. Milder. "Ray and wave invariants for SOFAR channel propagation." *J. Acoust. Soc. Am.*, Vol. 46, pp. 1259–1263, 1969.

[4] C. H. Harisson. "Three–dimentional ray paths in basins, troughs, and near seamounts by use of ray invariants." *J. Acoust. Soc. Am.*, Vol. 62, pp. 1382–1388, December 1977.

[5] R. Doolitale, A Tolstoy, and M. Buckingham. "Experimental confirmation of horizontal refraction of CW acoustic radiation from a point source in a wedge–shaped ocean environment." *J. Acoust. Soc. Am.*, Vol. 83, pp. 2117–2125, June 1988.

[6] C. H. Harisson. "Horizontal ray curvature effects in basins, troughs, and near seamounts by use of ray invariants." *NRL Report*, No. 8144, 1977.

[7] I. Dyer. *Lecture Notes of 13.851.* MIT, Cambridge, 1996.

[8] F. B. Jensen, W. A. Kuperman, M. B. Porter, and H. Schmidt. *Computational Ocean Acoustics.* AIP Press, New York, 1994.

[9] C. S. Clay and H. Medwin. *Acoustical Oceanography: Principles and Applications.* John wiley and Sons, New York, 1977.

[10] T. H. Bell, Jr. *Mesoscale sea floor roughness.* In: *Deep-Sea Research.* Vol. 26A, pp. 65-76. Pergamon Press Ltd., 1979.

[11] R. J. Urick, *Principle of underwater sound,* 3rd ed. Mcgraw-Hill, New York, 1983.

[12] G. M. Wenz, "Acoustical ambient noise in the ocean: spectra and sources." *J Acoust. Soc. Am.,* Vol. 34, pp. 1936-1956, 1962.

[13] A. B. Baggeroer, *Sonar signal processing.* In: *Applications of Digital Signal Processing,* edited by A. V. Oppenheim, Prentice-Hall, Englewood Cliffs, NJ, 1978.

[14] W. S. Burdic, *Underwater Acoustic System Analysis,* 2nd ed., Prentice-Hall, Englewood Cliffs, NJ, 1991.

[15] G. V. Frisk, *Ocean and Seabed Acoustics - A theory of Wave Propagation,* Prentice-Hall, Englewood Cliffs, NJ, 1994.

[16] I. Tolstoy, C. S. Clay, *Ocean Acoustics - Theory and Experiments in Underwater Sound,* AIP-Press, New York, 1987.

[17] G. Almagor, J. K. Hall, "Morphology of the Mediterranean continental margin of Israel." *Isr. Geol. Surv.,* No. 77, pp. 1-31, 1984.

[18] N. Kran, "Analysis of bathymetric data and sedimentation near Ashdod Harbor." *Isr. Geol. Surv.,* Rep. No. MG/6/80, 1980.

[19] D. Neev, "Submarine geological studies in the continental shelf and slope off the Mediterranean coat of Israel." *Isr. Geol. Surv.,* N.S.F. Grant No. G-19796, 1965.

[20] K. F. Herzfeld, And T. A. Litovitz, *Absorption and Dispersion of Waves*, Academic Press, New York, 1959.

[21] F. H. Fisher, and V. P. Simmons, "Sound absorption in sea water," *J. Acoust. Soc. Amer.* Vol. 62, pp. 558-564, 1977.

[22] J. W. Horton, *Fundamentals of Sonar*, U.S. Naval Institue, Annapolis, Maryland, 1959.

[23] C. T. Molloy, "Calculation of the directivity index for various types of radiators." *J. Acoust. Soc. Am.*, Vol. 20, pp. 387-405, 1948.

[24] R. J. Bobber, "Diffraction canstants of tranducers." *J. Acoust. Soc. Am.*, Vol. 37, pp. 591-595, 1965.

[25] J. A. Shotter, T. E. Demary, A. F. Wittenborn, "Depth dependence of noise resulting from ship traffic and wind," *J. Oceanic Eng.*, Vol. 15, pp. 292-298, 1990.

[26] H. Shmidt, "SAFARI," user's guide, 1994.

[27] V. C. Anderson, J. C. Munson, "Directivity of spherical arrays." *J. Acoust. Soc. Am.*, Vol. 35, pp. 1162-1168, 1963.

[28] A. Tolstoy, D. H. Berman, E. R. Franch. "Ray theory versus the parabolic equation in a long range duct environment." *J. Acoust. Soc. Am.*, Vol. 78, pp. 176-189, 1985.

[29] D. Neev, "Submarine geological studies in the continental shelf and slope off the Mediterranean coast of Israel." *Isr. Geol. Surv.*, Rep. No. G-19796, May 1965.

[30] A. V. Oppenheim, A. S. Willsky, I. T. Young, *Signals and Systems*. Prentice-Hall, Englewood Cliffs, NJ, 1994.

[31] P. Brasseur, J. M. Beckers, J. M. Brankart, "Seasonal temperature and salinity fields in the Mediterranean Sea: Climatological analysis of an historical data set." *dsr*, in press 1996.